

Unravelling reactive oxygen species production in low temperature, atmospheric pressure plasmas

Benjamin Harris

Doctor of Philosophy

University of York

School of Physics, Engineering and Technology

April 2024

Abstract

Low temperature plasmas (LTPs) are efficient sources of reactive oxygen and nitrogen species (RONS) at atmospheric pressure. Understanding how different parameters influence RONS production is essential for optimising LTP devices for biomedical applications. Several plasma sources are investigated here. First, a numerical model is used to study the influence of pulse repetition frequency on the plasma chemistry of a nanosecond-pulsed, He+H₂O plasma. Increasing the pulse repetition frequency increases the density of H, O, and OH radicals. H₂O₂ and O₃ are formed throughout the afterglow, and their density is instead found to depend on the afterglow duration, gas temperature, and radical densities. Next, cavity ring-down spectroscopy is used to determine the spatial distribution of H₂O₂ in the effluent of a COST-Jet and a kINPen-sci in He+H₂O. The H₂O₂ density near the jet nozzle is $2.3 \times 10^{14} \text{ cm}^{-3}$ for the kINPen-sci and $1.4 \times 10^{14} \text{ cm}^{-3}$ for the COST-Jet. The average H₂O₂ density in the effluent of the kINPen-sci is a factor of two higher than for the COST-Jet. The H₂O₂ distribution in the COST-Jet effluent is uniform near the jet nozzle but diluted beyond 15 mm. For the kINPen-sci, the H₂O₂ density near the nozzle has a comparatively pronounced radial spread, while dilution is more gradual at further distances. Finally, O₃ production is investigated for a He+O₂, radio-frequency plasma jet driven with tailored voltage waveforms. Increasing the number of harmonics in the driving waveform for a fixed peak-to-peak voltage enhances the O₃ density but significantly increases the gas temperature. Increasing the number of harmonics for a constant RF power allows the O₃ density in the effluent to be increased by a factor of 4, to a maximum of $5.7 \times 10^{14} \text{ cm}^{-3}$, without significant change to the gas temperature. It is hoped that the results presented in this work may help to optimise RONS production by biomedical plasma devices.

Contents

Abstract	2
List of Tables	6
List of Figures	7
Acknowledgements	11
Declaration	12
List of publications and communications	13
1 Introduction	15
1.1 Thesis motivation	15
1.2 Thesis outline	17
2 Fundamentals of low temperature plasmas	18
2.1 What is a plasma?	18
2.1.1 Sheaths	19
2.1.2 Atmospheric pressure plasmas	20
2.2 Nanosecond-pulsed discharges	22
2.2.1 Streamers	23
2.2.2 The afterglow	24
2.3 Radio-frequency discharges	24
2.3.1 Capacitively coupled plasmas	25
2.3.2 Operational modes in capacitively coupled plasmas	26
2.4 Dielectric barrier discharges	27

<i>CONTENTS</i>	4
2.5 Plasmas for biomedicine	28
2.5.1 Electron energy distribution function	29
2.5.2 Neutral plasma chemistry	31
2.5.3 Reactive oxygen and nitrogen species in the human body	32
2.5.4 Applications of plasmas in biomedicine	32
2.5.5 Atmospheric pressure plasma jets	33
2.6 Principles of plasma modelling	34
2.7 Principles of optical diagnostics	37
2.7.1 Line profiles	40
3 Plasma sources	42
3.1 COST Reference Microplasma Jet (COST-Jet)	42
3.2 Sealed atmospheric pressure plasma jet (S-APPJ)	43
3.3 kINPen-sci	44
3.4 Pin-to-pin plasma source	45
4 The influence of pulse repetition frequency on the plasma chemistry of a nanosecond-pulsed discharge in He+H₂O	47
4.1 Motivation	47
4.2 Methods	49
4.2.1 <i>GlobalKin</i>	49
4.2.2 He+H ₂ O+O ₂ chemistry set	52
4.2.3 Model parameters	53
4.3 Results and discussion	56
4.3.1 Electron behaviour	56
4.3.2 Radical chemistry	57
4.3.3 H ₂ O ₂ chemistry	61
4.3.4 O ₃ chemistry	65
4.4 Chapter summary	69
5 The spatial density distribution of H₂O₂ in the effluent of the COST-Jet and the kINPen-sci supplied with He+H₂O	70
5.1 Motivation	70

<i>CONTENTS</i>	5
5.2 Methods	73
5.2.1 Operating the COST-Jet and the kINPen-sci	73
5.2.2 Continuous wave cavity ring-down spectroscopy	74
5.2.3 Data analysis procedure	77
5.3 Results	79
5.3.1 Determination of the pressure broadening coefficient	79
5.3.2 Determination of spatially resolved densities	81
5.4 Discussion	86
5.4.1 Comparison of the distinct spatial distribution of H ₂ O ₂	86
5.4.2 Influence of the discharge type on the chemical pathways of H ₂ O ₂	87
5.4.3 Comparison of the pressure broadening coefficient	89
5.4.4 Comparison of argon and helium as a feed gas for the kINPen-sci	89
5.5 Chapter summary	91
6 O₃ production by an He+O₂ radio-frequency plasma jet driven by tailored voltage waveforms	92
6.1 Motivation	92
6.2 Methods	94
6.2.1 Tailored voltage waveforms	94
6.2.2 Description of the experimental setup	95
6.2.3 Ozone density from Fourier transform infrared spectroscopy	97
6.2.4 Gas temperature from optical emission spectroscopy	100
6.3 Results and discussion	102
6.3.1 Influence of the O ₂ admixture concentration	102
6.3.2 Influence of the peak-to-peak voltage	104
6.3.3 Influence of the applied harmonics I: Constant peak-to-peak voltage	107
6.3.4 Influence of the applied harmonics II: Constant RF power	112
6.4 Chapter summary	115
7 Summary and conclusions	117
A Reactions included in the He+H₂O+O₂ chemistry set	120
References	140

List of Tables

4.1	The 46 species included in the He+H ₂ O+O ₂ chemistry set.	52
A.1	Electron reactions included in the He+H ₂ O+O ₂ chemistry set	120
A.2	Ion-ion reactions included in the He+H ₂ O+O ₂ chemistry set	125
A.3	Ion-neutral reactions included in the He+H ₂ O+O ₂ chemistry set	131
A.4	Neutral reactions included in the He+H ₂ O+O ₂ chemistry set	136

List of Figures

2.1	Paschen curves for a selection of gases.	21
2.2	Representation of the complex interplay between operational parameters and plasma phenomena.	28
2.3	Model Maxwellian and Druyvesteyn electron energy distribution functions and electron energy probability functions.	30
2.4	Timescales spanned by different plasma processes.	35
3.1	Schematic of the COST-Jet.	42
3.2	Schematic of the S-APPJ.	43
3.3	Schematic of the kINPen-sci.	44
3.4	Schematic of the pin-to-pin plasma source.	45
4.1	The connections between <i>GlobalKin</i> 's core modules.	50
4.2	Characteristic current, voltage and power signals supplied by a nanosecond-pulsed negative voltage generator.	54
4.3	Modelled gas temperature, OH density and H ₂ O ₂ density as a function of the number of power cycles for a nanosecond-pulsed plasma source.	55
4.4	Average peak electron density per cycle as a function of the pulse repetition frequency.	56
4.5	Average atomic hydrogen density in equilibrium as a function of the pulse repetition frequency.	57
4.6	Average atomic oxygen density in equilibrium as a function of the pulse repetition frequency.	58
4.7	Average hydroxyl density in equilibrium as a function of the pulse repetition frequency.	58

4.8	Density of atomic hydrogen over one cycle as a function of normalised time for different pulse repetition frequencies.	59
4.9	Density of atomic oxygen over one cycle as a function of normalised time for different pulse repetition frequencies.	59
4.10	Density of hydroxyl over one cycle as a function of normalised time for different pulse repetition frequencies.	60
4.11	Average hydrogen peroxide density in equilibrium as a function of the pulse repetition frequency.	61
4.12	Rates of dominant H_2O_2 production reactions over one cycle for 1 kHz, 10 kHz, and 100 kHz pulse repetition frequencies.	62
4.13	Density of H_2O_2 over one cycle as a function of normalised time for different pulse repetition frequencies.	63
4.14	Rates of dominant H_2O_2 consumption reactions over one cycle for 1 kHz, 10 kHz, and 100 kHz pulse repetition frequencies.	63
4.15	Average gas temperature in equilibrium as a function of the pulse repetition frequency.	64
4.16	Average ozone density in equilibrium as a function of the pulse repetition frequency.	65
4.17	Rates of dominant O_3 production reactions over one cycle for 1 kHz, 10 kHz, and 100 kHz pulse repetition frequencies.	66
4.18	Density of O_3 over one cycle as a function of normalised time for different pulse repetition frequencies.	67
4.19	Rates of dominant O_3 consumption reactions over one cycle for 1 kHz, 10 kHz, and 100 kHz pulse repetition frequencies.	68
5.1	Schematic of the experimental setup used to supply the COST-Jet and the kINPen-sci with a $\text{He}+\text{H}_2\text{O}(0.33\%)$ gas mixture.	73
5.2	Schematic of the continuous wave cavity ring-down spectroscopy setup used to study the density of H_2O_2 in the effluent of the COST-Jet and the kINPen-sci.	74
5.3	Characteristic single ring-down event measured in the effluent of a $\text{He}+\text{H}_2\text{O}(0.33\%)$ plasma.	76

5.4	Model fit of a cavity loss spectrum measured by cw-CRDS in the effluent of the kINPen-sci, including a linear baseline fit and contributions from individual H_2O_2 transitions.	79
5.5	Relative change of the normalised line-integrated absorbance as a function of wavenumber for different axial positions.	80
5.6	The obtained pressure broadening coefficient, γ_L as a function of the axial position.	81
5.7	Measured radial distribution of the line-of-sight integrated H_2O_2 density at several positions along the effluent axis of the COST-Jet, together with applied Gaussian fits.	83
5.8	Measured radial distribution of the line-of-sight integrated H_2O_2 density at several axial positions along the effluent of the kINPen-sci, together with applied Gaussian fits.	83
5.9	The density amplitude n_0 and the Gaussian width w as a function of the axial position.	84
5.10	Density distribution of H_2O_2 in the effluent region of the COST-Jet and the kINPen-sci.	85
5.11	Relative uncertainty in the density of H_2O_2 in the effluent region of the COST-Jet and the kINPen-sci.	86
6.1	Representative peaks and sawtooth-up voltage waveforms for $N = 1$ to $N = 5$ consecutive harmonics.	95
6.2	Schematic of the experimental setup used to measure the ozone density and gas temperature of an APPJ driven by tailored voltage waveforms.	96
6.3	Comparison between measured applied voltage waveform and targeted waveform for peaks and sawtooth-up, with $N = 3$ harmonics.	97
6.4	Schematic of a Michelson interferometer used in Fourier transform infrared spectroscopy.	98
6.5	Measured FTIR absorption spectrum obtained in the far effluent of a $\text{He}+\text{O}_2(0.5\%)$ plasma.	99
6.6	Measured $\text{N}_2(C-B)$ optical emission spectrum and best fit for a $\text{He}+\text{O}_2$ plasma with trace amounts of N_2	102
6.7	Ozone density in the far effluent as a function of the O_2 admixture concentration.	103

6.8	Ozone density measured in the far effluent and the RF power deposited into the plasma as a function of the peak-to-peak voltage of the driving waveform, for a peaks waveform with different numbers of applied voltage harmonics. . .	105
6.9	Ozone density measured in the far effluent as a function of the RF power deposited into the plasma.	107
6.10	Ozone density measured in the far effluent, the RF power deposited into the plasma, and the ozone production efficiency as a function of the applied harmonics in the driving voltage waveform. A constant peak-to-peak voltage is used.	108
6.11	Gas temperature within the plasma channel as a function of the applied harmonics in the driving voltage waveform. A constant peak-to-peak voltage is used.	111
6.12	Ozone density measured in the far effluent and the peak-to-peak voltage of the driving waveform as a function of the number of applied harmonics. The RF power deposited in the plasma is 8 W.	112
6.13	Gas temperature within the plasma channel as a function of the number of applied harmonics in the driving voltage waveform. The RF power deposited in the plasma is 8 W.	114

Acknowledgments

My sincerest thanks goes to my supervisor, Erik Wagenaars, whose support, encouragement, and considerable patience cannot be overstated. His guidance has been essential to this project, especially when navigating the turbulence of the COVID-19 pandemic.

I would like to express my gratitude to Kari Niemi for his considerable help with all things experimental, to James Dedrick for his valuable insight when shaping this project, and to Helen Davies and Alexandra Brisset for their advice in my early days as a PhD student.

I am thankful to Levin Krös, Andy Nave, Jean-Pierre van Helden, Norbert Lang, and the rest of the Department of Plasma Diagnostics for welcoming me to the INP and allowing me to work alongside you to produce a fruitful collaboration. Further thanks to Mark Kushner for developing and sharing *GlobalKin*.

I also wish to thank the admin and finance staff at the YPI and School of PET, especially Ruth Lowman, Hillary Marshall, and Donna Cook, for their tireless work in keeping everything running smoothly behind the scenes. Additionally, I am deeply appreciative of the financial support of the Norma Ann Christie Scholarship.

It would be remiss of me to not give my heartfelt thanks to Emma Hume, Christina Ingleby, Alex Carter, Adam Dearling, Celine Schaumans, Matt Hill, Ryan Magee, Luke Thompson, Bob Davies, Koki Imada, and Mihai Mocanu for making my time at York so enjoyable. I wish you all the best for the future.

Mum and Dad, grateful words cannot repay the debt I owe you. Alas, I also can't repay it with money so you'll have to make do. You guided me along this path from my earliest years; as a child, you patiently indulged my endless, and possibly maddening, curiosity. "*Why? Because 'y' has a very long tail.*" As a teen, you pushed me, kept me focused, and bent over backwards to help me in school. You supported me through my adult life, and always provided a home when I needed it. Thank you for 26 years of care, sarcasm, and sage wisdom.

Finally, my amazing partner, Emma. Your love and optimism has kept me going throughout this PhD. Thank you for being you.

Declaration

This thesis has not previously been accepted for any degree and is not being concurrently submitted in candidature for any degree other than Doctor of Philosophy of the University of York. This thesis is the result of my own investigations, except where otherwise stated. All other sources are acknowledged by explicit references.

The He+H₂O+O₂ chemistry set used in chapter 4 was developed by Dr. Andrew Gibson and Dr. Sandra Schröter, and modified by Dr. Alexandra Brisset and later myself. The modelling data presented in this chapter was generated, analysed and interpreted solely by myself.

The experimental measurements presented in chapter 5 were performed jointly by myself and Levin Krös, under the direct supervision of Dr Andy Nave, while resident at the Leibniz Institute for Plasma Science and Technology (INP). The experimental setup was updated from one assembled by Sarah-Johanna Klose. Levin Krös and I processed the experimental data in parallel. This collaborative project was overseen by Prof. Erik Wagenaars and Dr. Jean-Pierre van Helden.

The experimental setup used in chapter 6 was constructed under the guidance of Dr. Kari Niemi and Dr. James P. Dedrick, and operated by myself. Experimental data from the setup was analysed and interpreted solely by myself. The LabVIEW code used to fit N₂(C-B) spectra was developed by Dr. Kari Niemi.

Each of the three investigations in this thesis has been prepared as a peer-reviewed journal article. I am the corresponding author of these works. The investigations in chapters 4 and 5 have been published in the Journal of Applied Physics and Plasma Sources Science and Technology, respectively. The investigation in chapter 6 has been submitted to Plasma Sources Science and Technology. Prose from these journal articles is used throughout this thesis.

This research was funded by the UK EPSRC (grant reference numbers: EP/S026584/1 & EP/S025790/1) and the Norma Ann Christie Scholarship. Chapter 5 was partly funded by INP internal funding.

List of publications and communications

Publications

“The influence of pulse repetition frequency on reactive oxygen species production in pulsed He+H₂O plasmas at atmospheric pressure”

B. Harris and E. Wagenaars, (2023).

Journal of Applied Physics, **134**, **10**.

“The spatial density distribution of H₂O₂ in the effluent of the COST-Jet and the kINPen-sci operated with a humidified helium feed gas”

B. Harris, L. Krös, A. S. C. Nave, E. Wagenaars, and J. H. van Helden, (2023).

Plasma Sources Science and Technology, **32**, **11**.

“Ozone production by an He+O₂ atmospheric pressure radio-frequency plasma jet driven by tailored voltage waveforms”

B. Harris, J. P. Dedrick, K. Niemi and E. Wagenaars.

Submitted to Plasma Sources Science and Technology.

Communications

“The H₂O₂ density distribution of He+H₂O plasmas in the effluent of a COST-Jet and kIN-Pen”

B. Harris, L. Krös, A. S. C. Nave, E. Wagenaars, and J. H. van Helden, (2023).

25th International Symposium on Plasma Chemistry (oral), Kyoto, Japan.

“The H_2O_2 density distribution of He+ H_2O plasmas in the effluent of a COST-Jet and kIN-Pen”

B. Harris, L. Krös, A. S. C. Nave, E. Wagenaars, and J. H. van Helden, (2023).

49th IOP Plasma Physics Conference (oral), Oxford, United Kingdom.

“Modifying O_3 production in He+ O_2 atmospheric-pressure plasmas using tailored voltage waveforms”

B. Harris and E. Wagenaars, (2022).

9th Plasma Science & Entrepreneurship Workshop (oral), York, United Kingdom.

“Bioactive Species Production in He+ H_2O Pin-Pin Pulsed Helium Discharges: Dependence on Cycle Frequency”

B. Harris and E. Wagenaars, (2022).

COST CA20114 – Fundamental Aspects on Plasma Medicine: 1st Training School (poster), Caparica, Portugal.

“Tailoring H_2O_2 and O_3 Production in Pulsed He+ H_2O Plasmas: Effects of Pulse Repetition Frequency”

B. Harris and E. Wagenaars, (2022).

48th IOP Plasma Physics Conference (poster), Liverpool, United Kingdom.

Chapter 1

Introduction

1.1 Thesis motivation

Plasmas are abundant in the natural world. The hot, dense plasma at the core of the sun fuses isotopes of hydrogen into helium, bathing the solar system in light and providing our planet with the energy needed to support life. In the night sky, the faint glimmer of stars offers evidence of the same plasma processes unfolding untold times across the observable universe. In the space between those stars, vast clouds of cold, sparse plasma comprise the interstellar medium [1], and towering nebulae act as stellar nurseries by providing the hot plasma necessary for new stars to form [2]. Closer to home, the upper layers of the sun cast off the solar wind, disturbing plasma in the Earth's magnetosphere and creating striking aurorae at the Earth's poles [3]. Throughout our atmosphere, charge accumulation in clouds causes lightning to arc through the sky, turning the air itself into a plasma [4].

These phenomena have inspired awe and reverence since the earliest days of humanity. In the modern age, however, rapid technological progress has allowed us to harness plasma for our own collective benefit. Plasmas are now found in lighting, industry, and water treatment systems [5]. Technological plasmas are used to manufacture semiconductors, an essential component of all digital technology [6]. In a multi-generational undertaking, researchers across the world collaborate to realise controlled nuclear fusion as a source of clean energy, using either a magnetically confined plasma or one confined by the inertia of a shockwave [7]. Fusion plasmas are classified as thermal plasmas, high temperature environments in which the constituent particles are locked in thermodynamic equilibrium and share the same temperature. In recent decades, it has also become possible to generate millimetre-scale plasmas at

low temperatures and atmospheric pressure. Unlike their thermal counterparts, low temperature plasmas are highly non-equilibrium environments. The electrons of a low temperature plasma are energetic and mobile, while the high inertial mass of ions and neutral species keeps them close to room temperature. This partitioning of kinetic energy drives a reactive plasma chemistry. Depending on the choice of feed gas, low temperature plasmas are efficient sources of reactive species desirable in biomedicine, agriculture, environmental science, green industry, and materials processing [8–10].

For biomedical applications, an especially useful class of plasma-produced species is reactive oxygen and nitrogen species (RONS). These are essential for the day-to-day functions of the human body, with different RONS acting as cell signalling molecules in the immune and cardiovascular systems, to scratch only the surface of their roles [8]. As such, RONS production by low temperature plasmas has drawn significant interest within the plasma community. It has been shown that RONS produced by plasma devices can be used to trigger programmed cell death in cancerous tissue [11]. Plasma-produced RONS are also highly effective at signalling the immune system to begin healing chronic wounds, and can sterilise potential harmful microbes while leaving human cells relatively unscathed [12]. The process of treating patients with low temperature plasma has been streamlined by the development of small-scale plasma devices that can be operated in ambient conditions and by hand [13–16]. Despite this progress, there is still much left to be understood about controlling the production of RONS by low temperature plasmas. As a category of reactive species, RONS have a significant array of effects on the human body. Whether or not a patient experiences these effects is dependent on their received dose of each RONS; if too high a dose of a certain species is received, the outcome may be detrimental to a patient's health. The successful application of low temperature plasmas in biomedicine hinges on RONS production being optimised for a given role, and establishing a degree of selectivity when generating different RONS in order to minimise any risk of harm. This is no trivial task, and has been an active area of research for many years [17].

This thesis contributes to the challenge at hand by exploring a number of ways in which the chemistry of low temperature, atmospheric pressure plasmas may be controlled and better understood. Focus is given to investigating the fundamental operating conditions that affect a plasma, such as the electrode geometry of the plasma source and the frequency and shape of the driving voltage. A variety of experimental and numerical techniques are applied to

determine the influence of different parameters on the production of RONS. The results of these studies are intended to assist in the optimisation of biomedical plasma devices used to treat patients.

1.2 Thesis outline

This thesis is structured as follows:

Chapter 2 provides background information on low temperature plasmas that is necessary to understand the methodologies and results of this work. Fundamental plasma physics concepts are first presented, building to a description of the key aspects of an atmospheric pressure plasma environment. Different methods of sustaining a plasma are then introduced. Additionally, the basic principles of studying LTPs are described in terms of both plasma modelling and optical diagnostic techniques.

Chapter 3 describes the four plasma sources investigated throughout this work, including design specifications and an overview of their histories.

Chapter 4 presents a modelling study in which the pulse repetition frequency of a nanosecond-pulsed, pin-to-pin discharge in He+H₂O is varied in the range of 1 to 100 kHz. A global model with an extensive reaction chemistry is used to ascertain the influence of the pulse repetition frequency on the densities and reaction pathways of key plasma species.

Chapter 5 uses cavity ring-down spectroscopy and a sophisticated analytical technique to determine the spatially-resolved density distribution of H₂O₂ in the effluent of two widely-used plasma jets, the COST-Jet and the kINPen-sci. Both jets are supplied with a He+H₂O gas mixture. The measured distributions are compared and discussed in terms of the plasma source geometries and modes of plasma sustainment.

Chapter 6 investigates the emergent effects of driving a capacitively-coupled, He+O₂ plasma jet with asymmetric tailored voltage waveforms. Fourier transform infra-red spectroscopy is used to characterise the influence of different waveform parameters on the density of O₃ in the far plasma effluent. Similarly, the effect on the gas temperature of the plasma channel is determined through N₂(C–B) optical emission spectroscopy.

Chapter 7 summarises key outcomes and concludes this work.

Chapter 2

Fundamentals of low temperature plasmas

2.1 What is a plasma?

In etymological terms, the word ‘plasma’ is derived from the ancient Greek word meaning ‘to mold’ [18]. This, admittedly, does not do much to answer the question. It was in 1928 that Irving Langmuir first used the term ‘plasma’ to describe a region of balanced ion and electron charges at the centre of an electrical discharge [19]. Langmuir’s collaborators, Tonks and Mott-Smith, later recounted that he chose the name because the electron and ion behaviour reminded him of red and white corpuscles carried by plasma in the blood [20, 21]. In the decades following the work of Langmuir and his associates, the term has come to define the ‘fourth state of matter’, comprising 99.9% of normal matter in the known universe, including stars, solar wind, stellar nebulae and interstellar clouds [22]. A more comprehensive definition of a plasma is offered by Chen [23]:

A plasma is a quasi-neutral gas of charged and neutral particles which exhibits collective behaviour.

Let us consider this further. In its simplest terms, a plasma is created by supplying matter with kinetic energy. By progressively adding energy to a system, a solid becomes a liquid, which becomes a gas, which becomes a plasma. When a plasma is created, the energy input is sufficient to separate electrons from their parent nuclei, ionising them. Given this boundary it is important to note that not every ionised gas is a plasma. For an ionised gas to be

considered a plasma, it must be quasi-neutral. Following on from Langmuir's original work, quasi-neutrality requires that the number of negative charges in the gas be roughly equal to the number of positive charges, making it electrically neutral at a macroscopic level. The second requirement is that the ionised gas exhibits collective behaviour through the Coulomb force. On small length scales, charged particles in a plasma can form localised charge concentrations, generating electric fields. The motion of these charged particles induces electrical currents, generating magnetic fields in turn. These fields influence other charged particles at range. Thus, the behaviour of charged particles on local scales causes emergent, non-local plasma behaviour that acts on macroscopic scales. An ionised gas satisfying these two requirements can therefore be considered a plasma.

Following Chen's definition, a plasma can contain electrically neutral particles [23]. Notably, the fraction of particles that can be neutral is not specified. This is helpful in the case of low temperature plasmas (LTPs), where the ionisation fraction is typically less than a single percent. LTPs, the focus of this work, are often generated by partially ionising a gas with an electrical discharge. This creates a highly non-equilibrium environment; the mobile electrons are accelerated to high kinetic energies by the electric field, while the ions and neutral species remain close to room temperature due to their high inertial mass.

Despite a low ionisation fraction, the energetic electrons in LTPs drive a complex neutral chemistry, making them efficient sources of reactive species for a wide variety of applications. The remainder of this section discusses some key aspects of LTPs, including important considerations for generating them at atmospheric pressure.

2.1.1 Sheaths

The active region at the centre of an LTP exhibits collective behaviour and quasi-neutrality. However, in the space between the active plasma and a surface, the conventional definition of a plasma is strained as quasi-neutrality breaks down. This was noticed by Langmuir and Tonks during their pioneering work in the 1920s. This region was named the 'sheath', and the pair dubbed the boundary point between the sheath and the plasma bulk the 'sheath edge' [19, 24].

To conceptualise the sheath region, imagine a plasma held within a vessel. Charged particles exiting the plasma bulk impinge on the vessel walls and are lost to recombination. Of these,

the electrons reach the vessel walls faster than the ions due to their greater mobility, causing the sheath edge to become positively charged. This imbalance forms a potential gradient through the sheath region. Electrons are repelled back into the plasma bulk, while positive ions are accelerated towards the vessel walls. Thus, quasi-neutrality is violated within the sheath. For a sheath in equilibrium, the flux of positive and negative charge carriers are balanced, and so the net conduction current is zero.

2.1.2 Atmospheric pressure plasmas

Consider a gas contained between two parallel electrodes. Applying a potential difference between the electrodes generates an electric field. In standard conditions, any gas will have a low, but nonzero, free electron population due to sporadic ionisation by cosmic rays or radioactivity [25]. These electrons, unbound from atomic nuclei, are accelerated to high kinetic energies by the electric field. Some of the energetic electrons may collide with neutral atoms and molecules in the gas and trigger a cascade of additional ionisation events, known as an electron avalanche. Secondary electrons are generated by ions striking the negative electrode after being accelerated through the sheath, or by successive electron avalanches in the gas phase. If the applied electric field is sufficiently strong, the rate of secondary ionisation will exceed the rate at which electrons are lost to recombination or through collisions with the vessel walls. Thus, a low temperature plasma is ignited.

For a given electrode separation, the threshold above which a plasma can be sustained is quantified by the breakdown voltage of the gas, V_B . The breakdown voltage depends on the ionisation energies of neutral species within the gas. Hence, different gas mixtures exhibit different breakdown voltages. For a given gas mixture in a DC electric field, the breakdown voltage is dictated by the product of the gas pressure and the width of the electrode gap, $p \cdot d$. This relationship is given by the Paschen criterion [26]:

$$V_B = \frac{Bpd}{\ln(Apd) - \ln(\ln[1 + \gamma^{-1}])}. \quad (2.1)$$

Here, A and B are constants determined by the gas mixture, and γ is a coefficient describing the rate of secondary electron production per ion. The breakdown voltage as a function of $p \cdot d$, known as a Paschen curve, is shown in figure 2.1 for a selection of different gases.

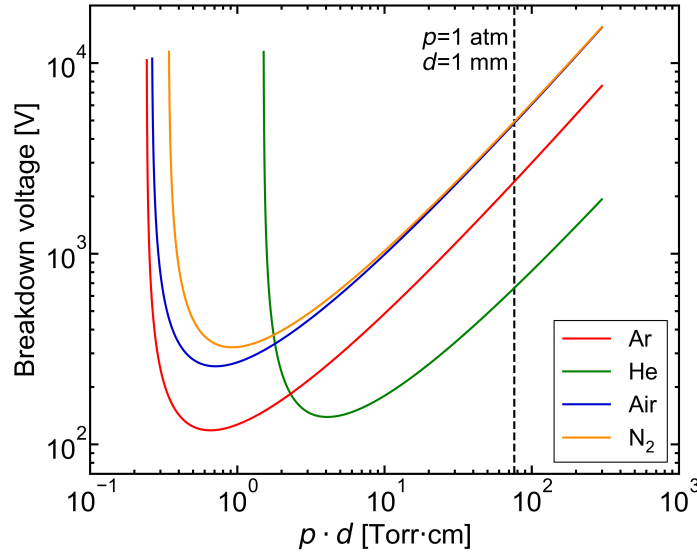


Figure 2.1: Paschen curves, the breakdown voltage as a function of the product of the gas pressure and the electrode gap, for a selection of gases. The dotted line shows breakdown voltages at atmospheric pressure for a gap with of 1 mm. Coefficients taken from [27, 28].

Physically speaking, the Paschen criterion arises from the limiting factors at the extremes of the $p \cdot d$ scale. At low values of $p \cdot d$, the mean free path of an accelerated electron becomes significant compared to the electrode gap. Collisions between electrons and heavy species are infrequent, meaning a higher applied voltage is required to trigger enough ionisations to sustain a plasma. The electron mean free path is much lower than the electrode gap for high values of $p \cdot d$, either due to the size of the electrode gap or the pressure of the gas. Collisions with neutral species hamper electron acceleration, again requiring a higher applied voltage to sustain the rate of ionisation. It follows that a $p \cdot d$ value of minimum breakdown voltage exists between these two limits at which a plasma can be generated with the greatest electrical efficiency.

Low pressure (1 – 200 mTorr) discharges, such as those used to etch silicon wafers for semiconductor manufacturing [6], can theoretically achieve the minimum breakdown voltage with an electrode gap on the scale of tens of centimetres. The same cannot be said for atmospheric pressure discharges, the focus of this work. Atmospheric pressure plasmas are highly collisional environments. High densities of neutral species limit electron mobility, requiring high breakdown voltages unless the discharge gap is very thin. At the same time, the smallest achievable electrode gap is restricted to a few hundred microns due to the width of the plasma sheath. Below this limit, the plasma bulk shrinks and disappears, leaving only the sheath

region and violating quasi-neutrality [29]. Consequentially, the discharge gap of atmospheric pressure plasmas is usually on the order of 1 mm. This is marked on figure 2.1 as a dotted line. Under these conditions, helium has an appreciably lower breakdown voltage than the other gases shown, followed by argon. It is for this reason that atmospheric pressure plasmas are often generated from a helium or argon feed gas, although in some cases air is utilised instead. Unlike in low pressure plasmas, ion impact at the electrodes is not a significant source of secondary electrons at atmospheric pressure [30]. The discharge is instead sustained by volumetric ionisation in the sheath and plasma bulk [31].

The discharge setup considered thus far is a slight simplification of the plasma environment. In truth, there are many ways of sustaining LTPs at atmospheric pressure, including nanosecond-pulsed discharges, radio-frequency (RF) discharges, dielectric barrier discharges (DBDs), and microwave discharges [32]. Out of these, nanosecond-pulsed discharges, RF discharges, and DBDs are investigated in this work. The following sections explore these discharge types in greater detail.

2.2 Nanosecond-pulsed discharges

The plasma setup discussed in chapter 2.1.2 is a simple direct current (DC) discharge. In a DC discharge, the direction of the electric field is constant. Ions and electrons experience unidirectional acceleration by the electric field, and so a direct current flows between the two electrodes. Supplying power in this manner is an inefficient way of sustaining an LTP at atmospheric pressure, and can cause the neutral gas to overheat [33]. Instead, it is often preferable to sustain a plasma through repetitive voltage pulses. Applying a high-voltage pulse for nanosecond timescales, cycled at kHz frequencies, generates a strong electric field that accelerates electrons, allowing a plasma to be sustained with a relatively low time-averaged power. Thus, nanosecond-pulsed plasma sources are more efficient than continuous DC sources, and can tolerate much higher peak voltages [33, 34]. This is typically achieved with pin-to-pin or pin-to-plate electrode geometries, both of which locally enhance the applied electric field in a small volume near the powered electrode [35, 36].

2.2.1 Streamers

The electrical breakdown of gas in a pulsed discharge proceeds through charge carriers being accelerated during the voltage pulse and triggering an avalanche of successive ionisations. At atmospheric pressure, the mean free path of charge carriers is very short due to the high density of neutral species. An ionisation avalanche therefore occurs within a very small volume, enhancing the electric field in the region. If the local electric field grows to exceed the applied electric field within the discharge gap, the avalanche develops into a streamer [37]. As the streamer propagates, ionisation within the discharge predominantly occurs at the head of the streamer, with the local electric field further distorted by photoionisation at the streamer head. Photoionisation acts as a source of pre-ionisation in front of the streamer, allowing the streamer to propagate at high velocities [38, 39]. The streamer velocity can also be enhanced if it is propagating through an electronegative gas, such as gases containing air-like impurities, due to the formation of an anion sheath that focuses electrons towards the streamer core [39, 40].

Streamers fall into one of two categories. Negative streamers are sustained by electrons in the streamer head propagating towards the anode, leaving positive ions distributed throughout the streamer channel. Positive streamers, meanwhile, are sustained by positive ions being accelerated towards the cathode in the wake of an ionisation avalanche. This process is thought to require efficient photoionisation at the streamer head to be tenable, although some studies question its importance compared to other ionisation mechanisms [41].

It is important that the pulse duration is restricted to prevent a streamer from reaching the opposite electrode. Should this happen, the streamer channel forms a conductive short-circuit allowing a huge current to flow [42]. The plasma becomes a spark discharge, characterised by high power consumption and significant gas heating.

A typical streamer discharge exhibits spatially concentrated ionisation and photoemission. However, it is possible for a nanosecond-pulsed discharge to generate a diffuse plasma. In this regime, a very short voltage rise time makes streamer propagation occur on timescales faster than photoionisation, limiting the concentration of photons at the streamer head [34]. The plasma is instead sustained through a persistent population of fast electrons [43, 44], resulting in a glow discharge characterised by relatively homogeneous emission throughout the plasma channel [35].

2.2.2 The afterglow

The portion of the voltage cycle between two successive pulses is called the afterglow. The short lifetime of free electrons leads them to rapidly recombine after each voltage pulse, so the electron density in the afterglow is minimal and the rate of electron-neutral interactions plummets. Despite this, the high electron densities generated by nanosecond-pulsed operation stimulate a highly reactive neutral chemistry, with reactions between heavy species occurring on longer timescales throughout the afterglow phase. Moreover, neutral gas heating can be reduced by increasing the afterglow duration to allow energetic particles to disperse or recombine, allowing the plasma to remain close to room temperature [35]. A very low density population of residual electrons can still accumulate between pulses, allowing the discharge to be reignited more efficiently once the plasma has reached equilibrium. This is known as the memory effect [45].

2.3 Radio-frequency discharges

The LTPs discussed thus far have been generated by DC discharges, with ions and electrons each accelerated unidirectionally towards a given electrode depending on the fixed polarity of the voltage pulse. It is also possible to use an alternating current (AC) electric field to sustain a plasma. In an AC discharge, the applied voltage, $V(t)$ and current, $I(t)$ oscillate in time according to

$$V(t) = V_0 \sin(2\pi ft + \theta) , \quad I(t) = I_0 \sin(2\pi ft + \theta) . \quad (2.2)$$

Here, V_0 and I_0 are the peak voltage and current amplitudes, respectively, f is the frequency of the waveform, and θ is the phase angle. These waveforms are usually applied at radio frequencies. In the field of plasma physics, the term ‘radio-frequency’ typically encompasses frequencies between 1 MHz and 1 GHz [46]. Conventional RF plasma sources are operated at specific frequencies approved for industrial and scientific use by the International Telecommunications Union [47]. As such, the AC field is most commonly driven at 13.56 MHz, or its respective second and third harmonics, 27.12 MHz and 40.68 MHz [48]. In this frequency range, electrons follow the oscillations of the electric field and gain kinetic energy. The ions, meanwhile, cannot respond to the field due to their high inertia and remain close to the temperature of the neutral gas [30]. As a result, RF power is primarily coupled into the

plasma via the electrons. The alternating electric field also helps to confine electrons within the plasma bulk.

2.3.1 Capacitively coupled plasmas

An RF plasma can be sustained through two different methods of power coupling: inductive or capacitive. In an inductively coupled plasma (ICP), an RF voltage waveform drives an inductive coil positioned in, or near, the discharge region. This generates an alternating magnetic field, which itself induces an RF electric field in accordance with Faraday's Law [49]. The electric field accelerates electrons within the discharge volume, generating a plasma. In this way, an ICP is effectively electrodeless as the plasma acts as the secondary coil of a transformer.

At atmospheric pressure, sustaining an ICP becomes challenging. Ignition requires a high voltage, and the plasma itself is energetically inefficient, prone to instabilities and significantly hotter than room temperature [50, 51]. Hence, outside of select industrial processes it is generally more favourable to generate atmospheric pressure LTPs through capacitive coupling. It is for this reason that the RF discharges investigated throughout this work are capacitively coupled.

A standard capacitively coupled plasma (CCP) setup consists of two uncovered parallel-plate electrodes separated by a gas. An RF voltage is applied directly to one electrode and the other electrode is grounded, creating a capacitor geometry [52]. A time-varying electric field forms between the electrodes, accelerating electrons to produce a plasma. An impedance matching network must be positioned between the RF generator and the powered electrode to ensure that RF power is efficiently coupled into the plasma [53]. Otherwise, losses occur due to reflected power.

Atmospheric pressure, radio-frequency CCPs generate highly collisional sheaths in which the electron mean free path is much shorter than the sheath width [30]. The sheath dynamics vary in time within the RF cycle due to the changing electric field [54]. In the positive RF half-cycle, the voltage rises and electrons are accelerated towards the temporary anode. The resulting space charge forms a sheath between the anode and plasma bulk, accelerating positive ions through the sheath. The sheath region expands until the maximum voltage amplitude is reached, before contracting as the voltage falls. When the driving voltage passes zero, the polarity of the electric field switches, forming a new temporary anode at

the opposite electrode. The process of sheath expansion and collapse is then repeated in the negative RF half-cycle at the opposite electrode.

2.3.2 Operational modes in capacitively coupled plasmas

Capacitively coupled, atmospheric pressure LTPs are often driven by RF voltage waveforms with low voltage amplitudes (a few hundred volts) and a single applied frequency of 13.56 MHz [15, 55]. Operation in this manner produces a homogeneous glow discharge known as the Ω -mode, defined by volumetric electron heating [56]. In the Ω -mode, a high drift electric field within the plasma bulk triggers ionisation maxima during times of sheath expansion and collapse [57]. The gas temperature in the Ω -mode is relatively low, close to room temperature [58]. If the feed gas of an atmospheric pressure LTP is a Penning mixture, such as He+O₂ or He+N₂, increasing the amplitude of the driving voltage waveform changes the mode of power coupling and the plasma transitions from the Ω -mode into the Penning-mode [31, 59]. A Penning mixture is defined as a binary gas mixture in which the excitation energy of the metastable state of the main component exceeds the ionisation energy of the minor component [60, 61]. In these mixtures, Penning ionisation of the molecular admixture by electronically-excited helium metastables is an important process for plasma sustainment [62–64]. Penning ionisation becomes the dominant ionisation process in the Penning-mode, with ionisation maxima occurring within the sheaths at times of maximum sheath expansion [57]. The Ω -mode and Penning-mode are sometimes referred to in literature as the α -mode and γ -mode, respectively, due to similarities with the low pressure plasma modes of the same name [64, 65]. In recent years, it has become clear that the fundamental mechanisms of the atmospheric pressure Ω -mode differ from those of the low pressure α -mode [31]. The same is true of the Penning-mode and the γ -mode [31]. As such, the low pressure mode names are not used in this work so as to avoid confusion.

Increasing the driving voltage amplitude eventually transitions the discharge into a constricted mode, characterised by filamentary behaviour. In this mode, ionisation is confined to the strongly contracted sheath regions [66, 67]. Operating plasma devices in the constricted mode is best avoided, as the high gas temperature and current density pose a risk of thermal damage to the device and/or substrate [15, 64].

2.4 Dielectric barrier discharges

Some capacitive discharges cover at least one electrode with a dielectric material, such as quartz, glass, or a ceramic. This is known as a dielectric barrier discharge. The dielectric layer acts as a current limiter, preventing spark formation and maintaining a low neutral gas temperature [68]. It has been shown that atmospheric pressure DBDs supplied with helium or argon allow a stable plasma to be maintained at higher discharge currents than can be achieved by conventional glow discharges with uncovered electrodes [69, 70]. Power is typically transferred to the plasma via an AC high voltage in the kHz frequency range [71], with the dielectric layer becoming less effective at higher frequencies.

Most parallel-plate DBDs are self-pulsing under standard conditions; breakdown occurs twice per RF period, during times of rising voltage magnitude [71]. Breakdown proceeds via the streamer mechanism (see chapter 2.2.1), with clusters of streamers forming distinct, thin discharge channels as they propagate towards the anode [72]. The discharge then collapses due to charge accumulation at the dielectric layer. When the voltage polarity reverses, the same negative charge accumulated at the anode stimulates new streamer clusters within the same discharge channels, resulting in bright, spatially localised plasma filaments [72]. Such regimes are known as filamentary discharges. The kINPen-sci, a filamentary, DBD-like plasma jet, is investigated in chapter 5 of this work.

Under specific conditions, it is also possible to sustain a diffuse or glow plasma in an atmospheric pressure DBD by suppressing the filamentary nature of the discharge. This regime is ideal for applications that require homogeneous treatment of a surface by reactive species. Similar to nanosecond-pulsed discharges, a diffuse plasma is more easily achieved in helium due to its relatively high rate of electron multiplication at low electric field strengths [73]. This effect is significantly enhanced in the presence of small admixtures of nitrogen or oxygen through Penning ionisation of the molecular gas by metastable helium [73]. By extension, the glow regime favours reduced operating voltages. Higher driving frequencies also provide optimal conditions for diffuse plasmas in DBDs because electrons and metastables are able to accumulate within the electrode gap [74].

DBDs can also be operated with kHz pulsed or AC RF voltages. A comprehensive review of DBD configurations and operating regimes is provided by Brandenburg [71].

2.5 Plasmas for biomedicine

Atmospheric pressure plasmas are efficient sources of RONS for biomedical applications. They are also complex environments, and the production of RONS by an LTP is sensitive to a wide array of interconnected phenomena. As illustrated in figure 2.2, the design of the plasma source, feed gas composition and mode of power coupling all influence the electron dynamics in the plasma. This influences electron-neutral reaction pathways, which ultimately determine the neutral plasma chemistry and the production of reactive species. This poses a variety of challenges for controlling RONS production and requires that numerous aspects of the plasma environment are well understood.

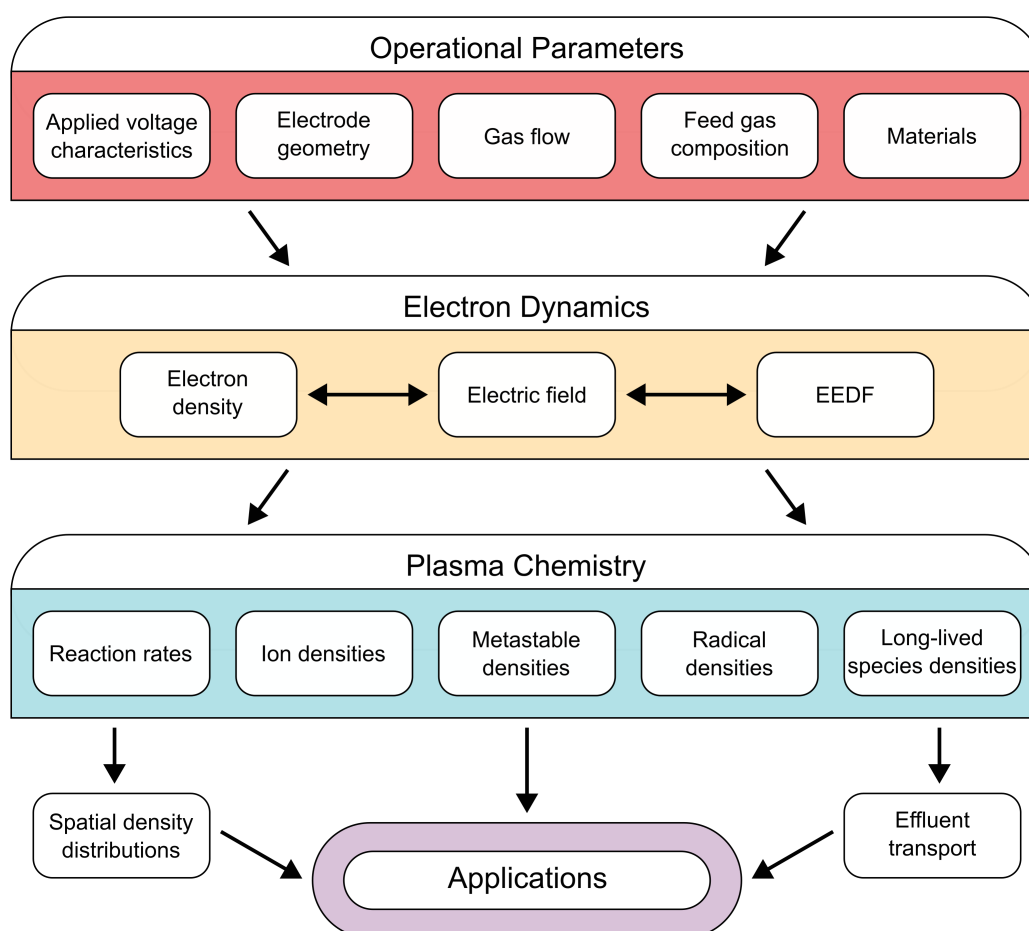


Figure 2.2: Representation of the complex interplay between operational parameters and plasma phenomena. The operational conditions of the plasma source determine electron behaviour, which in turn dictates the plasma chemistry and the production of reactive species. Adapted from Bruggeman and Brandenburg [53].

To fully appreciate the potential for LTPs in biomedicine, it is necessary to understand the mechanisms of key plasma processes and the ways in which they are connected. To this end, the following sections cover the behaviour of electrons as the driving force behind reactive species production in atmospheric pressure LTPs, alongside the fundamentals of the heavy particle plasma chemistry, the effects of RONS on biological tissue and the resulting applications, and some considerations for medical plasma source design.

2.5.1 Electron energy distribution function

Consider an ideal gas bound within a finite volume. The total kinetic energy of the gas is divided between its constituent particles, which move randomly and exchange kinetic energy in collisions. Given enough time, the system reaches thermodynamic equilibrium. Once this occurs, the spread of kinetic energy between the particles is described by a Maxwellian distribution. From this, the temperature of the population, a measure of the average energy of a particle, can be obtained. The same can be true of electrons in a plasma. If electron-electron collisions are frequent enough for the population to thermalise, the electron energy distribution function (EEDF) becomes Maxwellian. However, the low electron density of LTPs causes electron-neutral collisions to be the dominant process in shaping the EEDF. At increased pressures, the high energy tail of the EEDF is depleted through inelastic collisions with neutral species [75]. In this case, the EEDF may be more accurately represented by a Druyvesteyn distribution, which predicts a reduced electron population at high energies when compared with a Maxwellian distribution. Additionally, some low pressure plasmas exhibit two- or three-temperature Maxwellian EEDFs, composite functions with different electron temperatures that are valid for discreet energy intervals [76, 77]. This can be driven by selective heating mechanisms or secondary electron emission from the vessel wall. Model Maxwellian and Druyvesteyn EEDFs are shown in figure 2.3. Also shown are the corresponding electron energy probability functions (EEPFs), a normalised form of the EEDF that gives the relative probability of an electron possessing a given kinetic energy.

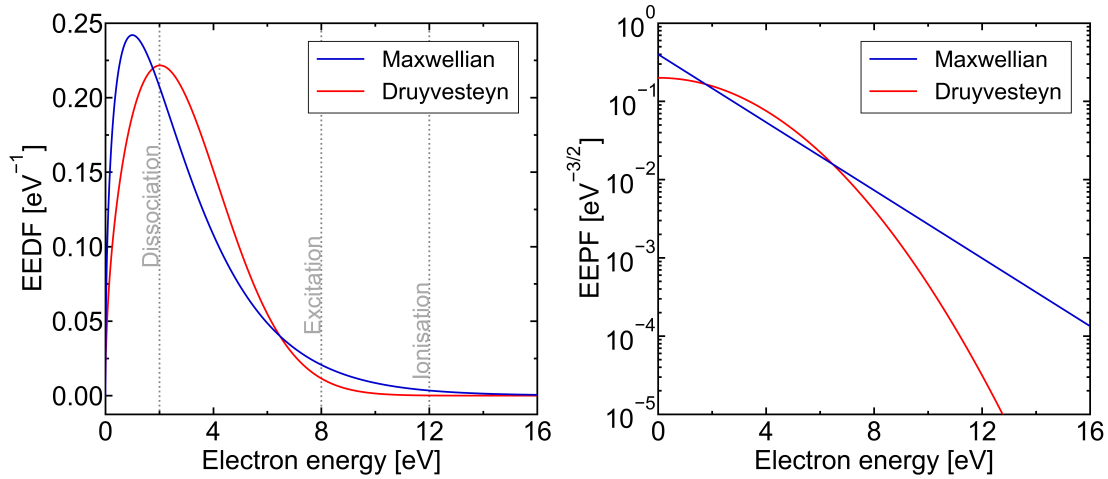


Figure 2.3: Maxwellian and Druyvesteyn electron energy distribution functions and electron energy probability functions, modelled according to [75] for an electron temperature of 2 eV. Typical kinetic energy thresholds of electron-neutral collisional processes are marked with dotted lines.

The kinetic energy of an electron determines the reactions it can facilitate in collisions with neutral species. These interactions can be grouped into dissociation, excitation, or ionisation events. Dissociation reactions typically require the lowest kinetic energy to break a molecule apart. Electronic excitation of atoms and molecules require higher energies than dissociation processes, while rotational or vibrational excitation of molecules can be achieved with comparatively low energies. Electron impact ionisation processes require the greatest kinetic energy and generate additional free electrons. Approximate energy thresholds for these interactions are marked on figure 2.3. The true kinetic energies needed for these processes are discrete values dictated by the energy levels of an atom or molecule.

The EEDF and electron dynamics of an LTP are strongly affected by the composition of the feed gas. For example, in argon, nearly all of the power coupled into the plasma is used for ionisation while a majority of the power coupled into a helium plasma is spent in non-ionising electron-neutral collisions [78]. This results in helium plasmas displaying lower electron densities than in argon, compensated by higher electron temperatures needed to sustain the plasma through ionisation [78]. Ionisation mechanics are further complexified by the addition of molecular admixtures to a helium or argon feed gas. As previously discussed, Penning ionisation of a molecular admixture by noble gas metastables can become the dominant source of ionisation in a plasma.

The accumulation of these factors can contribute to a strongly non-Maxwellian EEDF in

atmospheric pressure LTPs. Predicting the EEDF of an LTP is, therefore, difficult, but practical solutions have been developed. The use of computational models to investigate the EEDF and other plasma processes is discussed further in chapter 2.6.

2.5.2 Neutral plasma chemistry

As exemplified by the Paschen curves in figure 2.1, argon and helium make ideal feed gases for LTPs due to their low breakdown voltage at atmospheric pressure when compared with molecular gases. In pure argon or helium plasmas, energetic electrons sustain the plasma and drive the formation of excited species, including high-energy noble gas metastables. The inert nature of noble gases means that the plasma chemistry in these cases is relatively simplistic. A significantly more complex reaction chemistry is produced if a noble gas plasma contains small concentrations of a molecular gas. Plasma-produced electrons and noble gas metastables dissociate the molecular gas, generating highly reactive radical species. These, in turn, react with other neutral species to form longer-lived reactive molecules. This behaviour allows LTPs to generate RONS with relatively low input power. In these plasmas, the EEDF is the driving force behind the emergent neutral chemistry. The rates of electron-impact reactions are determined by the EEDF, while heavy particle reaction rates are most often dependent on the neutral gas temperature.

Molecular gases used for RONS production include nitrogen, oxygen, and water vapour [79–81]. These species may originate as impurities in the gas supply [82], or they may be present from a plasma plume interacting with the open air [83]. Both of these options add a degree of inconsistency due to uncontrolled changes in ambient conditions, such as humidity, as the densities of RONS produced by a plasma are generally dependent on the concentration of the parent species. Instead, RONS can be generated in controllable quantities by admixing known concentrations of a molecular gas into the gas feed.

The active region of LTPs is a rich mixture of photons, charged particles, excited states and reactive species. Outside the active plasma region, where no power is deposited, electrons exiting the plasma rapidly recombine and photon emission ceases. Radicals, highly reactive species with short effective lifetimes, are also depleted outside the plasma through interactions with other neutral species. This process occurs on nanosecond to microsecond timescales – fast, but not as fast as electron recombination. Longer lived RONS formed in a plasma, such as ozone or hydrogen peroxide, are more stable than radicals. Outside the plasma, they can

comfortably exist for minutes at a time before reacting or decomposing.

2.5.3 Reactive oxygen and nitrogen species in the human body

RONs exhibit a complex array of effects on the human body, whether they are produced *in vivo* or delivered through plasma treatment. For example, the nitric oxide (NO) radical plays a crucial role as a cell signalling molecule in the cardiovascular system [84]. NO is also the main precursor of all reactive nitrogen species in biological systems [85]. The hydroxyl (OH) radical is highly reactive and readily oxidises proteins and DNA molecules, causing cell damage and instability in healthy and cancerous tissue alike [86]. Similarly, the peroxynitrite radical (ONOO⁻) is a powerful oxidiser that promotes tissue damage [87]. There is evidence to suggest that this trait is weaponised by the immune system, with macrophages producing ONOO⁻ as an antimicrobial agent [88]. Hydrogen peroxide (H₂O₂) primarily acts as a cell signalling molecule, mediating immune responses [89]. Depending on its concentration it can also inhibit the growth of bacterial infections, while at too high a dose it causes damage to human cells due to oxidative stress [90]. Like H₂O₂, ozone (O₃) is known to stimulate the immune system and inactivate microorganisms, although it is toxic in high concentrations [91]. Additionally, ultraviolet photons emitted by de-excitation processes in the plasma work synergistically with RONS to inactivate bacteria and biomolecules [92].

Given this range of functionality, it is evident that the plasma chemistry should be tightly controlled to optimise a plasma for a specific role.

2.5.4 Applications of plasmas in biomedicine

To date, LTPs have seen success in numerous medical treatments. Possibly the most prolific of these is the sterilisation of medical equipment [93]. In this procedure, the mixture of RONS and ultraviolet photons generated by a cold plasma is effective at inactivating microbes on materials that would otherwise be damaged by thermal sterilisation techniques [94]. Plasma treatment has been shown to be effective at eliminating antibiotic-resistant biofilms at a time when antimicrobial resistance poses a significant threat to healthcare systems around the globe [95, 96].

Another promising application of LTPs is for the treatment of chronic wounds. Many people with diabetes or vascular disease suffer from chronic ulcers on the legs and feet that will not naturally heal, and become infected [91]. In addition to the physical and psychological burden

on the patient, conventional treatments span long periods of time and are costly for healthcare providers to administer [97]. Direct plasma treatment offers an alternative approach to wound healing through a two-fold process of inactivating microbes and stimulating the immune system. Although the exact mechanisms of plasma-assisted wound healing are a topic of active investigation, it is generally thought that RONS from the LTP cause oxidative stress and trigger apoptosis (programmed cell death) in bacteria infecting the wound [98]. At the same time, it is believed that RONS stimulate the immune system in the area, allowing the wound to heal [91]. In clinical trials, chronic wounds treated with purpose-built plasma devices have shown significant reductions in both bacterial load and wound size [99, 100].

More recently, LTPs have seen interest as a novel cancer therapeutic [101]. Cancerous tumours can develop when ordinary cells do not undergo apoptosis, and instead begin to multiply out of control while evading the immune system. Fridman *et al* found that treating melanoma skin cancer cells with an LTP triggers apoptosis at low plasma doses, while high doses of plasma cause immediate cell death [102]. Subsequent studies have once again highlighted the importance of plasma-produced RONS in these processes [103]. If a tumour can be reached by a plasma source, plasma treatment may be a preferable alternative to chemotherapy or more invasive procedures due to the detrimental side effects associated with them. Further details on the roles of LTPs in medicine and the current state of the field are given in a comprehensive review by Laroussi *et al* [104].

2.5.5 Atmospheric pressure plasma jets

Low temperature, atmospheric pressure plasmas have a wide range of applications. It is no surprise, then, that an equally large variety of plasma source configurations exist to optimise LTPs for a given role. Though all linked by the slim electrode spacing needed to ignite discharges at atmospheric pressure, the geometry of the electrodes can vary greatly. Surface discharges have been used in cases where a large surface area requires plasma treatment, such as for enhancing seed germination [105] or sterilising food products [106]. In biomedicine, it is important that LTPs can target a specific area of a patient in order to minimise the exposure of healthy tissue to RONS and ultraviolet radiation. Consequentially, biomedical plasma sources are often designed with millimetre-scale exhausts that form a small plasma jet [13–16]. Such a device is known as an atmospheric pressure plasma jet (APPJ), and their design strongly influences the emergent plasma behaviour.

Some APPJs cover an electrode with a dielectric material to prevent the formation of a spark or arc discharge in gas mixtures with poor thermal conductivity [16,68]. The electrode configuration also influences the mixture of species that a patient or substrate is exposed to. Using two APPJ designs, Walsh and Kong demonstrated that electric fields positioned parallel to the gas flow (linear-field) promote the transport of charged particles along the plasma plume for a more active downstream chemistry, while perpendicular electric fields (cross-field) confine charged particles to the plasma channel [107]. This can influence the optimal APPJ configuration for a given treatment. Linear-field APPJs may be preferable if higher radical and photon fluxes are desired, while cross-field APPJs can restrict exposure to these species in favour of longer-lived RONS.

Further choices are presented by a plasma source's power scheme. It is common for APPJs to utilise RF voltage waveforms or nanosecond-pulsed voltages in the kHz – MHz frequency range, although some sources are operated at microwave frequencies on the order of GHz [32]. Nanosecond-pulsed discharges tend to have a lower gas temperature on time-average due to the long afterglow period, although the plasma must effectively be reignited with each successive pulse. Meanwhile, the continuous voltage applied to RF discharges yields a plasma that is more homogeneous in time. Microwave-driven discharges offer very high power coupling efficiencies for applications where minimising power losses is a priority, but their operation is comparatively more complex than RF or nanosecond-pulsed discharges. These aspects should be considered when designing an APPJ, a process that may be made somewhat easier by first investigating potential plasma source designs with a numerical model. The following section explores the field of plasma modelling in greater detail and presents an overview of a number of popular methods of modelling an LTP.

2.6 Principles of plasma modelling

In many scenarios, it is beneficial to use computational models to simulate the behaviour of low temperature, atmospheric pressure plasmas [108,109]. Detailed modelling allows key plasma parameters to be estimated to a good degree of accuracy without the time and expensive equipment required for physical measurements. When paired with experimental data, plasma models can be a powerful tool for validating results or investigating plasma behaviour beyond what can be tested experimentally. Modelling atmospheric pressure plasmas can prove

challenging as they encompass an extensive array of particles, reactions and timescales. This is illustrated in figure 2.4, adapted from a diagram by Kushner [110]. The timescales of physical processes can range from picoseconds for electron dynamics to milliseconds for plasma chemistry, and up to minutes or even days for plasma-treated biological tissue [111]. This is further complexified by the wide variation in the minimum time resolution required for a model to properly resolve each type of interaction [110].

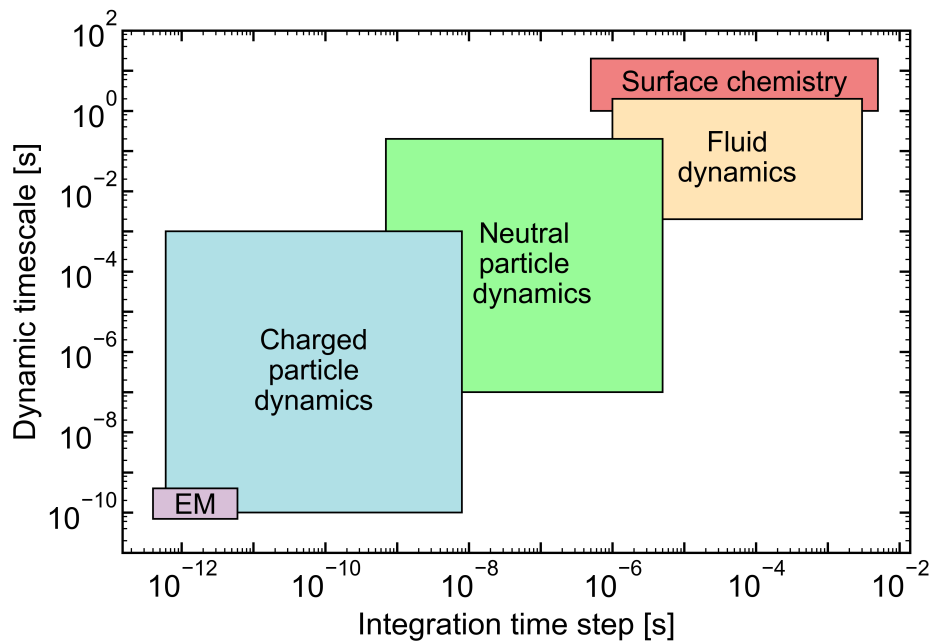


Figure 2.4: Timescales spanned by different plasma processes. The dynamic timescale is the time taken for a physical process to reach equilibrium, while the integration time step is the resolution required for the process to be resolved in a numerical model. Adapted from Kushner [110].

To minimise the processing time of plasma simulations and optimise the output, a balance must be struck between a model's temporal resolution, reaction chemistry, treatment of particles and fields, and number of considered spatial dimensions. To this end, many types of model have been developed to explore the different aspects of LTPs. Broadly speaking, modern atmospheric pressure plasma models typically fall under one of four categories: particle-in-cell [112], fluid [113], global [114], or hybrid [110].

Particle-in-cell (PIC) codes stem from early plasma models in the late 1950s and early 1960s that described plasma behaviour by computing the motion of individual charged particles in an electric field [115, 116]. Over the next twenty years, faster models were developed by considering the movement of particles grouped in discrete cells [117]. Thus, PIC codes

were born. While versatile, pure PIC models compute particle trajectories and fields but do not consider collisional effects – something essential to the behaviour of atmospheric pressure LTPs [108]. Many modern PIC codes therefore implement probabilistic Monte Carlo collision (MCC) schemes to compute particle collisions and scattering behaviour [118, 119]. This combined approach has been shown to offer excellent approximations of LTPs when validated against physical setups, in addition to providing useful charged particle information [120]. In general, PIC codes carry a significant computational cost. Practical implementation requires concessions to be made in the accuracy of the model through the chosen grid size, number of cells, and time step.

Popularised in the late 1980s by their application to reduced-pressure technological plasmas [121, 122], fluid models of LTPs reduce computational complexity by considering plasma behaviour on a macroscopic scale. This is achieved by taking velocity moments of the Boltzmann equation to obtain continuity equations for the conservation of density, energy and momentum in a plasma [108]. These equations describe key heavy species parameters as averaged properties of the fluid, namely the mean density, mean velocity and mean energy, offering faster runtimes than PIC codes at the cost of increased uncertainty [109]. Complex reaction chemistries must also be simplified to minimise the computation time. Consequentially, it has been shown that fluid models cannot accurately simulate low pressure, capacitively coupled plasmas due to an inadequate consideration of electron and ion kinetic motion in low-collisionality environments [120]. Fluid models of atmospheric pressure plasmas, while highly collisional, may also prove invalid in cases where a Maxwellian EEDF is assumed [123]. Global models of LTPs offer a more streamlined approach to plasma simulations. While fluid or PIC models compute plasma behaviour over time in one, two, or sometimes even three spatial dimensions, global models are volume-averaged under the assumption of a spatially uniform plasma. Because of this, the runtime of global models is often no more than a few hours on a standard desktop PC. In contrast, it is not uncommon for fluid models to take days to complete, or for modern PIC simulations to take weeks to complete on multiple-core machines. Much like fluid models, species densities are calculated from moments of the Boltzmann equation. However, global models neglect all spatially-dependent terms, thus producing a simple balance equation where the density of a species is determined by the rates of relevant chemical reactions and interactions with the vessel walls [114]. Electron and heavy particle temperatures are obtained in a similar manner. The EEDF is often calculated by

an integrated Boltzmann solver that processes a two-term approximation of the Boltzmann equation [124]. Ultimately, dimensional resolution is sacrificed to attain rapid computation times and the ability to handle substantial chemistry sets. It is for these reasons that global models are also referred to as 0D chemical kinetics models. A powerful tool for exploring reaction pathways beyond what is feasible experimentally, global models have been operated with chemistry sets encompassing hundreds or thousands of reactions. To name a few, these chemistry sets span gas mixtures including dry air [125], He+O₂ [80], He+H₂O [126], argon in humid air [127], and He+O₂ with N₂, H₂O and CO₂ impurities [82]. In spite of their benefits, caution should be exercised when using a global model. The assumption of a uniform plasma, though often a good approximation, neglects any phenomena that arise from the motion or distribution of particles. Furthermore, inclusion of incorrect reaction rate coefficients in a chemistry set may result in an inaccurate representation of LTPs [114]. A global model is used in chapter 4 to investigate the reaction chemistry of a nanosecond-pulsed He+H₂O plasma.

Finally, hybrid models combine aspects of multiple plasma models. This is often done with the intent of reducing computational strain while preserving the accuracy and quantity of generated information [128]. Alternatively, the constituent parts of a hybrid model may synergise to generate complementary sets of information about a plasma [110]. The last two decades have seen a proliferation of hybrid models of atmospheric pressure LTPs that take advantage of their duality, such as models that pair a fluid treatment of heavy particles with a PIC-MCC scheme for electrons [129], and models that switch between a PIC-MCC and a fluid scheme to describe the voltage pulse and the afterglow phase, respectively [130].

Computational models are an essential part of any plasma physicist's toolkit. However, these models must be validated against experimental measurements before they can be presumed accurate. The following section establishes the core principles of experimental plasma diagnostics, with a focus on optical diagnostic techniques applied to atmospheric pressure plasmas.

2.7 Principles of optical diagnostics

Experimental measurements can reveal a great deal about the plasma environment. As shown by the Paschen curves in figure 2.1, millimetre-scale electrode gaps are required to

sustain atmospheric pressure plasmas at low driving voltages. These small geometries prevent physical diagnostics, such as the Langmuir probe, from accessing the plasma without also perturbing it. As such, optical diagnostic techniques are the preferred choice for obtaining information about atmospheric pressure LTPs. Optical diagnostics can be divided into two categories: passive and active optical techniques.

Passive optical techniques measure light spontaneously emitted by a plasma. They are non-invasive and do not require the plasma to be interacted with directly. The most simplistic passive technique, optical emission spectroscopy (OES), uses a spectrograph to record emission spectra. In a plasma, photons of discrete frequencies are emitted by the spontaneous decay of excited species. For a species in an excited state decaying to a lower state by transition t , the intensity I_t of radiation emitted from a plasma (in units of $\text{W}\cdot\text{m}^{-3}$) is given by [131]

$$I_t = A_t h c \nu_0 n_u. \quad (2.3)$$

Here, A_t is the Einstein emission probability of the transition, h is the Planck constant, c is the speed of light, ν_0 is the central wavenumber of the transition, and n_u is the number density of particles in the upper state. Hence, excited species in a plasma can be identified from intensity peaks in measured emission spectra. Providing a number of assumptions are valid, OES can also be used to estimate the gas temperature of a plasma by fitting a model to a rotational band of the $\text{N}_2(C-B)$ or $\text{OH}(A-X)$ transitions [132]. This technique is used in chapter 6 to determine the gas temperature in the plasma channel of an APPJ. While emission measurements are straightforward to perform, species with ground state energies cannot be measured at all. Moreover, absolute densities cannot be calculated for excited species without first implementing an absolute calibration of the system, or by applying a complex population model that makes assumptions of the distribution of energy levels in the plasma. Given the challenges associated with both methods, passive techniques are most often used to measure relative change in a plasma. For example, phase resolved optical emission spectroscopy (PROES) measures the temporal and spatial evolution of excitation processes in a plasma at high resolutions, offering insights into the electron dynamics [133]. Moving on from passive techniques, active techniques expose a plasma to a light source and use the resulting absorption, fluorescence, or scattering of the light to obtain information about the plasma. The most straightforward active optical technique is absorption spec-

troscopy, where measurements are performed by recording the intensity of light after it passes through a plasma. This is compared to the initial light intensity, allowing the absorbance of the plasma to be calculated with the Beer-Lambert law:

$$A_t(\nu) = -\ln\left(\frac{I(\nu)}{I_0(\nu)}\right) = n_k\sigma_t(\nu)d. \quad (2.4)$$

Here, $A_t(\nu)$ is the absorbance of transition t at wavenumber ν , $I_0(\nu)$ is the intensity of light without a plasma, $I(\nu)$ is the intensity of light after passing through the plasma, n_k is the number density of absorbing species k , $\sigma_t(\nu)$ is the absorption cross-section of transition t at wavenumber ν , and d is the absorption length of light travelling through the plasma. The Beer-Lambert law is presented here in terms of the wavenumber, ν , which is often used in absorption measurements (especially in the infrared range) to represent the equivalent spectral frequency. Provided the absorption cross-section of a transition is known, the absolute density of an absorbing species can be calculated from a measured absorption feature.

Many types of light source can be employed in absorption measurements. Narrow-band tunable lasers, such as dye, diode, or quantum cascade lasers, boast thin spectral line widths [134]. Tuning through a range of laser frequencies allows absorption spectra to be recorded with high spectral resolution. A laser is also used in cavity-enhanced absorption techniques, such as cavity ring-down spectroscopy (CRDS). CRDS is described further in chapter 5, where it is used to measure the spatial density distribution of hydrogen peroxide in the effluent of two APPJs. As an alternative to lasers, ultraviolet broadband light sources enable absorption features to be measured by a spectrograph without frequency tuning [135–137]. A broadband light source is also used in Fourier transform infrared (FTIR) spectroscopy to rapidly measure spectra over a wide frequency range, allowing large numbers of transitions to be recorded at the cost of spectral resolution. Chapter 6 describes this technique in greater detail, where FTIR is used to obtain ozone density measurements in the far effluent of an APPJ.

Another active optical technique, laser-induced fluorescence (LIF), measures the fluorescence from a species when it decays from a higher energy level into a lower energy level after excitation by a laser [138]. Similarly, two-photon absorption LIF (TALIF) is employed for measurements of atomic species when single-photon measurements would require laser frequencies in the strongly-absorbed vacuum ultraviolet range [139]. LIF and TALIF measure reactive species densities with higher sensitivity than conventional absorption techniques [140], but calibration against either Rayleigh scattering or species with similar energy levels is required

to obtain absolute values.

2.7.1 Line profiles

In measured emission and absorption spectra, optical transitions are visible as spectral lines. The quantisation of energy levels means that each transition originates at a discrete frequency. However, several mechanisms broaden the spectral width of a line around its origin frequency. The resulting spectral intensity distribution is called a line profile, and its shape is dictated by a convolution of the dominant broadening mechanisms for that transition. The prevalence of these mechanisms are, in turn, determined by the plasma environment.

Natural broadening arises from the natural lifetime of a particle. The uncertainty in the lifetime of the state is intrinsically linked to the uncertainty in its energy due to the Heisenberg uncertainty principle, causing a broadening of transition frequencies. This is often the smallest broadening effect [141]. A similar mechanism is followed by collisional broadening, which becomes significant at atmospheric pressure. High particle collision frequencies reduce the effective lifetime of an absorbing or emitting particle, increasing the spectral line width according to the uncertainty in the energy of the state. Collisional broadening can be subdivided into two components: pressure (van der Waals) broadening, which occurs between two particles that do not share a resonant transition, and resonance broadening, where two colliding particles share similar energy levels [142]. Pressure broadening tends to dominate other physical sources of broadening in atmospheric pressure plasmas.

Another source of line broadening arises from the thermal motion of particles relative to an observer. Compared to a particle at rest, the transition frequencies, and hence the energy levels, of a particle in motion are Doppler shifted according to its velocity. As such, Doppler broadening of a spectral line is dependent on the velocity distribution of the absorbing or emitting species. The influence of Doppler broadening is often negligible in optical measurements of LTPs due to the low neutral gas temperature, but its contribution to the line shape must be accounted for at higher temperatures [142]. The energy levels of a particle can also be shifted by the transient electric fields of charged particles due to the Stark effect, causing Stark broadening. Compared to other line broadening mechanisms, Stark broadening is insignificant in atmospheric pressure LTPs on account of the high neutral density and low ionisation fraction [143]. If the electron density of a plasma is sufficiently high, though, measurements of the electron density can be obtained from argon or hydrogen Balmer emission

lines by deconvolving the Stark broadening contribution [81, 143].

The influence of the detector must also be considered, as spectral lines are further broadened by the measurement instrument. If the instrumental line width is larger than the spectral line width, assessing the influence of other broadening mechanisms becomes difficult due to large uncertainties in the deconvolution process [142].

Overall, line broadening produces a continuous intensity or absorbance distribution in measured spectra, despite transition frequencies being quantised. When using the Beer-Lambert law to calculate the density of an atom or molecule from an absorption feature, this distribution is accounted for by relating the absorption cross-section of a transition to its line strength, S_t and the line shape function, $f(\nu, \nu_t)$:

$$A(\nu) = n_k \sigma_t(\nu) d = n_k S_t f(\nu, \nu_t) d. \quad (2.5)$$

Line strengths and transition frequencies for different species can be accessed in data repositories such as the HITRAN database [144], while the line shape function is unique to each set of conditions and contains the contributions from all relevant line broadening mechanisms. Contributions from natural, pressure, or Stark broadening are Lorentzian in shape

$$f_L(\nu, \nu_t) = \frac{1}{\pi} \frac{\gamma_L}{(\nu - \nu_t)^2 + \gamma_L^2}. \quad (2.6)$$

Here, γ_L is the Lorentzian half width at half maximum (HWHM), or the broadening coefficient. Doppler broadening, and instrumental broadening in many conventional spectrometers [141], takes the form of a Gaussian distribution

$$f_G(\nu, \nu_t) = \sqrt{\frac{\ln(2)}{\pi \gamma_G^2}} \cdot \exp\left(-\frac{(\nu - \nu_t)^2 \ln(2)}{\gamma_G^2}\right), \quad (2.7)$$

where γ_G is the Gaussian HWHM. If multiple mechanisms contribute significantly to a measured line profile, the line shape function can be described by convolving the Lorentzian and Gaussian components into a Voigt profile [142].

Additional information about active and passive optical techniques, line profiles, and previous applications of optical diagnostic methods to atmospheric pressure plasmas can be found in the following works [134, 142, 145].

Chapter 3

Plasma sources

The following chapter details the four plasma sources investigated in this work, including design specifications and their development history.

3.1 COST Reference Microplasma Jet (COST-Jet)

The COST Reference Microplasma Jet (abbreviated to COST-Jet) is a capacitively-coupled atmospheric pressure plasma source developed through a collaboration under the European COST action MP1011 [146]. The COST-Jet was created to act as a reference standard and make the comparison of experimental data more accessible between different research groups [15]. The COST-Jet has also been investigated for direct applications [147], including industrial etching [148], surface modification [149], CO₂ conversion [150], treating cancerous biological material [151], bacterial sterilisation [152], and biocatalysis [153]. A full specification of the COST-Jet is given by Golda *et al* in [15], and a schematic is presented in figure 3.1.

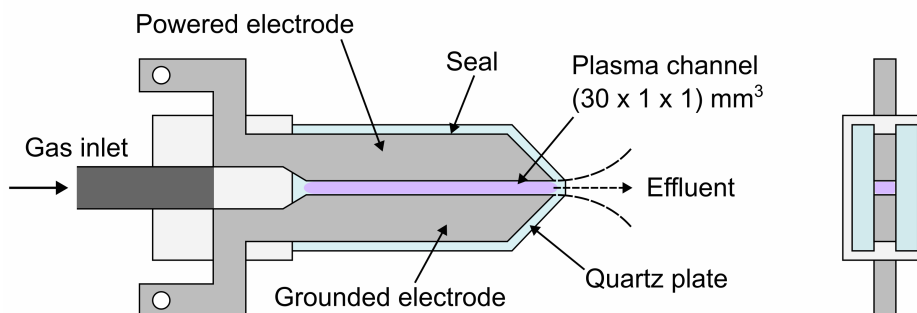


Figure 3.1: Schematic of the COST-Jet.

To summarise, the COST-Jet utilises two parallel-plate stainless steel electrodes, each with a length of 30 mm and a width of 1 mm. One electrode is powered, the other grounded. The outside of the electrodes broadens into wings to connect a power supply, grounding wire, and current and voltage probes. The electrodes are separated by a 1 mm gap through which the feed gas flows, forming a diffuse glow discharge when RF power is supplied [66]. The direction of gas flow is perpendicular to the electric field, which confines charged particles to the active plasma region. The dimensions of the plasma channel are 30 mm \times 1 mm \times 1 mm. The electrodes and plasma channel are vacuum sealed between two quartz panes with a gap at the nozzle for the plasma effluent, with the quartz panes protecting the plasma channel from the outside environment while retaining a clear line of sight for optical diagnostics [154]. The simplistic geometry of the plasma channel makes the COST-Jet and its analogues ideal for the benchmarking of computational plasma models, with a variety having been developed that describe aspects of the COST-Jet plasma environment [155–157]. The COST-Jet is most easily operated with a helium carrier gas, although it can sustain an argon plasma under specific conditions [78]. Golda *et al*'s COST-Jet specification includes a housing, attached to the wings of the electrode assembly, that contains an internal tuning capacitor with dedicated current and voltage probe connectors. These components are not utilised in the present work, and the source is instead impedance matched externally.

3.2 Sealed atmospheric pressure plasma jet (S-APPJ)

The sealed atmospheric pressure plasma jet (S-APPJ) is a capacitively-coupled, RF plasma source first described by Dedrick *et al*. A schematic of the device is shown in figure 3.2.

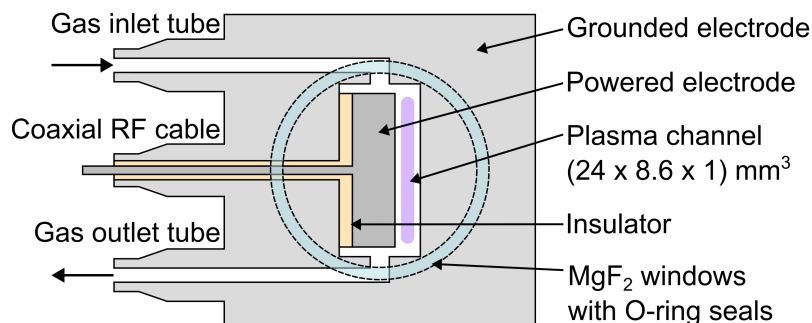


Figure 3.2: Schematic of the S-APPJ.

The plane-parallel stainless steel electrode assembly is designed to be similar to that of the

COST-Jet [15] and its precursor, the μ APPJ [55]. The electrode gap of 1 mm is the same, the length of 24 mm comparable, but the width of 8.6 mm much larger than the original 1 mm. This design offers a longer absorption beam path for previous measurements of atomic oxygen [136] and nitrogen [158] ground state densities by vacuum ultraviolet spectroscopy at the DESIRS beamline of the SOLEIL synchrotron facility [159]. As such, the S-APPJ has a smaller surface-area-to-volume ratio and an appreciably larger plasma volume than the COST-Jet and the μ APPJ. The electrodes are sealed between two circular MgF_2 windows. The grounded electrode also forms the housing of the plasma source. The gas outlet of the device is sealed to allow isolated measurements of the plasma effluent.

3.3 kINPen-sci

The term ‘kINPen’ refers to a family of DBD-like plasma jet devices developed by the Leibniz Institute for Plasma Science and Technology (INP) in Greifswald, Germany. The kINPen is the first device of its kind to be CE-certified and made commercially available for medical use [16, 160]. Consequently, the kINPen has proven useful for many biomedical applications, including the inactivation of bacteria [161], fungi [162] and pathogenic mites [163], the treatment of chronic wounds [164], and as a novel cancer therapeutic [165]. In addition to its uses in medicine, the kINPen has been investigated for roles in food safety [166] and surface modification [167]. The kINPen-sci, a version of the kINPen developed purely for research, is used in the present work [16, 168]. A schematic of the kINPen-sci is given in figure 3.3, and a detailed review and specification is presented by Reuter *et al* [16].

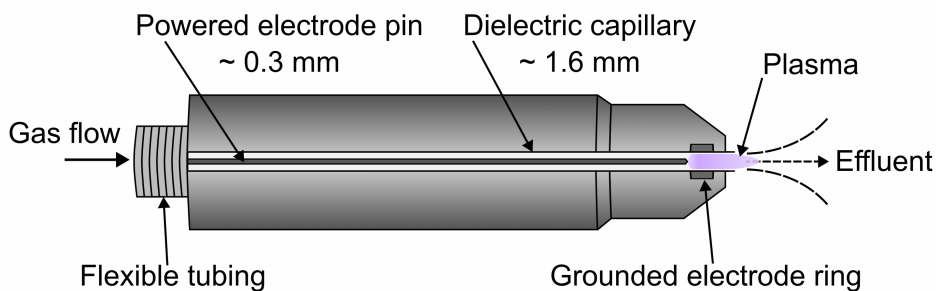


Figure 3.3: Schematic of the kINPen-sci.

The kINPen-sci plasma jet is a DBD-like, non-thermal plasma source that consists of a powered pin-type electrode inside a dielectric capillary, with the end of this capillary surrounded by a grounded electrode ring. The feed gas is introduced via the capillary, which has an inner

diameter of 1.6 mm. The kINPen-sci may be operated with an argon or helium carrier gas, both of which generate a filamentary discharge when the plasma is ignited [40, 169]. The active plasma region visibly extends for a few millimetres past the nozzle exit. A shielding device has been developed that attaches to the head of the kINPen-sci and surrounds the active plasma region with a gas curtain to reduce the influence of ambient species [170]. The shielding device is not utilised in the present work so as to better investigate the case of an unrestricted plasma effluent. The kINPen-sci includes a purpose-built power supply with automatic impedance matching and ports for current and voltage probes, in addition to a dial on the power supply unit that controls the applied voltage [16].

3.4 Pin-to-pin plasma source

The pin-to-pin plasma source was designed for fundamental studies of the plasma chemistry, rather than for applied use. Diverging from the previous three source designs, the pin-to-pin plasma source does not produce a plasma jet. Instead, a filamentary discharge is formed between two pin-type electrodes in a vessel much larger than the plasma volume itself. A transparent front cover and ports on the vessel walls provide ideal conditions for studying atmospheric pressure plasma chemistry within the active plasma region. A schematic is shown in figure 3.4.

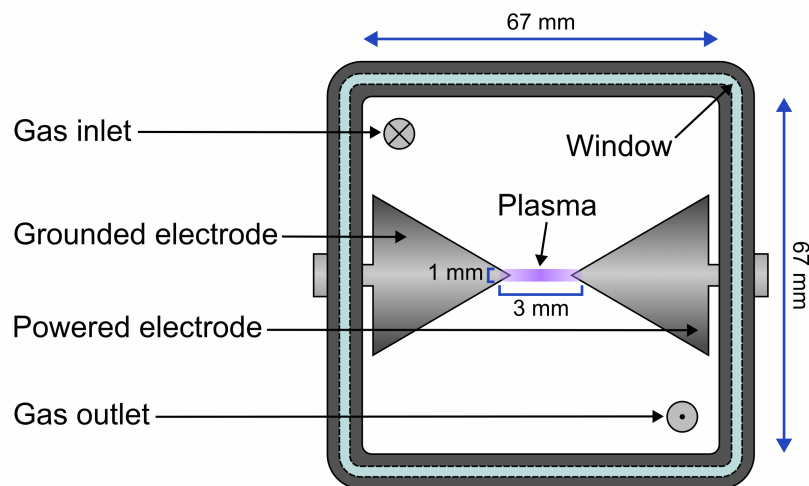


Figure 3.4: Schematic of the pin-to-pin plasma source.

This device was first described by Brisset *et al* [81]. To summarise, the source is a nanosecond-pulsed, pin-to-pin discharge housed in a 67 mm cubic vessel. The vessel has a volume of

0.3 L. The pin-type electrodes are made of stainless steel. They are conical in shape with a parabolic tip, with an approximate radius of curvature of 500 μm . They are fixed at a separation of 3 mm. The plasma produced between them has a radius of roughly 1 mm. DC power is supplied through high negative voltage, nanosecond-timescale pulses that trigger the breakdown of gas between the electrodes. The pin-to-pin discharge is sustained by higher peak voltages (typically a few kilovolts) than continuous plasma sources due to the short pulse duration.

Brisset *et al* previously used the pin-to-pin plasma source to study the effect of feed gas humidity on electron dynamics and streamer propagation, with a global model used to determine dominant electron production reactions [81]. The pin-to-pin plasma source was used again by Brisset *et al* in a subsequent work, in which the spatio-temporal evolution of O and H radicals in a He+H₂O plasma was investigated using picosecond two-photon absorption laser induced fluorescence (ps-TALIF) and a complementary 1D fluid model [171].

Chapter 4

The influence of pulse repetition frequency on the plasma chemistry of a nanosecond-pulsed discharge in He+H₂O

The following investigation has been published in the Journal of Applied Physics [172].

4.1 Motivation

LTPs can generate a wide array of RONS. As the ideal mixture of RONS varies by application, it is essential that methods of control are explored so that the plasma chemistry may be finely tuned for a given purpose. There are many ways to modify the chemistry of LTPs. One of the more simplistic approaches is to vary the reactive admixture concentration; though effective, this necessitates mechanical changes to the system which may not always be practical. Another highly effective approach is to alter the time-averaged power supplied to the plasma by increasing the amplitude of the driving voltage pulse or waveform. While straightforward, in some cases the strong gas temperature scaling may also cause issues. Moreover, this method provides only limited control over selective species production. For discharges operated with pulsed power schemes, the number of pulses per second can be modified while

the pulse itself is left unchanged. This parameter, the pulse repetition frequency, presents a seemingly straightforward way of tuning the plasma chemistry. This is due in part to the parameter being altered by purely electrical means. The lack of mechanical action reduces the risk of component wear over time, while also allowing the plasma chemistry to be modified at a rate restricted only by the effluent transit time. Previous studies have investigated the use of pulse repetition frequency as a control parameter for pulsed-power atmospheric pressure plasmas. The influence of pulse repetition frequency on discharge behaviour [173, 174] and electron parameters [175, 176] in dielectric barrier discharges has been reported, in addition to its effects on efficiency and selectivity in the conversion of methane and CO_2 [177]. It has also been demonstrated that the repetition frequency of $\text{He}+\text{O}_2$ plasmas can be altered to improve their effectiveness in biomedical roles, such as for triggering apoptosis in cancerous cells [178] or for treating tissue beneath a thin layer of liquid [179].

When considering pulsed plasma sources, operation with nanosecond-scale pulses can efficiently generate energetic electrons, driving an active plasma chemistry while also suppressing excessive gas heating due to the long afterglow period relative to the pulse [180]. Fundamental studies have been conducted that investigate the influence of pulse repetition frequency on atmospheric pressure, nanosecond-pulsed plasmas for a number of gas compositions, including helium [181], air [182], $\text{Ar}+\text{CH}_4$ [180], $\text{Ne}+\text{Ar}$ [183], H_2+air [184], and CH_4+air [185]. However, the influence of pulse repetition frequency on RONS production, and the overall plasma chemistry, in the bulk of a $\text{He}+\text{H}_2\text{O}$ plasma has not yet been studied in detail. Developing a power supply capable of covering a large range of pulse repetition frequencies while maintaining a constant high-voltage pulse would be a significant undertaking, both complex and time-consuming. It is therefore practical to undertake an initial modelling investigation to explore this parameter space so that the results may inform further studies on the effect of the pulse repetition frequency. This chapter presents a model study in which the pulse repetition frequency of a $\text{He}+\text{H}_2\text{O}$ plasma is varied so as to characterise its effect on RONS production across the power cycle.

4.2 Methods

4.2.1 *GlobalKin*

A global numerical model, *GlobalKin*, is utilised in this work. This is primarily due to its ability to handle the extensive reaction chemistries generated from He+H₂O gas mixtures. Moreover, the spatial profile of the investigated discharge is relatively homogeneous, allowing plasma properties to be well approximated without a comprehensive treatment of spatial dimensions. *GlobalKin* is a plasma-chemical kinetics model developed by Kushner and associates, and described in detail in [186]. It is a zero-dimensional model that computes plasma processes iteratively with user-defined time steps in order to simulate the evolution of a plasma in time. Alternatively, combining the time dimension with a gas flow rate may be used to run pseudo-one-dimensional simulations, although this is only an approximation. *GlobalKin* requires a detailed set of input files. This includes a file listing initial plasma parameters such as the gas temperature, flow rate, power profile, and starting fractions of species in the feed gas. Another must be a chemistry set containing a list of all species present in the plasma, the possible reactions between them, and the relevant reaction rate equations. With these inputs, *GlobalKin* models the evolution of a plasma through the interplay of three distinct modules. These are the chemistry and transport module, the ordinary differential equation (ODE) solver, and the Boltzmann solver. An overall schematic of the interactions between *GlobalKin*'s core modules is illustrated in figure 4.1, with explanations offered below. For each iterative time step, the chemistry and transport module constructs an ODE for the density of each species included in the model, describing their rate of change with respect to time. These density ODEs fit the form

$$\frac{dn_i}{dt} = \sum_j \left\{ (a_{ij}^R - a_{ij}^L) k_j \prod_l n_l^{a_{lj}^L} \right\} + \frac{S}{V} \left(-\frac{D_i n_i \gamma_i}{\gamma_i \Lambda + \frac{4D_i}{v_{th,i}}} + \sum_j \frac{D_j n_j \gamma_j f_{ji}}{\gamma_j \Lambda + \frac{4D_j}{v_{th,j}}} \right), \quad (4.1)$$

where n is the number density of species i . The first term describes the gas phase chemistry, where a_{ij}^R is the stoichiometric coefficient of species i in reaction j on the right-hand side of the reaction and a_{ij}^L is the stoichiometric coefficient on the left-hand side. The bracketed term is, therefore, the difference between these coefficients, giving the change in species i per reaction. k_j is the rate coefficient of reaction j , and $\prod_l n_l^{a_{lj}^L}$ accommodates for the reaction partners. The second term quantifies the gain and loss of particles due to collisions with the

vessel wall, where $\frac{S}{V}$ is the surface area to volume ratio of the plasma, D is the diffusion coefficient, γ is the sticking coefficient of a heavy particle colliding with the reactor wall, Λ is the diffusion length, v_{th} is the thermal velocity of the particle, and f is the return fraction of a species from the walls.

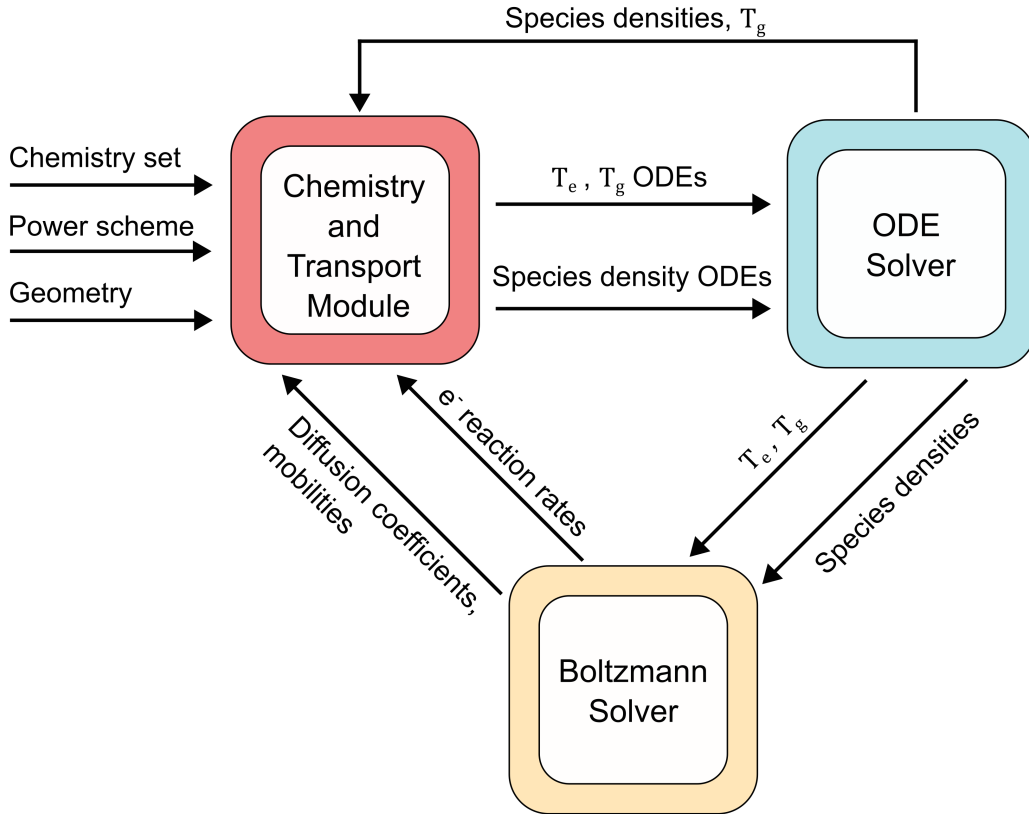


Figure 4.1: The connections between *GlobalKin*'s core modules. Further detail given in text.

The chemistry and transport module also constructs ODEs to describe the rate of change in the electron and gas temperatures. The electron temperature ODE is given as

$$\frac{d}{dt} \left(\frac{3}{2} n_e k_B T_e \right) = P_e - \sum_i \frac{3}{2} n_e \nu_{mi} \left(\frac{2m_e}{M_i} \right) k_B (T_e - T_i) + \sum_l n_e k_l n_l \Delta \epsilon_l, \quad (4.2)$$

where n_e is the electron density, k_B is the Boltzmann constant, T_e and T_i are the electron and neutral gas temperatures, P_e is the power supplied to the electrons at time t , ν_{mi} is the momentum transfer collision frequency, m_e and M_i are the electron and heavy particle masses, k_l is the rate coefficient of reaction l , n_l is the density of the collision partner in reaction l , and $\Delta \epsilon_l$ is the change in electron energy due to the collision. These are arranged such that the left-hand side of the equation describes the rate of change in the total kinetic

energy of the electrons. The first term on the right-hand side gives the rate of electron energy gain through power deposition. The second and third terms describe the energy exchange through elastic and inelastic collisions, respectively, with heavy particles. In this work, the gas temperature is estimated using a simplified form of the equation used by Lietz *et al* [186]. The gas temperature, T_g is calculated by considering the balance of the power deposition and conductive heat losses,

$$\frac{d}{dt} \left(\frac{3}{2} N_g c_p T_g \right) = P_{in} - \frac{\kappa}{\Lambda^2} (T_g - T_w) \quad (4.3)$$

where N_g , c_p and κ are the gas mixture's total density, specific heat and thermal conductivity, respectively. P_{in} is the power deposited into the plasma at time t , and T_w is the temperature of the bounding surfaces. Equations 4.1, 4.2 and 4.3 are passed to the ODE solver, which solves for the relevant parameters and passes them back to the chemistry and transport module for the next iteration.

As described by Stafford and Kushner in [187], the Boltzmann solver is responsible for calculating electric field parameters. This module is called less frequently than the others to save processing power, as very small changes in the EEDF should have minimal impact on the overall plasma chemistry. When invoked, the Boltzmann solver obtains the EEDF through iterative solution of the two-term expansion of the Boltzmann equation [188]. The module then creates tables of electron parameters, namely energies, transport coefficients and rate constants, for a pre-determined range of reduced electric field (E/N_g) values. The average electron energy at a given time is found through integration of equation 4.2, with the electron parameters and reduced electric field at this energy deduced by interpolating the tabulated data. These parameters are then passed to the chemistry and transport module, updating them for the next iteration.

PumpKin, a software package developed by Markosyan *et al*, is used to streamline the reaction pathway data generated by *GlobalKin*. The reaction kinetics of LTPs can be incredibly complex, and some reaction pathways involve numerous intermediary stages with very short lifetimes and negligible impact on the surrounding chemistry. Outputs pertaining to these unimportant reactions are reduced by *PumpKin* to improve the efficiency of the model. By considering the branching reaction pathways of a single short-lived species, pathways that combine to yield no net change are neglected in the output, as are pathways with low reaction rates. Furthermore, short-lived intermediary stages are decomposed in favour of the overall

simplified pathway.

4.2.2 He+H₂O+O₂ chemistry set

In this work, computational modelling of humidified helium plasmas is performed using a reaction chemistry set collated in Brisset *et al* [137]. Compatible with *GlobalKin*, it comprises 46 species and 576 reactions covering He, H₂O, and O₂ gas mixtures. Table 4.1 lists the included species, while the full reaction set can be found in appendix A.

Table 4.1: The 46 species included in the He+H₂O+O₂ chemistry set.

	Neutral	Positive	Negative
He	He, He(2 ³ S), He ₂ *	He ⁺ , He ₂ ⁺	
O	O, O(¹ D), O(¹ S), O ₂ , O ₂ (a ¹ Δ), O ₂ (b ¹ Σ), O ₃	O ⁺ , O ₂ ⁺ , O ₃ ⁺ , O ₄ ⁺	O ⁻ , O ₂ ⁻ , O ₃ ⁻ , O ₄ ⁻
H	H, H ₂		H ⁻
OH	OH, HO ₂ , H ₂ O, H ₂ O ₂	OH ⁺ , O ₂ ⁺ (H ₂ O), H ⁺ (H ₂ O) _{n=1-9} , H ₂ O ⁺ (H ₂ O) _{n=0,1}	OH ⁻ , H ₂ O ₂ ⁻ , OH ⁻ (H ₂ O) _{n=1-3}
Other			e ⁻

The He+H₂O+O₂ chemistry set is largely built upon the He+H₂O chemistry presented by Schröter *et al* [136], with the addition of O-based ions and adjustments to certain reaction rate coefficients based on He+O₂ chemistries given in [80, 135, 189]. As noted by Brisset *et al*, the model does not include a full treatment of photons stemming from ro-vibrational transitions [81]. Energy loss through radiative emission in electron - heavy particle collisions is accounted for, although radiation absorption mechanisms that redistribute the energy among excited states are not considered. Efforts to model H₂O-containing LTPs with a dedicated photon treatment have revealed that around 22% of the total electron energy is lost to ro-vibrational excitation [190], and that increasing the concentration of H₂O admixture enhances the rate of excitation, reducing the electron energy and causing a drop in H, O and OH radical densities at high H₂O concentrations [191, 192]. Nonetheless, the influence of ro-vibrational transitions is expected to be minimal under both the conditions investigated in this work and those investigated previously by Brisset *et al*. The chemistry set has been validated

against experimental measurements of O and OH densities [137] and time-resolved electron densities [81], and has proven to yield accurate results.

4.2.3 Model parameters

Despite being a spatially averaged model, *GlobalKin* requires geometric inputs, in the forms of the surface-area-to-volume ratio and radius of the plasma, in order to accurately account for surface losses. As such, the dimensions used in this model are matched to the pin-to-pin plasma source (see chapter 3.4). Assuming the discharge to be approximately cylindrical, the initial plasma volume is $9.42 \times 10^{-3} \text{ cm}^3$. The volume of the vessel is 300 cm^3 and the plasma is generated at its centre, meaning interactions with the plasma and vessel walls are negligible and the surface area of the vessel is ignored in the model. The surface area in contact with the plasma is instead set to 0.0524 cm^2 , the approximate area of the electrodes that bulk plasma emission extends across. A helium feed gas with a 0.25% water vapour admixture, equivalent to 2500 parts-per-million by volume, is supplied to the vessel.

The width and amplitude of the nanosecond-pulsed power profile are based on current and voltage measurements of the physical setup, with a typical pulse shown in figure 4.2. The scheme utilises a negative voltage pulse with an amplitude of 2.5 kV, a rise time of 3 ns and a duration of roughly 80 ns. LTPs generated in this manner have been observed to be reasonably homogeneous along the discharge channel [81]. It is therefore expected that the 0D global model described above will provide a good approximation of the plasma chemistry. The current and voltage signals are multiplied together to find the power supplied to the plasma over time, before being simplified slightly to streamline the model input. The experimentally measured pulse and its approximation are also shown in figure 4.2. The power deposition used in the model is 0 outside the width of the simplified profile. The duration of power deposition is 89 ns per cycle, with a rise time to peak of 67 ns. The pulse amplitude and duration are kept constant for all repetition frequencies. As such, by altering the pulse repetition frequency the afterglow is the phase of the cycle that is modified. The use of this pulse scheme produces model electron densities comparable to experimental measurements presented in [81].

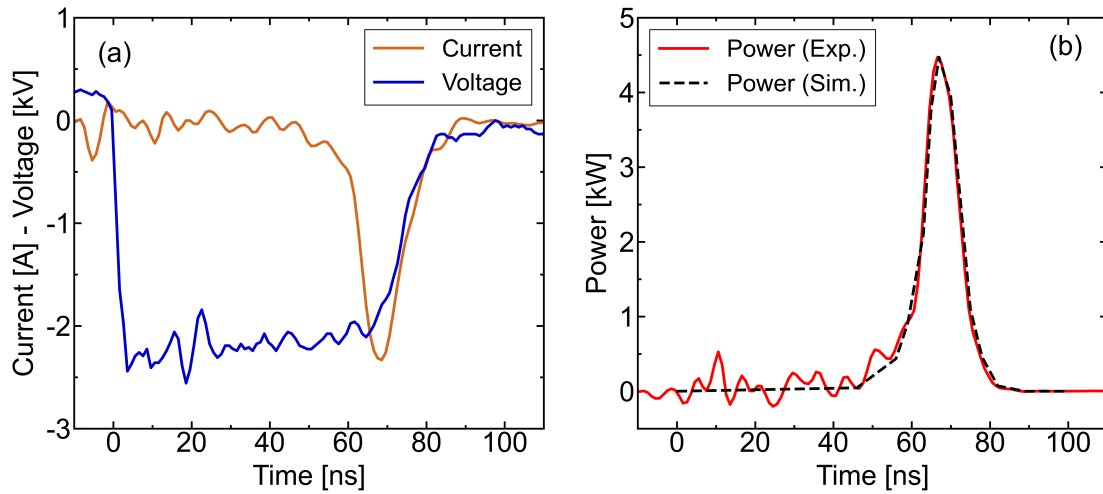


Figure 4.2: (a) Characteristic current and voltage signals supplied by a nanosecond-pulsed negative voltage generator, and (b) an experimental power profile overlaid with a simplified version used in the model.

The pulse repetition frequency is varied in the range of 1–100 kHz. Across this frequency range, the pulse width is significantly shorter than the overall cycle time. In addition to this, the plasma chemistry during and shortly after the pulse is driven by electron interactions occurring on very short timescales, whereas the late stage of the cycle is dominated by heavy particle interactions on comparatively longer timescales. Consequently, the time steps used in the model must allow the plasma chemistry in the pulse to be captured in high resolution, while using longer time steps in the afterglow phase to relax computational demand and produce a more efficient output. This is achieved by setting each subsequent time step to increase by a constant factor determined by the given repetition frequency. The time step then resets with the following cycle.

To examine the plasma chemistry in steady-state conditions, simulations are run until the plasma reaches an equilibrium. Electrons and radicals tend to equilibrate within a short number of cycles, while O_3 and H_2O_2 take a greater number of cycles to equilibrate due to being tertiary reaction products. Increasing the pulse repetition frequency increases the number of cycles needed before steady-state is achieved. The change in gas temperature and the densities of OH and H_2O_2 as a function of completed cycles is shown in 4.3. Given the presented timescales, data is analysed after a minimum of 300 cycles.

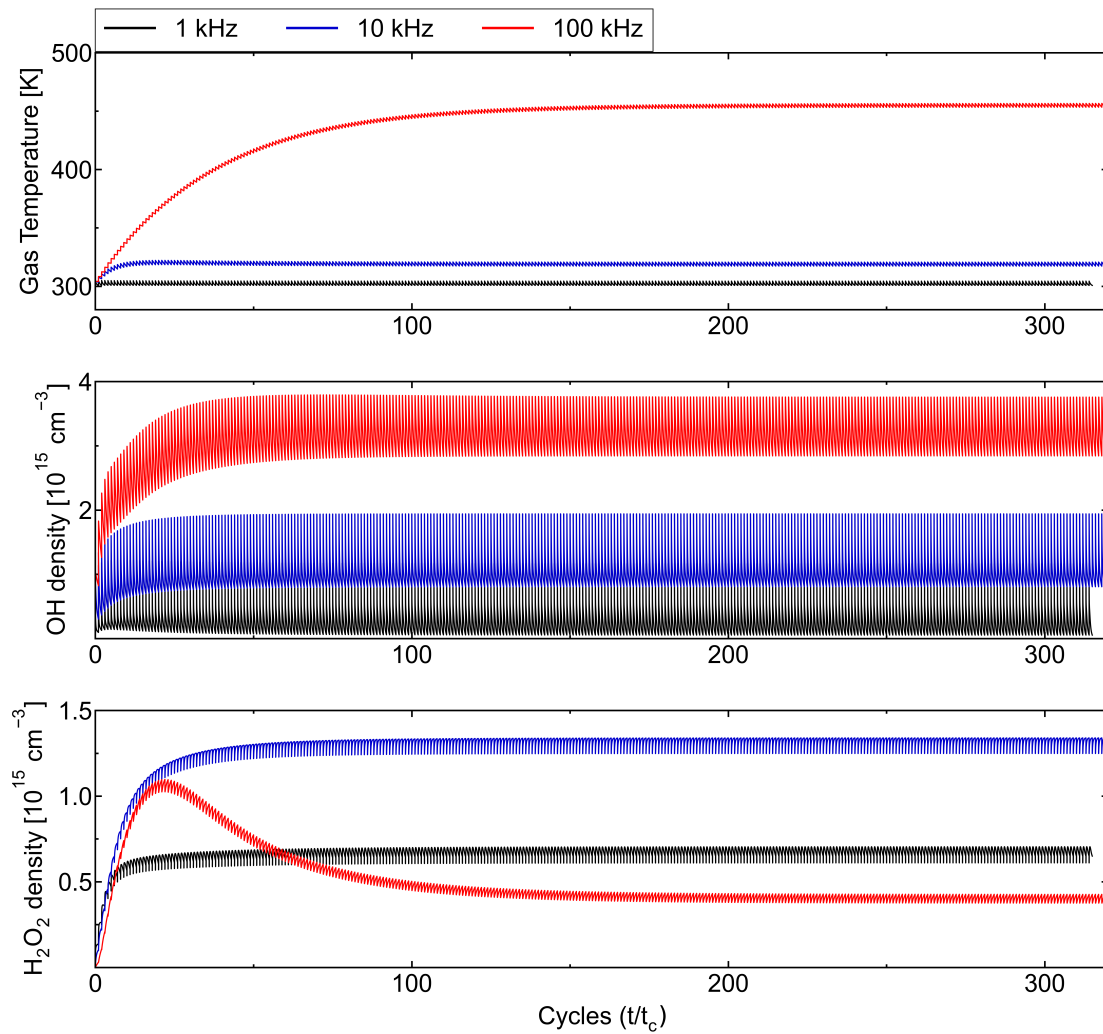


Figure 4.3: Modelled gas temperature, OH density and H_2O_2 density as a function of the number of power cycles for a nanosecond-pulsed plasma source.

The time-averaged density of a species is found by taking the mean of its density across cycles 300 to 310. This allows a good degree of confidence in the results. For the same reason, the average peak electron density per cycle is taken as the mean of the peak electron density across the same cycles. Time-resolved measurements are taken across one cycle in equilibrium, specifically cycle 305. Analysis of time-resolved parameters is achieved by normalising the time in the cycle to the total duration of a cycle at the given repetition frequency, with $t = 0$ being the instant of maximum power deposition. Data on reaction pathways in the plasma is extracted and streamlined to find dominant reaction rates using *PumpKin*.

4.3 Results and discussion

4.3.1 Electron behaviour

The effect of pulse repetition frequency on the average peak electron density when the plasma is in equilibrium is shown in figure 4.4. The peak electron density is only weakly affected by pulse repetition frequency, changing by 9% between the maximum and minimum values recorded. This is unsurprising, as most of the electrons created by the pulse recombine on timescales significantly shorter than the cycle time.

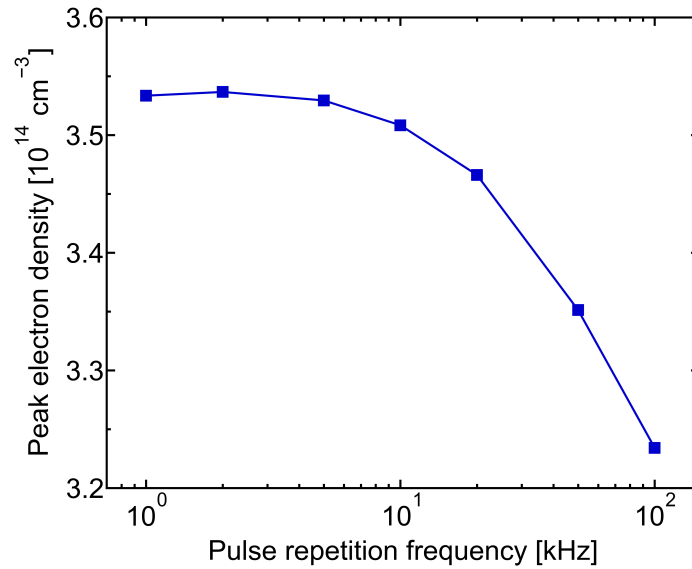


Figure 4.4: Average peak electron density per cycle as a function of the pulse repetition frequency.

A very small increase in the peak electron density is observed from 1 to 2 kHz. This can likely be attributed to the memory effect [45], with its dependence on repetition frequency identified in studies by Walsh *et al* [174] and Liu *et al* [175]. Here, increasing the repetition frequency reduces the duration of the afterglow, such that a larger electron population remains by the end of the cycle. The presence of residual electrons at the start of the next pulse shortens the breakdown phase of the plasma and increases the peak electron density. In this case, the memory effect is near-negligible due to the rapid recombination of the electrons at all repetitions frequencies investigated. At higher frequencies, the memory effect is offset by an expansion of the plasma that arises as a result of an increased gas temperature, increasing the overall volume occupied by the electrons and therefore reducing the electron density. The data presented here are in good agreement with previous experimental measurements

of the pin-to-pin discharge setup modelled in this study [81]. For the same gas composition, nanosecond pulsing at a repetition frequency of 5 kHz yielded a similar electron decay curve with time. The peak spatially averaged electron density measured in those conditions was around $2.5 \times 10^{14} \text{ cm}^{-3}$, the same order of magnitude and similar value to $3.5 \times 10^{14} \text{ cm}^{-3}$ found in the present study.

4.3.2 Radical chemistry

Figures 4.5, 4.6 and 4.7 show the change in time-averaged atomic hydrogen, atomic oxygen and hydroxyl densities, respectively, with pulse repetition frequency.

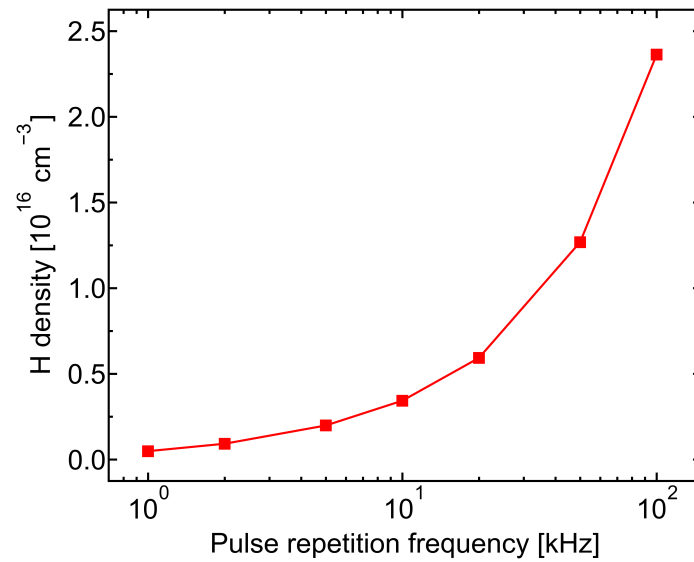


Figure 4.5: Average atomic hydrogen density in equilibrium as a function of the pulse repetition frequency.

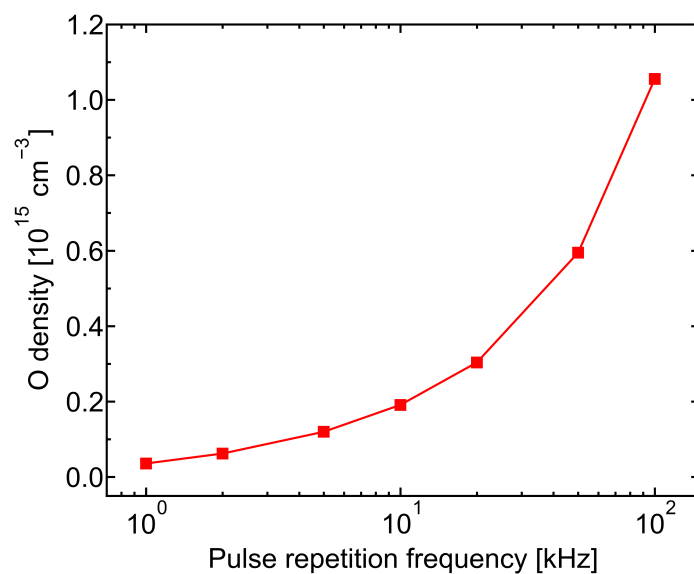


Figure 4.6: Average atomic oxygen density in equilibrium as a function of the pulse repetition frequency.

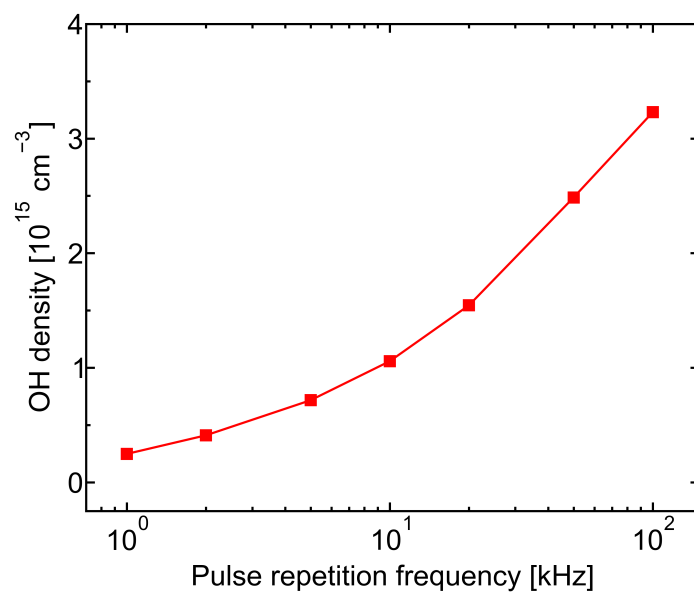


Figure 4.7: Average hydroxyl density in equilibrium as a function of the pulse repetition frequency.

H and O exhibit similar density trends, undergoing minimal change at low repetition frequencies and a more substantial increase in the high frequency range. Meanwhile, OH increases more steadily with repetition frequency. In spite of the hundredfold increase in the power supplied per unit time as the pulse repetition frequency is increased from 1 to 100 kHz, the density of these radicals only increases by factors of 13–50. However, this is still a stark in-

crease when compared to the electron density, especially as these species are predominantly formed through electron impact processes. To investigate this further, the densities of these radicals are plotted as a function of relative time within a cycle in figures 4.8, 4.9 and 4.10.

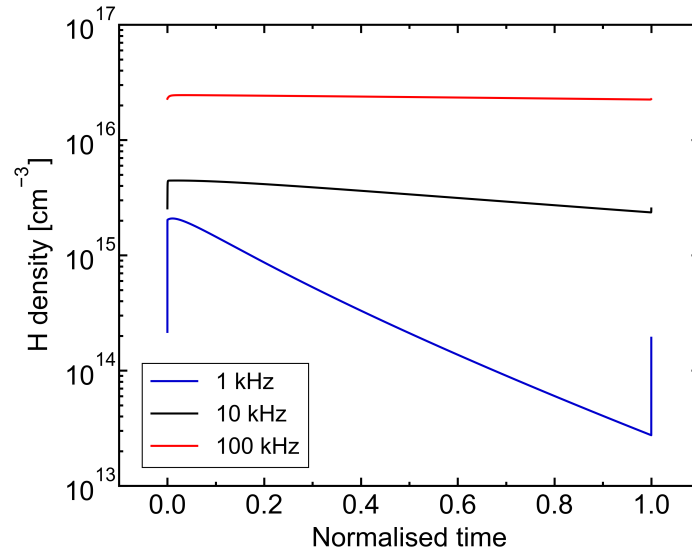


Figure 4.8: Density of atomic hydrogen over one cycle as a function of normalised time for different pulse repetition frequencies.

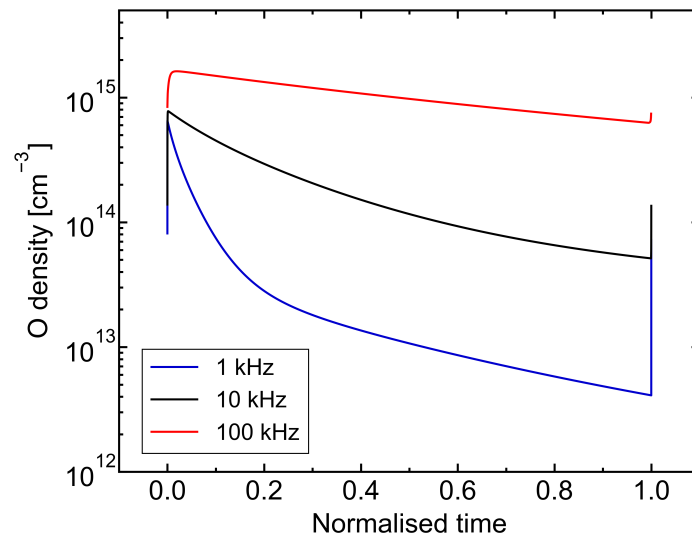


Figure 4.9: Density of atomic oxygen over one cycle as a function of normalised time for different pulse repetition frequencies.

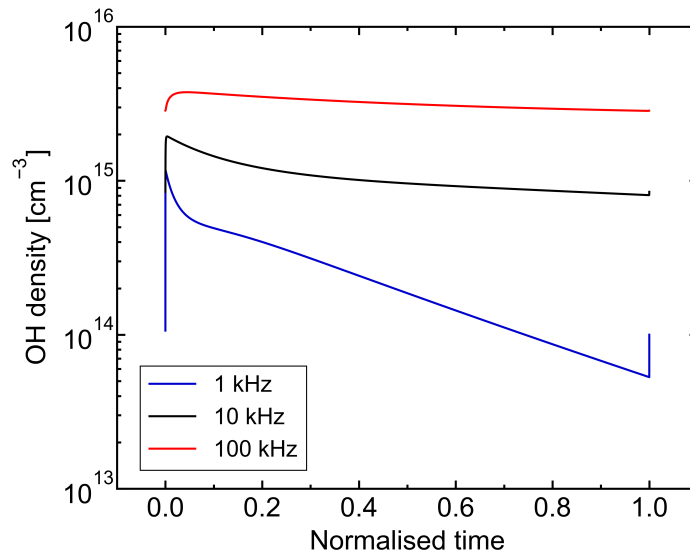


Figure 4.10: Density of hydroxyl over one cycle as a function of normalised time for different pulse repetition frequencies.

Density maxima occur shortly after the pulse for the radicals due to the associated peak in the electron density. The density of all three radicals drops substantially over the course of the afterglow at low pulse repetition frequencies. This effect is reduced toward higher repetition frequencies, where the reduced afterglow period limits the time available for the densities to decay. Indeed, once equilibrium is reached at a repetition frequency of 100 kHz the time-resolved density of H is nearly constant. Additionally, an increase in the background gas temperature slightly enhances the radical densities in the range 50–100 kHz.

The H, O, and OH radicals decay significantly slower than the electrons; even at lower frequencies, the electron density decays by several orders of magnitude more than that of the radicals. This leads to the radical densities experiencing a more pronounced memory effect compared to the electrons, with the latter decaying to near background densities at low repetition frequencies. In contrast, the significant radical densities remaining at the start of the next pulse further increase their peak densities until an equilibrium is reached. Similar effects were noted by Pan *et al* in a modelling study of pulsed He+O₂ plasmas, where increasing the pulse repetition frequency was found to increase the density of the O radical and the excited states O(¹D) and O₂(¹Δ_g) [176]. Likewise, an increase in the H radical density with repetition frequency is also seen in Ar+CH₄ mixtures [180], and an increase in OH with repetition frequency is seen in CH₄+air and H₂+air mixtures [184,185]. As with the present work, the authors of these previous studies attribute the increased radical densities to

accumulation with decreasing afterglow duration. These results indicate that the afterglow period is important for determining the final densities of H, O, and OH despite their short lifetimes.

4.3.3 H₂O₂ chemistry

Figure 4.11 shows the relationship between the pulse repetition frequency and the average H₂O₂ density. The density of H₂O₂ initially increases with the repetition frequency, before peaking at 20 kHz and dropping sharply towards 100 kHz.

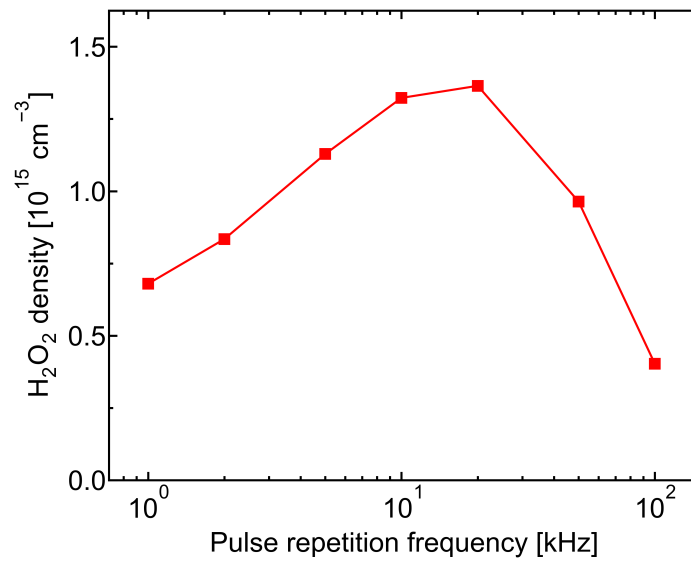


Figure 4.11: Average hydrogen peroxide density in equilibrium as a function of the pulse repetition frequency.

Analysis of the dominant reaction pathways is necessary to explain this trend. Figure 4.12 shows the change in the rate of these reactions over one cycle. For all pulse repetition frequencies modelled, H₂O₂ formation is seen to take place throughout the full cycle. This occurs predominantly through the three-body recombination of two OH radicals,



This reaction is generally accepted to be the main mechanism of H₂O₂ production in atmospheric pressure plasmas with water vapour admixtures [126, 193]. There is also a small spike in H₂O₂-producing ion interactions close to the pulse. The peaks of these reaction rates are mostly unaffected by the pulse repetition frequency, although their duration relative to the

cycle period increases as the repetition frequency is raised.

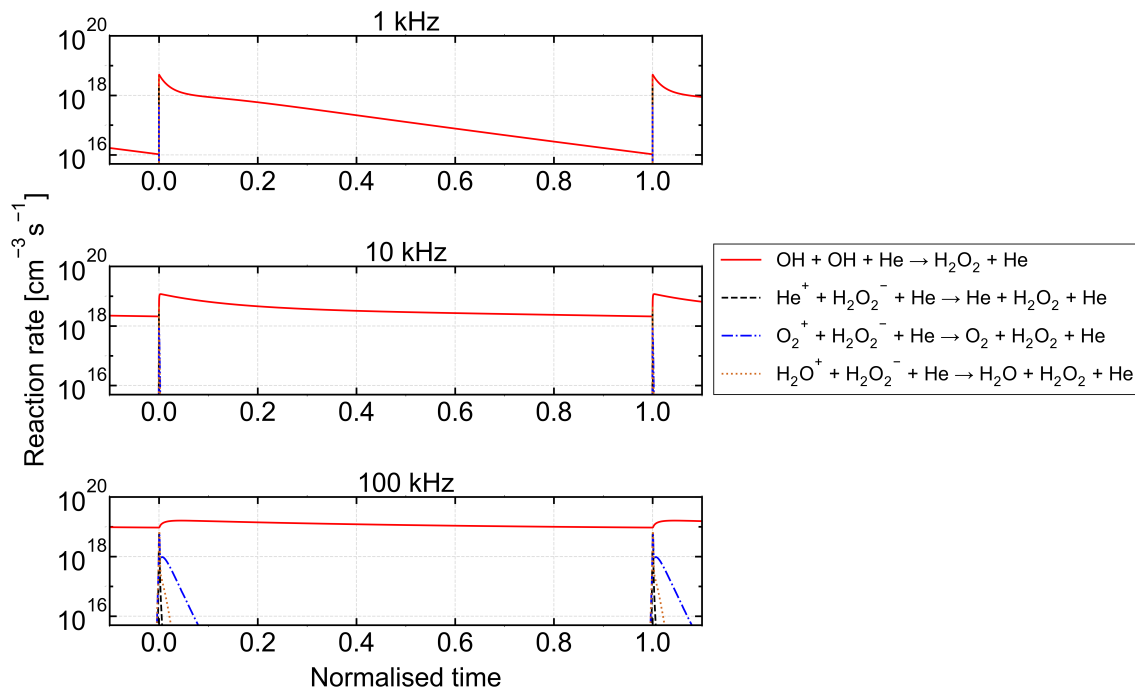


Figure 4.12: Rates of dominant H_2O_2 production reactions over one cycle for 1 kHz, 10 kHz, and 100 kHz pulse repetition frequencies.

The increase in H_2O_2 density in the low repetition frequency range is likely a consequence of the steady increase in OH over the same frequency range. However, the peak and subsequent decrease in the H_2O_2 density seen at repetition frequencies above 20 kHz does not match the trend shown for OH in figure 4.7. To investigate this, figure 4.13 shows the density of H_2O_2 as a function of normalised time over one cycle in equilibrium. H_2O_2 is seen to accumulate through the early to mid afterglow at 1 kHz and throughout the full afterglow at 10 kHz and 100 kHz, primarily through OH recombination in reaction R4.1. Another feature of importance is the decrease in the H_2O_2 density during and shortly after the pulse. Figure 4.14 shows that this is tied to a significant increase in the rates of dissociation reactions between electrons and H_2O_2 shortly after the pulse, along with an increase in the rate of H_2O_2 dissociation by the electronically excited $\text{He}(2^3S)$ [194].

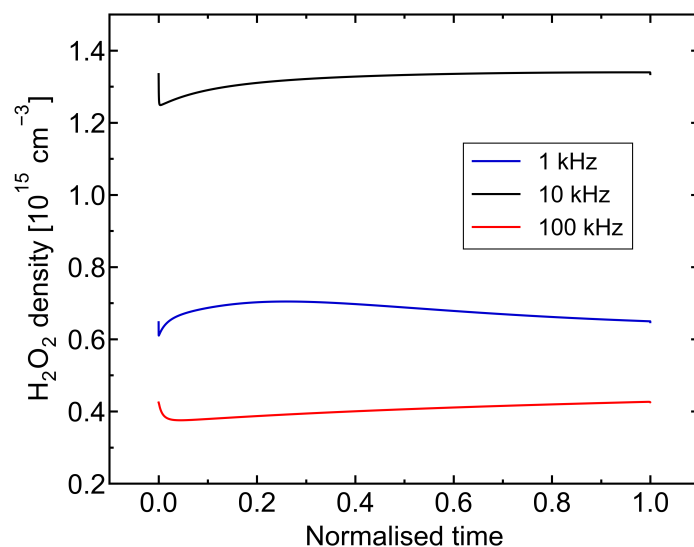


Figure 4.13: Density of H_2O_2 over one cycle as a function of normalised time for different pulse repetition frequencies.

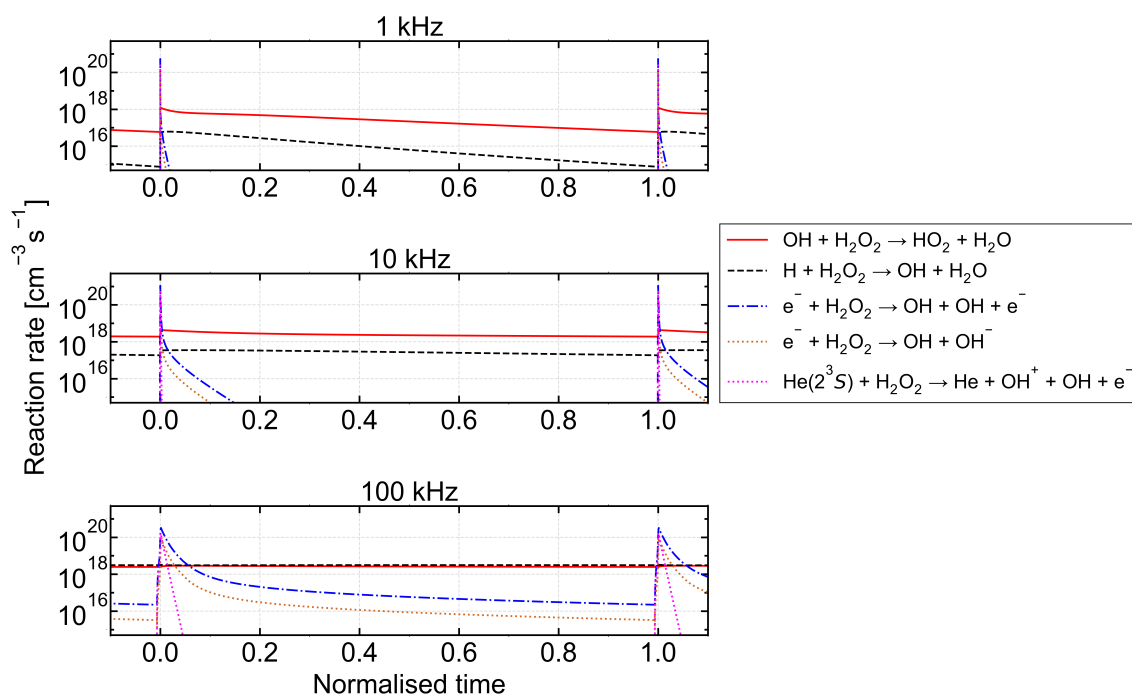


Figure 4.14: Rates of dominant H_2O_2 consumption reactions over one cycle for 1 kHz, 10 kHz, and 100 kHz pulse repetition frequencies.

As the pulse repetition frequency is increased, these reactions remain at high rates for increasingly longer fractions of the cycle. Though less significant than during the pulse phase, H_2O_2 consumption is relatively consistent in the afterglow after these processes die out. The

dominant contribution comes from a reaction with OH. Despite this, the consumption from OH is lower than the production from OH via reaction R4.1, meaning that there is still a net increase in H_2O_2 from OH. Another source of consumption is the reaction between H_2O_2 and atomic hydrogen, a process whose rate in the late afterglow increases significantly with pulse repetition frequency. It so follows that a reduction in the afterglow period with increasing repetition frequency restricts the time available for OH to react to form H_2O_2 , whilst also increasing the fraction of the cycle where H_2O_2 is destroyed by electrons and metastables. This is the case despite the high OH densities seen at higher pulse repetition frequencies. It can be concluded that at the peak in H_2O_2 density at 20 kHz, the limiting factor in its production changes from OH availability at lower repetition frequencies to the afterglow duration at higher repetition frequencies.

Another factor that impacts the density of H_2O_2 is the temperature of the background gas. Figure 4.15 shows the change in time-averaged gas temperature with pulse repetition frequency.

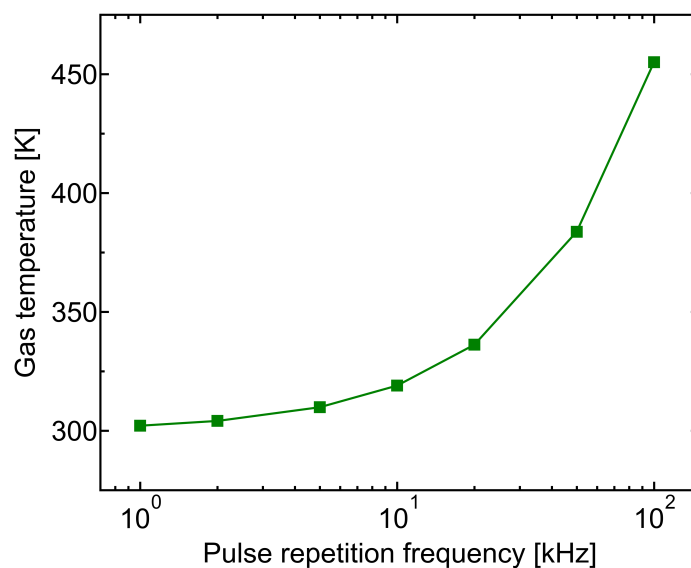


Figure 4.15: Average gas temperature in equilibrium as a function of the pulse repetition frequency.

The gas temperature increases steadily with the pulse repetition frequency, with a minimum of 300 K at 1 kHz and peaking at 455 K at 100 kHz. H_2O_2 is known to undergo thermal decomposition at high temperatures, with this effect contributing to the drop in H_2O_2 seen above 20 kHz as the gas temperature increases appreciably in the same range [195]. Nevertheless, the influence of gas heating only exacerbates the existing trend seen for H_2O_2 .

Simulations with a constant gas temperature of 300 K show the same trend, albeit with the peak and drop in the H_2O_2 density shifted towards higher pulse repetition frequencies.

4.3.4 O_3 chemistry

O_3 is produced in significantly lower quantities in plasmas with water vapour admixtures when compared to plasmas with admixtures of oxygen gas due to the preferential formation of hydrogen-containing species over O or O_3 . Analysis of the reaction chemistry suggests that this phenomenon arises from the plasma conditions supporting hydrogen catalytic cycles, whereby hydrogen-containing radicals catalyse the decay of O and O_3 into O_2 [196,197]. The densities of the radicals, namely H, OH, and HO_2 , are largely unaffected by these cycles. Figure 4.16 shows a complex relationship between the density of O_3 and the pulse repetition frequency.

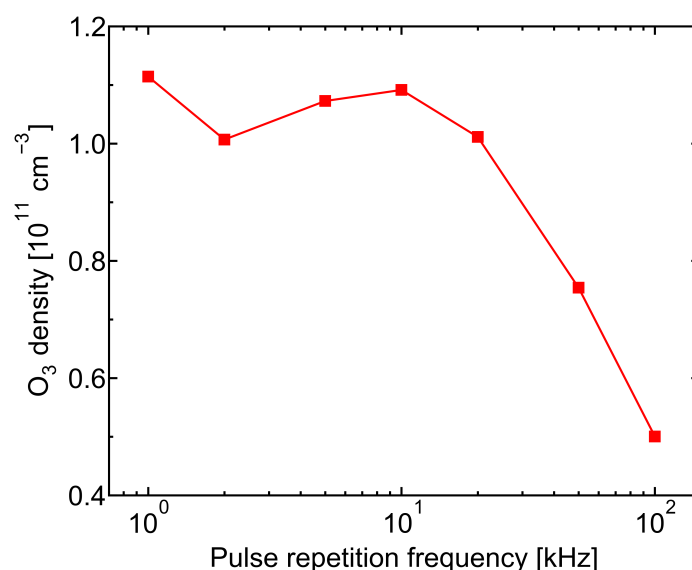


Figure 4.16: Average ozone density in equilibrium as a function of the pulse repetition frequency.

The maximum O_3 density occurs at a frequency of 1 kHz, with this density dropping towards 2 kHz and rising to a second, smaller peak at 10 kHz. The O_3 density drops sharply as the repetition frequency is further increased. This relationship is largely influenced by the changing reaction chemistry, and so the dominant mechanisms must be considered. Figure 4.17 shows that O_3 is predominantly formed through the three-body recombination of O and O_2 with background He:



The rate of this reaction is consistent across the full cycle at higher pulse repetition frequencies, while at low repetition frequencies the longer afterglow duration causes the rate to drop by around two orders of magnitude by the end of the cycle as O is depleted. O_3 is also produced through ion interactions close to the pulse, with these processes increasing in rate and extending through a larger portion of the afterglow towards higher pulse repetition frequencies, although this effect becomes insignificant compared to the rising gas temperature.

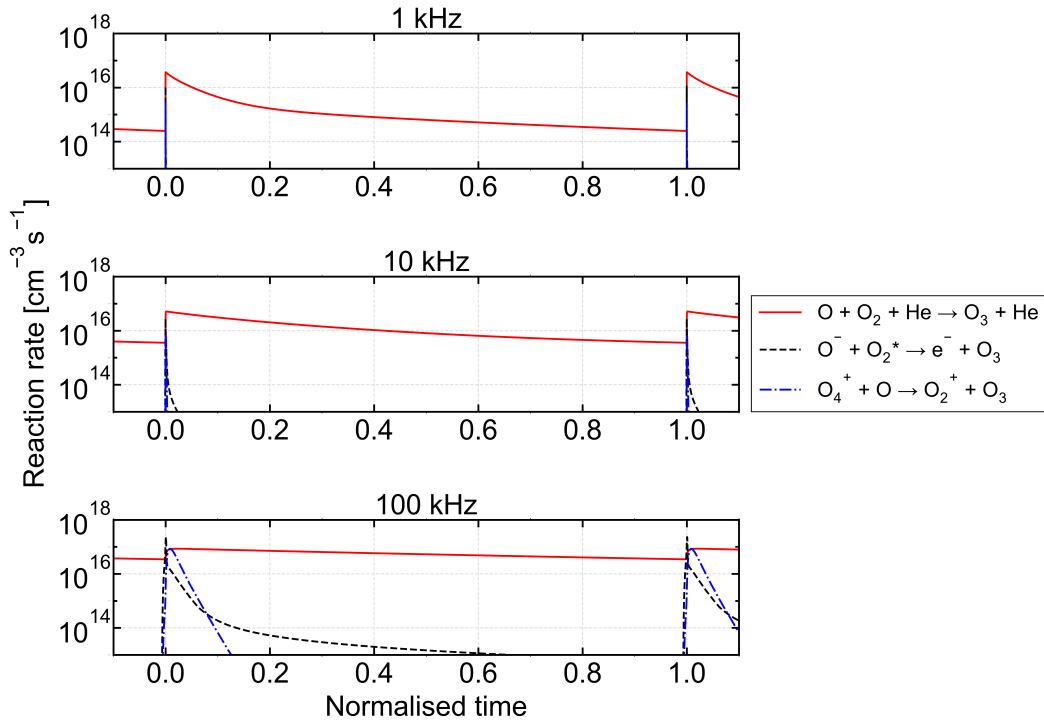


Figure 4.17: Rates of dominant O_3 production reactions over one cycle for 1 kHz, 10 kHz, and 100 kHz pulse repetition frequencies.

Examining the change in the O_3 density over one cycle at 1 kHz, 10 kHz, and 100 kHz, given in figure 4.18, shows that the peak density of O_3 is reached shortly after the pulse. This peak decreases with the repetition frequency. In all cases, the peak is followed by a decline in the O_3 density. This decline persists throughout the full afterglow at 10 kHz and 100 kHz. At 1 kHz, a minimum is reached a quarter of the way through the cycle, with the O_3 density increasing again through the remaining afterglow.

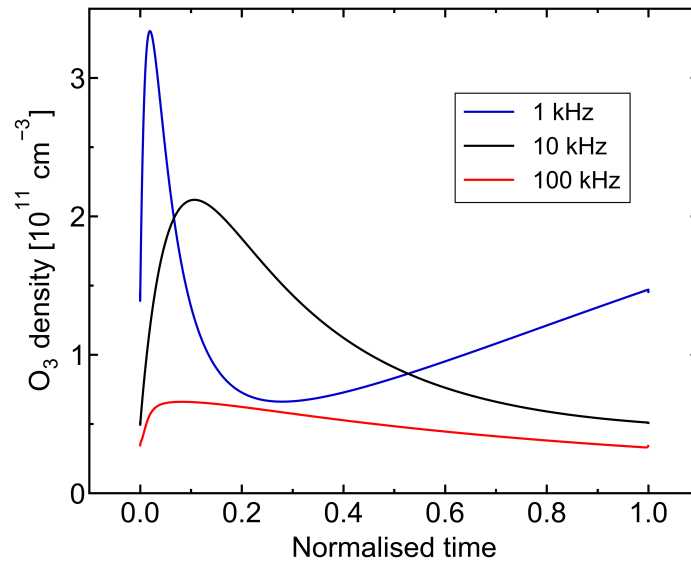


Figure 4.18: Density of O_3 over one cycle as a function of normalised time for different pulse repetition frequencies.

Figure 4.19 shows the rates of key O_3 consumption reactions during one cycle in equilibrium. The primary O_3 consumption pathway is as follows:



This reaction dominates the afterglow phase because of an abundance of H atoms, due largely to the electron-impact dissociation of H_2O and H_2 during the pulse. There is also a spike in electron-impact processes that destroy O_3 near the pulse. The rate of reaction R4.3 is dependent on afterglow duration, staying roughly constant at high repetition frequencies but dropping by two orders of magnitude in the 1 kHz case wherein the afterglow lasts for long enough for the density of H to be severely depleted. Increasing the repetition frequency also increases the overall peak rate of reaction R4.3. It can therefore be concluded that the production of O_3 seen in the afterglow at 1 kHz is due to the lack of availability of atomic hydrogen. Thus, the decrease in the average O_3 density at 2 kHz shown in figure 4.16 can be attributed to a reduction of the afterglow as compared to the 1 kHz case, such that the density of H is not depleted as significantly. This limits the late-afterglow buildup of O_3 at 2 kHz. The change in the O density from 1 to 2 kHz is minimal, resulting in negligible extra O_3 production from reaction R4.2. As the pulse repetition frequency is increased from 2 to 10 kHz, a more appreciable increase in the density of O enhances O_3 production through reaction R4.2,

outmatching the effects of the reduced afterglow and H abundance and increasing the overall mean density. The subsequent decay seen from 10 to 100 kHz is heavily dictated by the rising gas temperature, as O_3 is highly sensitive to thermal decomposition [198]. This is corroborated by simulating the plasma with a constant background gas temperature; under these conditions, a minimum is still reached at 2 kHz and the density of O_3 rises above 10 kHz rather than decaying.

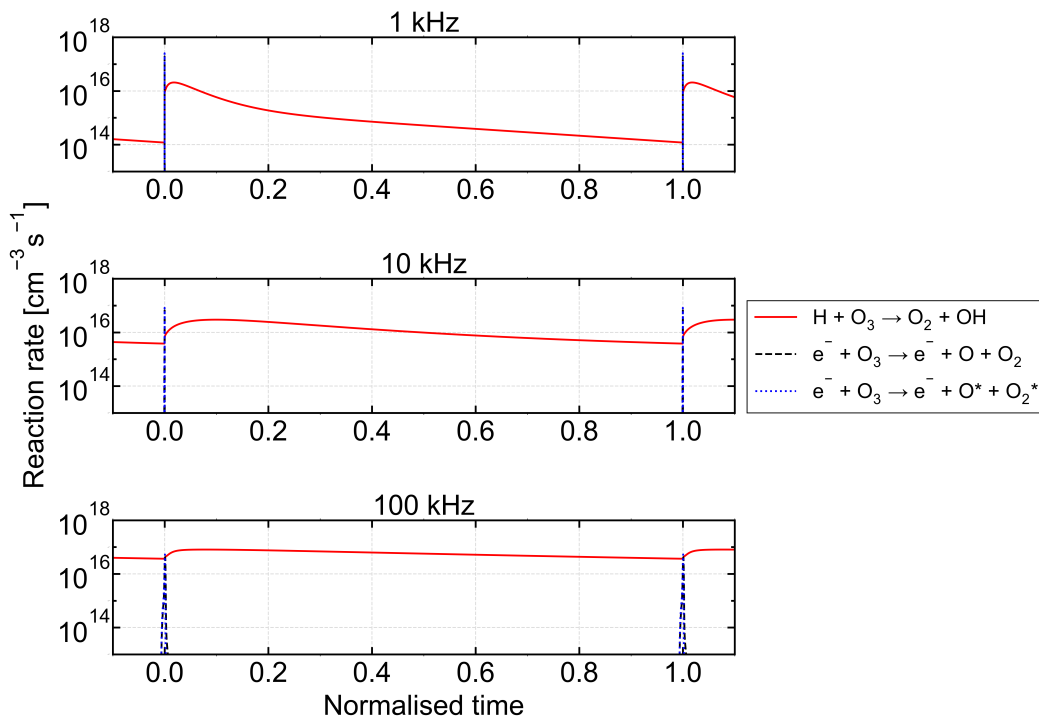


Figure 4.19: Rates of dominant O_3 consumption reactions over one cycle for 1 kHz, 10 kHz, and 100 kHz pulse repetition frequencies.

An experimental study by Sands and Ganguly showed that ozone exhibits a similar relationship with pulse repetition frequency in $He+O_2$ mixtures [199]. The ozone density was found to rise with the pulse repetition frequency up to a maximum before decreasing towards higher frequencies, with the frequency needed to generate this maximum being dependent on the gas flow rate, admixture concentration and applied voltage [199].

To summarise these results, the observed dependence of O_3 density on pulse repetition frequency in $He+H_2O$ mixtures results from the interplay between O and H reactant availability and afterglow duration at low frequencies, while at high frequencies the influence of background gas heating dominates.

4.4 Chapter summary

Pulse repetition frequency shows potential as a parameter for controlling RONS production in pulsed-power He+H₂O plasmas. Here, a nanosecond-pulsed, pin-to-pin He+H₂O plasma is modelled using *GlobalKin* with a *PumpKin* plugin. The plasma is simulated at different pulse repetition frequencies with a constant pulse shape, thus varying the duration of the afterglow phase. The reduction in afterglow duration with increasing repetition frequency increases the influence of the memory effect. This results in a greater residual electron population by the end of the cycle, in turn causing a slight increase in the peak electron density at 2 kHz. However, this effect is outmatched by gas expansion in the 5–100 kHz range. The densities of short-lived species (namely H, O, and OH) decay much more slowly than the electron density, dropping by several orders of magnitude less than the electron density by the end of the cycle. This results in a more pronounced memory effect, boosting the peak radical densities until an equilibrium is reached. The density of H₂O₂ exhibits a more complex relationship with the repetition frequency as it has a comparatively longer lifetime and is mainly produced throughout the afterglow. As such, the pulse repetition frequency can be used to modulate the density of H₂O₂ provided that its relationship with this parameter is clearly understood. Finally, the density of O₃ is dependent on the afterglow duration and availability of O and H as reactants, although at high repetition frequencies an increase in the gas temperature drives a strong O₃ decay. These findings highlight the importance of the pulse repetition frequency, and by extension the afterglow duration, when optimising a nanosecond-pulsed plasma for biomedical applications. Though the pulse repetition frequency can indeed be used to tune the plasma composition, it is clear that the effects on the plasma chemistry are significant and a thorough understanding of the chemistry is needed to effectively utilise this parameter to optimise a plasma.

Chapter 5

The spatial density distribution of H_2O_2 in the effluent of the COST-Jet and the kINPen-sci supplied with $\text{He}+\text{H}_2\text{O}$

*The following investigation has been published in
Plasma Sources Science and Technology [200].*

5.1 Motivation

As evidenced in the previous chapter, the operational parameters of a plasma source can be used to tailor the production of RONS within the active plasma region for biomedical applications. However, the transport of these plasma-produced RONS to a target area poses another challenge when designing and optimising a plasma source. This is especially true in the case of APPJs, where the complex mixture of RONS in the plasma effluent is commonly carried through open air to a surface, liquid, or biological tissue. The spatial distribution in the effluent varies for different RONS, influenced by a given species' mass and available reaction pathways. Hence, the dosage and mixture of RONS received through direct APPJ treatment is dependent on the position of the substrate relative to the jet nozzle. It is therefore crucial to know how key RONS are spatially distributed throughout the effluent in order to

understand their production mechanisms, as well as to be able to tailor the amount of each RONS depending on the application. This can be demanding for computational models due to the strong spatial dependence of the system and the extensive reaction chemistry required to describe the plasma effluent mixing with open air. Moreover, spatially resolved density measurements of species in the plasma effluent pose a challenge for conventional diagnostics. While optical absorption techniques are excellent for measuring absolute number densities, the millimetre-scale geometries yield a short absorption path and are therefore hampered by a poor signal-to-noise ratio [142]. Multi-pass cells may be employed to increase the absorption path length through the gas mixture of the effluent, but the increased signal comes at the cost of any spatial resolution [201, 202]. To achieve both good sensitivity and spatial resolution, more complex experimental methods must be utilised. One such option is the use of cavity-enhanced spectroscopy techniques, which utilise an optical cavity, composed of two highly reflective mirrors, positioned around the sample. Coupling a laser beam into the cavity allows the beam to pass through the sample repeatedly to substantially increase its optical path length while maintaining high spatial resolution [203]. Cavity-enhanced spectroscopy techniques offer detection sensitivities with upper limits in the parts-per-trillion range at atmospheric pressure [204].

CRDS is an established technique for the analysis of atmospheric pressure plasma jets, starting with the measurement of OH in microwave plasma jets [205, 206]. Zaplotnik *et al* demonstrated its use for radio-frequency plasmas by characterising the density of the $He(2^3S_1)$ metastable along the radial and symmetry axes in the effluent of a pulsed-power pure helium APPJ [207]. Likewise, Benedikt *et al* presented radial and axial density distributions of the OH radical in the effluent of a humidified helium plasma generated with a COST-Jet-like plasma source [208]. Gianella *et al* employed optical feedback cavity-enhanced absorption spectroscopy to measure the HO_2 radical in the effluent of the kINPen-sci plasma jet supplied with a humidified argon feed gas [209] and later used their experimental measurements applying continuous wave CRDS (cw-CRDS) to develop and benchmark a HO_2 reaction kinetics model [210]. However, those measurements only yield line-of-sight integrated information. As a next step, Klose *et al* applied an Abel inversion to the obtained line-of-sight integrated densities, allowing the full spatial density distributions of HO_2 and H_2O_2 to be measured throughout the effluent of a kINPen-sci plasma jet supplied with a humidified argon feed gas [211, 212]. Other diagnostic techniques are also capable of probing the plasma effluent

with good sensitivity and spatial resolution. LIF was used by Verreycken *et al* to measure the density distribution of OH along the effluent of the kINPen09 in humidified argon [213], while Yatom *et al* employed the technique to obtain the time evolution of atomic hydrogen in the effluent of a nanosecond-pulsed, humidified argon APPJ [214]. Klose *et al* also measured the spatial distributions of atomic oxygen and hydrogen in the effluent of the kINPen-sci in humidified argon with picosecond-TALIF (ps-TALIF) [215]. Consequently, there is now a plethora of data available on the spatial distributions of different RONS and their precursors in humidified argon plasmas. Spatially resolved measurements of humidified helium plasmas have also been obtained. In addition to Benedikt *et al*'s aforementioned study of OH for a COST-Jet-like plasma source [208], Schröter *et al* applied ps-TALIF to the COST-Jet to investigate the influence of feed gas humidity on radical chemistry [216]. ps-TALIF was also employed by Myers *et al*, who presented the spatial density distribution of atomic oxygen in the effluent of the COST-Jet for pure helium, humidified helium, and $He+O_2$ gas mixtures [217]. The relative spatial distribution of OH in the effluent of the COST-Jet was obtained by Stapelmann *et al* using LIF, in an investigation mapping the transport of radicals from the effluent, through a liquid and to a model biological target [218]. Recently, van den Bekerom *et al* also used LIF to obtain the two-dimensional spatial distribution of OH and H_2O_2 mole fractions in a nanosecond-pulsed dielectric barrier discharge [219]. The absolute number density of H_2O_2 in humidified helium mixtures was measured by Willems *et al*, who used molecular beam mass spectrometry (MBMS) to obtain the H_2O_2 density distribution along the effluent of a COST-Jet-like plasma source [220].

Overall, though, full spatial distributions of species in the effluent of APPJs remain relatively scarce for $He+H_2O$ plasmas. The distribution of a species is also expected to vary between APPJ designs as a result of the different types of discharge due to, for example, different electrode arrangement and methods of power coupling. This therefore influences which APPJ design is best suited for a given application. For these reasons, this chapter investigates the absolute number density of H_2O_2 in the effluent of two widely-used APPJs, the COST-Jet and the kINPen-sci, operated with humidified helium as a feed gas.

5.2 Methods

5.2.1 Operating the COST-Jet and the kINPen-sci

A schematic of the setup used to operate the COST-Jet and the kINPen-sci is shown in figure 5.1. For the COST-Jet, a continuous voltage waveform with a frequency of 13.56 MHz and a peak-to-peak voltage of 850 V is applied to the powered electrode by a radio-frequency signal generator (RFG 150-13, Coaxial Power Systems). The other electrode is grounded. While the source is designed to match the electrode assembly laid out in the original COST-Jet schematic [15], it lacks an internal tuning capacitor and is instead impedance matched via an external L-network unit (MMN 150-13, Coaxial Power Systems). For the kINPen-sci, its purpose-built power supply is used to supply the electrode pin with a continuous voltage waveform with a peak-to-peak voltage of 3 kV at a frequency of 860 kHz.

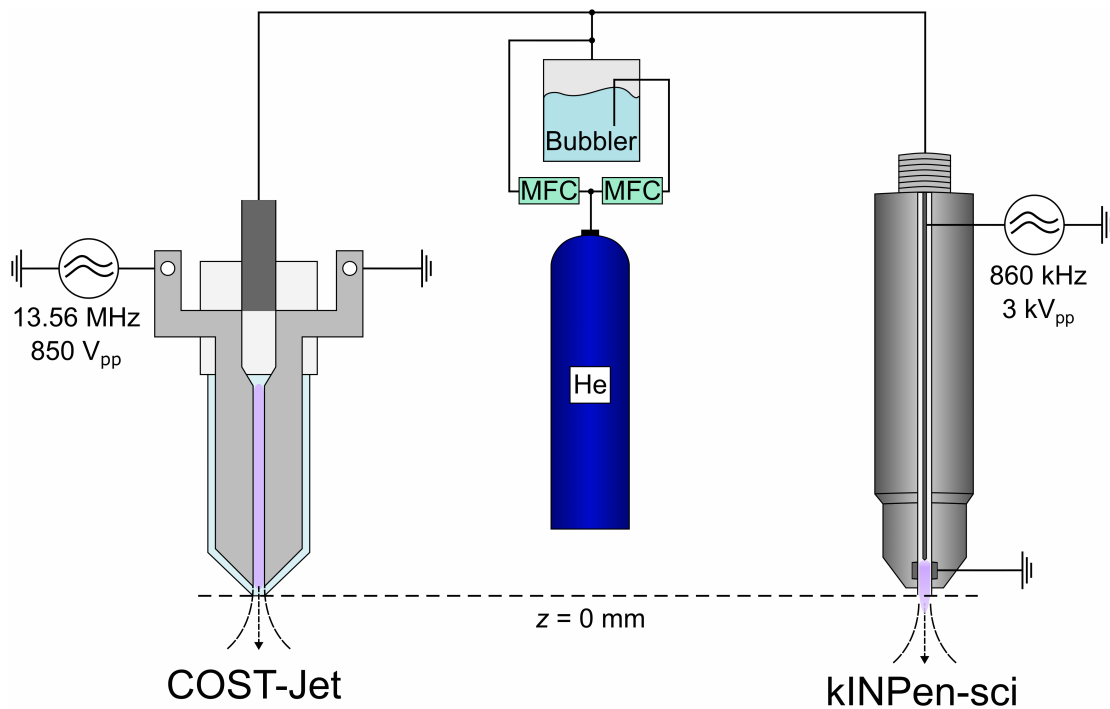


Figure 5.1: Schematic of the experimental setup used to supply the COST-Jet and the kINPen-sci with a $He+H_2O(0.33\%)$ gas mixture. MFC: Mass flow controller.

Mass flow controllers (MFCs) control the flow of helium to the plasma sources. Both APPJs are operated with humidified helium containing the same admixture of water vapour. The mixture is achieved by passing helium at a flow rate of 0.2 slm through a bubbler containing deionised water (volume: 500 ml, temperature: 296 K), which is then combined with dry

helium flowing at 0.8 slm. The APPJs are thus operated with a total feed gas flow of 1 slm humidified helium. The feed gas humidity is measured with a hygrometer (DewMaster, Edgetech) to contain (3300 ± 100) ppm H_2O by volume, or an admixture of 0.33%.

The symmetry axis of the plasma effluent is defined as the z -axis. For both APPJs, this position is normalised to the tip of the respective jet's nozzle, such that the effluent exits the source at $z = 0$. There is no visible photon emission in the effluent of the COST-Jet, while photon emission is seen to extend up to $z = 7.5$ mm for the kINPen-sci. The effluent is allowed to protrude freely into open air, rather than being directed at a surface.

5.2.2 Continuous wave cavity ring-down spectroscopy

Measurements of H_2O_2 are performed using cw-CRDS, using the experimental setup described by Klose *et al* [212]. A schematic of the cw-CRDS setup used to measure line-of-sight-integrated densities of H_2O_2 is shown in figure 5.2.

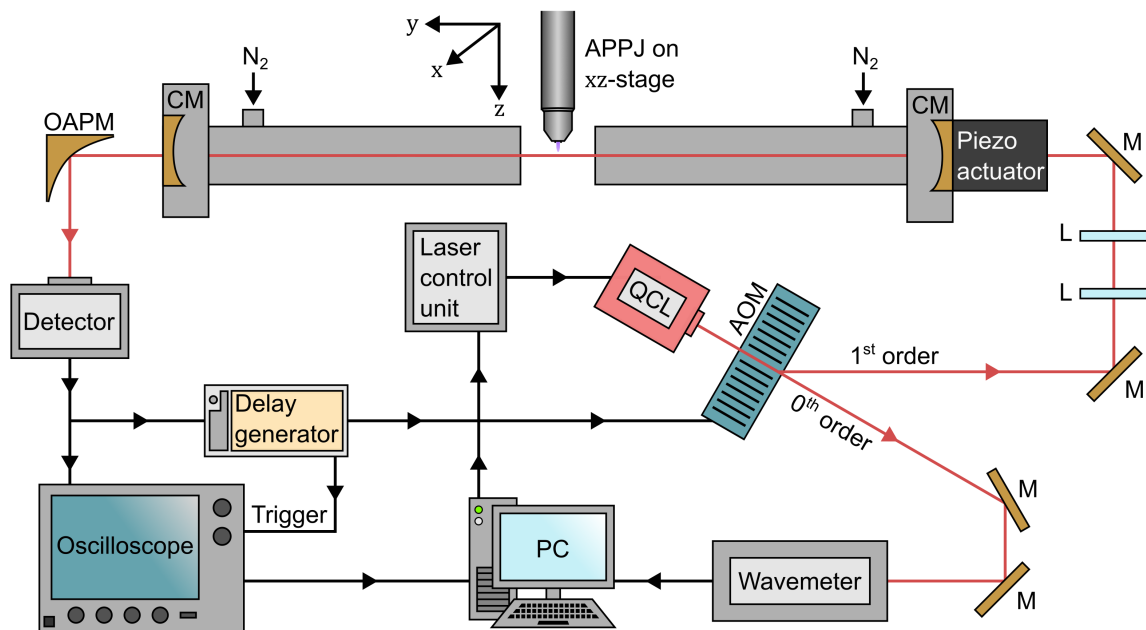


Figure 5.2: Schematic of the cw-CRDS setup used to study the density of H_2O_2 in the effluent of the COST-Jet and the kINPen-sci. QCL: quantum cascade laser, AOM: acousto-optic modulator, M: gold-coated mirror, L: mode matching lens, CM: cavity mirror, OAPM: off-axis parabolic mirror.

The optical cavity is composed of two highly reflective mirrors (Lohnstar Optics, reflectivity 99.98%, radius of curvature 100 cm), separated by a distance of 54.5 cm and mounted within

mirror holders on a rail. The first cavity mirror holder is connected to a piezoelectric ring actuator (RA12-24, Piezosystem Jena) and a function generator (AFG 3000 C, Tektronix), so that the cavity length is continuously modulated by 4 μm . The cavity is partially covered by two metal tubes and purged with nitrogen gas flowing at 1 slm to minimise the influence of airborne pollutants, such as particulate matter (e.g. dust) and other absorbing species, notably water. The metal tubes are each 20 cm long and 5 cm in diameter. The inner ends of the tubes are left open, forming an outlet for the purging gas. The large outlet surface area relative to the nitrogen flow rate ensures that the efflux of nitrogen does not disturb the plasma effluent.

An infrared quantum cascade laser (QCL) with a tuning range of 1224 – 1234 cm^{-1} (HHL-223, Alpes Lasers) is used, allowing optical transitions in the ν_6 band of H_2O_2 to be probed [221–223]. The laser control unit comprises a low-noise QCL driver (QCL1000, Wavelength Electronics) and temperature controller (PTC5K-CH, Wavelength Electronics). A multifunctional data acquisition card (USB-6341 X Series, National Instruments) controls the laser power and frequency by setting the values of the supplied current and temperature. The laser beam is split into two diffraction orders by guiding it through an acousto-optic modulator (AOM) (1208-G80-4, Isomet), with the zeroth diffraction order guided to a wavemeter (Laser Spectrum Analyser 771 B, Bristol Instruments) to monitor the laser frequency during operation. The AOM couples 85% of the laser power into the first diffraction order, which is in turn coupled into the optical cavity through a system of gold-coated mirrors and mode matching lenses, in order to match the beam shape of the laser to the cavity modes. An off-axis parabolic mirror focuses the laser beam exiting the cavity onto a fast detector (PVI-4TE-8-1x1, Vigo Systems, 790 MHz high cut-off frequency), with the signal recorded by an oscilloscope (Waverunner Xi-A, Teledyne LeCroy, band width: 400 MHz, sample rate: 5 GS/s) connected to a personal computer (PC). The intracavity power is allowed to increase until the detector signal reaches a pre-set threshold of typically 1 V. Once this occurs, a delay generator (DG535, Stanford Research Systems) temporarily cuts the radio-frequency supply of the AOM, which stops the first diffraction order of the beam from reaching the cavity and causes the intensity in the cavity to decay exponentially. From this, the ring-down time τ , defined as the time taken for the laser intensity inside the cavity to decay to $(1/e)$ of its initial intensity, is determined. A characteristic ring-down event for a given laser frequency is shown in figure 5.3. Varying the laser frequency, referred to in terms of the equivalent

wavenumber ν , allows a cavity loss spectrum $\frac{1}{c\tau(\nu)}$ to be measured. Each data point in a cavity loss spectrum is the mean of up to 600 individual ring-down events, with outliers filtered by discarding ring-down times more than three standard deviations different to the data average.

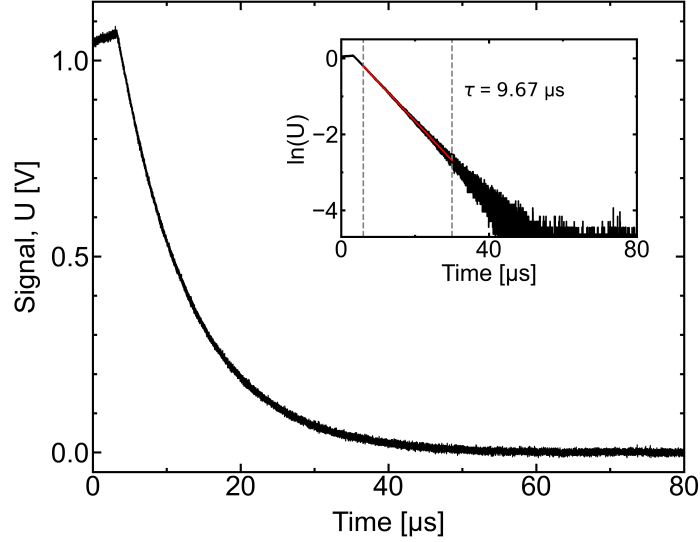


Figure 5.3: Characteristic single ring-down event measured in the effluent of a He+H₂O(0.33%) plasma. The ring-down time, τ is calculated from the linear gradient of the natural log of the detector signal between two fixed limits. Laser wavenumber: 1231.78 cm⁻¹. Laser power: 3.0 mW.

The symmetry axis of the plasma effluent is defined as the z -axis and the optical axis of the cavity is defined as the y -axis. The axis perpendicular to the z - and y -axes is defined as the x -axis. An APPJ is investigated by mounting it on two stepper motors (LNR502E/M, ThorLabs), such that the plasma effluent intersects the centre of the optical cavity. Two stepper motor controllers (BSC101, ThorLabs) move the APPJ in the (x,z) -plane to measure cavity loss spectra at different radial and axial positions in the effluent.

The best achievable spatial resolution of the optical cavity is estimated by the spot size of its lowest order transversal electromagnetic mode (TEM), typically referred to as the TEM₀₀. The beam waist of the TEM₀₀ in the centre of the cavity is given by

$$w_0 = \sqrt{\frac{L}{\pi\nu}} \left(\frac{1+g}{4(1-g)} \right)^{1/4}, \quad (5.1)$$

where L is the cavity length and $g = 1 - L/r$, the g -factor of the cavity mirrors with radius of curvature r . The beam waist w_0 is defined as the distance from the beam centre at which

its intensity is equal to I_0/e^2 , where I_0 is the beam's intensity at its centre. For a Gaussian intensity profile, the beam waist is equal to the Gaussian width, i.e. $w_0 = 2 \cdot \sigma$. More details on this topic can be found in [224]. Using equation 5.1, the best achievable spatial resolution in the centre of the optical cavity is 2.76 mm (a $2.576 \cdot \sigma$ interval, containing 99% of the total intensity). However, Klose *et al* determined the spatial resolution for the optical cavity used in this work to be 5.5 mm [212]. This indicates that a higher order TEM is used for the measurements. In order to prevent any interference between the APPJ nozzle and the cavity mode structure, no measurements are performed closer to the nozzle than $z = 3$ mm.

5.2.3 Data analysis procedure

The ring-down time of the laser light in the optical cavity depends on absorption by species along the optical path, in addition to loss mechanisms such as transmission through the cavity mirrors and scattering due to particulate matter (i.e. dust) or refractive index gradients [210]. Only effects due to optical absorption exhibit a strong dependence on the wavenumber of the laser. The cavity loss spectrum and absorption due to H₂O₂ can be related as follows:

$$\frac{1}{c\tau(\nu)} = \frac{A_{int}(\nu)}{L} + \frac{1}{c\tau_0(\nu)} \quad (5.2)$$

where c is the speed of light in a vacuum, $\tau(\nu)$ is the ring-down time measured at the wavenumber ν , $A_{int}(\nu)$ is the line-of-sight integrated absorbance of H₂O₂, L is the length of separation between the cavity mirrors, and $\tau_0(\nu)$ includes contributions to the ring-down time from the aforementioned cavity losses and the optical absorption of any other species present. Through the Beer-Lambert law (see equation 2.5), the line-of-sight integrated absorbance can be defined as the density of H₂O₂ integrated along the line of sight multiplied by the sum of all overlapping broadened absorption lines at a given wavenumber, i.e.

$$A_{int}(\nu, x, z) = \int \alpha(\nu, x, y, z) dy = n_{int}(x, z) \sum_t [S_t \cdot f(\nu, \nu_t)], \quad (5.3)$$

with

$$n_{int}(x, z) = \int n(x, y, z) dy \quad \left[\frac{\text{molec.}}{\text{cm}^2} \right]. \quad (5.4)$$

Here, $\alpha(\nu)$ is the spectral absorption coefficient and n_{int} is the line-of-sight integrated den-

sity of H₂O₂. S_t is the line strength of transition t centred at wavenumber ν_t at 296 K, as the effluent of the APPJs are almost at room temperature, with these two spectroscopic parameters provided by the HITRAN database [144, 221–223]. In this work, the measured transitions of H₂O₂ are expected to be in thermal equilibrium due to the high collision rates at atmospheric pressure. $f(\nu, \nu_t)$ is the line shape function of transition t at wavenumber ν . It is expected that Doppler broadening is negligible due to the relatively low temperatures typically observed in the effluents of both APPJs [225, 226]. Given this, and the high collisionality at atmospheric pressure, it is assumed that the line shape function is largely dictated by pressure broadening and can therefore be described by a Lorentzian function given by equation 2.6. The Lorentzian pressure broadening coefficient γ_L is discussed further in chapter 5.3.1. To determine the line-of-sight integrated density n_{int} from a cavity loss spectrum, the following model is applied:

$$\frac{1}{c\tau(\nu)} = \frac{n_{int}}{\pi L} \sum_t \left[S_t \cdot \frac{\gamma_L}{(\nu - \nu_t)^2 + \gamma_L^2} \right] + b_1\nu + b_0. \quad (5.5)$$

In this model, the assumption is made that the remaining contributions to the cavity losses besides the absorption of H₂O₂ can be approximated by a linear baseline, with baseline coefficients b_1 and b_0 . A detailed discussion regarding this approximation is given in [212]. Using this model, a least-squares fitting routine is employed to obtain the line-of-sight integrated H₂O₂ density and baseline coefficients. This routine utilises the SciPy package for Python [227]. Spectra are fitted using 391 transitions of H₂O₂ between 1229 cm⁻¹ and 1236 cm⁻¹, selecting transitions with a line strength higher than 10⁻²³ cm⁻¹/(molec. · cm⁻²). An example of a spectrum and applied fit are shown in figure 5.4. The fit is a close match to the data at the higher end of the wavenumbers measured. Towards lower wavenumbers the quality of the fit deteriorates. This is most likely due to the presence of a water absorption line centred at 1229.4 cm⁻¹ skewing the shape of the absorption feature. While the line strength of the water absorption line is a factor of 10³ lower than the more prominent H₂O₂ absorption lines, it is expected to significantly contribute to cavity loss due to the density of water contained in the effluent. Computational modelling of humidified helium APPJs revealed that only about 3.8% of the H₂O admixture was dissociated in the plasma channel under comparable conditions to this study [216]. Furthermore, if it is assumed that the primary consumption pathway of H₂O in the plasma is through dissociation into OH

and H, previous experimental measurements of OH taken shortly after the jet nozzle can be compared with the initial humidity concentration in the feed gas to yield approximate H_2O dissociation degrees of under 0.5% in the effluent [136, 208, 220]. These estimates pertain only to diffuse glow discharges due to the scarcity of OH measurements for relevant DBD-like APPJs in humidified helium. However, due to their broadly similar plasma chemistries it is likely that the concentration of water in the effluent is close to the initial admixture concentration for both discharge types investigated here. Accordingly, the absorption feature within the spectral range $1231.57 - 1232.00 \text{ cm}^{-1}$, highlighted by the grey box, is selected for the investigation of H_2O_2 due to a better agreement with the model fit.

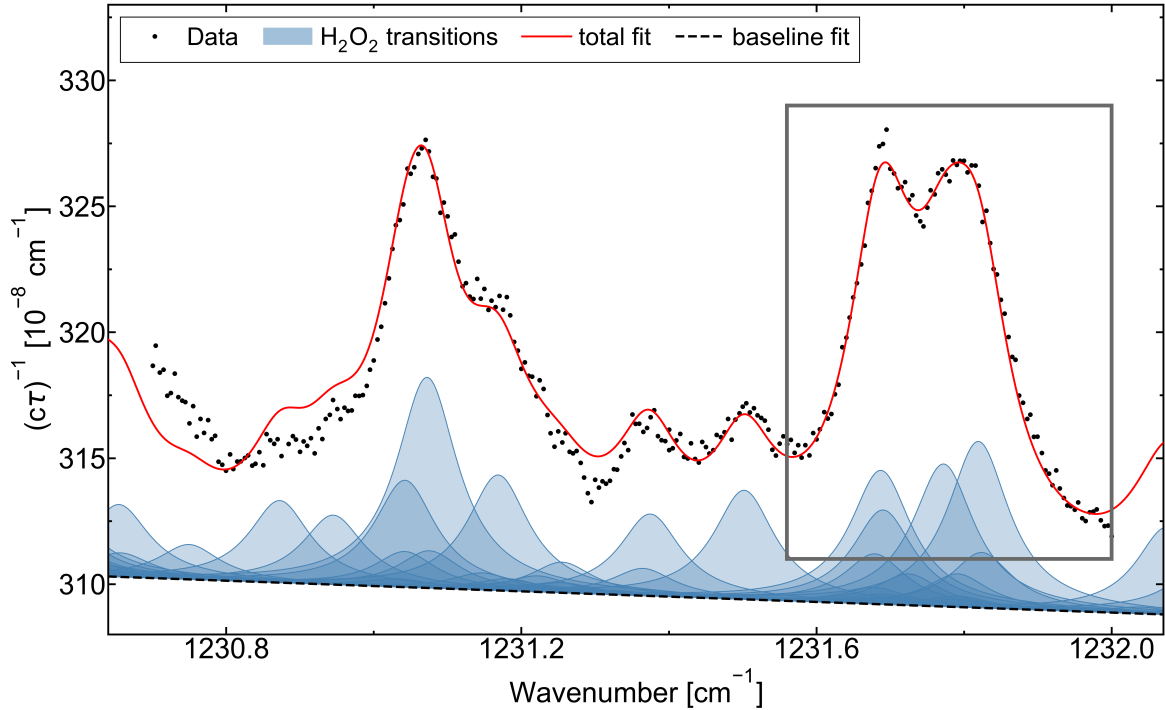


Figure 5.4: Model fit of a cavity loss spectrum measured by cw-CRDS in the effluent of the kINPen-sci, including a linear baseline fit and contributions from individual H_2O_2 transitions. The grey box encompasses the spectral region of best fit chosen for the investigation of H_2O_2 in this work.

5.3 Results

5.3.1 Determination of the pressure broadening coefficient

In order to determine the line-of-sight integrated densities from the measured cavity loss spectra using equation 5.5, the pressure broadening coefficient, γ_L , must first be known.

This parameter depends strongly on the temperature and gas composition of the effluent. Both of these parameters are expected to change with increasing distance from the nozzle, as the effluent gas mixes with the air and cools to the ambient temperature. The pressure broadening coefficient for H_2O_2 is only known for air and can therefore not be calculated independently. Using the established fitting model, treating the pressure broadening coefficient as an additional free-fit parameter allows it to be estimated, with only a selection of spectra with a good signal-to-noise ratio used to ensure reliable fitting. Figure 5.5 shows fitted spectra at different positions along the effluent for both APPJs. The selected spectra are taken at positions within the Gaussian full width at half maximum of a radial distribution of line-of-sight-integrated H_2O_2 densities for a given axial position (see chapter 5.3.2).

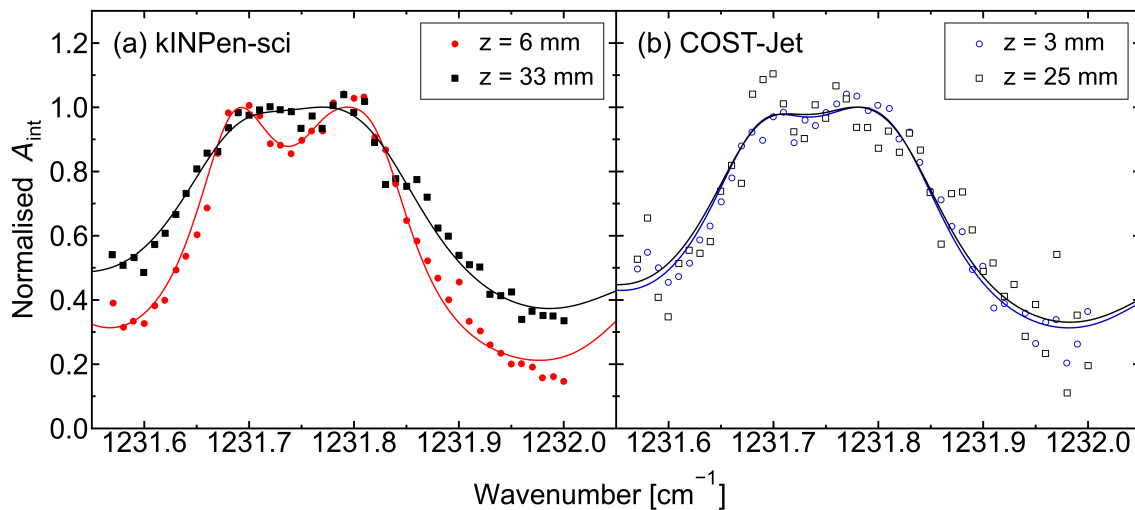


Figure 5.5: Relative change of the normalised line-integrated absorbance as a function of wavenumber. Fitted spectra are shown at different axial positions z for (a) the kINPen-sci and (b) the COST-Jet.

In the case of the kINPen-sci, the absorption feature is appreciably more broadened further away from the nozzle. In contrast, there is little difference in the shape of the two normalised COST-Jet spectra. It is evident that the pressure broadening coefficient differs between the two APPJs. The highest signal-to-noise ratio is observed along the centre of the effluent, as the highest density of H_2O_2 is found in this region. Given that the measured signal diminishes along the effluent radius, attempting to fit spectra taken at larger radii with several free-fit parameters introduces an appreciable margin of error. Accordingly, variations of the pressure broadening coefficient as a function of radial position are not considered in this work. The assumption is made that the pressure broadening coefficient does not vary

in the radial direction, allowing this parameter to be fixed radially and reducing the number of free-fit parameters in the model. The values of the pressure broadening coefficient along the effluent are obtained by taking the mean pressure broadening coefficient of a number of fitted spectra at each axial position, with all chosen spectra taken close to the effluent centre on the x -axis. The result of this is shown in figure 5.6, with lines indicating the trend added for ease of interpretation. For the kINPen-sci, the pressure broadening coefficient increases with increasing distance from the nozzle, rising from $0.051 \text{ cm}^{-1}\text{atm}^{-1}$ at $z = 6 \text{ mm}$ to $0.079 \text{ cm}^{-1}\text{atm}^{-1}$ at $z = 33 \text{ mm}$. Therefore, all spectra of the kINPen-sci are processed with the pressure broadening coefficient fixed to the mean at the corresponding axial position. In contrast, no change in axial direction is observed within the margin of error for the COST-Jet. Spectra recorded for the COST-Jet also have a lower signal amplitude than those for the kINPen-sci, increasing the relative error margin. As such, there is not enough evidence to treat the pressure broadening coefficient independently for each axial position, and it is fixed for the COST-Jet spectra as $0.07 \pm 0.01 \text{ cm}^{-1}\text{atm}^{-1}$. See chapter 5.4.3 for a discussion on the possible causes of the observed trends.

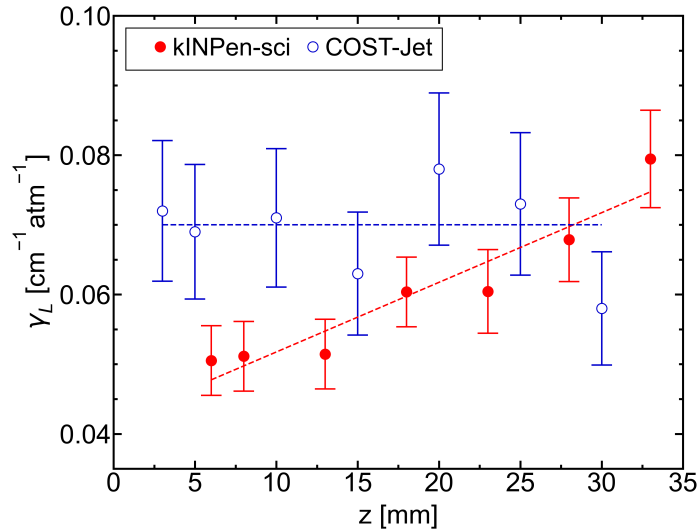


Figure 5.6: The obtained pressure broadening coefficient, γ_L as a function of the axial position. Lines indicating a trend are included for the kINPen-sci and for the COST-Jet.

5.3.2 Determination of spatially resolved densities

In figures 5.7 and 5.8, the line-of sight integrated density of H_2O_2 is shown as a function of the radial distance x to the effluent's centre measured at different axial positions z for the COST-Jet and the kINPen-sci, respectively. For any given axial position, the radial distribution of

line-of-sight integrated H₂O₂ densities can be represented by a Gaussian function

$$n_{int}(x) = n_0 w \sqrt{\frac{\pi}{2}} \cdot \exp \left[-2 \frac{x^2}{w^2} \right]. \quad (5.6)$$

Here, n_0 is the density amplitude of H₂O₂ at the radial centre of the effluent, w is the Gaussian width, and the x -coordinate is normalised to the centre of the Gaussian to account for any minor axial tilt of the mounted APPJ. Under the assumption that the effluent, and therefore the distribution of H₂O₂, is rotationally symmetric, an Abel inversion yields the following expression for the radial distribution of the absolute H₂O₂ number density

$$n(r) = n_0 \cdot \exp \left[-2 \frac{r^2}{w^2} \right], \quad (5.7)$$

where $r = \sqrt{x^2 + y^2}$ defines the radial distance from the centre of the effluent in polar coordinates. It follows that n_0 and w can be extracted from Gaussian fits of the line-of-sight integrated density and substituted into equation 5.7 to obtain a continuous distribution of the density of H₂O₂ on the (x,y) plane. These fits are shown in figure 5.7 for the COST-Jet as blue curves and in figure 5.8 for the kINPen-sci as red curves.

A detailed error analysis is performed to determine the error of each data point. This included the error of fitting the cavity loss spectra, the uncertainty of the pressure broadening coefficient and the uncertainty of the measurement method itself. Within the fitting procedure of the Gaussian functions, each data point is weighted based on their relative error. Consequently, data points with a lower relative error contribute more to the fit than data points with a higher relative error. Deviations from the Gaussian shape occur more prominently on the wings of the distribution. Some data points even have negative line-of-sight integrated densities as a result of fitting a cavity loss spectrum with a low signal-to-noise ratio. Those data points contribute very little to the fit and are intentionally not excluded from the data set, in order to transparently show the difficulties of measurements with this experimental setup. Moreover, an additional source of error in the determined H₂O₂ densities arises from the temperature uncertainty. Employing the HITRAN Application Programming Interface (HAPI) [228], it is determined that an increase in gas temperature from 293 K to 320 K results in a 4% increase in the sum of line strengths used to fit the measured H₂O₂ spectra. This demonstrates that small temperature changes have negligible effect on the H₂O₂ densities determined in this work.

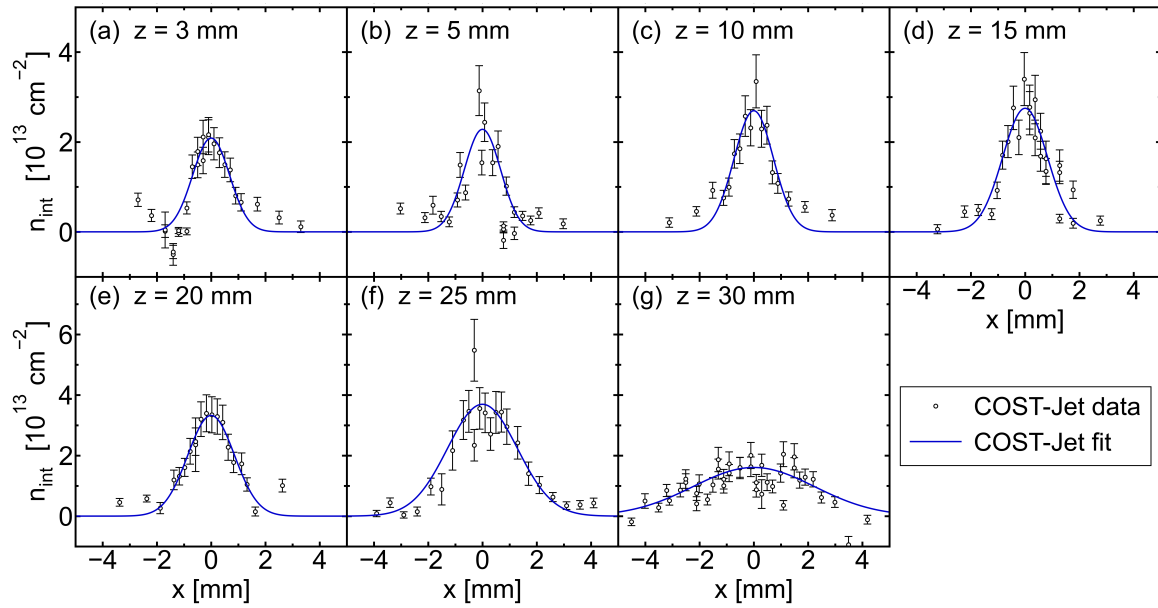


Figure 5.7: Measured radial distribution of the line-of-sight integrated H_2O_2 density at several positions along the effluent axis of the COST-Jet, together with applied Gaussian fits.

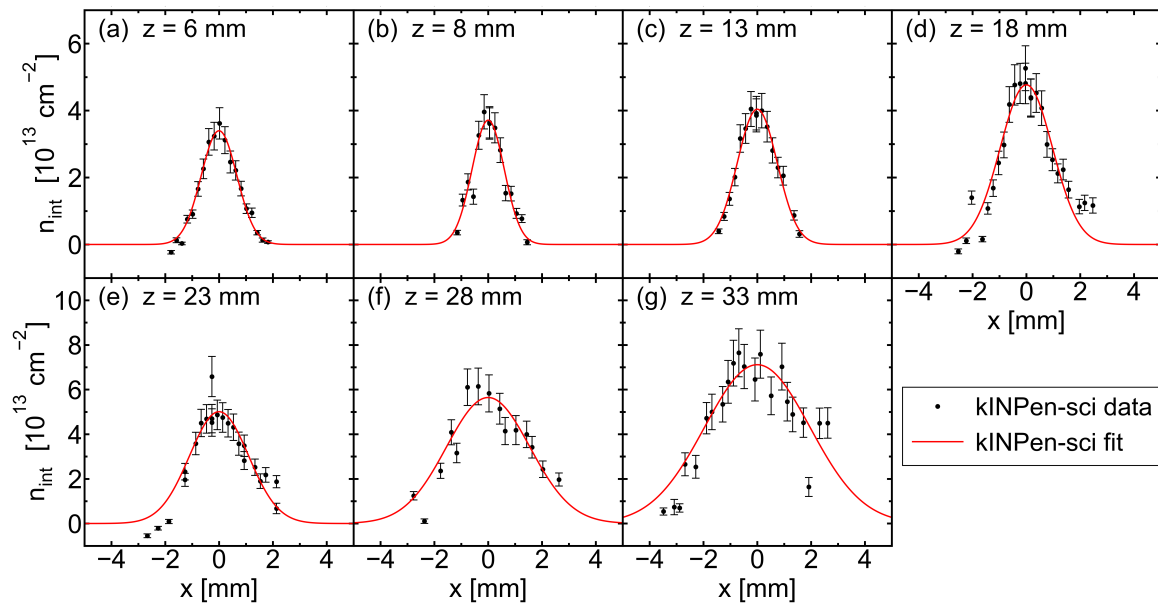


Figure 5.8: Measured radial distribution of the line-of-sight integrated H_2O_2 density at several axial positions along the effluent of the kINPen-sci, together with applied Gaussian fits.

Given that all radial profiles can be represented by a Gaussian function, determining n_0 and w for a range of axial positions allows these parameters to be fit with polynomial functions, thus characterising the behaviour of H_2O_2 along the effluent axis. Polynomials of the form

$$f(z) = a \cdot z^b + c \quad (5.8)$$

are used, where $f(z)$ is the density amplitude n_0 or the Gaussian width w as a function of axial position, b is the integer polynomial order, and a and c are fitted coefficients. In figures 5.9(a) and 5.9(b), the density amplitude and the Gaussian width are shown as a function of axial position, respectively.

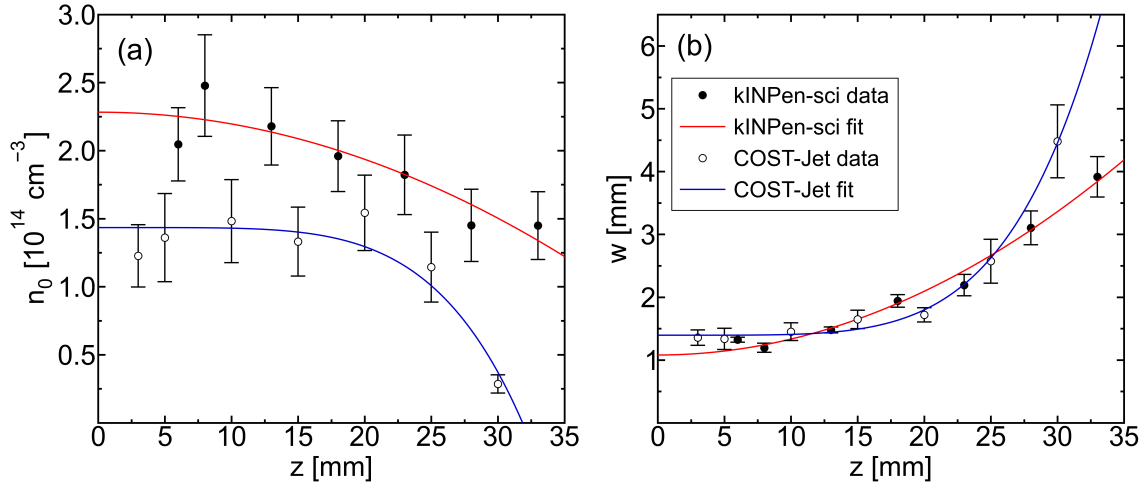


Figure 5.9: (a) The density amplitude n_0 as a function of axial position, and (b) the Gaussian width w as a function of axial position. $z = 0$ is the tip of the jet nozzle. Both parameters are best described by a fifth order polynomial for the COST-Jet, and by a second order polynomial for the kINPen-sci.

Both parameters are found to be described best by fifth order polynomials for the COST-Jet, while for the kINPen-sci they are best described by second order polynomials. Notably, there appears to be a slight initial increase in H₂O₂ density amplitude along the z -axis for both jets, based on the closest data points to the nozzle in figure 5.9(a).

Substituting the polynomial functions into equation 5.7 interpolates between the experimental data, yielding a continuous, spatially resolved density distribution of H₂O₂. In figure 5.10, cross-sections of the H₂O₂ distribution on the $y = 0$ plane for both APPJs are shown. The maximum H₂O₂ density in the effluent of the COST-Jet is $1.4 \times 10^{14} \text{ cm}^{-3}$, measured at $z = 3 \text{ mm}$ at the radial centre. At the same axial position, Willems *et al* measured a similar H₂O₂ density of around $1.2 \times 10^{14} \text{ cm}^{-3}$ for a COST-Jet supplied with a helium feed gas with roughly 2800 ppm H₂O [220]. The peak in figure 5.10(a) remains largely constant up to $z = 15 \text{ mm}$, with a decay of a factor of 3.5 in H₂O₂ density from $z = 15 \text{ mm}$ to $z = 30 \text{ mm}$.

The radial distribution of the H_2O_2 density is about 4 mm between $z = 3$ mm and $z = 15$ mm, widening past this to a maximum value of around 12 mm at $z = 30$ mm. The maximum density in the effluent of the kINPen-sci is $2.3 \times 10^{14} \text{ cm}^{-3}$, found at the closest measured position to the nozzle, $z = 6$ mm and $x = 0$ mm. The density through the centre of the effluent remains high over the range measured, dropping by a factor of 1.6 by $z = 33$ mm. The radial distribution of the H_2O_2 density is around 4 mm close to the nozzle, increasing to a width of about 10 mm by $z = 33$ mm.

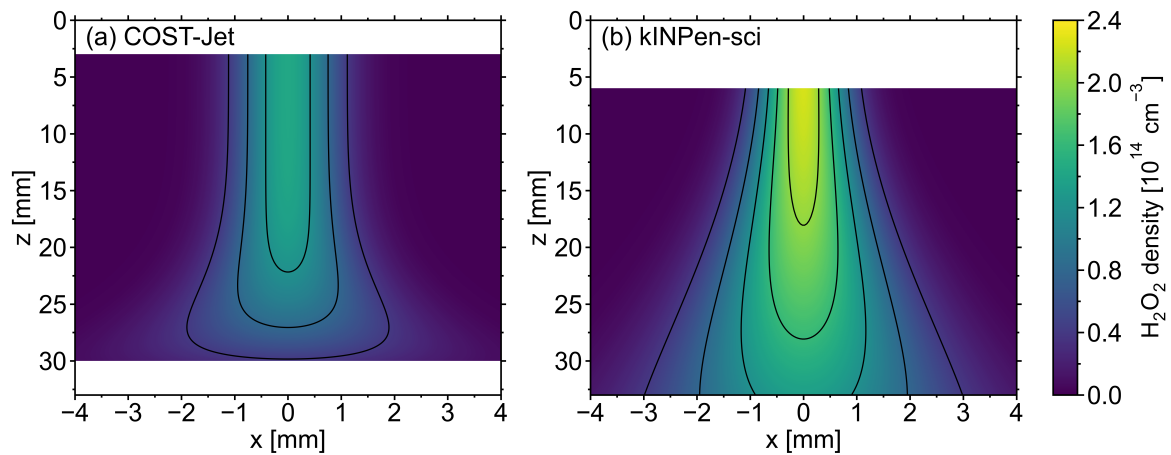


Figure 5.10: Density distribution of H_2O_2 in the effluent region of (a) the COST-Jet and (b) the kINPen-sci. $y = 0$ in both cases. The effluent protrudes freely into open air.

Estimates of the experimental uncertainty in the spatially resolved density of H_2O_2 can be obtained from the sources of error previously identified in the measurement of ring-down spectra. These uncertainties are percolated through the data analysis procedure by fitting for the upper and lower limits given by the uncertainty in calculated parameters, yielding a spatial distribution of the relative uncertainty in the H_2O_2 density at a given position. This is shown in figure 5.11. From this procedure, the upper limit for the uncertainty in the H_2O_2 density is determined to be $\pm 16\%$ for the COST-Jet and $\pm 12\%$ for the kINPen-sci, within the measurement area.

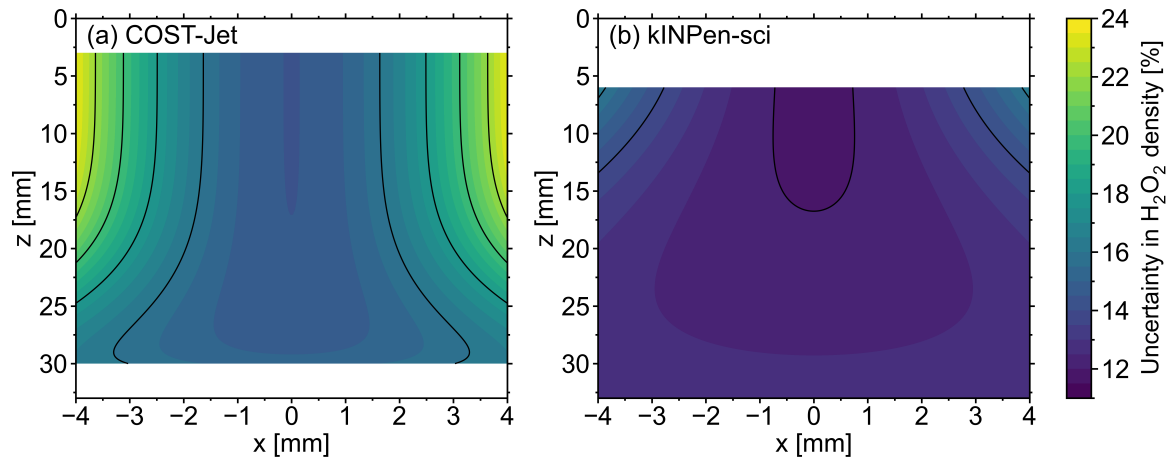


Figure 5.11: Relative uncertainty in the density of H_2O_2 in the effluent region of (a) the COST-Jet and (b) the kINPen-sci. $y = 0$ in both cases. The effluent protrudes freely into open air.

5.4 Discussion

5.4.1 Comparison of the distinct spatial distribution of H_2O_2

The spatial distribution of H_2O_2 in the effluent of the COST-Jet suggests minimal mixing of H_2O_2 with the ambient air up to $z = 15$ mm. At $z = 15 - 20$ mm, the H_2O_2 starts to diffuse into the surrounding air, with the density dropping sharply past this point. This is reflected in the fit of the COST-Jet's density amplitude and the associated Gaussian width, shown as a function of axial position in figures 5.9(a) and 5.9(b), respectively. Both parameters are largely constant for the first 15 mm from the nozzle, with the Gaussian width increasing sharply at further distances and the density amplitude at the centre of the effluent decreasing in turn. For the kINPen-sci, the H_2O_2 distribution starts expanding radially much closer to the jet nozzle. However, the mixing of H_2O_2 with the surrounding air is much more gradual further into the effluent, with around 60% of the maximum density still present in the effluent core at the limit of the range measured. H_2O_2 is measured up to 33 mm from the nozzle of the kINPen-sci without having reached the detection limit, while the detection limit is reached at $z = 30$ mm for the COST-Jet. The difference in the distinct spatial distribution of H_2O_2 in the effluent of both APPJs is evident in the different polynomial functions best describing their associated Gaussian width and their density amplitude as a function of the axial coordinate. For the kINPen-sci both parameters are best described by a steady second order polynomial, while for the COST-Jet a comparably steep fifth order polynomial fits best.

The distribution of H_2O_2 close to the nozzle of the kINPen-sci may be a result of its electrode arrangement. The electrode pin positioned in the centre of the capillary may obstruct the feed gas flow, creating a volatile flow pattern that causes the H_2O_2 to mix more readily with the ambient air 5 mm after the nozzle [226]. Contrary to this, the COST-Jet's plasma channel is 30 mm long and unobstructed [225]. This likely forces heavy species into a highly consistent flow pattern by the time they exit the nozzle, resulting in less initial mixing with the ambient air.

5.4.2 Influence of the discharge type on the chemical pathways of H_2O_2

On average, the H_2O_2 densities measured for the kINPen-sci are roughly a factor of 2 higher than those measured for the COST-Jet. It is known that the density of H_2O_2 generated by atmospheric pressure plasmas is correlated with the plasma dissipated power [190, 229]. Based on the COST-Jet specifications, the conditions used in this work are estimated to supply roughly 1 W of power to the plasma [15]. The kINPen-sci is also expected to supply approximately 1 W of power to the plasma [16]. However, for the COST-Jet the power is expected to be deposited over the full length of the electrodes, while for the kINPen-sci the electrode arrangement allows the power to be deposited in a more localised volume, which results in a higher energy density. It was not possible to experimentally match the power deposited into both plasmas beyond these estimates. As such, it is possible that a mismatch in coupled power may contribute to the different densities observed between the two APPJs. A study of this contribution remains for future investigations.

Furthermore, the discharge physics might also be different for the two APPJs [71]. The COST-Jet is a capacitively coupled non-thermal plasma source that produces, under the operational conditions of this study, a diffuse glow discharge distributed homogeneously between the two electrodes. It is assumed that the electric fields mostly confine the electrons to the plasma channel, as evidenced by photon emission not extending past the electrode housing. On the other hand, the kINPen-sci is a DBD-like, non-thermal plasma source, which shows filamentary behaviour when operated with argon as well as with helium [40]. The high electric fields of such filaments are expected to stimulate the production of higher densities of hot electrons than found in the diffuse plasma bulk of the COST-Jet, and in a more localised volume. These hot electrons can readily dissociate the water admixture



The hydroxyl radicals produced through this dissociation can form H₂O₂ in reaction R4.1, a three-body reaction between hydroxyl and the helium available in the feed gas, resulting in a higher formation of H₂O₂. It can be concluded that the higher H₂O₂ densities observed in the effluent of the kINPen-sci are a result of a greater fraction of water admixture being dissociated when compared to the COST-Jet, which consequently results in a different chemical composition of the effluent between the two APPJs.

The presented spatial distributions can also be used to infer where H₂O₂ formation occurs. For both APPJs their maximum H₂O₂ density is found in the effluent core at the closest axial position to the nozzle measured, with the density dropping with increasing distance from the nozzle. It can be concluded that most H₂O₂ formation occurs either within, or shortly after, the plasma channel. This observation is in agreement with the reaction chemistry presented in [202], in which it is expected that the bulk of H₂O₂ is produced in the active plasma region, via the chain of reactions R5.1 and R4.1. Beyond the active plasma region, free electrons rapidly recombine with heavy particles. Based on visible photon emission, in this work the electron density is estimated to diminish to background levels by $z = 7.5$ mm for the kINPen-sci and by the nozzle exit for the COST-Jet. Beyond these positions, the lack of electrons and short effective lifetime of OH results in an exponential decay in OH density. Previous studies reported a decrease in OH density by a factor of five in the first 5 – 10 mm after the active plasma region depending on the feed gas humidity [136, 208]. The net production of H₂O₂ in the far effluent via this pathway is therefore expected to be negligible. This is further reinforced by findings from Gorbanev *et al*, who treated an aqueous sample with a COST-Jet supplied with humidified helium [157]. Combining experiment and computational modelling, they determined that the H₂O₂ concentration in the treated liquid was largely unaffected by the ambient humidity in the effluent or the distance between the COST-Jet and the sample. From this, they concluded that the H₂O₂ measured in the liquid was predominantly formed within the plasma channel. Willems *et al* made a similar observation, measuring a H₂O₂ density distribution along the effluent of a COST-Jet analogue that peaked at around $z = 2$ mm and gradually decreased with axial position [220]. They compared this to a computational model in the same study and suggested that the trend is due to the radial diffusion losses of H₂O₂ outstripping the availability of OH with distance from the nozzle.

5.4.3 Comparison of the pressure broadening coefficient

The pressure broadening coefficient as a function of the axial position, as shown in figure 5.6, is markedly different between the COST-Jet and the kINPen-sci. For the first 28 mm of the effluent, the pressure broadening coefficient for the COST-Jet is consistently higher than those determined for the kINPen-sci. As the kINPen-sci is, due to its DBD-like discharge type, more efficient in dissociating H_2O , the higher amount of water present in the effluent of the COST-Jet may lead to higher pressure broadening of the absorption lines of H_2O_2 .

The increase in the broadening coefficient along the effluent of the kINPen-sci is likely due to mixing with the ambient air. Helium has a lower relative mass than nitrogen and oxygen, and should exert a lower degree of pressure broadening as a result. If the effluent of the kINPen-sci is initially relatively pure and is progressively diluted by mixing with ambient air along its axis, the change in gas composition may lead the pressure broadening coefficient to increase with increasing distance from the nozzle. In addition, a larger pressure broadening coefficient is found for the kINPen-sci operated with humidified argon as a feed gas, suggesting an effect of the atomic or molecular mass of the feed gas of choice [212]. Moreover, possible temperature gradients, stemming from equalisation of the gas temperature in the effluent to room temperature, may also contribute to the trend in the pressure broadening coefficient observed for the kINPen-sci. It remains for future investigations to elucidate why the same linear increase would not then be observed along the effluent axis of the COST-Jet, and whether this is due to the differences in the chemical composition of the effluent or simply the result of an overall lower absorption signal due to the on average lower densities of H_2O_2 .

5.4.4 Comparison of argon and helium as a feed gas for the kINPen-sci

First insights into the impact of the chosen primary feed gas on the H_2O_2 density distribution can be obtained by comparing the spatial distribution of H_2O_2 in the effluent of the kINPen-sci in figure 5.10(b) with the spatial distribution of H_2O_2 in the effluent of the same jet supplied with humidified argon as a feed gas, reported by Klose *et al* [212]. The argon mixture is introduced at a flow rate of 3 slm compared to 1 slm in the helium case. This accounts for helium having a higher thermal conductivity than argon, as lower flow rates (and therefore increased residence times) may be more ideal for sustaining the plasma chemistry of helium mixtures [230]. The radial distribution of the H_2O_2 density in the first 10 mm of the effluent is larger for the reported argon case than for the present helium case. At $z = 10$ mm, the

H₂O₂ is distributed across a diameter of 4 mm in helium, whereas in argon it is present in appreciable densities across a diameter of roughly 6 mm. This is likely due to the difference in carrier gas density. Argon is ten times heavier than helium and should therefore undergo more vigorous mixing with the surrounding air due to its higher momentum, especially when coupled with the higher flow rate used in the argon case.

The feed gas humidity reported in the argon case is 1600 ppm, while (3300 ± 100) ppm is used in the present helium study. It has been shown that the production of H₂O₂ scales strongly with increasing humidity for low feed gas concentrations, before gradually saturating above 4000 ppm H₂O [157, 190, 220]. Given this scaling, an appreciably lower H₂O₂ density may be expected for the argon case due to the 50% lower H₂O concentration. However, the magnitude of absolute H₂O₂ densities is notably similar between the carrier gases. The maximum density of H₂O₂ is $2.3 \times 10^{14} \text{ cm}^{-3}$ for the helium-dominated feed gas, while a maximum density of approximately $2.0 \times 10^{14} \text{ cm}^{-3}$ is reported for the argon-dominated mixture [212]. As these values cannot be distinguished within the bounds of experimental uncertainty, this indicates that the choice of carrier gas plays an important role in determining the production of H₂O₂ by APPJs. Numerous studies comparing the discharge properties of argon and helium plasmas at atmospheric pressure have shown that argon plasmas typically possess higher electron densities than helium plasmas, while helium plasmas are sustained with a higher electron temperature than in argon [78, 231–233]. This has been attributed to helium having a higher first ionisation energy and first excitation energy than argon [78]. As discussed in chapter 5.4.2, the electron impact dissociation of H₂O into OH and H is expected to scale with electron density, in turn determining the production of H₂O₂ through OH recombination in reaction R4.1. This is supported by measurements from Du *et al* in a comparative study of OH densities in helium and argon plasmas [191]. The density of OH was found to be roughly three times higher in argon than in helium for a feed gas humidity comparable to the present work. Hence, it can be posited that the greater electron density of argon plasmas is partly responsible for the near equal peak H₂O₂ densities measured in the effluent of the kINPen-sci when operated with humidified argon or humidified helium, despite the H₂O concentration being 50% lower in the argon case [212].

5.5 Chapter summary

APPJs are efficient sources of H₂O₂, a RONS key to the application of plasmas in biomedicine. Different RONS vary in how they are distributed throughout the plasma effluent, with these distributions affected by a species' mass, available reaction pathways, and also the discharge type of the APPJ. As such, the mixture and dosage of species received by a substrate is strongly dependent on its position relative to the plasma source. Here, the spatial distribution of H₂O₂ is obtained for the effluent region of a COST-Jet and a kINPen-sci supplied with a He+H₂O feed gas. The measurements are performed using CRDS, with a feature in the ν_6 absorption band of H₂O₂ probed within the spectral range of 1231.57 – 1232.00 cm⁻¹ to obtain its line-of-sight integrated density at different positions in the effluent. Absolute number densities of H₂O₂ are obtained by performing an Abel inversion on the radial distribution of line-of-sight integrated densities. Polynomial fits for the density amplitude as well as for the Gaussian width are used to obtain a continuous, spatially resolved distribution of H₂O₂ for both APPJs.

The H₂O₂ distribution close to the COST-Jet nozzle appears to undergo minimal mixing with the ambient air when compared with the density distribution of H₂O₂ for the kINPen-sci, although this mixing occurs very rapidly at more than 15 mm into the effluent of the COST-Jet. For the kINPen-sci, the H₂O₂ has a wider radial distribution close to the nozzle, but the distribution widens more gradually further into the effluent than in case of the COST-Jet. These observations may stem from the electrode arrangement affecting the flow properties of the effluent. It is also noted that the majority of H₂O₂ production occurs within, or up to a few millimetres after, the plasma channel. The maximum H₂O₂ densities determined in the effluent of the COST-Jet and kINPen-sci are 1.4×10^{14} cm⁻³ and 2.3×10^{14} cm⁻³, respectively. The average density of H₂O₂ in the effluent of the kINPen-sci is roughly twice as large as determined for the COST-Jet. There is evidence that the higher H₂O₂ densities observed in the effluent of the kINPen-sci are a result of a greater fraction of water being dissociated when compared to the COST-Jet, although a mismatch in deposited power cannot be excluded. Near-equivalent densities of H₂O₂ are observed for the kINPen-sci and a similar work that utilises argon as a feed gas instead of helium, despite a factor of 2 difference in humidity concentration. These results highlight the differences in the distinct spatial distribution of H₂O₂ in the effluent of the COST-Jet and the kINPen-sci when considering their direct application in biomedicine.

Chapter 6

O₃ production by an He+O₂ radio-frequency plasma jet driven by tailored voltage waveforms

*The following investigation has been submitted to
Plasma Sources Science and Technology.*

6.1 Motivation

The production of RONS by an APPJ is strongly dependent on the EEDF of the plasma. The EEDF dictates the rates of dissociation, excitation, and ionisation reactions between electrons and heavy particles, thus governing the resulting plasma chemistry. As evidenced by the previous chapter, the COST-Jet is usually driven by a single-frequency, sinusoidal voltage waveform. As described in chapter 2.3.2, such RF glow discharges are stable when operated at low voltages in the Ω -mode, or at slightly higher voltages in the Penning-mode. In the Ω -mode and the Penning-mode, electron power absorption is symmetrical in both space and time within the RF period and the plasma is spatially uniform. This limits the extent to which the EEDF can be altered when applying a sinusoidal voltage. By customising the driving voltage waveform to make the power absorption asymmetric within the RF cycle, there is a pathway towards modifying the EEDF.

Controlling the EEDF via the driving voltage waveform is certainly an attractive concept. It would allow the plasma chemistry to be tailored conveniently, without the need for physical

adjustments to the plasma source. Much like the nanosecond-pulsed plasma source investigated in chapter 4, the frequency of the driving voltage may be used as a control parameter for RF glow discharges. Increasing the driving frequency of an RF plasma source effectively increases the power deposition per unit time, increasing the electron density and inducing a more reactive plasma chemistry [234,235]. However, the electron temperature, and hence the EEDF, is not strongly affected by the driving frequency or the power deposition [236]. This has prompted research into alternative RF voltage waveforms as a means of directly altering the EEDF. One prospect is dual-frequency operation, where a plasma is driven with a voltage waveform containing one low-frequency and one high-frequency component [237–239]. Driving APPJs with dual-frequency voltage waveforms was shown to allow independent control of the electron density and the electron temperature, thereby influencing the EEDF [240]. Further development of this method arose from the use of tailored voltage waveforms (TVWs), a technique originally applied to low pressure plasma sources [241–243]. TVWs are generated as a finite Fourier series of N consecutive harmonics of a fundamental frequency, f_0 . Common types of TVW include the ‘peaks’ waveform, with its inverse known as the ‘valleys’ waveform [244]. Similarly, there is the ‘sawtooth-up’ waveform and its inverse counterpart, the ‘sawtooth-down’ waveform [244].

At atmospheric pressure, Gibson *et al* found that TVWs break the spatio-temporal symmetry of electron power absorption and allow the EEDF of an APPJ to be tailored directly [245]. By comparing PROES measurements with the results of a PIC-MCC model, they showed that sawtooth waveforms induce temporally asymmetric electron heating, with maxima found at only one time within the RF cycle. Meanwhile, peaks and valleys waveforms induce electron heating that is asymmetric in both time and space, with maxima restricted to one electrode and at one time within the RF cycle. Hence, the EEDF is strongly influenced by the electron heating confinement induced by both types of waveform [245]. Following this, Korolov *et al* found that the spatio-temporally asymmetric electron heating of the peaks waveform stems from a short sheath collapse occurring only at the powered electrode [246]. The flux of ions to the powered electrode is compensated by the formation of a strong electric field. This causes electrons to be strongly accelerated close to the powered electrode, resulting in highly localised power absorption. Using a valleys waveform reverses the geometry of this process, instead localising power absorption to the region near the grounded electrode [247]. Confining the electron heating to small regions of space and time in this way enhances the high energy

tail of the EEDF, allowing reactive species to be generated with increased efficiency and at higher densities when compared with single-frequency operation [248]. Another important aspect of TVW operation is that increasing the number of applied harmonics in the driving voltage waveform enhances the asymmetry of power absorption. Korolov *et al* demonstrated that increasing the number of harmonics can be used to optimise the densities of reactive species, including metastable helium, atomic nitrogen, and atomic oxygen [247, 249].

Overall, the effects of TVW operation on the electron dynamics and the production of radicals and metastables in the plasma channel of APPJs now appear well-understood. However, the extent to which TVWs influence long-lived RONS in the effluent, such as ozone, has not yet been explored in detail. Nor has the impact of TVWs on the gas temperature of an APPJ been investigated. These two aspects are crucial when considering the safe and effective application of TVW-driven APPJs in medicine or industry. With this in mind, this chapter investigates the influence of TVWs on the density of ozone in the far effluent of an APPJ.

6.2 Methods

6.2.1 Tailored voltage waveforms

TVWs are generated as a sum of N consecutive harmonics with fundamental frequency $f_0 = 13.56$ MHz. ‘Peaks’- and ‘valleys’-type waveforms are generated according to [250]

$$\phi(t) = \sum_{k=1}^N \phi_k \cos(2\pi k f_0 t + \theta_k), \quad (6.1)$$

where $\phi(t)$ is the voltage amplitude at time t . ϕ_k and θ_k are the amplitude and phase angle of individual harmonic k , respectively. ϕ_k is set according to

$$\phi_k = \phi_{pp} \frac{2(N - k + 1)}{(N + 1)^2}, \quad (6.2)$$

in which ϕ_{pp} is the peak-to-peak voltage of the waveform. Setting all phase angles to zero produces a peaks waveform, while changing the phase angles of all even harmonics to $\theta_k = \pi$ yields a valleys waveform. Example peaks waveforms are shown in figure 6.1(a). ‘Sawtooth’-type waveforms are generated with a separate function [251]:

$$\phi(t) = \phi_0 \sum_{k=1}^N \frac{N-k+1}{N} \cos(2\pi k f_0 t + \theta_k), \quad (6.3)$$

where the voltage amplitude prefactor ϕ_0 is set to give the desired peak-to-peak voltage. Setting all the phase angles to $\theta_k = \pi/2$ produces a sawtooth-up waveform, while a sawtooth-down waveform is attained by changing all the phase angles to $\theta_k = 3\pi/2$. Example sawtooth-up waveforms are shown in figure 6.1(b).

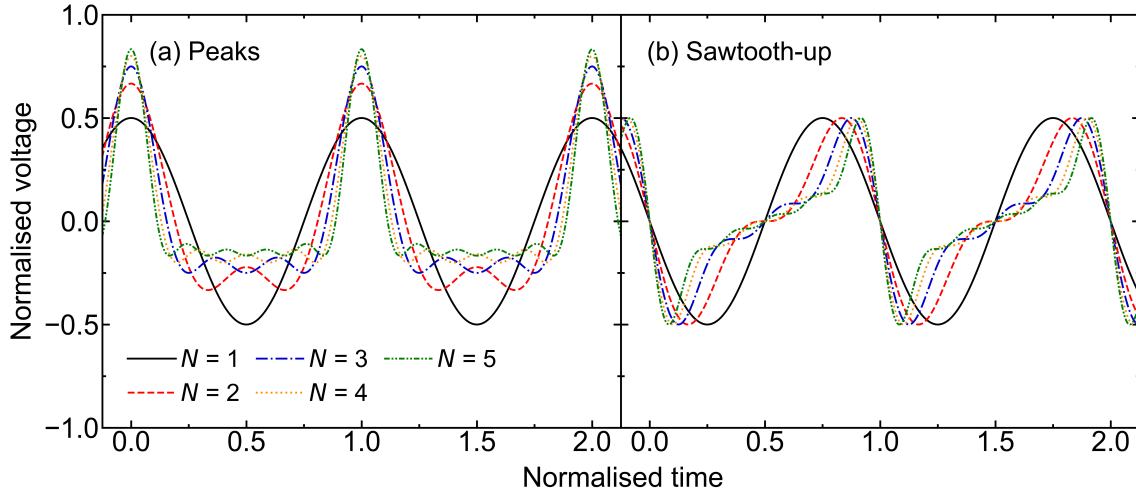


Figure 6.1: Representative (a) peaks and (b) sawtooth-up voltage waveforms for $N = 1$ to $N = 5$ consecutive harmonics, generated according to equations 6.1 and 6.3, respectively. The voltage axis is normalised to ϕ_{pp} . The time axis is normalised to the RF period, $1/f_0$.

6.2.2 Description of the experimental setup

The plasma source used in this work is the S-APPJ, as described in chapter 3.2. Figure 6.2 shows the full experimental setup, including diagnostics and the equipment used to drive the S-APPJ with TVWs. Mass flow controllers (MFCs) supply the S-APPJ with 5 SLM of helium and small admixtures of O₂ in the range of 0.1% to 1.0%. The O₂ admixture concentration is chosen to maximise the range of applied voltage harmonics that can be investigated under equivalent conditions. The RF power, current, and applied voltage waveforms are measured with a Vigilant Power Monitor (VPM-13.56-1000-1F-1M, SOLAYL SAS, rating: 1 kW), abbreviated to VPM [252]. The plasma power, P_{RF} , is defined as the RF power deposited into the plasma. For a given voltage waveform, P_{RF} is determined by taking the difference between the total measured RF power with and without plasma at a constant current, to account for all parasitic power losses in the system [253].

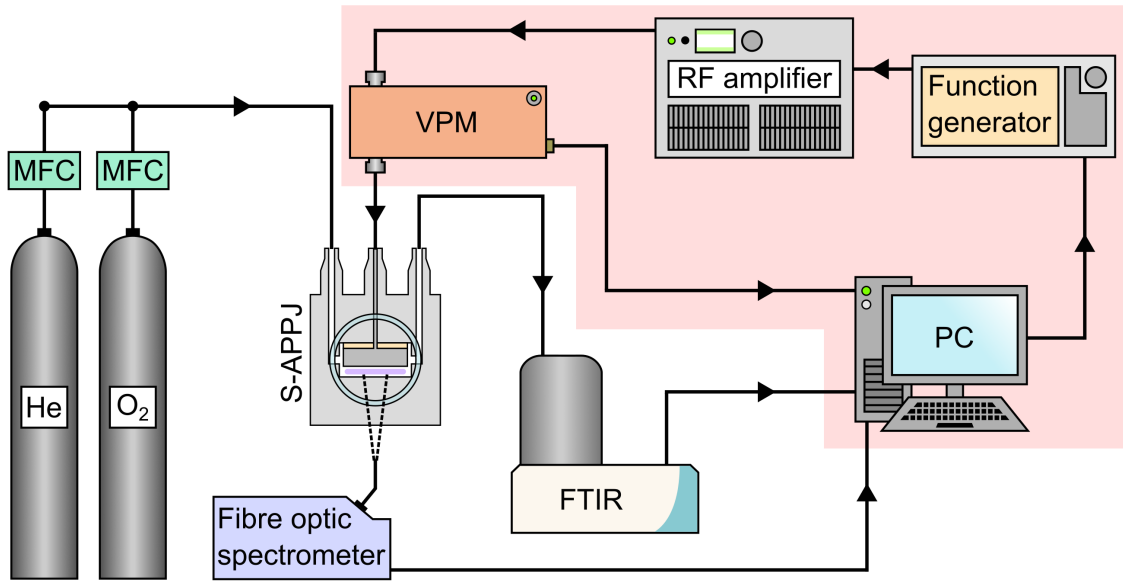


Figure 6.2: Schematic of the experimental setup used to measure the ozone density and gas temperature of an APPJ driven by tailored voltage waveforms. The shaded region shows the iterative feedback loop used to achieve a desired voltage waveform shape. For single frequency measurements this loop is replaced with an RF power generator and an impedance matching network. VPM: Vigilant Power Monitor. MFC: Mass flow controller

For single-frequency operation (i.e. $N = 1$), power is supplied by a 13.56 MHz RF power generator (RFG 150-13, Coaxial Power Systems) through an L-type impedance matching network unit (MMN 150-13, Coaxial Power Systems), with the VPM connected in series directly before the APPJ. For operation with TVWs (i.e. $N > 1$), an iterative feedback loop is implemented to achieve the desired waveform shapes. This system was described by Doyle *et al* [254], and a summary is provided here. An initial seed waveform is set with an arbitrary function generator (33621A, Keysight) and amplified with a broadband power amplifier (GN500D, PRANA R&D, rating: 500 W), before being applied to the APPJ. The peak-to-peak voltage of the seed waveform is limited to $\phi_{pp}^{seed} \leq 2$ V. The VPM is connected directly before the APPJ. The system is not impedance matched. Reflected power is instead dissipated within the amplifier, which is able to withstand 100% reflected power. Solutions have been developed to impedance match multi-frequency TVWs for industrial applications, but are not strictly necessary for the fundamental investigations in this work [255–257]. Separate USB cables connect the function generator and the VPM to a PC, thus completing the feedback loop. The type of TVW, the peak-to-peak voltage and the number of applied harmonics are set on the PC with a companion software suite to the VPM (Vigilant RF lab,

SOLAYL SAS). The software then reads the applied waveform from the VPM and modifies the harmonics, phases and amplitudes of the seed waveform in the arbitrary function generator. This process is iterated until the target waveform is achieved, and then stopped for taking measurements. The amplitude and shape of the applied voltage waveforms were previously found to be within 5% of the targeted waveforms [254]. Figure 6.3 shows representative examples of experimentally measured peaks and sawtooth-up voltage waveforms for $N = 3$ applied harmonics. To illustrate the degree of agreement, figure 6.3 also shows theoretical waveforms generated with equations 6.1 and 6.3, with the same peak-to-peak voltage as their measured equivalent.

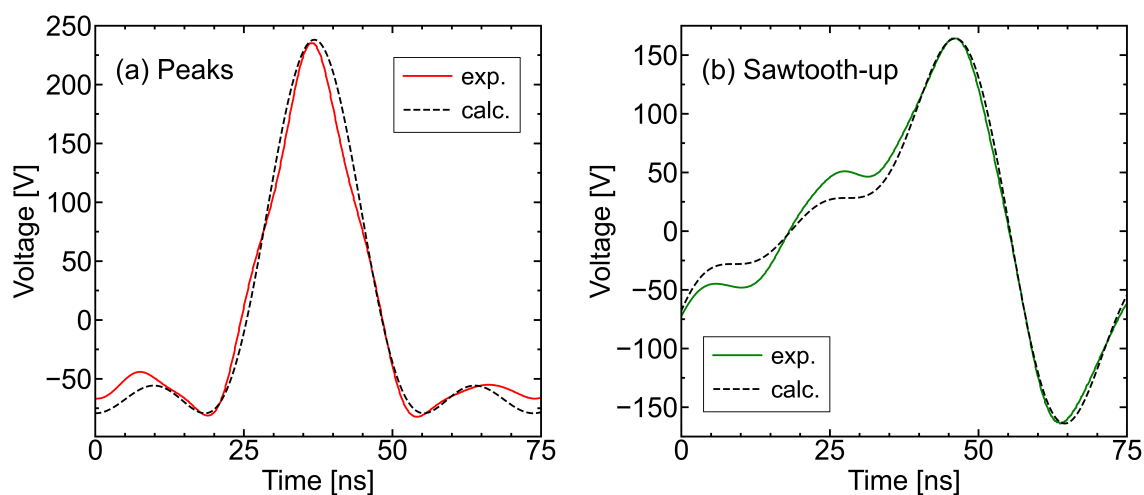


Figure 6.3: Comparison between measured applied voltage waveform and targeted waveform: (a) peaks and (b) sawtooth-up, for $N = 3$ harmonics according to equations 6.1 and 6.3. The feed gas is He+O₂(0.1%).

6.2.3 Ozone density from Fourier transform infrared spectroscopy

The space- and time-averaged ozone density in the far effluent of the S-APPJ is measured by Fourier transform infrared (FTIR) spectroscopy. FTIR is an optical absorption technique that uses broadband infrared light to measure the densities of infrared-active molecules. To be infrared-active, an absorbing species must be able to undergo vibrational excitation. Only heteronuclear diatomic molecules or molecules with three or more atoms are infrared-active, as vibrational excitation requires a change in the dipole moment of a species [258]. This is also applicable to the tunable infrared laser used to measure hydrogen peroxide densities by cw-CRDS in chapter 5.

The key components of an FTIR system are a broadband infrared light source, a Michelson

interferometer, and a detector. A diagram of a typical Michelson interferometer is shown in figure 6.4. A Michelson interferometer uses a beam splitter to separate incident radiation into two perpendicular beams; one beam is reflected by a movable mirror, and the other is reflected by a fixed mirror. The reflected beams then intersect, interfering with respect to the displacement of the movable mirror. Thus, moving the mirror along its axis modulates the phase angle of the beams to generate an interference pattern in the shape of a cosine wave. This signal, varying in the time domain as a function of the mirror position, is called an interferogram. After passing through the sample, the constituent frequencies of the interferogram are deconvolved via Fourier transform to produce a time- and position-averaged absorption spectrum that varies in the frequency domain [258].

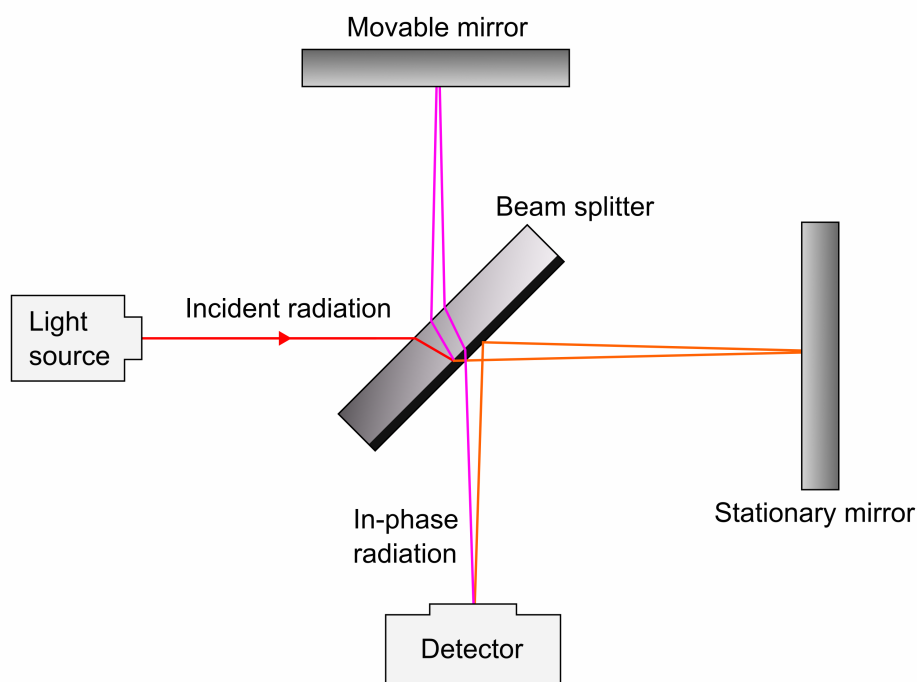


Figure 6.4: Schematic of a Michelson interferometer used in FTIR spectroscopy. Incident radiation is separated into two perpendicular beams that are reflected by mirrors. Moving one mirror along its axis produces a time-varying interferogram when the two reflected beams are recombined.

To measure the ozone density with FTIR, the effluent gas mixture is piped through a 2 m long tube (perfluoroalkoxy material) into an optical multi-pass absorption gas cell (volume 2 L, absorption length 10 m) of a commercial Fourier transform spectrometer (Nicolet iS50, Thermo Fisher Scientific). The gas lines and the internal FTIR unit are flushed with compressed air when not in use to prevent ambient humidity from settling and causing damage to

the optical components. At the start of a measurement session, the gas lines are flushed with He+O₂ mixture to remove the accumulated gas. The setup is also flushed with He+O₂ between scans to remove reactive species from the previous scan. The chosen spectral resolution is 4.0 cm⁻¹.

A typical FTIR spectrum, from an average of 128 individual scans and after background subtraction, is shown in figure 6.5. As shown in the figure, the electronic ground state of the ozone molecule exhibits an asymmetric top geometrical configuration with three fundamental modes: symmetric bending at $\nu_2 = 701$ cm⁻¹, asymmetric stretching at $\nu_3 = 1042$ cm⁻¹, and symmetric stretching at $\nu_1 = 1103$ cm⁻¹ [259, 260]. The corresponding ro-vibrational bands appear in the measured absorbance spectrum, as well as the overtone and combination bands, e.g. $2\nu_3$ at 2084 cm⁻¹ and $\nu_1 + \nu_3$ at 2110 cm⁻¹ [259].

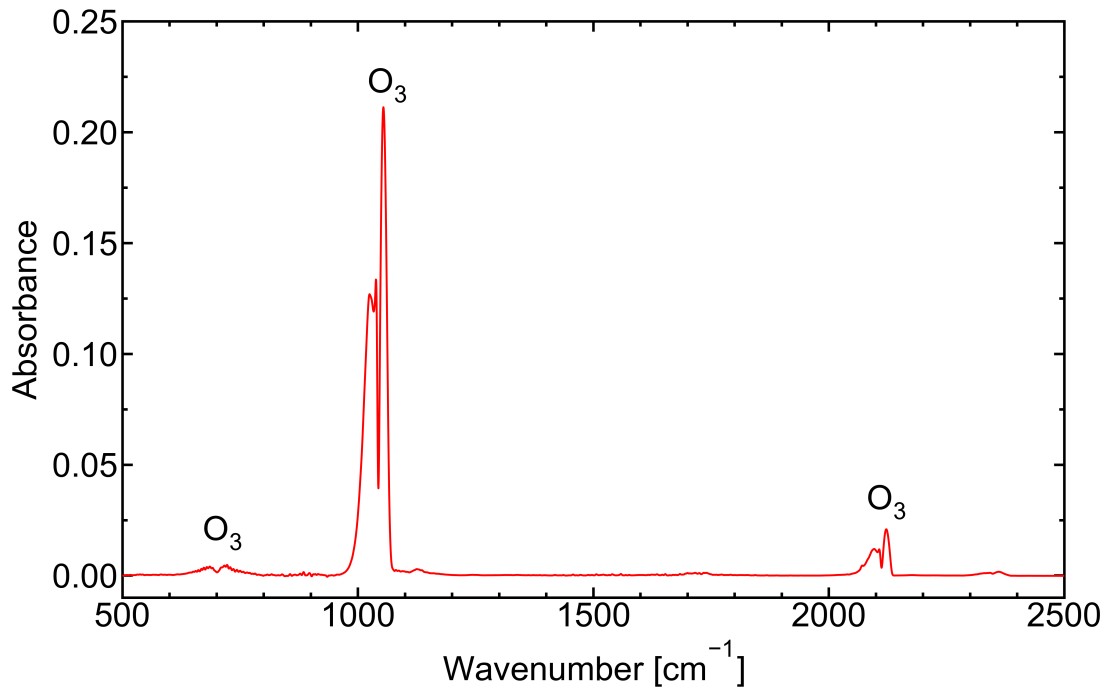


Figure 6.5: Measured FTIR absorption spectrum obtained in the far effluent of a He+O₂(0.5%) plasma, corresponding to an ozone density of 5.11×10^{14} cm⁻³. Measurements are taken in optically thin conditions. Spectral structure explained in text.

The data in the mid-infrared region between 550 cm⁻¹ and 2200 cm⁻¹ is analysed as follows. Assuming the gas mixture to be distributed homogeneously within the multi-pass cell, the optical absorbance can be described by the Beer-Lambert law (see equation 2.5). Summing the contributions from all overlapping absorption lines at wavenumber ν gives

$$A_{int}(\nu) = nd\sigma(\nu) = nd \sum_t [S_t \cdot f(\nu, \nu_t)], \quad (6.4)$$

where A_{int} is the measured absorbance integrated along absorption length d , n is the ozone density, and $\sigma(\nu)$ is the absorption cross-section of ozone at wavenumber ν . S_t is the line strength of transition t , centred at wavenumber ν_t , at 296 K, as the effluent gas is expected to relax to room temperature before reaching the multi-pass cell [225]. Line strengths and positions are taken from the HITRAN database [144]. Included transitions are restricted to those with a line strength above $10^{-22} \text{ cm}^{-1} / (\text{molec.} \cdot \text{cm}^{-2})$, with the largest line strength in the range probed being $4.17 \times 10^{-20} \text{ cm}^{-1} / (\text{molec.} \cdot \text{cm}^{-2})$, centred at 1042 cm^{-1} . $f(\nu, \nu_t)$ is the line shape function of transition t at wavenumber ν . Since instrumental broadening is by far the dominant line broadening mechanism, a common Gaussian line shape (as defined in equation 2.7) is assumed for all transitions. The theoretical absorbance spectrum is then calculated and numerically fitted to the measured spectra using a least squares fitting routine to determine the ozone density. Fitting is performed with the SciPy package for Python [227]. An uncertainty in the measured ozone densities of approximately $\pm 10\%$ is established, based on the standard deviation of the numerical fit and the reproducibility of the measurements.

6.2.4 Gas temperature from optical emission spectroscopy

The gas temperature within the core plasma of the S-APPJ is measured by OES. A thorough description of this technique and a history of its applications are given by Bruggeman *et al* [132]. A fibre optic spectrograph (HR4000, Ocean Optics, spectral resolution: 0.03 nm) is used to measure the optical emission of molecular nitrogen through the $\text{N}_2(C^3\Pi_u-B^3\Pi_g)$ second positive system, which is collected from the centre of the plasma channel. Measurements are controlled with a dedicated software suite (OceanView, Ocean Optics). No $\text{N}_2(C-B)$ emission is observed under standard operating conditions due to the sealed He+O₂ plasma environment. As such, small amounts of N₂ (up to 0.1%) are admixed into the feed gas before OES measurements are taken. The electrical characteristics of the discharge were found to be unaffected by this. OES measurements are performed separately to ozone density measurements to ensure that no trace N₂ is present to disrupt the oxygen plasma chemistry. Despite the measurements being time-averaged, no strong time variation in gas temperature

is expected once the plasma has reached equilibrium due to the slow dynamic timescale of the bulk neutral gas relative to the varying RF voltage.

The rotational band of the $v' = 0 \rightarrow v'' = 0$ vibrational transition, centred near 337 nm, has the highest signal-to-noise ratio in the measurement range and is therefore chosen for analysis. The spectra show no overlap of the ($v = 0 \rightarrow 0$) band with other spectral features. It is assumed that the rotational levels of the upper N₂(C) state are in thermal equilibrium with the background gas; this is expected in atmospheric pressure helium discharges due to the short ro-translational relaxation time of N₂(C) relative to the effective lifetime of the state [261,262]. Equation 2.3 relates the emission intensity of a transition to the population of the upper excited state. Assuming a Boltzmann distribution of rotational levels, the emission intensity of a rotational transition from upper rotational level J' to lower rotational level J'' of a homonuclear, diatomic molecule is given by [263]

$$I_{J',J''} = A_{J',J''} h c \nu_0 n_{J'} = A_{J',J''} h c \nu_0 \frac{g_{J'} g_n n_{v'}}{Q_r(T_r)} \cdot \exp\left(-\frac{E_{J'}}{k_B T_r}\right). \quad (6.5)$$

Here, $A_{J',J''}$ is the Einstein emission coefficient of the transition, h is the Planck constant, c is the speed of light, and ν_0 is the central wavenumber of the transition. $n_{J'}$ is the number density of the upper rotational state, and $n_{v'}$ is the total number density of vibrational state v' . Q_r , $E_{J'}$, and T_r are the rotational partition function, transition energy, and rotational temperature, respectively. $g_{J'} = (2J' + 1)$ and g_n accounts for nuclear spin degeneracy [264]. An example of a measured N₂(C–B) ($v = 0 \rightarrow 0$) spectrum and simulated fit are shown in figure 6.6. Measured spectra are fitted with a code used in previous studies [135, 155, 158, 265–267]. The simulation is modelled according to Herzberg [268], with rotational constants from Roux *et al* [269] and line strengths calculated from Kovács [270] and Schadee [271]. Λ-doubling is omitted. The resulting gas temperature readings have a characteristic uncertainty of ±12 K. This value is calculated based only on the variation between repeat readings and the standard deviation between the model fit and experimental data.

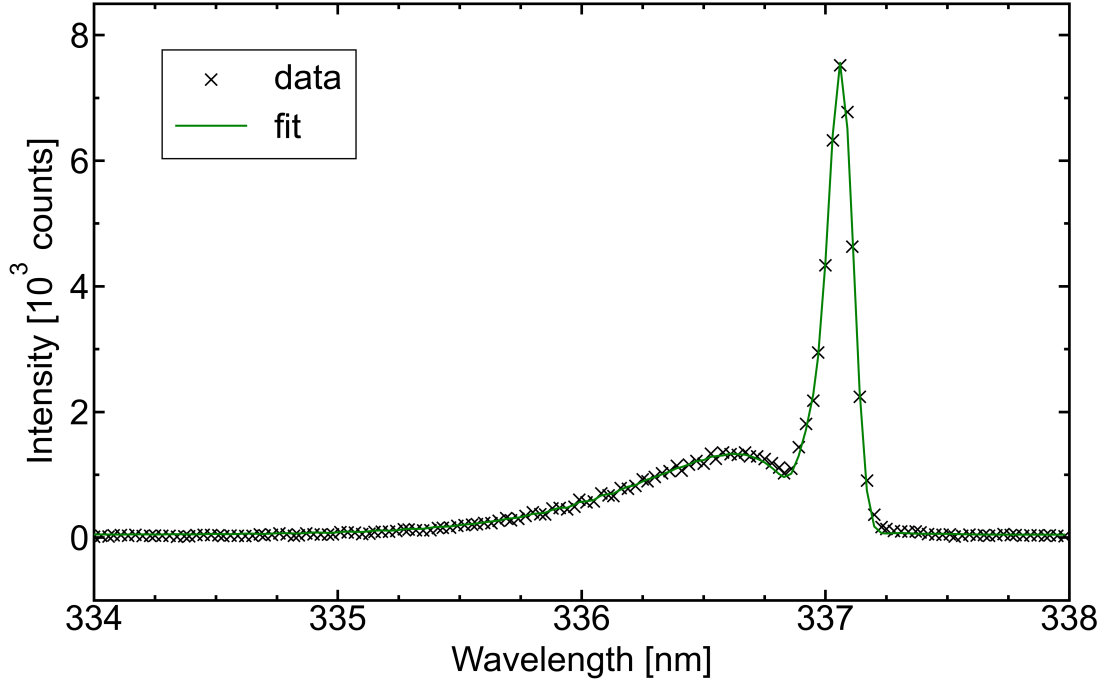


Figure 6.6: Measured optical emission spectrum and best fit of the $N_2(C^3\Pi_u - B^3\Pi_g)$ ($v = 0 \rightarrow 0$) rotational band for a $He+O_2(0.5\%)$ plasma with trace amounts of N_2 . Fit corresponds to a gas temperature of 300 K.

6.3 Results and discussion

6.3.1 Influence of the O₂ admixture concentration

Figure 6.7 shows the measured ozone density in the far effluent as a function of the O₂ admixture for different types of TVW. The O₂ admixture concentration is varied from 0.2% to 1.0%. The peak-to-peak voltage is $\phi_{pp} = 420$ V. Each TVW is composed of $N = 3$ consecutive harmonics, as shown in figure 6.3. $N = 3$ harmonics is chosen as this generates a distinct shape for each type of TVW while still offering a reasonable operational range. The density of ozone in the effluent increases linearly with the O₂ concentration for all four types of TVW. Both sawtooth waveforms produce a minimum ozone density of around $4 \times 10^{14} \text{ cm}^{-3}$ at 0.2% O₂ admixture, rising to a maximum ozone density of a little under $8 \times 10^{14} \text{ cm}^{-3}$ at 0.9% O₂. Meanwhile, peaks and valleys waveforms generate slightly higher ozone densities, with a minimum of roughly $8 \times 10^{14} \text{ cm}^{-3}$ at 0.4% O₂ admixture and a maximum of $1.1 \times 10^{15} \text{ cm}^{-3}$ and $1.0 \times 10^{15} \text{ cm}^{-3}$, respectively, at 1.0% O₂.

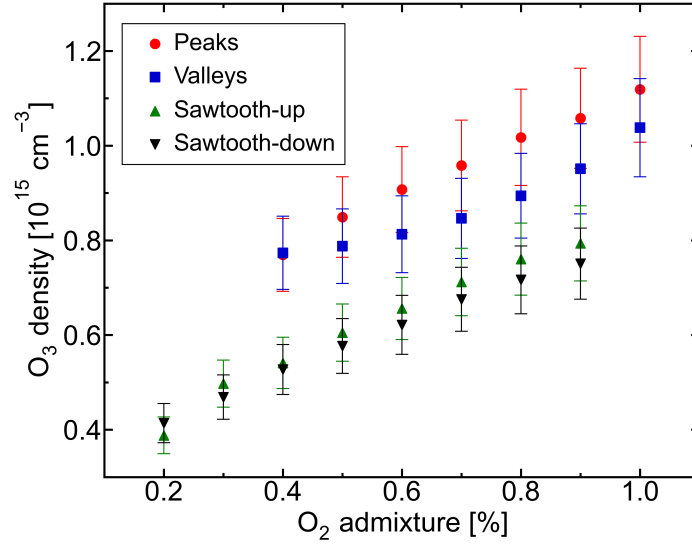


Figure 6.7: Ozone density in the far effluent as a function of the O₂ admixture concentration. The different voltage waveforms all contain $N = 3$ consecutive harmonics, with $\phi_{pp} = 420$ V.

This trend and the magnitude of the ozone densities are comparable to measurements of single-frequency plasmas. This includes measurements of the plasma channel [135], where the ozone density was found to increase from around 1×10^{14} cm⁻³ to 1.2×10^{15} cm⁻³ between 0.1% and 0.9% O₂ admixture, and measurements of the early effluent [272], where the ozone density increases from close to zero at 0.1% O₂ up to 1×10^{15} cm⁻³ at 1.0% O₂ admixture. Numerical modelling of these regions shows that ozone is primarily generated through the three-body recombination of O and O₂ with background helium [80]. It is generally accepted that this process forms ozone in a vibrationally excited state, O₃(v), which is rapidly quenched by collisions with the background gas [273–275]:



As shown by Turner [80] and Wijaikhum *et al* [135], ozone is primarily destroyed in the plasma bulk through collisions with O₂(b¹Σ_u⁺):



With these pathways in mind, the measured relationship between the ozone density and the concentration of O₂ is consistent with the explanation of Turner [80]. In brief, raising the O₂ admixture concentration increases the rate of ozone production via reaction R6.1. This

also increases the quenching rate of O₂(b¹Σ_u⁺), reducing the O₂(b¹Σ_u⁺) available to sustain reaction R6.2. Thus, a higher equilibrium density of ozone is reached.

Moving to the differences between the distinct types of TVW, the two sawtooth waveforms have very similar ozone density distributions. Likewise, the ozone densities generated by the peaks and valleys waveforms are within experimental error of each other, although the measured values for the peaks waveform are slightly higher than the valleys waveform overall. A much more significant difference is found when comparing peaks and valleys waveforms with sawtooth-up and sawtooth-down waveforms. For measurements at equivalent O₂ concentrations, peaks and valleys waveforms produce an average of 1.3 times more ozone than the sawtooth waveforms.

The operational range of O₂ concentrations differs between peaks and valleys waveforms and sawtooth waveforms. This range is bounded at low O₂ concentrations by the plasma transitioning to a constricted mode, characterised by high power deposition and a high gas temperature. At high O₂ concentrations, the operational range is bounded by the plasma failing to ignite. The difference in operational range is likely caused by the time asymmetry of peaks and valleys waveforms generating stronger local electric fields than the sawtooth waveforms [245], producing electrons and helium metastables with increased efficiency and coupling more power into the plasma overall. The consequences of this phenomenon are discussed in more detail in chapters 6.3.3 and 6.3.4.

These results demonstrate that the type of TVW impacts both the operational range of O₂ admixture and the density of plasma-produced ozone carried to the far effluent when the peak-to-peak driving voltage, fundamental frequency and number of applied voltage harmonics are fixed.

6.3.2 Influence of the peak-to-peak voltage

The peak-to-peak voltage of the driving waveform is varied to assess its influence on the RF power deposited into the plasma and the resulting ozone density measured in the far effluent. The peaks waveform is investigated for this purpose, as its ability to break the spatial symmetry of electron heating means that it affects plasma behaviour more significantly than sawtooth waveforms [245]. Figure 6.8(a) shows the change in ozone density with the applied peak-to-peak voltage for peaks waveforms with $N = 1, 2,$ and 4 consecutive harmonics. $N = 1$ harmonics corresponds to a sinusoidal, single-frequency voltage waveform. The $N = 2$ case

is akin to conventional dual-frequency operation [240]. $N = 4$ harmonics is used instead of $N = 3$ to clearly differentiate from the dual-frequency case, while still offering a greater operational range than $N = 5$ harmonics. The O₂ admixture concentration is 0.5% in all cases. All harmonic compositions show an approximately linear increase in ozone density with peak-to-peak voltage. A minor exception is the upper voltage range of $N = 4$, where the ozone density starts to saturate.

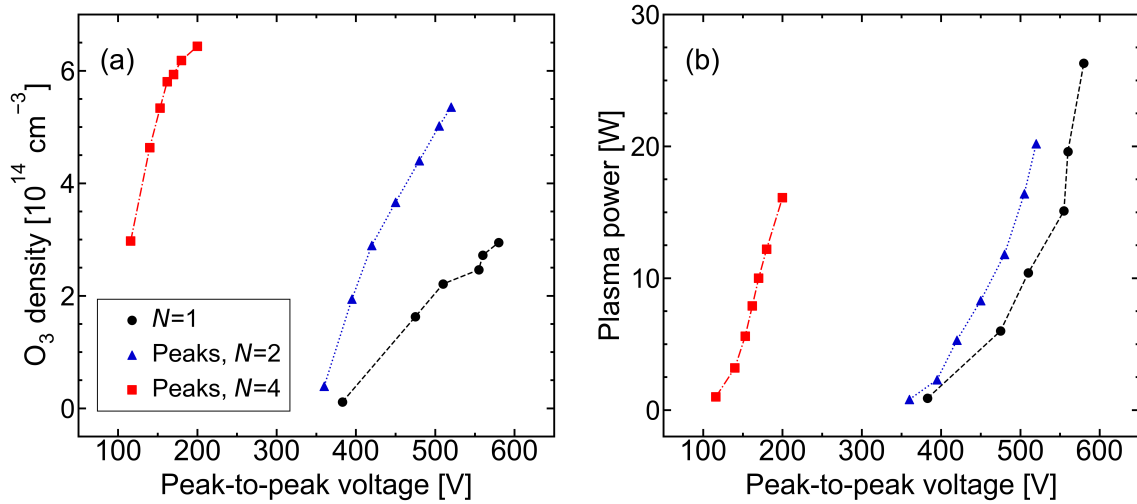


Figure 6.8: (a) Ozone density measured in the far effluent and (b) RF power deposited into the plasma as a function of the peak-to-peak voltage of the driving waveform, for a peaks waveform with different numbers of applied voltage harmonics. $N = 1$ denotes a sinusoidal, single-frequency waveform. The feed gas is He+O₂(0.5%). Characteristic measurement error in the ozone density is $\pm 10\%$.

The range of peak-to-peak voltages capable of generating a stable plasma is strongly affected by the number of applied harmonics in the driving voltage waveform. A single-frequency driving waveform allows a stable plasma to be generated with a peak-to-peak voltage in the range 380 V to 580 V. If the driving waveform contains $N = 4$ consecutive harmonics, this range is reduced to just 115 V to 200 V. $N = 2$, dual-frequency operation permits a similar voltage range to single-frequency use. However, using $N = 2$ harmonics allows a higher ozone density to be produced for an equivalent peak-to-peak voltage, with the difference in ozone density between dual- and single-frequency operation increasing with the peak-to-peak voltage. The highest ozone densities are produced with $N = 4$ harmonics, increasing from 3.0×10^{14} cm⁻³ to 6.4×10^{14} cm⁻³ within the operational voltage range, compared with 1×10^{13} cm⁻³ to 2.9×10^{14} cm⁻³ using single-frequency excitation. These findings are supported by data from Korolov *et al*, who showed that the atomic oxygen density in the plasma

channel of a COST-Jet scaled linearly with the applied peak-to-peak voltage, and that it could be further enhanced by increasing the number of voltage harmonics in a peaks driving waveform [249]. As reaction R6.1 is both the dominant mechanism for the destruction of atomic oxygen and the primary source of ozone in He+O₂ plasmas [156, 189], it follows that an increase in atomic oxygen density with peak-to-peak voltage or number of applied harmonics leads to enhanced ozone densities in the far effluent.

The relationship between the peak-to-peak voltage and the RF power deposited into the plasma is shown in figure 6.8(b). For all harmonic compositions, raising the peak-to-peak voltage of the driving waveform causes more RF power to be coupled into the plasma. Additionally, increasing the number of applied harmonics lowers the peak-to-peak voltage needed to achieve a given RF power deposition and reduces the maximum RF power that can be deposited into the plasma before it transitions to a constricted mode. These results agree with findings from Korolov *et al*, who found that driving a COST-Jet with a valleys waveform composed of $N = 4$ harmonics allowed a greater RF power to be deposited before the formation of the constricted mode, and for lower peak-to-peak voltages, when compared to single-frequency operation with the same fundamental frequency [248]. The power range is an order of magnitude larger in the present work, which is attributed to the S-APPJ having a plasma channel volume that is approximately seven times larger than the plasma channel volume of the COST-Jet.

Figure 6.9 presents the ozone density as a function of the RF power deposited into the plasma. For all harmonic compositions, raising the RF power increases the density of ozone in the effluent, although it appears to plateau with increasing RF power. Raising N also increases the density of ozone in the effluent within the operational RF power range. The overall trend between ozone density and deposited RF power agrees with ozone measurements in the far effluent of a COST-Jet by Riedel *et al*, who used a single-frequency driving waveform [154]. In contrast, measurements taken for single-frequency operation by Wijaiikum *et al* show that the ozone density within the plasma channel decreases as a function of deposited RF power. This was attributed to two factors. Firstly, the density of O₂(b¹Σ_u⁺) increases with RF power, with O₂(b¹Σ_u⁺) destroying ozone via reaction R6.2 [135]. Secondly, the temperature of the background gas increases with the deposited RF power. This lowers the rate of reaction R6.1, thus decreasing the production of ozone [135].

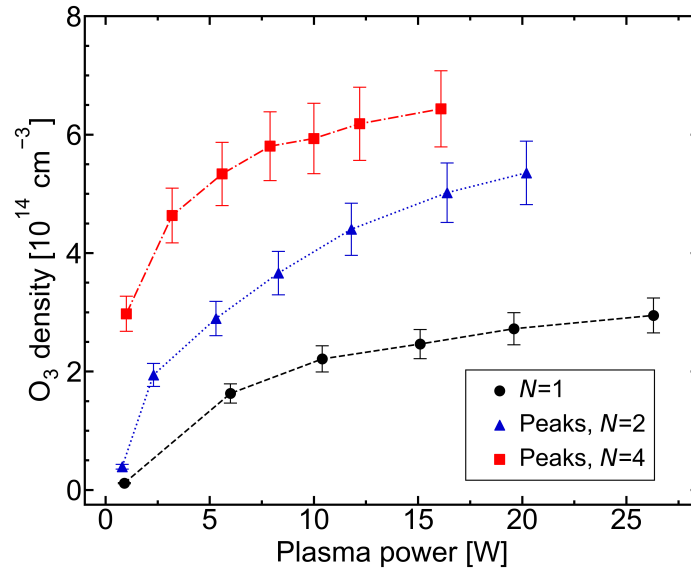


Figure 6.9: Ozone density measured in the far effluent as a function of the RF power deposited into the plasma. $N = 1$ denotes a sinusoidal, single-frequency waveform. The feed gas is He+O₂(0.5%).

Additionally, ozone is sensitive to thermal decomposition and decomposes more rapidly as the gas temperature is increased, ultimately reforming O₂ [135,198]. In the effluent, however, an absence of supplied power leads to a sharp decay in radical and excited species densities, and the gas temperature returns to room temperature [225,276]. For operation with a helium carrier gas, atomic oxygen in the effluent is rapidly converted into ozone, driving an increase in the ozone density along the first few centimetres of the effluent until reaching saturation [277]. Beyond this point, the ozone density is expected to remain stable due to its long lifetime in the absence of effective reaction partners [278]. As the density of atomic oxygen scales with RF power [154], it follows that ozone production in the early effluent via reaction R6.1 is responsible for the trend seen in figure 6.9. Thus, much like with atomic oxygen, the peak-to-peak voltage or deposited RF power of TVWs can be used to control the production of ozone by an APPJ.

6.3.3 Influence of the applied harmonics I: Constant peak-to-peak voltage

In chapters 6.3.1 and 6.3.2, it has been established that the number of applied harmonics can be used in tandem with the O₂ admixture concentration, peak-to-peak voltage, and RF power to tailor the ozone density in the effluent of an APPJ. Fixing the peak-to-peak voltage and admixture concentration is an often-taken approach for isolating the effects of TVW

harmonics [247, 249, 279]. Here, the ozone density in the effluent, the gas temperature in the plasma channel, and the deposited RF power are investigated for different types of TVW with varying numbers of harmonics. The peak-to-peak voltage is set to $\phi_{pp} = 315$ V and the O₂ admixture concentration is 0.1%, with these values selected to maximise the range of applied harmonics that can be investigated.

The effect of the number of applied voltage harmonics on the ozone density in the far effluent is shown in figure 6.10(a) for different types of TVW.

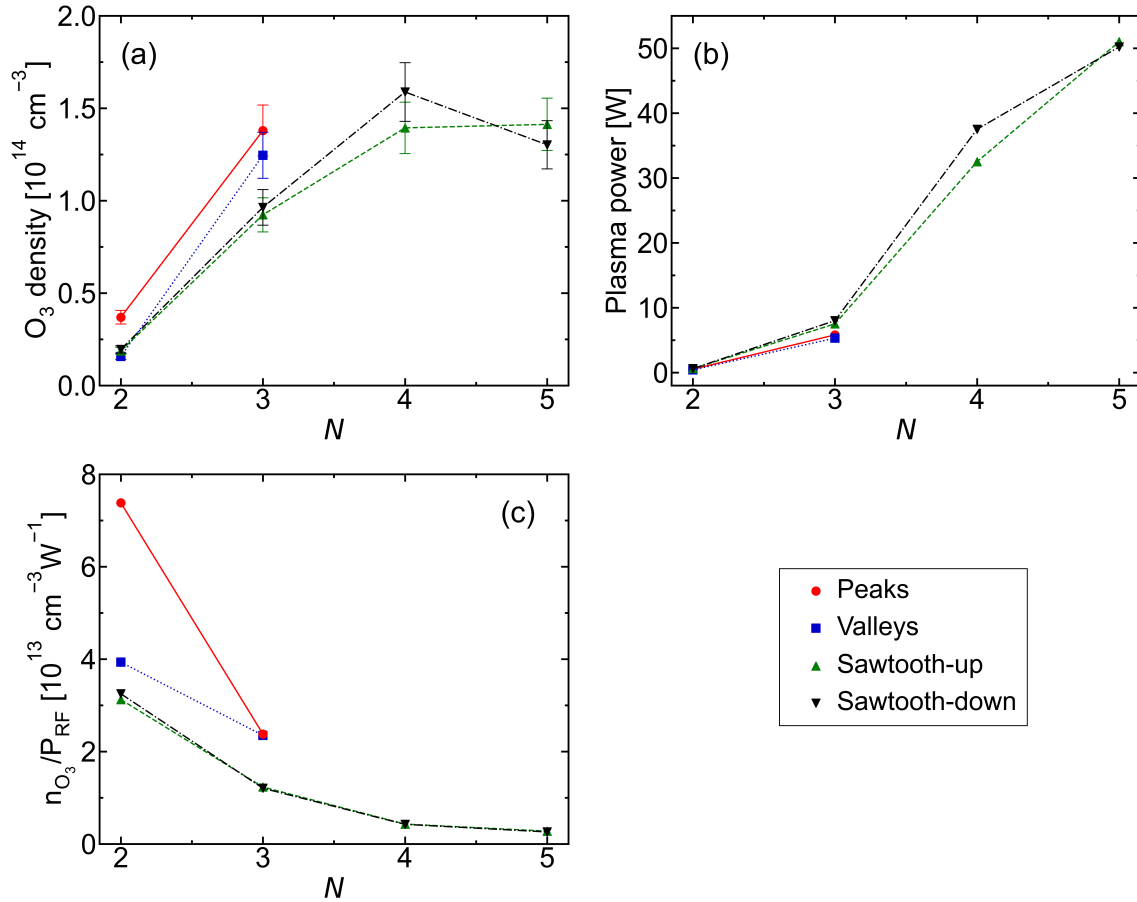


Figure 6.10: (a) Ozone density measured in the far effluent, (b) RF power deposited into the plasma, and (c) ozone production efficiency, as a function of the applied harmonics in the driving voltage waveform. A constant peak-to-peak voltage, $\phi_{pp} = 315$ V is used. The feed gas is He+O₂(0.1%). Plasma operation unstable for peaks and valleys waveforms when $N > 2$.

Starting at $N = 2$ harmonics, the ozone density is close to $2 \times 10^{13} \text{ cm}^{-3}$ for the valleys and both sawtooth waveforms, and $3.7 \times 10^{13} \text{ cm}^{-3}$ for the peaks waveform. For the peaks and valleys waveforms, $N = 3$ is the highest number of voltage harmonics that can be applied before

the plasma transitions to a constricted mode. Measurements were not performed for higher values of N due to the risk of damage to the plasma device. For the sawtooth waveforms, the ozone density increases steadily up to $N = 4$, reaching $1.4 \times 10^{14} \text{ cm}^{-3}$ for the sawtooth-up waveform and $1.6 \times 10^{14} \text{ cm}^{-3}$ for the sawtooth-down waveform. At $N = 5$ applied harmonics, the density achieved by the sawtooth-down waveform decreases to $1.3 \times 10^{14} \text{ cm}^{-3}$, while for the sawtooth-up waveform it plateaus.

Detailed computational modelling by Liu *et al* suggests that the spatial density distribution of ozone in the plasma channel is not strongly affected by the symmetry-breaking effect of the valleys waveform [129]. This is because ozone is generated from interactions between neutral species and is therefore not directly affected by the electron dynamics. It is therefore reasonable to suggest that the observed enhancement of ozone densities with applied harmonics is a spatially non-localised effect that is coupled to its parent species, atomic oxygen. Atomic oxygen is primarily produced in the plasma channel through electron-impact dissociation of the O₂ admixture. This occurs either directly, or through a two-stage quenching process in which O₂ first dissociates into O and the metastable O* [156]. It is known that increasing the number of harmonics in the driving voltage waveform enhances the high-energy tail of the EEDF, whether through temporal electron heating confinement with sawtooth waveforms or spatio-temporal electron heating confinement with peaks and valleys waveforms [245, 247]. Through this mechanism, it has been shown that the density of atomic oxygen in the plasma channel can be significantly enhanced by increasing the number of applied harmonics in a peaks waveform from $N = 1$ to $N = 4$ while maintaining a constant peak-to-peak voltage [249]. This suggests that the increase in ozone density with the number of applied harmonics results from an enhancement in atomic oxygen density that stems from localised electron heating, ultimately driving a spatially-uniform recombination of atomic oxygen into ozone in the early afterglow.

The behaviour at $N = 5$ is thought to result from the plasma becoming unstable from high RF power deposition and the deformation of the driving voltage waveform, although the plasma does not fully transition to a constricted mode. This is supported by figure 6.10(b), which shows the change in deposited RF power with the number of applied voltage harmonics. For the sawtooth waveforms, a significant increase in deposited power occurs between $N = 3$ and $N = 4$, reaching a maximum at $N = 5$. The difference in deposited RF power between sawtooth and peaks or valleys waveforms is negligible within experimental uncertainty at

both $N = 2$ and $N = 3$ applied harmonics. However, the fact that a stable plasma could not be generated with peaks and valleys waveforms for more than $N = 3$ applied harmonics suggests that these waveforms deposit appreciably more power into the plasma than sawtooth waveforms when $N > 3$. These findings align with a study by Hübner *et al.*, who showed that increasing the number of applied voltage harmonics in a valleys waveform from $N = 1$ to $N = 4$ increases the power density dissipated in the plasma channel of a COST-Jet by approximately a factor of 5 for a constant peak-to-peak voltage and fundamental frequency [235]. These observations were explained by Vass *et al.* For a valleys waveform, increasing the number of applied harmonics causes stronger electron acceleration during the sheath collapse at the grounded electrode, increasing the time-averaged electron power absorption and thus the total RF power deposition [279].

Increasing the number of applied harmonics with constant peak-to-peak voltage generates energetic species, such as metastable helium, with greater efficiency [248]. However, this seemingly does not extend to ozone production as a downstream process. Normalising the measured ozone densities by the RF power deposited into the plasma, n_{O_3}/P_{RF} , provides an estimate of the efficiency of ozone production. This is shown in figure 6.10(c) as a function of the applied harmonics, for a constant peak-to-peak voltage. Increasing the number of applied harmonics reduces the efficiency of ozone production for all waveforms. For the sawtooth waveforms, the efficiency drops by more than one order of magnitude between $N = 2$ and $N = 5$. As such, the observed increases in ozone density with the number of applied harmonics can be explained by the overall increased power deposition achieved by these waveforms.

Figure 6.11 shows that the increased power coupled into the plasma is tied to a significant rise in the gas temperature within the plasma channel. For all types of TVW, the gas temperature from $N = 2$ to $N = 3$ rises no higher than 356 K. Increasing the number of applied voltage harmonics to $N = 4$ yields gas temperatures of 482 K and 514 K with the sawtooth-up and sawtooth-down waveform, respectively. A slight decrease in gas temperature is seen at $N = 5$, again attributed to the driving voltage waveform becoming unstable.

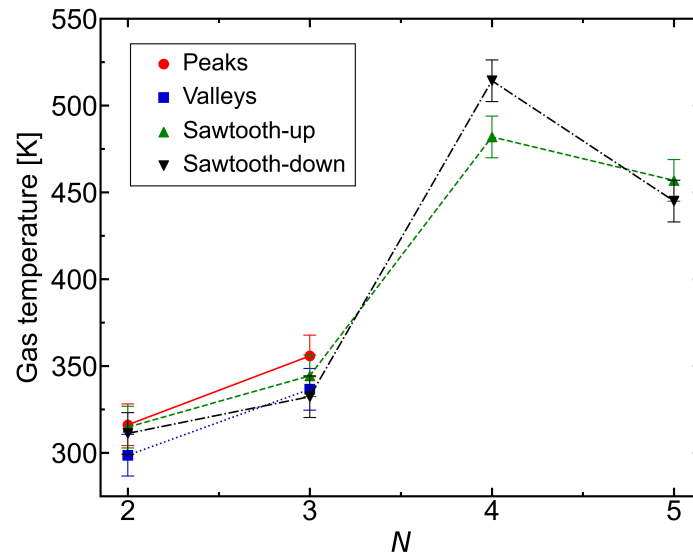


Figure 6.11: Gas temperature within the plasma channel as a function of the applied harmonics in the driving voltage waveform. A constant peak-to-peak voltage, $\phi_{pp} = 315$ V is used. The feed gas is He+O₂(0.1%).

The gas temperatures observed at $N = 4$ or more applied harmonics are significantly higher than measurements from a previous study that drives the same plasma source with single-frequency voltages, which gave a typical value of around 305 K [136]. They are also much higher than the upper limits achieved in single-frequency studies of the COST-Jet [15,225]. A similar gas heating effect was reported by Zhang *et al* in a numerical study of an atmospheric pressure, radio-frequency dielectric barrier discharge driven by TVWs, in which the gas temperature at the centre of the reactor increased steadily with the number of applied voltage harmonics in a sawtooth-down waveform [280]. The sharp rise in gas temperature with the number of applied harmonics is likely a result of the significant power deposition causing a sustained, localised gas heating effect by electron-neutral collisions. Operating an APPJ at these temperatures for extended periods poses a significant risk of device damage, and could potentially cause harm to biological tissues or polymer surfaces that are treated by the plasma source. The observed gas heating may also contribute to the poor ozone production efficiency seen at high numbers of applied harmonics. Moreover, the largest variation in ozone density achieved by this method is less than an order of magnitude. Similar tuning ranges are achievable with single-frequency excitation through variation of the O₂ admixture; while this requires mechanical changes that are not needed when changing the applied harmonics of a TVW, the gas temperature is consistently much lower [135].

These results demonstrate that the density of ozone in the plasma effluent can be controlled via the number of applied harmonics in the driving voltage waveform, without changing the peak-to-peak voltage. However, increasing the number of harmonics can cause significant gas heating in the plasma channel and lower the efficiency of ozone production. Despite this, it may still be possible to control ozone production through the number of applied harmonics, in a manner that is efficient and independent of the gas temperature. To explore this option, the next section investigates the use of TVWs with a fixed RF power deposition.

6.3.4 Influence of the applied harmonics II: Constant RF power

The following measurements are taken for a constant deposited RF power of $P_{RF} = 8$ W. As such, the peak-to-peak voltage varies based on the voltage waveform shape and harmonic content. An O₂ admixture of 0.5% is utilised to maximise the range of operating parameters that can be compared. These operating conditions allow a stable plasma to be generated with driving voltage waveforms containing $N = 1$ to $N = 5$ applied harmonics. Figure 6.12(a) shows the effect of the applied voltage harmonics on the ozone density in the far effluent for a fixed RF power deposition.

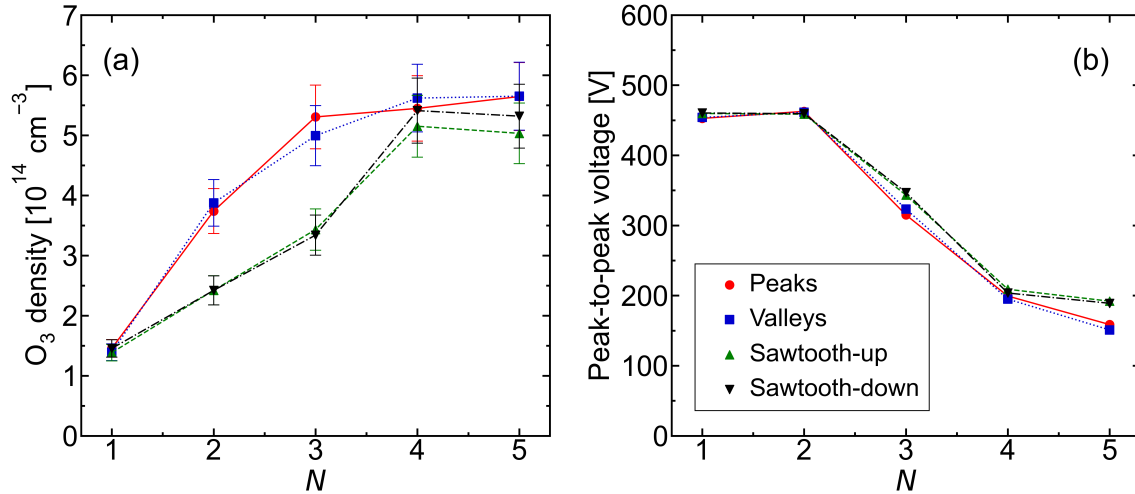


Figure 6.12: (a) Ozone density measured in the far effluent and (b) the peak-to-peak voltage of the driving waveform, as a function of the number of applied harmonics. The RF power deposited in the plasma, P_{RF} is 8 W. The feed gas is He+O₂(0.5%).

The sinusoidal, $N = 1$ case generates the lowest density of ozone, at a little over 1.4×10^{14} cm⁻³. For peaks and valleys waveforms, increasing the number of applied harmonics to $N = 3$ increases the ozone density by a factor of 3.6. The same harmonic change yields factor 2.3 and

2.5 increases for the sawtooth-up and sawtooth-down waveforms, respectively. The increase in ozone density with the number of applied harmonics for a fixed RF power deposition suggests that ozone is being produced with increased efficiency. For an equivalent power density, Hübner *et al* found that increasing the number of applied harmonics from $N = 1$ to $N = 4$ increases the electron density, the helium metastable density, and the dissociation rate of molecular admixture within the plasma channel [235]. However, it should be noted that this is based on two data points with different fundamental frequencies. This aside, an increase in the dissociation rate of O₂ admixture would increase the ozone density in the effluent via reaction R6.1. Further evidence for higher numbers of applied harmonics sustaining a more active plasma chemistry can be seen in figure 6.12(b), which shows the peak-to-peak voltage required to sustain the fixed RF power deposition of 8 W. Increasing the number of applied voltage harmonics above $N = 2$ allows the same RF power to be deposited into the plasma for a significantly lower peak-to-peak voltage. Raising the number of applied harmonics steepens the voltage gradients of the driving waveform, stimulating an increasingly short sheath collapse that accelerates electrons to high energies to compensate the ion flux on time average [235, 245]. This allows more power to be deposited into the plasma relative to the peak-to-peak voltage of the driving waveform.

As discussed in chapter 6.1, different types of TVW exert different symmetry-breaking effects on the plasma; electron heating is confined only in time by sawtooth waveforms, while peaks and valleys waveforms restrict electron heating in both time and space [245]. This improved localisation of power transfer enables peaks and valleys waveforms to drive a more efficient production of atomic oxygen than the sawtooth waveforms, with its recombination resulting in the greater ozone densities generated with peaks and valleys waveforms at $N = 2$ and $N = 3$ when compared to the sawtooth waveforms. Interestingly, all four waveforms appear to reach a similar upper limit in the ozone density at $N = 4$ applied voltage harmonics, with negligible change seen if N is increased to 5. While the physical cause of this limit is unclear, it is feasible that increasing the number of applied harmonics enhances the ozone density until an upper threshold is reached. Referring to the model TVWs in figure 6.1, as the number of applied harmonics rises, the relative change in the voltage gradient between consecutive harmonics decreases, as does the relative change in the duration of periods of high voltage gradient. Furthermore, increasing the number of harmonics also decreases the relative change in the asymmetrical displacement of peaks and valleys waveforms along the

voltage axis, although this last effect may differ in practice due to the formation of a DC self-bias voltage [246]. The progressively decreasing relative change in these parameters may lead to a ‘diminishing returns’ effect at high numbers of harmonics. In this case, electron heating cannot be further restricted in time or space in a way that would noticeably affect the plasma chemistry, nor can the strong electric field generated by the voltage slope be appreciably increased. This would limit the degree to which the high-energy tail of the EEDF can be enhanced, in turn limiting the production of atomic oxygen through electron-impact dissociation of O_2 and creating an upper threshold in the density of ozone produced through the recombination of atomic oxygen. This is beyond the scope of the present study; it remains for future works to investigate a possible upper limit to atomic oxygen production with TVWs.

Figure 6.13 shows the change in the gas temperature of the plasma channel with the number of applied harmonics for a fixed RF power deposition. Tuning between $N = 2$ and $N = 5$ applied voltage harmonics with constant RF power results in a much lower change in the gas temperature of the plasma channel when compared to operation with a constant peak-to-peak voltage, with the temperature change almost negligible outside of the experimental uncertainty. The measured gas temperature does not exceed 340 K, and a minimum gas temperature of 305 K is obtained by using a sawtooth-down waveform with $N = 2$ applied harmonics.

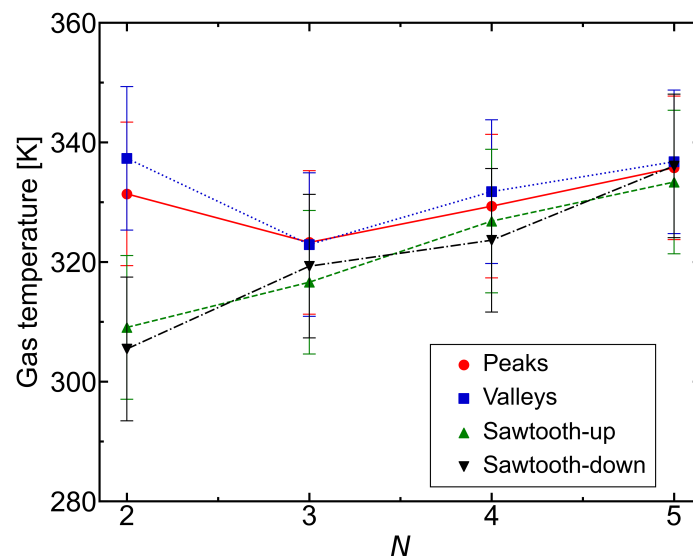


Figure 6.13: Gas temperature within the plasma channel as a function of the number of applied harmonics in the driving voltage waveform. The RF power deposited in the plasma, P_{RF} is 8 W. The feed gas is He+ O_2 (0.5%).

The presented gas temperatures are within the range of previous measurements of a COST-Jet driven with single-frequency voltages [15, 225], indicating that the S-APPJ can be safely operated under these conditions. Evidently, operation with a fixed RF power deposition prevents excessive gas heating while still allowing the density of ozone to be controlled and the efficiency of ozone production to be increased.

These results highlight the difference between TVW operation with a fixed peak-to-peak voltage and TVW operation with a fixed RF power. As demonstrated in chapter 6.3.3, raising the number of applied voltage harmonics for a fixed peak-to-peak voltage increases the RF power deposited into the plasma through the electrons. The increased RF power significantly influences the heavy species chemistry in a comparable fashion to single-frequency operation, obscuring the effects of TVW operation and limiting independent control of the ozone density. By fixing the RF power, this behaviour is negated. The observed increase in the ozone density with the number of applied harmonics is instead due to the available RF power being utilised more efficiently – a direct effect of TVW operation. A consequence of this is a proportionally smaller range of achievable ozone densities when compared with operation at a fixed peak-to-peak voltage, but this method allows the ozone density to be controlled independently of the deposited RF power and gas temperature. It is therefore concluded that fixing the RF power deposition allows the ozone density to be modified through the number of applied voltage harmonics, while maintaining a relatively low gas temperature within the plasma channel.

6.4 Chapter summary

The production of RONS by radio-frequency APPJs is strongly tied to the EEDF. It is difficult to control the EEDF of APPJs driven with single-frequency, sinusoidal voltage waveforms due to the symmetry of electron heating. Tailored voltage waveforms, composed of a number of consecutive harmonics of a fundamental frequency, offer a promising alternative. This chapter details the first investigation into the effects of tailored voltage waveforms on long-lived reactive species carried through the effluent of an APPJ. The S-APPJ is supplied with helium and small admixtures of O_2 , and driven by tailored voltage waveforms composed of up to five consecutive voltage harmonics with a fundamental frequency of 13.56 MHz. The density of ozone in the far effluent is measured by Fourier transform infrared spectroscopy and the gas temperature in the plasma channel is determined by optical emission spectroscopy.

Driving a plasma with a peaks waveform is found to increase the density of ozone in the effluent when compared to single-frequency operation, with the density of ozone increasing with the number of harmonics. Peaks and valleys waveforms are found to generate more ozone than sawtooth waveforms under equivalent conditions. For a fixed peak-to-peak voltage, increasing the number of harmonics enhances the ozone density but significantly increases the gas temperature within the plasma channel due to rising RF power deposition. Efficient control of the ozone density is instead achieved by changing the number of applied harmonics for a fixed RF power deposition. This allows the ozone density to be enhanced without appreciably changing the gas temperature in the plasma channel. The results highlight that tailored voltage waveforms can be used to control the ozone density in the plasma effluent, offering more methods of control than with single-frequency voltage waveforms. However, since many of the effects of tailored voltage waveforms are related to increased power deposition, it is important to carefully monitor the gas temperature alongside the ozone density for temperature-sensitive applications.

Chapter 7

Summary and conclusions

Low temperature, atmospheric pressure plasmas are efficient sources of RONS, making them ideal tools for biomedical treatments such as cancer therapy, wound healing, and microbial sterilisation. The purpose of this work was to investigate different methods of controlling the production of RONS by LTPs, while furthering our collective understanding of the plasma-chemical processes that govern RONS production. It was established in chapter 1 that focus would be placed on the form of the applied voltage and the electrode geometry of the plasma source. To understand the production and delivery of RONS to a substrate, one must consider their journey from feed gas to far effluent. To this end, different aspects of the plasma system were explored throughout this work: the plasma core in chapter 4, the early-to-mid effluent in chapter 5, and the far effluent in chapter 6. Four plasma devices were studied: A pin-to-pin plasma source, a COST-Jet, a kINPen-sci, and an S-APPJ. Information about the plasma environment was obtained with a global numerical model and a number of optical diagnostic techniques.

Chapter 4 investigated the influence of the pulse repetition frequency on the chemistry of a nanosecond-pulsed plasma. This was achieved by simulating a He+H₂O(0.5%) plasma with the 0D plasma-chemical kinetics model, *GlobalKin*. Operational parameters were based on the physical specifications of a pin-to-pin plasma source. *GlobalKin* was supplied with a chemistry set containing 46 species and 576 reactions covering He, H₂O, and O₂ gas mixtures, allowing the densities and reaction pathways of key RONS in the active plasma region to be analysed. It was found that raising the pulse repetition frequency increases the influence of the memory effect. This increased the equilibrium densities of H, O, and OH radicals by limiting their decay through the afterglow. For the electrons, this effect was outmatched by

both the rapid population decay in the afterglow and the plasma volume increasing due to gas heating. The relationship between pulse repetition frequency and the densities of species with longer lifetimes, namely H_2O_2 and ozone, was shown to be markedly more complex, as their density depends on the availability of reactant species, the afterglow duration, and the gas temperature. It was concluded that the pulse repetition frequency can be used to control the production of RONS by a nanosecond-pulsed LTP. However, it is not a simple control parameter, especially for species that are predominantly produced in the afterglow. Detailed modelling and a good understanding of the chemistry is required to optimise a plasma using this parameter.

In chapter 5, cw-CRDS was used to measure the density of H_2O_2 in the effluent of two common APPJs, the COST-Jet and the kINPen-sci. The COST-Jet is a capacitively-coupled, radio-frequency plasma source and the kINPen-sci is a DBD-like plasma jet. Both devices were supplied with a $\text{He}+\text{H}_2\text{O}$ (0.33%) gas mixture. An Abel inversion was applied to line-of-sight integrated measurements, allowing the spatial density distribution of H_2O_2 in the effluent to be determined. The distribution of H_2O_2 in the effluent of the COST-Jet was initially highly uniform up to 15 mm from the jet nozzle, although it was rapidly diluted at further distances due to mixing with the ambient air. Comparatively, in the case of the kINPen-sci the density of H_2O_2 had a wider radial distribution close to the nozzle, while mixing with the ambient air was more gradual at further distances than with the COST-Jet. This was attributed in part to the plasma channel geometry of both APPJs. The average H_2O_2 density in the effluent of the kINPen-sci was found to be twice as high as in the effluent of the COST-Jet. It was proposed that the kINPen-sci generates higher H_2O_2 densities by sustaining a greater population of high-energy electrons in the plasma core, resulting in a larger fraction of water being dissociated in comparison to the COST-Jet. These results highlight the influence of the plasma source design on the production and effluent distribution of H_2O_2 by an APPJ. The geometry and voltage scheme of a plasma device should be considered when treating a target area with RONS.

Chapter 6 explored the mechanisms of ozone production by a radio-frequency APPJ driven with tailored voltage waveforms. The TVWs were composed of up to five harmonics of a fundamental frequency, $f_0 = 13.56$ MHz and generated experimentally through an iterative feedback loop. The APPJ was supplied with a helium feed gas with admixtures of oxygen in the range of 0.1% to 1.0%. FTIR was used to measure the ozone density in the far effluent,

and the gas temperature within the plasma channel was determined with OES. Voltage waveform tailoring was found to modify the production of ozone by a plasma jet and generate greater ozone densities in the effluent than could be achieved with a single-frequency voltage waveform. Increasing the number of applied harmonics in the driving voltage waveform for a fixed peak-to-peak voltage enhanced the ozone density but significantly increased the gas temperature within the plasma channel. The ozone density could instead be controlled in an efficient manner by changing the number of applied harmonics for a fixed RF power deposition. This increased the ozone density in the far effluent by up to a factor of 4 when compared to single-frequency operation, without strongly affecting the gas temperature. It was concluded that TVWs can be used to control the densities of RONS delivered through the effluent, while also enhancing production efficiency and minimising gas heating.

The investigations within this work highlight the importance of several plasma phenomena that govern the production and delivery of RONS by LTPs, from operating parameters, such as the plasma source design and applied voltage scheme, to plasma processes like the EEDF and heavy particle chemistry. While the EEDF is widely regarded as the key to controlling the plasma chemistry, attention must also be paid to the resulting afterglow chemistry and the operating parameters that directly influence it. Likewise, the relationship between the discharge geometry and the transport of RONS through the effluent is of the utmost importance when considering the delivery of RONS to a treatment area. It is concluded that each of these systems offers a pathway to controlling RONS production for biomedical applications. However, in practice, these aspects must all be considered collectively to achieve true control over the production of RONS by low temperature plasmas.

Appendix A

Reactions included in the He+H₂O+O₂ chemistry set

Table A.1: Electron reactions

No.	Reaction	Rate Coefficient ^{a,b}	Ref.
Electron scattering and momentum transfer			
1	$e^- + \text{He} \rightarrow \text{He} + e^-$	$f(\epsilon)$	[281, 282]
2	$e^- + \text{H}_2\text{O} \rightarrow \text{H}_2\text{O} + e^-$	$f(\epsilon)$	[283, 284]
3	$e^- + \text{O}_2 \rightarrow \text{O}_2 + e^-$	$f(\epsilon)$	[285]
Electron impact excitation and ionisation			
4	$e^- + \text{He} \rightarrow e^- + \text{He}(2^3\text{S})$	$f(\epsilon)$	[281, 282]
5	$e^- + \text{He} \rightarrow e^- + \text{He}(2^3\text{S})$	$f(\epsilon)$	[281, 282]
6	$e^- + \text{He} \rightarrow \text{He}^+ + e^- + e^-$	$f(\epsilon)$	[281, 282]
7	$e^- + \text{He}(2^3\text{S}) \rightarrow \text{He}^+ + 2e^-$	$f(\epsilon)$	[286] ^c
8	$e^- + \text{He}_2^* \rightarrow \text{He}_2^+ + 2e^-$	$2.06 \times 10^{-13} e^{-4.28/T_e}$	[287] ^d
9	$e^- + \text{OH} \rightarrow \text{OH}^+ + 2e^-$	$f(\epsilon)$	[288]
10	$e^- + \text{H}_2\text{O} \rightarrow \text{H}_2\text{O} + e^-$	$f(\epsilon)$	[283] ^e
11	$e^- + \text{H}_2\text{O} \rightarrow \text{H}_2\text{O} + e^-$	$f(\epsilon)$	[283] ^e
12	$e^- + \text{H}_2\text{O} \rightarrow \text{H}_2\text{O} + e^-$	$f(\epsilon)$	[283] ^e
13	$e^- + \text{H}_2\text{O} \rightarrow \text{H}_2\text{O}^+ + 2e^-$	$f(\epsilon)$	[283]

continued on next page

No.	Reaction	Rate Coefficient ^{a,b}	Ref.
14	$e^- + O \rightarrow O(^1D) + e^-$	$f(\epsilon)$	[289]
15	$e^- + O \rightarrow O(^1S) + e^-$	$f(\epsilon)$	[289]
16	$e^- + O \rightarrow O^+ + 2e^-$	$f(\epsilon)$	[289]
17	$e^- + O(^1D) \rightarrow O^+ + 2e^-$	$f(\epsilon)$	[286] ^c
18	$e^- + O(^1S) \rightarrow O^+ + 2e^-$	$f(\epsilon)$	[290] ^c
19	$e^- + O_2 \rightarrow O_2 + e^-$	$f(\epsilon)$	[285] ^f
20	$e^- + O_2 \rightarrow O_2 + e^-$	$f(\epsilon)$	[285] ^e
21	$e^- + O_2 \rightarrow O_2 + e^-$	$f(\epsilon)$	[285] ^e
22	$e^- + O_2 \rightarrow O_2 + e^-$	$f(\epsilon)$	[285] ^e
23	$e^- + O_2 \rightarrow O_2 + e^-$	$f(\epsilon)$	[285] ^e
24	$e^- + O_2 \rightarrow O_2 + e^-$	$f(\epsilon)$	[285] ^e
25	$e^- + O_2 \rightarrow O_2 + e^-$	$f(\epsilon)$	[285] ^e
26	$e^- + O_2 \rightarrow O_2(a^1\Delta) + e^-$	$f(\epsilon)$	[285]
27	$e^- + O_2 \rightarrow O_2(b^1\Sigma) + e^-$	$f(\epsilon)$	[285]
28	$e^- + O_2 \rightarrow O_2(b^1\Sigma) + e^-$	$f(\epsilon)$	[285]
29	$e^- + O_2 \rightarrow O_2^+ + 2e^-$	$f(\epsilon)$	[285]
30	$e^- + O_2(a^1\Delta) \rightarrow O_2(a^1\Delta) + e^-$	$f(\epsilon)$	As reaction 19 ^g
31	$e^- + O_2(a^1\Delta) \rightarrow O_2(a^1\Delta) + e^-$	$f(\epsilon)$	As reaction 20 ^g
32	$e^- + O_2(a^1\Delta) \rightarrow O_2(a^1\Delta) + e^-$	$f(\epsilon)$	As reaction 21 ^g
33	$e^- + O_2(a^1\Delta) \rightarrow O_2(a^1\Delta) + e^-$	$f(\epsilon)$	As reaction 22 ^g
34	$e^- + O_2(a^1\Delta) \rightarrow O_2(a^1\Delta) + e^-$	$f(\epsilon)$	As reaction 23 ^g
35	$e^- + O_2(a^1\Delta) \rightarrow O_2(a^1\Delta) + e^-$	$f(\epsilon)$	As reaction 24 ^g
36	$e^- + O_2(a^1\Delta) \rightarrow O_2(a^1\Delta) + e^-$	$f(\epsilon)$	As reaction 25 ^g
37	$e^- + O_2(a^1\Delta) \rightarrow O_2(b^1\Sigma) + e^-$	$f(\epsilon)$	[291] ^h
38	$e^- + O_2(a^1\Delta) \rightarrow O_2(b^1\Sigma) + e^-$	$f(\epsilon)$	As reaction 28 ^g
39	$e^- + O_2(a^1\Delta) \rightarrow O_2^+ + 2e^-$	$f(\epsilon)$	As reaction 29 ^g
40	$e^- + O_2(b^1\Sigma) \rightarrow O_2(b^1\Sigma) + e^-$	$f(\epsilon)$	As reaction 19 ^g
41	$e^- + O_2(b^1\Sigma) \rightarrow O_2(b^1\Sigma) + e^-$	$f(\epsilon)$	As reaction 20 ^g
42	$e^- + O_2(b^1\Sigma) \rightarrow O_2(b^1\Sigma) + e^-$	$f(\epsilon)$	As reaction 21 ^g
43	$e^- + O_2(b^1\Sigma) \rightarrow O_2(b^1\Sigma) + e^-$	$f(\epsilon)$	As reaction 22 ^g
44	$e^- + O_2(b^1\Sigma) \rightarrow O_2(b^1\Sigma) + e^-$	$f(\epsilon)$	As reaction 23 ^g
45	$e^- + O_2(b^1\Sigma) \rightarrow O_2(b^1\Sigma) + e^-$	$f(\epsilon)$	As reaction 24 ^g

continued on next page

No.	Reaction	Rate Coefficient ^{a,b}	Ref.
46	$e^- + O_2(b^1\Sigma) \rightarrow O_2(b^1\Sigma) + e^-$	$f(\epsilon)$	As reaction 25 ^g
47	$e^- + O_2(b^1\Sigma) \rightarrow O_2(b^1\Sigma) + e^-$	$f(\epsilon)$	As reaction 28 ^g
48	$e^- + O_2(b^1\Sigma) \rightarrow O_2^+ + 2e^-$	$f(\epsilon)$	As reaction 29 ^g
49	$e^- + O_3 \rightarrow O_3^+ + 2e^-$	$5.96 \times 10^{-15} T_e^{0.978} e^{-12.55/T_e}$	[80, 292, 293]
Super-elastic collisions			
50	$e^- + He(2^3S) \rightarrow He + e^-$	$f(\epsilon)$	[281, 282] ⁱ
51	$e^- + O(^1D) \rightarrow O + e^-$	$f(\epsilon)$	[289] ⁱ
52	$e^- + O(^1S) \rightarrow O + e^-$	$f(\epsilon)$	[289] ⁱ
53	$e^- + O_2(a^1\Delta) \rightarrow O_2 + e^-$	$f(\epsilon)$	[285] ⁱ
54	$e^- + O_2(b^1\Sigma) \rightarrow O_2 + e^-$	$f(\epsilon)$	[285] ⁱ
55	$e^- + O_2(b^1\Sigma) \rightarrow O_2(a^1\Delta) + e^-$	$f(\epsilon)$	As reaction 37 ⁱ
Electron impact dissociation			
56	$e^- + He_2^* \rightarrow 2He + e^-$	3.80×10^{-15}	[294]
57	$e^- + H_2O \rightarrow O(^1S) + 2H + e^-$	$f(\epsilon)$	[283, 295]
58	$e^- + H_2O \rightarrow H + OH + e^-$	$f(\epsilon)$	[283, 296]
59	$e^- + H_2O \rightarrow H + OH + e^-$	$f(\epsilon)$	[283]
60	$e^- + H_2O \rightarrow H_2 + O(^1D) + e^-$	$2.416 \times 10^{-14} T_n^{-0.062} e^{-22.4/T_e}$	[297] ^j
61	$e^- + H_2 \rightarrow 2H + e^-$	$f(\epsilon)$	[298]
62	$e^- + H_2 \rightarrow 2H + e^-$	$f(\epsilon)$	[299]
63	$e^- + OH \rightarrow O + H + e^-$	$f(\epsilon)$	[300] ^k
64	$e^- + H_2O_2 \rightarrow 2OH + e^-$	2.36×10^{-15}	[301] ^l
65	$e^- + O_2 \rightarrow 2O + e^-$	$f(\epsilon)$	[285]
66	$e^- + O_2 \rightarrow O + O(^1D) + e^-$	$f(\epsilon)$	[285]
67	$e^- + O_2 \rightarrow 2O(^1D) + e^-$	$f(\epsilon)$	[285]
68	$e^- + O_2(a^1\Delta) \rightarrow 2O + e^-$	$f(\epsilon)$	As reaction 65 ^g
69	$e^- + O_2(a^1\Delta) \rightarrow O + O(^1D) + e^-$	$f(\epsilon)$	As reaction 66 ^g
70	$e^- + O_2(a^1\Delta) \rightarrow 2O(^1D) + e^-$	$f(\epsilon)$	As reaction 67 ^g
71	$e^- + O_2(b^1\Sigma) \rightarrow 2O + e^-$	$f(\epsilon)$	As reaction 65 ^g
72	$e^- + O_2(b^1\Sigma) \rightarrow O + O(^1D) + e^-$	$f(\epsilon)$	As reaction 66 ^g
73	$e^- + O_2(b^1\Sigma) \rightarrow 2O(^1D) + e^-$	$f(\epsilon)$	As reaction 67 ^g
74	$e^- + O_3 \rightarrow O + O_2 + e^-$	$1.70 \times 10^{-14} T_n^{-0.57} e^{-2.48/T_e}$	[80, 302]
75	$e^- + O_3 \rightarrow O(^1D) + O_2(a^1\Delta) + e^-$	$3.22 \times 10^{-13} T_n^{-1.18} e^{-9.17/T_e}$	[80, 302]

continued on next page

No.	Reaction	Rate Coefficient ^{a,b}	Ref.
Dissociative ionisation			
76	$e^- + \text{H}_2\text{O} \rightarrow \text{OH}^+ + \text{H} + 2e^-$	$f(\epsilon)$	[283]
77	$e^- + \text{H}_2\text{O} \rightarrow \text{O}^+ + 2\text{H} + 2e^-$	$f(\epsilon)$	[283]
78	$e^- + \text{O}_2 \rightarrow \text{O} + \text{O}^+ + 2e^-$	$f(\epsilon)$	[303]
79	$e^- + \text{O}_2(\text{a}^1\Delta) \rightarrow \text{O} + \text{O}^+ + 2e^-$	$f(\epsilon)$	As reaction 78 ^g
80	$e^- + \text{O}_2(\text{b}^1\Sigma) \rightarrow \text{O} + \text{O}^+ + 2e^-$	$f(\epsilon)$	As reaction 78 ^g
Dissociative electron attachment			
81	$e^- + \text{H}_2\text{O} \rightarrow \text{OH} + \text{H}^-$	$f(\epsilon)$	[283, 304]
82	$e^- + \text{H}_2\text{O} \rightarrow \text{H}_2 + \text{O}^-$	$f(\epsilon)$	[283, 304]
83	$e^- + \text{H}_2\text{O} \rightarrow \text{OH}^- + \text{H}$	$f(\epsilon)$	[283, 304]
84	$e^- + \text{H}_2\text{O}_2 \rightarrow \text{H}_2\text{O} + \text{O}^-$	$f(\epsilon)$	[305]
85	$e^- + \text{H}_2\text{O}_2 \rightarrow \text{OH} + \text{OH}^-$	$f(\epsilon)$	[305]
86	$e^- + \text{O}_2 \rightarrow \text{O} + \text{O}^-$	$f(\epsilon)$	[285]
87	$e^- + \text{O}_2(\text{a}^1\Delta) \rightarrow \text{O} + \text{O}^-$	$f(\epsilon)$	[306]
88	$e^- + \text{O}_2(\text{b}^1\Sigma) \rightarrow \text{O} + \text{O}^-$	$f(\epsilon)$	As reaction 87 ^g
89	$e^- + \text{O}_3 \rightarrow \text{O}_2 + \text{O}^-$	$f(\epsilon)$	[307]
90	$e^- + \text{O}_3 \rightarrow \text{O}_2^- + \text{O}$	$f(\epsilon)$	[307]
Electron detachment			
91	$e^- + \text{H}^- \rightarrow \text{H} + 2e^-$	$f(\epsilon)$	[308]
92	$e^- + \text{OH}^- \rightarrow \text{OH} + 2e^-$	$f(\epsilon)$	[309]
93	$e^- + \text{O}^- \rightarrow \text{O} + 2e^-$	$f(\epsilon)$	[310]
94	$e^- + \text{O}_2^- \rightarrow \text{O}_2 + 2e^-$	$f(\epsilon)$	[311]
95	$e^- + \text{O}_3^- \rightarrow \text{O}_3 + 2e^-$	$2.12 \times 10^{-14} T_n^{0.51} e^{-5.87/T_e}$	[80, 312]
96	$e^- + \text{O}_3^- \rightarrow \text{O}_2 + \text{O} + 2e^-$	$7.12 \times 10^{-14} T_n^{-0.132} e^{-5.94/T_e}$	[80, 312]
97	$e^- + \text{O}_3^- \rightarrow 3\text{O} + 2e^-$	$1.42 \times 10^{-14} T_n^{-0.52} e^{-9.30/T_e}$	[80, 312]
Electron-ion recombination			
98	$e^- + \text{He}^+ \rightarrow \text{He}(2^3\text{S})$	$f(\epsilon)$	[313]
99	$e^- + \text{He}_2^+ \rightarrow \text{He} + \text{He}(2^3\text{S})$	$9.60 \times 10^{-17} T_n^{-0.5}$	[314]
100	$e^- + \text{H}_2\text{O}^+ \rightarrow \text{O} + 2\text{H}$	$3.05 \times 10^{-13} T_n^{-0.5}$	[315, 316]
101	$e^- + \text{H}_2\text{O}^+ \rightarrow \text{O} + \text{H}_2$	$3.87 \times 10^{-14} T_n^{-0.5}$	[315, 316]
102	$e^- + \text{H}_2\text{O}^+ \rightarrow \text{H} + \text{OH}$	$8.60 \times 10^{-14} T_n^{-0.5}$	[315, 316]

continued on next page

No.	Reaction	Rate Coefficient ^{a,b}	Ref.
103	$e^- + H^+(H_2O) \rightarrow H + H_2O$	$7.09 \times 10^{-14} T_n^{-0.5}$	[315, 317, 318]
104	$e^- + H^+(H_2O) \rightarrow OH + H_2$	$5.37 \times 10^{-14} T_n^{-0.5}$	[315, 317, 318]
105	$e^- + H^+(H_2O) \rightarrow OH + 2H$	$3.05 \times 10^{-13} T_n^{-0.5}$	[315, 317, 318]
106	$e^- + O_2^+(H_2O) \rightarrow O_2 + H_2O$	$7.22 \times 10^{-13} T_n^{-0.2}$	[319]
107	$e^- + H_2O^+(H_2O) \rightarrow H + OH + H_2O$	$9.63 \times 10^{-13} T_n^{-0.2}$	[319] ^m
108	$e^- + H^+(H_2O)_2 \rightarrow H + 2H_2O$	$1.87 \times 10^{-12} T_n^{-0.08}$	[320]
109	$e^- + H^+(H_2O)_3 \rightarrow H + 3H_2O$	$2.24 \times 10^{-12} T_n^{-0.08}$	[320]
110	$e^- + H^+(H_2O)_4 \rightarrow H + 4H_2O$	3.60×10^{-12}	[320]
111	$e^- + H^+(H_2O)_5 \rightarrow H + 5H_2O$	4.10×10^{-12}	[321]
112	$e^- + H^+(H_2O)_6 \rightarrow H + 6H_2O$	5.13×10^{-12}	[321]
113	$e^- + H^+(H_2O)_7 \rightarrow H + 7H_2O$	1.00×10^{-12}	[321]
114	$e^- + H^+(H_2O)_8 \rightarrow H + 8H_2O$	4.10×10^{-12}	As reaction 111
115	$e^- + H^+(H_2O)_9 \rightarrow H + 9H_2O$	4.10×10^{-12}	As reaction 111
116	$e^- + O^+ \rightarrow O(^1D)$	2.70×10^{-19}	[80, 319]
117	$e^- + O_2^+ \rightarrow 2O$	$3.79 \times 10^{-15} T_n^{-0.7}$	[322]
118	$e^- + O_2^+ \rightarrow O + O(^1D)$	$8.17 \times 10^{-15} T_n^{-0.7}$	[322]
119	$e^- + O_2^+ \rightarrow 2O(^1D)$	$5.85 \times 10^{-15} T_n^{-0.7}$	[322]
120	$e^- + O_3^+ \rightarrow 3O$	$2.07 \times 10^{-13} T_n^{-0.55}$	[80, 323]
121	$e^- + O_3^+ \rightarrow 2O + O(^1D)$	$6.69 \times 10^{-13} T_n^{-0.55}$	[80, 323]
122	$e^- + O_3^+ \rightarrow O + 2O(^1D)$	$1.55 \times 10^{-13} T_n^{-0.55}$	[80, 323]
123	$e^- + O_4^+ \rightarrow O + O(^1D) + O_2$	2.02×10^{-14}	[80, 314, 324]
124	$e^- + O_4^+ \rightarrow O(^1D) + O(^1S) + O_2$	1.35×10^{-14}	[80, 314, 324]

^a In $m^3 s^{-1}$ and $m^6 s^{-1}$ for two- and three-body processes, respectively.

^b $f(\epsilon)$ denotes rate coefficients that are calculated by the internal GlobalKin two-term Boltzmann equation solver using cross-sections obtained from the indicated literature.

^c Cross-sections are calculated from an expression in cited reference.

^d Calculated assuming a Maxwellian distribution function and cross-sections from the given reference.

^e Vibrational excitation cross-section included in cross section set for two-term Boltzmann solver. Vibrational states not simulated self-consistently in reaction kinetics.

^f Rotational excitation cross-section included in cross-section set for two-term Boltzmann solver. Rotational states not simulated self-consistently in reaction kinetics.

^g Cross-section estimated by shifting and scaling the corresponding cross-section for the ground state by the excitation threshold of the excited state.

^h Born-Bethe fit to data in the cited reference.

ⁱ Obtained from reverse process by detailed balance.

^j In the reference reaction rates were calculated using Bolsig+ [124] and cross sections obtained from the Morgan database [325] for a He+H₂O plasma.

^k Cross section assumed to be the same as that of CO.

¹ Value is approximated in reference based on cross section for electron impact dissociation of O₂.

^m Value is estimated in reference.

Table A.2: Ion-ion chemistry

No.	Reaction	Rate Coefficient ^{*,a}	Ref.
Three-body processes			
125	He ⁺ + O ⁻ + He → 2He + O	2.00 × 10 ⁻³⁷ T _n ^{-2.5}	[125] ^b
126	He ⁺ + O ₂ ⁻ + He → 2He + O ₂	2.00 × 10 ⁻³⁷ T _n ^{-2.5}	[125] ^b
127	He ⁺ + O ₃ ⁻ + He → 2He + O ₃	2.00 × 10 ⁻³⁷ T _n ^{-2.5}	[125] ^b
128	He ⁺ + O ₄ ⁻ + He → 2He + 2O ₂	2.00 × 10 ⁻³⁷ T _n ^{-2.5}	[125] ^b
129	He ⁺ + H ⁻ + He → 2He + H	2.00 × 10 ⁻³⁷ T _n ^{-2.5}	[125] ^b
130	He ⁺ + OH ⁻ + He → 2He + OH	2.00 × 10 ⁻³⁷ T _n ^{-2.5}	[125] ^b
131	He ⁺ + H ₂ O ₂ ⁻ + He → 2He + H ₂ O ₂	2.00 × 10 ⁻³⁷ T _n ^{-2.5}	[125] ^b
132	He ⁺ + OH ⁻ (H ₂ O) + He → 2He + H ₂ O + OH	2.00 × 10 ⁻³⁷ T _n ^{-2.5}	[125] ^b
133	He ⁺ + OH ⁻ (H ₂ O) ₂ + He → 2He + 2H ₂ O + OH	2.00 × 10 ⁻³⁷ T _n ^{-2.5}	[125] ^b
134	He ⁺ + OH ⁻ (H ₂ O) ₃ + He → 2He + 3H ₂ O + OH	2.00 × 10 ⁻³⁷ T _n ^{-2.5}	[125] ^b
135	He ₂ ⁺ + O ⁻ + He → 3He + O	2.00 × 10 ⁻³⁷ T _n ^{-2.5}	[125] ^b
136	He ₂ ⁺ + O ₂ ⁻ + He → 3He + O ₂	2.00 × 10 ⁻³⁷ T _n ^{-2.5}	[125] ^b
137	He ₂ ⁺ + O ₃ ⁻ + He → 3He + O ₃	2.00 × 10 ⁻³⁷ T _n ^{-2.5}	[125] ^b
138	He ₂ ⁺ + O ₄ ⁻ + He → 3He + 2O ₂	2.00 × 10 ⁻³⁷ T _n ^{-2.5}	[125] ^b
139	He ₂ ⁺ + H ⁻ + He → 3He + H	2.00 × 10 ⁻³⁷ T _n ^{-2.5}	[125] ^b
140	He ₂ ⁺ + OH ⁻ + He → 3He + OH	2.00 × 10 ⁻³⁷ T _n ^{-2.5}	[125] ^b
141	He ₂ ⁺ + H ₂ O ₂ ⁻ + He → 3He + H ₂ O ₂	2.00 × 10 ⁻³⁷ T _n ^{-2.5}	[125] ^b
142	He ₂ ⁺ + OH ⁻ (H ₂ O) + He → 3He + H ₂ O + OH	2.00 × 10 ⁻³⁷ T _n ^{-2.5}	[125] ^b
143	He ₂ ⁺ + OH ⁻ (H ₂ O) ₂ + He → 3He + 2H ₂ O + OH	2.00 × 10 ⁻³⁷ T _n ^{-2.5}	[125] ^b
144	He ₂ ⁺ + OH ⁻ (H ₂ O) ₃ + He → 3He + 3H ₂ O + OH	2.00 × 10 ⁻³⁷ T _n ^{-2.5}	[125] ^b
145	O ⁺ + O ⁻ + He → 2O + He	2.00 × 10 ⁻³⁷ T _n ^{-2.5}	[125] ^b
146	O ⁺ + O ₂ ⁻ + He → O + O ₂ + He	2.00 × 10 ⁻³⁷ T _n ^{-2.5}	[125] ^b
147	O ⁺ + O ₃ ⁻ + He → O + O ₃ + He	2.00 × 10 ⁻³⁷ T _n ^{-2.5}	[125] ^b
148	O ⁺ + O ₄ ⁻ + He → O + 2O ₂ + He	2.00 × 10 ⁻³⁷ T _n ^{-2.5}	[125] ^b
149	O ⁺ + H ⁻ + He → O + H + He	2.00 × 10 ⁻³⁷ T _n ^{-2.5}	[125] ^b
150	O ⁺ + OH ⁻ + He → O + OH + He	2.00 × 10 ⁻³⁷ T _n ^{-2.5}	[125] ^b
151	O ⁺ + H ₂ O ₂ ⁻ + He → O + H ₂ O ₂ + He	2.00 × 10 ⁻³⁷ T _n ^{-2.5}	[125] ^b

continued on next page

No.	Reaction	Rate Coefficient ^{*,a}	Ref.
152	$O^+ + OH^-(H_2O) + He \rightarrow O + H_2O + OH + He$	$2.00 \times 10^{-37} T_n^{-2.5}$	[125] ^b
153	$O^+ + OH^-(H_2O)_2 + He \rightarrow O + 2H_2O + OH + He$	$2.00 \times 10^{-37} T_n^{-2.5}$	[125] ^b
154	$O^+ + OH^-(H_2O)_3 + He \rightarrow O + 3H_2O + OH + He$	$2.00 \times 10^{-37} T_n^{-2.5}$	[125] ^b
155	$O_2^+ + O^- + He \rightarrow O_2 + O + He$	$2.00 \times 10^{-37} T_n^{-2.5}$	[125] ^b
156	$O_2^+ + O_2^- + He \rightarrow 2O_2 + He$	$2.00 \times 10^{-37} T_n^{-2.5}$	[125] ^b
157	$O_2^+ + O_3^- + He \rightarrow O_2 + O_3 + He$	$2.00 \times 10^{-37} T_n^{-2.5}$	[125] ^b
158	$O_2^+ + O_4^- + He \rightarrow 3O_2 + He$	$2.00 \times 10^{-37} T_n^{-2.5}$	[125] ^b
159	$O_2^+ + H^- + He \rightarrow O_2 + H + He$	$2.00 \times 10^{-37} T_n^{-2.5}$	[125] ^b
160	$O_2^+ + OH^- + He \rightarrow O_2 + OH + He$	$2.00 \times 10^{-37} T_n^{-2.5}$	[125] ^b
161	$O_2^+ + H_2O_2^- + He \rightarrow O_2 + H_2O_2 + He$	$2.00 \times 10^{-37} T_n^{-2.5}$	[125] ^b
162	$O_2^+ + OH^-(H_2O) + He \rightarrow O_2 + H_2O + OH + He$	$2.00 \times 10^{-37} T_n^{-2.5}$	[125] ^b
163	$O_2^+ + OH^-(H_2O)_2 + He \rightarrow O_2 + 2H_2O + OH + He$	$2.00 \times 10^{-37} T_n^{-2.5}$	[125] ^b
164	$O_2^+ + OH^-(H_2O)_3 + He \rightarrow O_2 + 3H_2O + OH + He$	$2.00 \times 10^{-37} T_n^{-2.5}$	[125] ^b
165	$O_3^+ + O^- + He \rightarrow O_3 + O + He$	$2.00 \times 10^{-37} T_n^{-2.5}$	[125] ^b
166	$O_3^+ + O_2^- + He \rightarrow O_3 + O_2 + He$	$2.00 \times 10^{-37} T_n^{-2.5}$	[125] ^b
167	$O_3^+ + O_3^- + He \rightarrow 2O_3 + He$	$2.00 \times 10^{-37} T_n^{-2.5}$	[125] ^b
168	$O_3^+ + O_4^- + He \rightarrow O_3 + 2O_2 + He$	$2.00 \times 10^{-37} T_n^{-2.5}$	[125] ^b
169	$O_3^+ + H^- + He \rightarrow O_3 + H + He$	$2.00 \times 10^{-37} T_n^{-2.5}$	[125] ^b
170	$O_3^+ + OH^- + He \rightarrow O_3 + OH + He$	$2.00 \times 10^{-37} T_n^{-2.5}$	[125] ^b
171	$O_3^+ + H_2O_2^- + He \rightarrow O_3 + H_2O_2 + He$	$2.00 \times 10^{-37} T_n^{-2.5}$	[125] ^b
172	$O_3^+ + OH^-(H_2O) + He \rightarrow O_3 + H_2O + OH + He$	$2.00 \times 10^{-37} T_n^{-2.5}$	[125] ^b
173	$O_3^+ + OH^-(H_2O)_2 + He \rightarrow O_3 + 2H_2O + OH + He$	$2.00 \times 10^{-37} T_n^{-2.5}$	[125] ^b
174	$O_3^+ + OH^-(H_2O)_3 + He \rightarrow O_3 + 3H_2O + OH + He$	$2.00 \times 10^{-37} T_n^{-2.5}$	[125] ^b
175	$O_4^+ + O^- + He \rightarrow 2O_2 + O + He$	$2.00 \times 10^{-37} T_n^{-2.5}$	[125] ^b
176	$O_4^+ + O_2^- + He \rightarrow 3O_2 + He$	$2.00 \times 10^{-37} T_n^{-2.5}$	[125] ^b
177	$O_4^+ + O_3^- + He \rightarrow 2O_2 + O_3 + He$	$2.00 \times 10^{-37} T_n^{-2.5}$	[125] ^b
178	$O_4^+ + O_4^- + He \rightarrow 4O_2 + He$	$2.00 \times 10^{-37} T_n^{-2.5}$	[125] ^b
179	$O_4^+ + H^- + He \rightarrow 2O_2 + H + He$	$2.00 \times 10^{-37} T_n^{-2.5}$	[125] ^b
180	$O_4^+ + OH^- + He \rightarrow 2O_2 + OH + He$	$2.00 \times 10^{-37} T_n^{-2.5}$	[125] ^b
181	$O_4^+ + H_2O_2^- + He \rightarrow 2O_2 + H_2O_2 + He$	$2.00 \times 10^{-37} T_n^{-2.5}$	[125] ^b
182	$O_4^+ + OH^-(H_2O) + He \rightarrow 2O_2 + H_2O + OH + He$	$2.00 \times 10^{-37} T_n^{-2.5}$	[125] ^b
183	$O_4^+ + OH^-(H_2O)_2 + He \rightarrow 2O_2 + 2H_2O + OH + He$	$2.00 \times 10^{-37} T_n^{-2.5}$	[125] ^b
184	$O_4^+ + OH^-(H_2O)_3 + He \rightarrow 2O_2 + 3H_2O + OH + He$	$2.00 \times 10^{-37} T_n^{-2.5}$	[125] ^b

continued on next page

No.	Reaction	Rate Coefficient ^{*,a}	Ref.
185	OH ⁺ + O ⁻ + He → OH + O + He	2.00×10 ⁻³⁷ T _n ^{-2.5}	[125] ^b
186	OH ⁺ + O ₂ ⁻ + He → OH + O ₂ + He	2.00×10 ⁻³⁷ T _n ^{-2.5}	[125] ^b
187	OH ⁺ + O ₃ ⁻ + He → OH + O ₃ + He	2.00×10 ⁻³⁷ T _n ^{-2.5}	[125] ^b
188	OH ⁺ + O ₄ ⁻ + He → OH + 2O ₂ + He	2.00×10 ⁻³⁷ T _n ^{-2.5}	[125] ^b
189	OH ⁺ + H ⁻ + He → OH + H + He	2.00×10 ⁻³⁷ T _n ^{-2.5}	[125] ^b
190	OH ⁺ + OH ⁻ + He → 2OH + He	2.00×10 ⁻³⁷ T _n ^{-2.5}	[125] ^b
191	OH ⁺ + H ₂ O ₂ ⁻ + He → OH + H ₂ O ₂ + He	2.00×10 ⁻³⁷ T _n ^{-2.5}	[125] ^b
192	OH ⁺ + OH ⁻ (H ₂ O) + He → 2OH + H ₂ O + He	2.00×10 ⁻³⁷ T _n ^{-2.5}	[125] ^b
193	OH ⁺ + OH ⁻ (H ₂ O) ₂ + He → 2OH + 2H ₂ O + He	2.00×10 ⁻³⁷ T _n ^{-2.5}	[125] ^b
194	OH ⁺ + OH ⁻ (H ₂ O) ₃ + He → 2OH + 3H ₂ O + He	2.00×10 ⁻³⁷ T _n ^{-2.5}	[125] ^b
195	H ₂ O ⁺ + O ⁻ + He → H ₂ O + O + He	2.00×10 ⁻³⁷ T _n ^{-2.5}	[125] ^b
196	H ₂ O ⁺ + O ₂ ⁻ + He → H ₂ O + O ₂ + He	2.00×10 ⁻³⁷ T _n ^{-2.5}	[125] ^b
197	H ₂ O ⁺ + O ₃ ⁻ + He → H ₂ O + O ₃ + He	2.00×10 ⁻³⁷ T _n ^{-2.5}	[125] ^b
198	H ₂ O ⁺ + O ₄ ⁻ + He → H ₂ O + 2O ₂ + He	2.00×10 ⁻³⁷ T _n ^{-2.5}	[125] ^b
199	H ₂ O ⁺ + H ⁻ + He → H ₂ O + H + He	2.00×10 ⁻³⁷ T _n ^{-2.5}	[125] ^b
200	H ₂ O ⁺ + OH ⁻ + He → H ₂ O + OH + He	2.00×10 ⁻³⁷ T _n ^{-2.5}	[125] ^b
201	H ₂ O ⁺ + H ₂ O ₂ ⁻ + He → H ₂ O + H ₂ O ₂ + He	2.00×10 ⁻³⁷ T _n ^{-2.5}	[125] ^b
202	H ₂ O ⁺ + OH ⁻ (H ₂ O) + He → 2H ₂ O + OH + He	2.00×10 ⁻³⁷ T _n ^{-2.5}	[125] ^b
203	H ₂ O ⁺ + OH ⁻ (H ₂ O) ₂ + He → 3H ₂ O + OH + He	2.00×10 ⁻³⁷ T _n ^{-2.5}	[125] ^b
204	H ₂ O ⁺ + OH ⁻ (H ₂ O) ₃ + He → 4H ₂ O + OH + He	2.00×10 ⁻³⁷ T _n ^{-2.5}	[125] ^b
205	H ⁺ (H ₂ O) + O ⁻ + He → OH + H ₂ O + He	2.00×10 ⁻³⁷ T _n ^{-2.5}	[125] ^b
206	H ⁺ (H ₂ O) + O ₂ ⁻ + He → H + H ₂ O + O ₂ + He	2.00×10 ⁻³⁷ T _n ^{-2.5}	[125] ^b
207	H ⁺ (H ₂ O) + O ₃ ⁻ + He → H + H ₂ O + O ₃ + He	2.00×10 ⁻³⁷ T _n ^{-2.5}	[125] ^b
208	H ⁺ (H ₂ O) + O ₄ ⁻ + He → H + H ₂ O + 2O ₂ + He	2.00×10 ⁻³⁷ T _n ^{-2.5}	[125] ^b
209	H ⁺ (H ₂ O) + H ⁻ + He → H ₂ + H ₂ O + He	2.00×10 ⁻³⁷ T _n ^{-2.5}	[125] ^b
210	H ⁺ (H ₂ O) + OH ⁻ + He → 2H ₂ O + He	2.00×10 ⁻³⁷ T _n ^{-2.5}	[125] ^b
211	H ⁺ (H ₂ O) + H ₂ O ₂ ⁻ + He → 2H ₂ O + OH + He	2.00×10 ⁻³⁷ T _n ^{-2.5}	[125] ^b
212	H ⁺ (H ₂ O) + OH ⁻ (H ₂ O) + He → 3H ₂ O + He	2.00×10 ⁻³⁷ T _n ^{-2.5}	[125] ^b
213	H ⁺ (H ₂ O) + OH ⁻ (H ₂ O) ₂ + He → 4H ₂ O + He	2.00×10 ⁻³⁷ T _n ^{-2.5}	[125] ^b
214	H ⁺ (H ₂ O) + OH ⁻ (H ₂ O) ₃ + He → 5H ₂ O + He	2.00×10 ⁻³⁷ T _n ^{-2.5}	[125] ^b
215	O ₂ ⁺ (H ₂ O) + O ⁻ + He → O ₂ + H ₂ O + O + He	2.00×10 ⁻³⁷ T _n ^{-2.5}	[125] ^b
216	O ₂ ⁺ (H ₂ O) + O ₂ ⁻ + He → 2O ₂ + H ₂ O + He	2.00×10 ⁻³⁷ T _n ^{-2.5}	[125] ^b
217	O ₂ ⁺ (H ₂ O) + O ₃ ⁻ + He → O ₂ + H ₂ O + O ₃ + He	2.00×10 ⁻³⁷ T _n ^{-2.5}	[125] ^b

continued on next page

No.	Reaction	Rate Coefficient ^{*,a}	Ref.
218	$O_2^+(H_2O) + O_4^- + He \rightarrow 3O_2 + H_2O + He$	$2.00 \times 10^{-37} T_n^{-2.5}$	[125] ^b
219	$O_2^+(H_2O) + H^- + He \rightarrow O_2 + H_2O + H + He$	$2.00 \times 10^{-37} T_n^{-2.5}$	[125] ^b
220	$O_2^+(H_2O) + OH^- + He \rightarrow O_2 + H_2O + OH + He$	$2.00 \times 10^{-37} T_n^{-2.5}$	[125] ^b
221	$O_2^+(H_2O) + H_2O_2^- + He \rightarrow O_2 + H_2O + H_2O_2 + He$	$2.00 \times 10^{-37} T_n^{-2.5}$	[125] ^b
222	$O_2^+(H_2O) + OH^-(H_2O) + He \rightarrow O_2 + 2H_2O + OH + He$	$2.00 \times 10^{-37} T_n^{-2.5}$	[125] ^b
223	$O_2^+(H_2O) + OH^-(H_2O)_2 + He \rightarrow O_2 + 3H_2O + OH + He$	$2.00 \times 10^{-37} T_n^{-2.5}$	[125] ^b
224	$O_2^+(H_2O) + OH^-(H_2O)_3 + He \rightarrow O_2 + 4H_2O + OH + He$	$2.00 \times 10^{-37} T_n^{-2.5}$	[125] ^b
225	$H_2O^+(H_2O) + O^- + He \rightarrow 2H_2O + O + He$	$2.00 \times 10^{-37} T_n^{-2.5}$	[125] ^b
226	$H_2O^+(H_2O) + O_2^- + He \rightarrow 2H_2O + O_2 + He$	$2.00 \times 10^{-37} T_n^{-2.5}$	[125] ^b
227	$H_2O^+(H_2O) + O_3^- + He \rightarrow 2H_2O + O_3 + He$	$2.00 \times 10^{-37} T_n^{-2.5}$	[125] ^b
228	$H_2O^+(H_2O) + O_4^- + He \rightarrow 2H_2O + 2O_2 + He$	$2.00 \times 10^{-37} T_n^{-2.5}$	[125] ^b
229	$H_2O^+(H_2O) + H^- + He \rightarrow 2H_2O + H + He$	$2.00 \times 10^{-37} T_n^{-2.5}$	[125] ^b
230	$H_2O^+(H_2O) + OH^- + He \rightarrow 2H_2O + OH + He$	$2.00 \times 10^{-37} T_n^{-2.5}$	[125] ^b
231	$H_2O^+(H_2O) + H_2O_2^- + He \rightarrow 2H_2O + H_2O_2 + He$	$2.00 \times 10^{-37} T_n^{-2.5}$	[125] ^b
232	$H_2O^+(H_2O) + OH^-(H_2O) + He \rightarrow 3H_2O + OH + He$	$2.00 \times 10^{-37} T_n^{-2.5}$	[125] ^b
233	$H_2O^+(H_2O) + OH^-(H_2O)_2 + He \rightarrow 4H_2O + OH + He$	$2.00 \times 10^{-37} T_n^{-2.5}$	[125] ^b
234	$H_2O^+(H_2O) + OH^-(H_2O)_3 + He \rightarrow 5H_2O + OH + He$	$2.00 \times 10^{-37} T_n^{-2.5}$	[125] ^b
235	$H^+(H_2O)_2 + O^- + He \rightarrow 2H_2O + OH + He$	$2.00 \times 10^{-37} T_n^{-2.5}$	[125] ^b
236	$H^+(H_2O)_2 + O_2^- + He \rightarrow 2H_2O + O_2 + H + He$	$2.00 \times 10^{-37} T_n^{-2.5}$	[125] ^b
237	$H^+(H_2O)_2 + O_3^- + He \rightarrow 2H_2O + O_3 + H + He$	$2.00 \times 10^{-37} T_n^{-2.5}$	[125] ^b
238	$H^+(H_2O)_2 + O_4^- + He \rightarrow 2H_2O + 2O_2 + H + He$	$2.00 \times 10^{-37} T_n^{-2.5}$	[125] ^b
239	$H^+(H_2O)_2 + H^- + He \rightarrow 2H_2O + H_2 + He$	$2.00 \times 10^{-37} T_n^{-2.5}$	[125] ^b
240	$H^+(H_2O)_2 + OH^- + He \rightarrow 3H_2O + He$	$2.00 \times 10^{-37} T_n^{-2.5}$	[125] ^b
241	$H^+(H_2O)_2 + H_2O_2^- + He \rightarrow 3H_2O + OH + He$	$2.00 \times 10^{-37} T_n^{-2.5}$	[125] ^b
242	$H^+(H_2O)_2 + OH^-(H_2O) + He \rightarrow 4H_2O + He$	$2.00 \times 10^{-37} T_n^{-2.5}$	[125] ^b
243	$H^+(H_2O)_2 + OH^-(H_2O)_2 + He \rightarrow 5H_2O + He$	$2.00 \times 10^{-37} T_n^{-2.5}$	[125] ^b
244	$H^+(H_2O)_2 + OH^-(H_2O)_3 + He \rightarrow 6H_2O + He$	$2.00 \times 10^{-37} T_n^{-2.5}$	[125] ^b
245	$H^+(H_2O)_3 + O^- + He \rightarrow 3H_2O + OH + He$	$2.00 \times 10^{-37} T_n^{-2.5}$	[125] ^b
246	$H^+(H_2O)_3 + O_2^- + He \rightarrow 3H_2O + O_2 + H + He$	$2.00 \times 10^{-37} T_n^{-2.5}$	[125] ^b
247	$H^+(H_2O)_3 + O_3^- + He \rightarrow 3H_2O + O_3 + H + He$	$2.00 \times 10^{-37} T_n^{-2.5}$	[125] ^b
248	$H^+(H_2O)_3 + O_4^- + He \rightarrow 3H_2O + 2O_2 + H + He$	$2.00 \times 10^{-37} T_n^{-2.5}$	[125] ^b
249	$H^+(H_2O)_3 + H^- + He \rightarrow 3H_2O + H_2 + He$	$2.00 \times 10^{-37} T_n^{-2.5}$	[125] ^b
250	$H^+(H_2O)_3 + OH^- + He \rightarrow 4H_2O + He$	$2.00 \times 10^{-37} T_n^{-2.5}$	[125] ^b

continued on next page

No.	Reaction	Rate Coefficient ^{*,a}	Ref.
284	H ⁺ (H ₂ O) ₆ + OH ⁻ (H ₂ O) ₄ + He → 10H ₂ O + He	2.00×10 ⁻³⁷ T _n ^{-2.5}	[125] ^b
285	H ⁺ (H ₂ O) ₇ + O ⁻ + He → 7H ₂ O + OH + He	2.00×10 ⁻³⁷ T _n ^{-2.5}	[125] ^b
286	H ⁺ (H ₂ O) ₇ + O ₂ ⁻ + He → 7H ₂ O + O ₂ + H + He	2.00×10 ⁻³⁷ T _n ^{-2.5}	[125] ^b
287	H ⁺ (H ₂ O) ₇ + O ₃ ⁻ + He → 7H ₂ O + O ₃ + H + He	2.00×10 ⁻³⁷ T _n ^{-2.5}	[125] ^b
288	H ⁺ (H ₂ O) ₇ + O ₄ ⁻ + He → 7H ₂ O + 2O ₂ + H + He	2.00×10 ⁻³⁷ T _n ^{-2.5}	[125] ^b
289	H ⁺ (H ₂ O) ₇ + H ⁻ + He → 7H ₂ O + H ₂ + He	2.00×10 ⁻³⁷ T _n ^{-2.5}	[125] ^b
290	H ⁺ (H ₂ O) ₇ + OH ⁻ + He → 8H ₂ O + He	2.00×10 ⁻³⁷ T _n ^{-2.5}	[125] ^b
291	H ⁺ (H ₂ O) ₇ + H ₂ O ₂ ⁻ + He → 8H ₂ O + OH + He	2.00×10 ⁻³⁷ T _n ^{-2.5}	[125] ^b
292	H ⁺ (H ₂ O) ₇ + OH ⁻ (H ₂ O) + He → 9H ₂ O + He	2.00×10 ⁻³⁷ T _n ^{-2.5}	[125] ^b
293	H ⁺ (H ₂ O) ₇ + OH ⁻ (H ₂ O) ₂ + He → 10H ₂ O + He	2.00×10 ⁻³⁷ T _n ^{-2.5}	[125] ^b
294	H ⁺ (H ₂ O) ₇ + OH ⁻ (H ₂ O) ₃ + He → 11H ₂ O + He	2.00×10 ⁻³⁷ T _n ^{-2.5}	[125] ^b
295	H ⁺ (H ₂ O) ₈ + O ⁻ + He → 8H ₂ O + OH + He	2.00×10 ⁻³⁷ T _n ^{-2.5}	[125] ^b
296	H ⁺ (H ₂ O) ₈ + O ₂ ⁻ + He → 8H ₂ O + O ₂ + H + He	2.00×10 ⁻³⁷ T _n ^{-2.5}	[125] ^b
297	H ⁺ (H ₂ O) ₈ + O ₃ ⁻ + He → 8H ₂ O + O ₃ + H + He	2.00×10 ⁻³⁷ T _n ^{-2.5}	[125] ^b
298	H ⁺ (H ₂ O) ₈ + O ₄ ⁻ + He → 8H ₂ O + 2O ₂ + H + He	2.00×10 ⁻³⁷ T _n ^{-2.5}	[125] ^b
299	H ⁺ (H ₂ O) ₈ + H ⁻ + He → 8H ₂ O + H ₂ + He	2.00×10 ⁻³⁷ T _n ^{-2.5}	[125] ^b
300	H ⁺ (H ₂ O) ₈ + OH ⁻ + He → 9H ₂ O + He	2.00×10 ⁻³⁷ T _n ^{-2.5}	[125] ^b
301	H ⁺ (H ₂ O) ₈ + H ₂ O ₂ ⁻ + He → 9H ₂ O + OH + He	2.00×10 ⁻³⁷ T _n ^{-2.5}	[125] ^b
302	H ⁺ (H ₂ O) ₈ + OH ⁻ (H ₂ O) + He → 10H ₂ O + He	2.00×10 ⁻³⁷ T _n ^{-2.5}	[125] ^b
303	H ⁺ (H ₂ O) ₈ + OH ⁻ (H ₂ O) ₂ + He → 11H ₂ O + He	2.00×10 ⁻³⁷ T _n ^{-2.5}	[125] ^b
304	H ⁺ (H ₂ O) ₈ + OH ⁻ (H ₂ O) ₃ + He → 12H ₂ O + He	2.00×10 ⁻³⁷ T _n ^{-2.5}	[125] ^b
305	H ⁺ (H ₂ O) ₉ + O ⁻ + He → 9H ₂ O + OH + He	2.00×10 ⁻³⁷ T _n ^{-2.5}	[125] ^b
306	H ⁺ (H ₂ O) ₉ + O ₂ ⁻ + He → 9H ₂ O + O ₂ + H + He	2.00×10 ⁻³⁷ T _n ^{-2.5}	[125] ^b
307	H ⁺ (H ₂ O) ₉ + O ₃ ⁻ + He → 9H ₂ O + O ₃ + H + He	2.00×10 ⁻³⁷ T _n ^{-2.5}	[125] ^b
308	H ⁺ (H ₂ O) ₉ + O ₄ ⁻ + He → 9H ₂ O + 2O ₂ + H + He	2.00×10 ⁻³⁷ T _n ^{-2.5}	[125] ^b
309	H ⁺ (H ₂ O) ₉ + H ⁻ + He → 9H ₂ O + H ₂ + He	2.00×10 ⁻³⁷ T _n ^{-2.5}	[125] ^b
310	H ⁺ (H ₂ O) ₉ + OH ⁻ + He → 10H ₂ O + He	2.00×10 ⁻³⁷ T _n ^{-2.5}	[125] ^b
311	H ⁺ (H ₂ O) ₉ + H ₂ O ₂ ⁻ + He → 10H ₂ O + OH + He	2.00×10 ⁻³⁷ T _n ^{-2.5}	[125] ^b
312	H ⁺ (H ₂ O) ₉ + OH ⁻ (H ₂ O) + He → 11H ₂ O + He	2.00×10 ⁻³⁷ T _n ^{-2.5}	[125] ^b
313	H ⁺ (H ₂ O) ₉ + OH ⁻ (H ₂ O) ₂ + He → 12H ₂ O + He	2.00×10 ⁻³⁷ T _n ^{-2.5}	[125] ^b
314	H ⁺ (H ₂ O) ₉ + OH ⁻ (H ₂ O) ₃ + He → 13H ₂ O + He	2.00×10 ⁻³⁷ T _n ^{-2.5}	[125] ^b

* T_n = T_g/300.^a In m⁶ s⁻¹.^b Value estimated in reference.

Table A.3: Ion-neutral chemistry

No.	Reaction	Rate Coefficient ^{*,a}	Ref.
Two-body processes—positive ions			
315	He ⁺ + OH → He + O ⁺ + H	1.10×10 ⁻¹⁵ T _n ^{-0.5}	[315, 326]
316	He ⁺ + H ₂ O → He + OH ⁺ + H	2.86×10 ⁻¹⁶	[315, 327]
317	He ⁺ + H ₂ O → He + H ₂ O ⁺	6.05×10 ⁻¹⁷	[315, 327]
318	He ⁺ + O → He + O ⁺	5.80×10 ⁻¹⁶	[80, 328–330]
319	He ⁺ + O(¹ D) → He + O ⁺	5.80×10 ⁻¹⁶	[80, 328–330]
320	He ⁺ + O(¹ S) → He + O ⁺	5.80×10 ⁻¹⁶	[80, 328–330]
321	He ⁺ + O ₂ → He + O ⁺ + O	1.10×10 ⁻¹⁵	[315, 331]
322	He ⁺ + O ₂ → He + O ₂ ⁺	3.30×10 ⁻¹⁷	[315, 331]
323	He ⁺ + O ₂ (a ¹ Δ) → He + O ⁺ + O	1.10×10 ⁻¹⁵	As reaction 321
324	He ⁺ + O ₂ (a ¹ Δ) → He + O ₂ ⁺	3.30×10 ⁻¹⁷	As reaction 322
325	He ⁺ + O ₂ (b ¹ Σ) → He + O ⁺ + O	1.10×10 ⁻¹⁵	As reaction 321
326	He ⁺ + O ₂ (b ¹ Σ) → He + O ₂ ⁺	3.30×10 ⁻¹⁷	As reaction 322
327	He ⁺ + O ₃ → He + O ₂ + O ⁺	2.20×10 ⁻¹⁵	[80, 328–330]
328	He ₂ ⁺ + OH → 2He + O ⁺ + H	1.10×10 ⁻¹⁵	As reaction 315
329	He ₂ ⁺ + H ₂ O → 2He + H ₂ O ⁺	6.05×10 ⁻¹⁷	As reaction 317
330	He ₂ ⁺ + H ₂ O → 2He + OH ⁺ + H	2.86×10 ⁻¹⁶	As reaction 316
331	He ₂ ⁺ + O → 2He + O ⁺	9.00×10 ⁻¹⁶	[80, 328–330]
332	He ₂ ⁺ + O(¹ D) → 2He + O ⁺	9.00×10 ⁻¹⁶	[80, 328–330]
333	He ₂ ⁺ + O(¹ S) → 2He + O ⁺	9.00×10 ⁻¹⁶	[80, 328–330]
334	He ₂ ⁺ + O ₂ → 2He + O + O ⁺	1.00×10 ⁻¹⁶	[80, 332]
335	He ₂ ⁺ + O ₂ → 2He + O ₂ ⁺	9.00×10 ⁻¹⁶	[80, 332]
336	He ₂ ⁺ + O ₂ (a ¹ Δ) → 2He + O ₂ ⁺	1.20×10 ⁻¹⁵	[80, 328–330]
337	He ₂ ⁺ + O ₂ (b ¹ Σ) → 2He + O ₂ ⁺	1.20×10 ⁻¹⁵	[80, 328–330]
338	He ₂ ⁺ + O ₃ → 2He + O ⁺ + O ₂	1.60×10 ⁻¹⁵	[80, 328–330]
339	OH ⁺ + H ₂ → H ₂ O ⁺ + H	1.01×10 ⁻¹⁵	[315, 333]
340	OH ⁺ + OH → H ₂ O ⁺ + O	7.00×10 ⁻¹⁶ T _n ^{-0.5}	[315, 326]
341	OH ⁺ + H ₂ O → H ₂ O ⁺ + OH	1.56×10 ⁻¹⁵	[334]
342	OH ⁺ + H ₂ O → H ⁺ (H ₂ O) + O	1.27×10 ⁻¹⁵	[334]
343	OH ⁺ + O → O ₂ ⁺ + H	7.10×10 ⁻¹⁶	[315, 326]
344	OH ⁺ + O(¹ D) → O ₂ ⁺ + H	7.10×10 ⁻¹⁶	As reaction 343

continued on next page

No.	Reaction	Rate Coefficient ^{*,a}	Ref.
345	OH ⁺ + O(¹ S) → O ₂ ⁺ + H	7.10×10 ⁻¹⁶	As reaction 343
346	OH ⁺ + O ₂ → O ₂ ⁺ + OH	5.90×10 ⁻¹⁶	[315, 333]
347	OH ⁺ + O ₂ (a ¹ Δ) → O ₂ ⁺ + OH	5.90×10 ⁻¹⁶	As reaction 346
348	OH ⁺ + O ₂ (b ¹ Σ) → O ₂ ⁺ + OH	5.90×10 ⁻¹⁶	As reaction 346
349	OH ⁺ + O ₃ → O ₃ ⁺ + OH	1.00×10 ⁻¹⁷	Estimated
350	H ₂ O ⁺ + H ₂ → H ⁺ (H ₂ O) + H	6.40×10 ⁻¹⁶	[315, 335]
351	H ₂ O ⁺ + OH → O + H ⁺ (H ₂ O)	6.90×10 ⁻¹⁶ T _n ^{-0.5}	[315, 326]
352	H ₂ O ⁺ + H ₂ O → OH + H ⁺ (H ₂ O)	2.05×10 ⁻¹⁵	[334]
353	H ₂ O ⁺ + O → H ₂ + O ₂ ⁺	4.00×10 ⁻¹⁷	[315, 336]
354	H ₂ O ⁺ + O(¹ D) → H ₂ + O ₂ ⁺	4.00×10 ⁻¹⁷	As reaction 353
355	H ₂ O ⁺ + O(¹ S) → H ₂ + O ₂ ⁺	4.00×10 ⁻¹⁷	As reaction 353
356	H ₂ O ⁺ + O ₂ → H ₂ O + O ₂ ⁺	3.30×10 ⁻¹⁶	[337]
357	H ₂ O ⁺ + O ₂ (a ¹ Δ) → H ₂ O + O ₂ ⁺	3.30×10 ⁻¹⁶	As reaction 356
358	H ₂ O ⁺ + O ₂ (b ¹ Σ) → H ₂ O + O ₂ ⁺	3.30×10 ⁻¹⁶	As reaction 356
359	O ₂ ⁺ (H ₂ O) (+ He) → O ₂ ⁺ + H ₂ O (+ He)	Effective	[338] ^{c,d}
360	O ₂ ⁺ (H ₂ O) + H ₂ O → O ₂ + H ₂ O ⁺ (H ₂ O)	1.00×10 ⁻¹⁵	[319] ^b
361	H ₂ O ⁺ (H ₂ O) + H ₂ O → OH + H ⁺ (H ₂ O) ₂	1.40×10 ⁻¹⁵	[319]
362	H ⁺ (H ₂ O) ₂ (+ He) → H ⁺ (H ₂ O) + H ₂ O (+ He)	Effective	[338] ^{c,d}
363	H ⁺ (H ₂ O) ₃ (+ He) → H ⁺ (H ₂ O) ₂ + H ₂ O (+ He)	Effective	[338] ^{c,d}
364	H ⁺ (H ₂ O) ₄ (+ He) → H ⁺ (H ₂ O) ₃ + H ₂ O (+ He)	Effective	[338] ^{c,d}
365	H ⁺ (H ₂ O) ₅ (+ He) → H ⁺ (H ₂ O) ₄ + H ₂ O (+ He)	Effective	[338] ^{c,d}
366	H ⁺ (H ₂ O) ₆ (+ He) → H ⁺ (H ₂ O) ₅ + H ₂ O (+ He)	Effective	[338] ^{c,d}
367	H ⁺ (H ₂ O) ₇ (+ He) → H ⁺ (H ₂ O) ₆ + H ₂ O (+ He)	Effective	[338] ^{c,d}
368	H ⁺ (H ₂ O) ₈ (+ He) → H ⁺ (H ₂ O) ₇ + H ₂ O (+ He)	Effective	[338] ^e
369	H ⁺ (H ₂ O) ₉ (+ He) → H ⁺ (H ₂ O) ₈ + H ₂ O (+ He)	Effective	[338] ^e
370	O ⁺ + H ₂ → OH ⁺ + H	1.70×10 ⁻¹⁵	[315, 339]
371	O ⁺ + OH → OH ⁺ + O	3.60×10 ⁻¹⁵ T _n ^{-0.5}	[315, 326]
372	O ⁺ + OH → O ₂ ⁺ + H	3.60×10 ⁻¹⁵ T _n ^{-0.5}	[315, 326]
373	O ⁺ + H ₂ O → O + H ₂ O ⁺	3.20×10 ⁻¹⁵	[339]
374	O ⁺ + O ₂ → O + O ₂ ⁺	2.00×10 ⁻¹⁷ T _n ^{-0.4}	[340]
375	O ⁺ + O ₃ → O ₂ + O ₂ ⁺	1.20×10 ⁻¹⁵	[80, 328–330]
376	O ₂ ⁺ + He(² 3S) → He + O + O ⁺	8.20×10 ⁻¹⁵	[80, 328, 329, 341]
377	O ₃ ⁺ + He(² 3S) → He + O + O ₂ ⁺	8.10×10 ⁻¹⁵	[80, 328, 329, 341]

continued on next page

No.	Reaction	Rate Coefficient ^{*,a}	Ref.
378	$O_3^+ + O(^1D) \rightarrow 2O + O_2^+$	3.00×10^{-16}	[80, 328–330]
379	$O_3^+ + O(^1S) \rightarrow 2O + O_2^+$	2.00×10^{-16}	[80, 328–330]
380	$O_3^+ + O_2 \rightarrow O_2^+ + O_3$	6.70×10^{-16}	[80, 328, 329, 342]
381	$O_4^+ + He \rightarrow O_2^+ + O_2 + He$	3.40×10^{-20}	[80, 332]
382	$O_4^+ + He(2^3S) \rightarrow He + O_2 + O_2^+$	8.00×10^{-15}	[80, 328, 329, 341]
383	$O_4^+ + H_2O \rightarrow O_2 + O_2^+(H_2O)$	1.70×10^{-15}	[343]
384	$O_4^+ + O \rightarrow O_3 + O_2^+$	3.00×10^{-16}	[319]
385	$O_4^+ + O(^1D) \rightarrow O + O_2 + O_2^+$	3.00×10^{-16}	[80, 328, 329, 344]
386	$O_4^+ + O(^1D) \rightarrow O_3 + O_2^+$	3.00×10^{-16}	[80, 328, 329, 344]
387	$O_4^+ + O(^1S) \rightarrow O + O_2 + O_2^+$	3.00×10^{-16}	[80, 328, 329, 344]
388	$O_4^+ + O(^1S) \rightarrow O_2^+ + O_3$	3.00×10^{-16}	[80, 328, 329, 344]
389	$O_4^+ + O_2 \rightarrow 2O_2 + O_2^+$	$1.00 \times 10^{-11} T_n^{-4.2} e^{-5400/T_g}$	[80, 319, 332]
390	$O_4^+ + O_2(a^1\Delta) \rightarrow 2O_2 + O_2^+$	6.00×10^{-16}	[80, 328–330]
391	$O_4^+ + O_2(b^1\Sigma) \rightarrow 2O_2 + O_2^+$	6.00×10^{-16}	[80]
Two-body processes—negative ions			
392	$H^- + He \rightarrow He + H + e^-$	$4.43 \times 10^{-17} e^{-5829/T_g}$	[345]
393	$H^- + H \rightarrow H_2 + e^-$	$4.32 \times 10^{-15} T_n^{-0.39} e^{-39.4/T_g}$	[346]
394	$H^- + H_2O \rightarrow OH^- + H_2$	4.80×10^{-15}	[315, 347]
395	$H^- + O \rightarrow OH + e^-$	1.00×10^{-15}	[326]
396	$H^- + OH \rightarrow H_2O + e^-$	1.00×10^{-16}	[326]
397	$OH^- + H \rightarrow H_2O + e^-$	1.40×10^{-15}	[315, 348]
398	$H_2O_2^- + H_2O \rightarrow OH^-(H_2O) + OH$	1.00×10^{-17}	[349] ^f
399	$O^- + He \rightarrow e^- + He + O$	$2.50 \times 10^{-24} T_n^{0.6}$	[80, 350, 351]
400	$O^- + He(2^3S) \rightarrow 2e^- + He + O^+$	8.70×10^{-15}	[80, 328, 329, 341]
401	$O^- + H_2O \rightarrow OH^- + OH$	1.40×10^{-15}	[304]
402	$O^- + O \rightarrow e^- + O_2$	$2.30 \times 10^{-16} T_n^{-1.3}$	[352, 353]
403	$O^- + O(^1D) \rightarrow 2O + e^-$	7.40×10^{-16}	[80, 328, 329, 344]
404	$O^- + O(^1S) \rightarrow e^- + 2O$	7.40×10^{-16}	[80, 328, 329, 344]
405	$O^- + O_2 \rightarrow O_3 + e^-$	1.00×10^{-18}	[80, 332]
406	$O^- + O_2 \rightarrow O_2^- + O$	1.00×10^{-18}	[80, 332]
407	$O^- + O_2(a^1\Delta) \rightarrow O_2^- + O$	$7.90 \times 10^{-16} e^{-890/T_g}$	[80, 354]
408	$O^- + O_2(a^1\Delta) \rightarrow O_3 + e^-$	6.10×10^{-16}	[80, 354]

continued on next page

No.	Reaction	Rate Coefficient ^{*,a}	Ref.
409	$O^- + O_2(b^1\Sigma) \rightarrow O_2^- + O$	$7.90 \times 10^{-16} e^{-890/T_g}$	As reaction 407
410	$O^- + O_2(b^1\Sigma) \rightarrow O_3 + e^-$	6.10×10^{-16}	As reaction 408
411	$O^- + O_3 \rightarrow e^- + 2O_2$	3.00×10^{-16}	[80, 332, 355]
412	$O^- + O_3 \rightarrow O + O_3^-$	2.00×10^{-16}	[80, 332, 355]
413	$O^- + O_3 \rightarrow O_2^- + O_2$	1.00×10^{-17}	[80, 332, 355]
414	$O_2^- + He \rightarrow e^- + He + O_2$	$3.90 \times 10^{-16} e^{-7400/T_g}$	[80, 356]
415	$O_2^- + He(2^3S) \rightarrow 2e^- + He + O_2^+$	8.30×10^{-15}	[80, 328, 329, 341]
416	$O_2^- + O \rightarrow O^- + O_2$	$8.50 \times 10^{-17} T_n^{-1.8}$	[353] ^g
417	$O_2^- + O \rightarrow O_3 + e^-$	$8.50 \times 10^{-17} T_n^{-1.8}$	[353] ^g
418	$O_2^- + O(^1D) \rightarrow e^- + O_3$	$8.50 \times 10^{-17} T_n^{-1.8}$	[80]
419	$O_2^- + O(^1D) \rightarrow O^- + O_2$	$8.50 \times 10^{-17} T_n^{-1.8}$	[80]
420	$O_2^- + O(^1S) \rightarrow O^- + O_2$	$8.50 \times 10^{-17} T_n^{-1.8}$	[80]
421	$O_2^- + O(^1S) \rightarrow e^- + O_3$	$8.50 \times 10^{-17} T_n^{-1.8}$	[80]
422	$O_2^- + O_2 \rightarrow e^- + 2O_2$	$2.70 \times 10^{-16} T_n^{0.5} e^{-5590/T_g}$	[319]
423	$O_2^- + O_2 \rightarrow O + O_3^-$	3.50×10^{-21}	[332]
424	$O_2^- + O_2(a^1\Delta) \rightarrow e^- + 2O_2$	7.00×10^{-16}	[354]
425	$O_2^- + O_2(b^1\Sigma) \rightarrow e^- + 2O_2$	7.00×10^{-16}	[80]
426	$O_2^- + O_3 \rightarrow O_2 + O_3^-$	6.00×10^{-16}	[332]
427	$O_3^- + He(2^3S) \rightarrow 2e^- + He + O + O_2^+$	8.10×10^{-15}	[80, 328, 329, 341]
428	$O_3^- + O \rightarrow e^- + 2O_2$	1.00×10^{-17}	[319]
429	$O_3^- + O \rightarrow O_2 + O_2^-$	2.50×10^{-16}	[332]
430	$O_3^- + O(^1D) \rightarrow O + O_2 + O^-$	3.00×10^{-16}	[80, 328–330]
431	$O_3^- + O(^1D) \rightarrow O + O_3 + e^-$	3.00×10^{-16}	[80, 328, 329, 344]
432	$O_3^- + O(^1S) \rightarrow e^- + O + O_3$	2.00×10^{-16}	[80, 328–330]
433	$O_3^- + O(^1S) \rightarrow 2O + O_2^-$	2.00×10^{-16}	[80, 328–330]
434	$O_3^- + O(^1S) \rightarrow O + O^- + O_2$	2.00×10^{-16}	[80, 328–330]
435	$O_3^- + O_2(b^1\Sigma) \rightarrow O^- + 2O_2$	$6.70 \times 10^{-16} e^{-1300/T_g}$	[80, 328–330]
436	$O_3^- + O_3 \rightarrow e^- + 3O_2$	8.50×10^{-16}	[80, 328–330]
437	$O_4^- + He \rightarrow He + O_2 + O_2^-$	$2.20 \times 10^{-11} T_n^{-1} e^{-6300/T_g}$	[319]
438	$O_4^- + He(2^3S) \rightarrow 2e^- + He + O_2 + O_2^+$	8.00×10^{-15}	[80, 328, 329, 341]
439	$O_4^- + O \rightarrow O_2 + O_3^-$	4.00×10^{-16}	[319, 332]
440	$O_4^- + O(^1D) \rightarrow e^- + O + 2O_2$	2.00×10^{-16}	[80, 328–330]
441	$O_4^- + O(^1D) \rightarrow O + O_2 + O_2^-$	2.00×10^{-16}	[80, 328–330]

continued on next page

No.	Reaction	Rate Coefficient ^{*,a}	Ref.
442	$O_4^- + O(^1D) \rightarrow 2O_2 + O^-$	2.00×10^{-16}	[80, 328–330]
443	$O_4^- + O(^1S) \rightarrow e^- + O + 2O_2$	2.00×10^{-16}	[80, 328–330]
444	$O_4^- + O(^1S) \rightarrow O + O_2 + O_2^-$	2.00×10^{-16}	[80, 328–330]
445	$O_4^- + O(^1S) \rightarrow O^- + 2O_2$	2.00×10^{-16}	[80, 328–330]
446	$O_4^- + O_2 \rightarrow 2O_2 + O_2^-$	$2.20 \times 10^{-11} T_n^{-1} e^{-6300/T_g}$	[319]
447	$O_4^- + O_2(a^1\Delta) \rightarrow 3O_2 + e^-$	3.00×10^{-16}	[80, 328–330]
448	$O_4^- + O_2(a^1\Delta) \rightarrow 2O_2 + O_2^-$	3.00×10^{-16}	[80, 328–330]
449	$O_4^- + O_2(b^1\Sigma) \rightarrow e^- + 3O_2$	3.00×10^{-16}	[80, 328–330]
450	$O_4^- + O_2(b^1\Sigma) \rightarrow 2O_2 + O_2^-$	3.00×10^{-16}	[80, 328–330]
451	$O_4^- + O_3 \rightarrow 2O_2 + O_3^-$	8.00×10^{-16}	[80, 328–330]
Three-body processes—positive ions			
452	$He^+ + 2He \rightarrow He + He_2^+$	$1.30 \times 10^{-43} T_n^{-0.6}$	[357]
453	$H^+(H_2O) + H_2O (+ He) \rightarrow H^+(H_2O)_2 (+ He)$	Effective	[338, 358] ^{c,d}
454	$H^+(H_2O)_2 + H_2O (+ He) \rightarrow H^+(H_2O)_3 (+ He)$	Effective	[338, 358] ^{c,d}
455	$H^+(H_2O)_3 + H_2O (+ He) \rightarrow H^+(H_2O)_4 (+ He)$	Effective	[338, 358] ^{c,d}
456	$H^+(H_2O)_4 + H_2O (+ He) \rightarrow H^+(H_2O)_5 (+ He)$	Effective	[338, 358] ^{c,d}
457	$H^+(H_2O)_5 + H_2O (+ He) \rightarrow H^+(H_2O)_6 (+ He)$	Effective	[338, 358] ^{c,d}
458	$H^+(H_2O)_6 + H_2O (+ He) \rightarrow H^+(H_2O)_7 (+ He)$	Effective	[338, 358] ^{c,d}
459	$H^+(H_2O)_7 + H_2O (+ He) \rightarrow H^+(H_2O)_8 (+ He)$	Effective	[338] ^e
460	$H^+(H_2O)_8 + H_2O (+ He) \rightarrow H^+(H_2O)_9 (+ He)$	Effective	[338] ^e
461	$He + O_2 + O_2^+ \rightarrow He + O_4^+$	$5.50 \times 10^{-43} T_n^{-2.7}$	[332, 359]
462	$O_2^+ + H_2O (+ He) \rightarrow O_2^+(H_2O) (+ He)$	Effective	[338] ^{c,d}
463	$He + O + O^+ \rightarrow He + O_2^+$	$5.50 \times 10^{-43} T_n^{-2.7}$	[80]
Three-body processes—negative ions			
464	$OH^- + H_2O + He \rightarrow OH^-(H_2O) + He$	8.00×10^{-42}	[360] ^h
465	$OH^-(H_2O) + H_2O + He \rightarrow OH^-(H_2O)_2 + He$	2.50×10^{-43}	[360] ^h
466	$OH^-(H_2O)_2 + H_2O + He \rightarrow OH^-(H_2O)_3 + He$	1.50×10^{-43}	[360] ^h
467	$O^- + H_2O + He \rightarrow H_2O_2^- + He$	1.30×10^{-40}	[349]
468	$O^- + O_2 + He \rightarrow He + O_3^-$	$3.70 \times 10^{-43} T_n^{-1}$	[319, 361]
469	$He + O_2 + O_2^- \rightarrow He + O_4^-$	$1.20 \times 10^{-43} T_n^{-2.7}$	[319, 361]

* $T_n = T_g/300$.

^a In s^{-1} , $m^3 s^{-1}$ and $m^6 s^{-1}$ for one-, two- and three-body reactions, respectively.

^b Value estimated in reference.

^c Effective rate coefficients calculated from pressure dependent rates as described by Sieck *et al* [338] for 1 atm and a Temperature range 280–350 K.

^d Background gas is (humid) air in given reference. Gas efficiency factors for He background gas are not known for these reactions, but could potentially change calculated reaction rate coefficients if taken into account.

^e Rate coefficients are estimated by extrapolating the coefficients k_0^{300} and A given by Sieck *et al* [338] using an exponential fit, and using constant values $n = 16$, $B = 5000$, and $k_L = 10^{-24}$.

^f Value is listed as a lower limit in reference.

^g Estimated branching ratio.

^h Third body is H₂O in reference.

Table A.4: Neutral chemistry

No.	Reaction	Rate Coefficient ^{*,a}	Ref.
Two-body processes			
470	He + O(¹ D) → He + O	7.00×10^{-22}	[362] ^b
471	He + O(¹ S) → He + O	7.00×10^{-22}	As reaction 470
472	He + O ₂ (a ¹ Δ) → He + O ₂	5.00×10^{-27}	[363]
473	He + O ₂ (b ¹ Σ) → He + O ₂ (a ¹ Δ)	$1.00 \times 10^{-23} T_n^{0.5}$	[364] ^c
474	He + O ₃ → He + O + O ₂	$5.61 \times 10^{-16} e^{-11400/T_g}$	[361]
475	2He(2 ³ S) → He + He ⁺ + e ⁻	4.50×10^{-16}	[64, 294]
476	2He(2 ³ S) → He ₂ ⁺ + e ⁻	1.05×10^{-15}	[64, 294]
477	He(2 ³ S) + He ₂ [*] → 2He + He ⁺ + e ⁻	5.00×10^{-16}	[294] ^d
478	He(2 ³ S) + He ₂ [*] → He + He ₂ ⁺ + e ⁻	2.00×10^{-15}	[294] ^d
479	He(2 ³ S) + H ₂ O → He + OH ⁺ + H + e ⁻	1.39×10^{-16}	[365, 366] ^e
480	He(2 ³ S) + OH → OH ⁺ + He + e ⁻	6.08×10^{-16}	As reaction 481
481	He(2 ³ S) + H ₂ O → He + H ₂ O ⁺ + e ⁻	6.08×10^{-16}	[365, 366] ^e
482	He(2 ³ S) + H ₂ O ₂ → He + OH ⁺ + OH + e ⁻	6.08×10^{-16}	As reaction 481
483	He(2 ³ S) + O ₂ → He + O ₂ ⁺ + e ⁻	2.54×10^{-16}	[367]
484	He(2 ³ S) + O(¹ D) → He + O ⁺ + e ⁻	2.54×10^{-16}	As reaction 483
485	He(2 ³ S) + O(¹ S) → He + O ⁺ + e ⁻	2.54×10^{-16}	As reaction 483
486	He(2 ³ S) + O → He + O ⁺ + e ⁻	2.54×10^{-16}	As reaction 483
487	He(2 ³ S) + O ₂ (a ¹ Δ) → He + O ₂ ⁺ + e ⁻	2.54×10^{-16}	As reaction 483
488	He(2 ³ S) + O ₂ (b ¹ Σ) → He + O ₂ ⁺ + e ⁻	2.54×10^{-16}	As reaction 483
489	He(2 ³ S) + O ₃ → He + O ₂ ⁺ + O + e ⁻	2.60×10^{-16}	[80] ^c
490	He ₂ [*] + He ₂ [*] → e ⁻ + He ⁺ + 3He	3.00×10^{-16}	[294, 368]
491	He ₂ [*] + He ₂ [*] → e ⁻ + 2He + He ₂ ⁺	1.20×10^{-15}	[294, 368]
492	He ₂ [*] + H ₂ O → 2He + H ₂ O ⁺ + e ⁻	2.20×10^{-15}	[369]

continued on next page

No.	Reaction	Rate Coefficient ^{*,a}	Ref.
493	He ₂ [*] + O → 2He + O ⁺ + e ⁻	3.60×10 ⁻¹⁶	As reaction 496
494	He ₂ [*] + O(¹ D) → 2He + O ⁺ + e ⁻	3.60×10 ⁻¹⁶	As reaction 496
495	He ₂ [*] + O(¹ S) → 2He + O ⁺ + e ⁻	3.60×10 ⁻¹⁶	As reaction 496
496	He ₂ [*] + O ₂ → 2He + O ₂ ⁺ + e ⁻	3.60×10 ⁻¹⁶	[369]
497	He ₂ [*] + O ₂ (a ¹ Δ) → 2He + O ₂ ⁺ + e ⁻	3.60×10 ⁻¹⁶	As reaction 496
498	He ₂ [*] + O ₂ (b ¹ Σ) → 2He + O ₂ ⁺ + e ⁻	3.60×10 ⁻¹⁶	As reaction 496
499	He ₂ [*] + O ₃ → 2He + O ₂ ⁺ + O + e ⁻	3.60×10 ⁻¹⁶	As reaction 496
500	H + OH → H ₂ + O	6.86×10 ⁻²⁰ T _n ^{2.8} e ^{-1950/T_g}	[370]
501	H + HO ₂ → O ₂ + H ₂	5.60×10 ⁻¹⁸	[371]
502	H + HO ₂ → 2OH	7.20×10 ⁻¹⁷	[371]
503	H + HO ₂ → H ₂ O + O	2.40×10 ⁻¹⁸	[371]
504	H + H ₂ O ₂ → H ₂ O + OH	1.70×10 ⁻¹⁷ e ^{-1800/T_g}	[372]
505	H + H ₂ O ₂ → H ₂ + HO ₂	2.80×10 ⁻¹⁸ e ^{-1890/T_g}	[372]
506	H + O ₃ → O ₂ + OH	1.40×10 ⁻¹⁶ e ^{-470/T_g}	[373, 374]
507	H ₂ + OH → H ₂ O + H	4.27×10 ⁻¹⁹ T _n ^{2.41} e ^{-1240/T_g}	[375]
508	H ₂ + O(¹ D) → OH + H	1.20×10 ⁻¹⁶	[371]
509	H ₂ + O(¹ S) → OH + H	1.20×10 ⁻¹⁶	As reaction 508
510	2OH → O + H ₂ O	6.20×10 ⁻²⁰ T _n ^{2.6} e ^{945/T_g}	[371]
511	OH + HO ₂ → O ₂ + H ₂ O	4.80×10 ⁻¹⁷ e ^{250/T_g}	[371, 372, 376]
512	OH + H ₂ O ₂ → HO ₂ + H ₂ O	2.90×10 ⁻¹⁸ e ^{-160/T_g}	[371]
513	OH + O → O ₂ + H	2.40×10 ⁻¹⁷ e ^{110/T_g}	[371, 377, 378]
514	OH + O(¹ D) → O ₂ + H	2.40×10 ⁻¹⁷ e ^{110/T_g}	As reaction 513
515	OH + O(¹ S) → O ₂ + H	2.40×10 ⁻¹⁷ e ^{110/T_g}	As reaction 513
516	OH + O ₃ → O ₂ + HO ₂	1.70×10 ⁻¹⁸ e ^{-940/T_g}	[371]
517	H ₂ O + O(¹ D) → 2OH	1.63×10 ⁻¹⁶ e ^{60/T_g}	[373]
518	H ₂ O + O(¹ S) → O + H ₂ O	4.50×10 ⁻¹⁷	[379]
519	H ₂ O + O(¹ S) → O(¹ D) + H ₂ O	1.50×10 ⁻¹⁶	[379]
520	H ₂ O + O(¹ S) → 2OH	3.05×10 ⁻¹⁶	[379]
521	H ₂ O + O ₂ (a ¹ Δ) → O ₂ + H ₂ O	4.80×10 ⁻²⁴	[373]
522	H ₂ O + O ₂ (b ¹ Σ) → O ₂ + H ₂ O	3.90×10 ⁻¹⁸ e ^{125/T_g}	[373]
523	HO ₂ + O → OH + O ₂	2.70×10 ⁻¹⁷ e ^{224/T_g}	[371, 372]
524	H ₂ O ₂ + O(¹ D) → H ₂ O + O ₂	5.20×10 ⁻¹⁶	[380]
525	H ₂ O ₂ + O(¹ S) → H ₂ O + O ₂	5.20×10 ⁻¹⁶	As reaction 524

continued on next page

No.	Reaction	Rate Coefficient ^{*,a}	Ref.
526	HO ₂ + O(¹ D) → OH + O ₂	5.20×10 ⁻¹⁶	As reaction 524
527	HO ₂ + O(¹ S) → OH + O ₂	5.20×10 ⁻¹⁶	As reaction 524
528	O + O(¹ D) → 2O	8.00×10 ⁻¹⁸	[381]
529	O + O(¹ S) → 2O	3.33×10 ⁻¹⁷ e ^{-300/T_g}	[364, 382] ^d
530	O + O(¹ S) → O + O(¹ D)	1.67×10 ⁻¹⁷ e ^{-300/T_g}	[364, 382] ^d
531	O + O ₂ (a ¹ Δ) → O + O ₂	1.00×10 ⁻²²	[373]
532	O + O ₂ (b ¹ Σ) → O + O ₂ (a ¹ Δ)	8.00×10 ⁻²⁰	[371, 373]
533	O + O ₃ → 2O + O ₂	1.20×10 ⁻¹⁵ e ^{-11400/T_g}	[361]
534	O + O ₃ → 2O ₂	8.00×10 ⁻¹⁸ e ^{-2060/T_g}	[80, 371, 373, 383]
535	O(¹ D) + O ₂ → O + O ₂ (b ¹ Σ)	2.56×10 ⁻¹⁷ e ^{67/T_g}	[371]
536	O(¹ D) + O ₂ → O + O ₂ (a ¹ Δ)	6.60×10 ⁻¹⁸ e ^{55/T_g}	[373]
537	O(¹ D) + O ₃ → 2O ₂	1.20×10 ⁻¹⁶	[371]
538	O(¹ D) + O ₃ → O ₂ + 2O	1.20×10 ⁻¹⁶	[371]
539	O(¹ S) + O ₂ → O + O ₂	3.00×10 ⁻¹⁸ e ^{-850/T_g}	[80, 319, 379]
540	O(¹ S) + O ₂ → O(¹ D) + O ₂	1.30×10 ⁻¹⁸ e ^{-850/T_g}	[80, 319, 379]
541	O(¹ S) + O ₂ (a ¹ Δ) → 3O	3.20×10 ⁻¹⁷	[80, 384–386]
542	O(¹ S) + O ₂ (a ¹ Δ) → O + O ₂ (b ¹ Σ)	1.30×10 ⁻¹⁶	[80, 384–386]
543	O(¹ S) + O ₂ (a ¹ Δ) → O(¹ D) + O ₂	3.60×10 ⁻¹⁷	[80, 384, 385]
544	O(¹ S) + O ₃ → O + O(¹ D) + O ₂	1.93×10 ⁻¹⁶	[387]
545	O(¹ S) + O ₃ → 2O ₂	1.93×10 ⁻¹⁶	[387]
546	O(¹ S) + O ₃ → 2O + O ₂	1.93×10 ⁻¹⁶	[387]
547	2O ₂ → 2O + O ₂	6.60×10 ⁻¹⁵ T _n ^{-1.5} e ^{-59000/T_g}	[319]
548	O ₂ + O ₂ (a ¹ Δ) → 2O ₂	3.00×10 ⁻²⁴ e ^{-200/T_g}	[371]
549	O ₂ + O ₂ (b ¹ Σ) → O ₂ + O ₂ (a ¹ Δ)	3.60×10 ⁻²³ T _n ^{0.5}	[364]
550	O ₂ + O ₃ → O + 2O ₂	7.26×10 ⁻¹⁶ e ^{-11435/T_g}	[387]
551	2O ₂ (a ¹ Δ) → O ₂ + O ₂ (b ¹ Σ)	1.80×10 ⁻²⁴ T _n ^{3.8} e ^{700/T_g}	[388, 389]
552	O ₂ (a ¹ Δ) + O ₂ (b ¹ Σ) → O ₂ + O ₂ (b ¹ Σ)	2.70×10 ⁻²³	[80]
553	O ₂ (a ¹ Δ) + O ₃ → 2O ₂ + O	5.20×10 ⁻¹⁷ e ^{-2840/T_g}	[373]
554	2O ₂ (b ¹ Σ) → O ₂ + O ₂ (b ¹ Σ)	2.70×10 ⁻²³	[80]
555	O ₂ (b ¹ Σ) + O ₃ → 2O ₂ + O	3.50×10 ⁻¹⁷ e ^{-135/T_g}	[373]
556	O ₂ (b ¹ Σ) + O ₃ → O ₂ + O ₃	5.50×10 ⁻¹⁸ e ^{-135/T_g}	[80, 373]
557	O ₂ (b ¹ Σ) + O ₃ → O ₂ (a ¹ Δ) + O ₃	5.50×10 ⁻¹⁸ e ^{-135/T_g}	[80, 373]
558	2O ₃ → O + O ₂ + O ₃	1.65×10 ⁻¹⁵ e ^{-11435/T_g}	[387]

continued on next page

No.	Reaction	Rate Coefficient ^{*,a}	Ref.
Three-body processes			
559	2He + He(2 ³ S) → He + He ₂ [*]	2.00×10 ⁻⁴⁶	[390]
560	He + He(2 ³ S) + H ₂ O → 2He + H ₂ O ⁺ + e ⁻	1.48×10 ⁻⁴¹	[365] ^e
561	He + He(2 ³ S) + O → e ⁻ + 2He + O ⁺	1.60×10 ⁻⁴³	[80]
562	He + He(2 ³ S) + O(¹ D) → e ⁻ + 2He + O ⁺	1.60×10 ⁻⁴³	[80]
563	He + He(2 ³ S) + O(¹ S) → e ⁻ + 2He + O ⁺	1.60×10 ⁻⁴³	[80]
564	He + He(2 ³ S) + O ₂ → e ⁻ + 2He + O ₂ ⁺	1.60×10 ⁻⁴³	[367]
565	He + He(2 ³ S) + O ₂ (a ¹ Δ) → e ⁻ + 2He + O ₂ ⁺	1.60×10 ⁻⁴³	[80]
566	He + He(2 ³ S) + O ₂ (b ¹ Σ) → e ⁻ + 2He + O ₂ ⁺	1.60×10 ⁻⁴³	[80]
567	He + He(2 ³ S) + O ₃ → e ⁻ + 2He + O + O ₂ ⁺	1.60×10 ⁻⁴³	[80]
568	He + 2H → He + H ₂	6.04×10 ⁻⁴⁵ T _n ⁻¹	[372, 374] ^f
569	He + H + OH → He + H ₂ O	9.23×10 ⁻⁴⁴ T _n ^{-1.527} e ^{-185/T_g}	[391, 392] ^g
570	He + H + O → OH + He	4.36×10 ⁻⁴⁴ T _n ⁻¹	[370] ^c
571	H + O ₂ (+ He) → HO ₂ (+ He)	Effective	[371, 393] ^{h,i}
572	2OH (+ He) → H ₂ O ₂ (+ He)	Effective	[371] ^{h,j}
573	He + 2O → He + O ₂ (a ¹ Δ)	2.00×10 ⁻⁴⁵ T _n ⁻¹ e ^{-170/T_g}	[80, 361, 394]
574	He + 2O → He + O ₂ (b ¹ Σ)	2.00×10 ⁻⁴⁵ T _n ⁻¹ e ^{-170/T_g}	[80, 361, 394]
575	He + O + O ₂ → He + O ₃	3.66×10 ⁻⁴⁶ T _n ^{-2.6}	[371, 395] ^k
576	He + O + O ₂ (a ¹ Δ) → He + O ₂ + O	4.00×10 ⁻⁴⁵	[396, 397]

* $T_n = T_g/300$.

^a In m³ s⁻¹ and m⁶ s⁻¹ for two- and three-body reactions, respectively.

^b Value is an upper limit in reference.

^c Estimated value in reference.

^d Estimated branching ratio.

^e Branching ratio taken from Sanders [366].

^f Third body is Ar instead of He in reference. The gas efficiency factor is assumed to be 1.

^g Third body is Ar instead of He in reference. The gas efficiency factor is assumed to be 0.65, calculated by dividing reaction rate coefficients for He and Ar as background gases for the same reaction measured by Zellner *et al* [392].

^h Effective rate coefficients calculated from pressure dependent rates for 1 atm and fitted by an Arrhenius expression in the Temperature range 280–350 K.

ⁱ Third body is N₂ instead of He in reference. The gas efficiency factor is assumed to be 0.43, calculated by dividing reaction rate coefficients for He and N₂ as background gases for the same reaction measured by Hsu *et al* [393].

^j Recommended rate coefficient in reference is for N₂ background gas instead of He. We apply a gas efficiency factor of 0.41 to the low-pressure limit reaction rate coefficient to account for this, calculated by dividing the room temperature rate coefficient from the given reference for He background gas (measured by Forster *et al* [398]) by the recommended value (measured by Fulle *et al* [399]).

^k Third body is N₂ instead of He in reference. The gas efficiency factor is assumed to be 0.61, calculated by dividing reaction rate coefficients for He and N₂ as background gases for the same reaction measured by Lin and Leu [395].

References

- [1] J. E. Dyson and D. A. Williams. *The Physics of the Interstellar Medium: First Edition*. Manchester University Press, 1980.
- [2] L. H. Aller. *Physics of thermal gaseous nebulae: Physical processes in gaseous nebulae*. D. Reidel Publishing Company, 1984.
- [3] G. Paschmann, S. Haaland, R. Treumann, and R. A. Treumann. *Auroral Plasma Physics*. Kluwer Academic Publishers, 2003.
- [4] J. R. Dwyer and M. A. Uman. The physics of lightning. *Physics Reports*, 534(4):147, 2014.
- [5] U. Kogelschatz. Dielectric-barrier discharges: their history, discharge physics, and industrial applications. *Plasma chemistry and plasma processing*, 23:1, 2003.
- [6] G. S. Oehrlein and S. Hamaguchi. Foundations of low-temperature plasma enhanced materials synthesis and etching. *Plasma Sources Science and Technology*, 27(2):023001, 2018.
- [7] E. Morse. *Nuclear Fusion*. Springer, 2018.
- [8] D. B. Graves. The emerging role of reactive oxygen and nitrogen species in redox biology and some implications for plasma applications to medicine and biology. *Journal of Physics D: Applied Physics*, 45(26):263001, 2012.
- [9] R. Brandenburg, et al. White paper on the future of plasma science in environment, for gas conversion and agriculture. *Plasma Processes and Polymers*, 16(1):1700238, 2019.

- [10] D. B. Graves. Plasma processing. *IEEE transactions on Plasma Science*, 22(1):31, 1994.
- [11] G. Bauer, D. Sersenová, D. B. Graves, and Z. Machala. Cold atmospheric plasma and plasma-activated medium trigger RONS-based tumor cell apoptosis. *Scientific reports*, 9(1):14210, 2019.
- [12] S. K. Dubey, S. Parab, A. Alexander, M. Agrawal, V. P. K. Achalla, U. N. Pal, M. M. Pandey, and P. Kesharwani. Cold atmospheric plasma therapy in wound healing. *Process Biochemistry*, 112:112, 2022.
- [13] E. Stoffels, A. Flikweert, W. Stoffels, and G. Kroesen. Plasma needle: a non-destructive atmospheric plasma source for fine surface treatment of (bio) materials. *Plasma Sources Science and Technology*, 11(4):383, 2002.
- [14] M. Laroussi and X. Lu. Room-temperature atmospheric pressure plasma plume for biomedical applications. *Applied Physics Letters*, 87(11), 2005.
- [15] J. Golda, et al. Concepts and characteristics of the ‘COST Reference Microplasma Jet’. *Journal of Physics D: Applied Physics*, 49(8):084003, 2016.
- [16] S. Reuter, T. Von Woedtke, and K.-D. Weltmann. The kINPen—A review on physics and chemistry of the atmospheric pressure plasma jet and its applications. *Journal of Physics D: Applied Physics*, 51(23):233001, 2018.
- [17] M. Laroussi. Low-temperature plasmas for medicine? *IEEE Transactions on plasma science*, 37(6):714, 2009.
- [18] H. Kragh. The names of physics: plasma, fission, photon. *The European Physical Journal H*, 39(3):263, 2014.
- [19] I. Langmuir. Oscillations in ionized gases. *Proceedings of the National Academy of Sciences*, 14(8):627, 1928.
- [20] L. Tonks. The birth of “plasma”. *American Journal of Physics*, 35(9):857, 1967.

- [21] H. M. Mott-Smith. History of “plasmas”. *Nature*, 233(5316):219, 1971.
- [22] H. Rausher, M. Perucca, and G. Buyle. Plasma Technology for Hyperfunctional Surfaces: Food, Biomedical and Textile Applications, 2010.
- [23] F. F. Chen. *Introduction to plasma physics and controlled fusion*, volume 1. Springer, 1984.
- [24] L. Tonks and I. Langmuir. A general theory of the plasma of an arc. *Physical review*, 34(6):876, 1929.
- [25] D. Berg. The fundamentals of electric breakdown in gases. In *1968 8th Electrical Insulation Conference*, pages 53–55. IEEE, 1968.
- [26] N. S. J. Braithwaite. Introduction to gas discharges. *Plasma sources science and technology*, 9(4):517, 2000.
- [27] A. Von Engel. *Ionized gases*, volume 198. Springer, 1955.
- [28] R. Massarczyk, P. Chu, C. Dugger, S. R. Elliott, K. Rielage, and W. Xu. Paschen’s law studies in cold gases. *Journal of Instrumentation*, 12(06):P06019, 2017.
- [29] J. Shi and M. Kong. Evolution of discharge structure in capacitive radio-frequency atmospheric microplasmas. *Physical review letters*, 96(10):105009, 2006.
- [30] P. J. Bruggeman, F. Iza, and R. Brandenburg. Foundations of atmospheric pressure non-equilibrium plasmas. *Plasma Sources Science and Technology*, 26(12):123002, 2017.
- [31] Y. Liu, I. Korolov, T. Hemke, L. Bischoff, G. Hübner, J. Schulze, and T. Mussenbrock. Electron heating mode transitions in radio-frequency driven micro atmospheric pressure plasma jets in He/O₂: a fluid dynamics approach. *Journal of Physics D: Applied Physics*, 54(27):275204, 2021.
- [32] J. Winter, R. Brandenburg, and K. Weltmann. Atmospheric pressure plasma jets: an overview of devices and new directions. *Plasma Sources Science and Technology*, 24(6):064001, 2015.

- [33] T. Shao, R. Wang, C. Zhang, and P. Yan. Atmospheric-pressure pulsed discharges and plasmas: mechanism, characteristics and applications. *High Voltage*, 3(1):14, 2018.
- [34] T. Shao, C. Zhang, R. Wang, P. Yan, and C. Ren. Atmospheric-pressure pulsed gas discharge and pulsed plasma application. *High Voltage Engineering*, 42(3):685, 2016.
- [35] D. Z. Pai, G. D. Stancu, D. A. Lacoste, and C. O. Laux. Nanosecond repetitively pulsed discharges in air at atmospheric pressure—the glow regime. *Plasma Sources Science and Technology*, 18(4):045030, 2009.
- [36] T. Shao, C. Zhang, H. Jiang, Z. Niu, P. Yan, and Y. Zhou. Nanosecond repetitively pulsed discharge of point–plane gaps in air at atmospheric pressure. *IEEE Transactions on Plasma Science*, 39(9):1881, 2011.
- [37] A. Fridman. *Plasma chemistry*. Cambridge University Press, 2008.
- [38] D. Breden, K. Miki, and L. L. Raja. Computational study of cold atmospheric nanosecond pulsed helium plasma jet in air. *Applied Physics Letters*, 99(11), 2011.
- [39] D. Breden, K. Miki, and L. Raja. Self-consistent two-dimensional modeling of cold atmospheric-pressure plasma jets/bullets. *Plasma Sources Science and Technology*, 21(3):034011, 2012.
- [40] A. Schmidt-Bleker, S. A. Norberg, J. Winter, E. Johnsen, S. Reuter, K. Weltmann, and M. J. Kushner. Propagation mechanisms of guided streamers in plasma jets: the influence of electronegativity of the surrounding gas. *Plasma Sources Science and Technology*, 24(3):035022, 2015.
- [41] S. Nijdam, F. Van De Wetering, R. Blanc, E. Van Veldhuizen, and U. Ebert. Probing photo-ionization: experiments on positive streamers in pure gases and mixtures. *Journal of Physics D: Applied Physics*, 43(14):145204, 2010.
- [42] A. Von Keudell and V. Schulz-Von Der Gathen. Foundations of low-temperature plasma physics—an introduction. *Plasma Sources Science and Technology*, 26(11):113001, 2017.

- [43] N. Y. Babaeva, C. Zhang, J. Qiu, X. Hou, V. F. Tarasenko, and T. Shao. The role of fast electrons in diffuse discharge formation: Monte Carlo simulation. *Plasma Sources Science and Technology*, 26(8):085008, 2017.
- [44] E. Baksht, A. Burachenko, I. Kostyrya, M. Lomaev, D. Rybka, M. Shulepov, and V. Tarasenko. Runaway-electron-preionized diffuse discharge at atmospheric pressure and its application. *Journal of Physics D: Applied Physics*, 42(18):185201, 2009.
- [45] J. Jiang and P. J. Bruggeman. Ion fluxes and memory effects in an Ar–O₂ modulated radiofrequency-driven atmospheric pressure plasma jet. *Plasma Sources Science and Technology*, 30(10):105007, 2021.
- [46] C. Tendero, C. Tixier, P. Tristant, J. Desmaison, and P. Leprince. Atmospheric pressure plasmas: A review. *Spectrochimica Acta Part B: Atomic Spectroscopy*, 61(1):2, 2006.
- [47] M. Moisan and M. Wertheimer. Comparison of microwave and rf plasmas: fundamentals and applications. *Surface and Coatings Technology*, 59(1-3):1, 1993.
- [48] International Telecommunications Union. *Radio Regulations*. International Telecommunications Union Publications, 2012.
- [49] J. Hopwood. Review of inductively coupled plasmas for plasma processing. *Plasma Sources Science and Technology*, 1(2):109, 1992.
- [50] J. Reece Roth. *Industrial Plasma Engineering—Volume 1: Principles*. Institute of Physics Publishing, 1995.
- [51] M. A. Razzak, K. Kondo, Y. Uesugi, N. Ohno, and S. Takamura. Transition from electrostatic-to-electromagnetic mode in a radio-frequency Ar inductively coupled plasma in atmospheric pressure. *Journal of applied physics*, 95(2):427, 2004.
- [52] Y. P. Raizer, M. N. Shneider, and N. A. Yatsenko. *Radio-frequency capacitive discharges*. CRC Press, 1995.

- [53] P. Bruggeman and R. Brandenburg. Atmospheric pressure discharge filaments and microplasmas: physics, chemistry and diagnostics. *Journal of physics D: applied physics*, 46(46):464001, 2013.
- [54] L. Wang, G. Dinescu, X. Deng, E.-R. Ionita, C. Leys, and A. Y. Nikiforov. Mechanisms of sustaining a radio-frequency atmospheric pressure planar discharge. *Plasma Sources Science and Technology*, 26(7):075012, 2017.
- [55] V. Schulz-von der Gathen, V. Buck, T. Gans, N. Knake, K. Niemi, S. Reuter, L. Schaper, and J. Winter. Optical diagnostics of micro discharge jets. *Contributions to Plasma Physics*, 47(7):510, 2007.
- [56] T. Hemke, D. Eremin, T. Mussenbrock, A. Derzsi, Z. Donkó, K. Dittmann, J. Meichsner, and J. Schulze. Ionization by bulk heating of electrons in capacitive radio frequency atmospheric pressure microplasmas. *Plasma Sources Science and Technology*, 22(1):015012, 2012.
- [57] L. Bischoff, et al. Experimental and computational investigations of electron dynamics in micro atmospheric pressure radio-frequency plasma jets operated in He/N₂ mixtures. *Plasma Sources Science and Technology*, 27(12):125009, 2018.
- [58] V. Schulz-Von Der Gathen, L. Schaper, N. Knake, S. Reuter, K. Niemi, T. Gans, and J. Winter. Spatially resolved diagnostics on a microscale atmospheric pressure plasma jet. *Journal of Physics D: Applied Physics*, 41(19):194004, 2008.
- [59] D. Schröder, S. Burhenn, T. De los Arcos, and V. Schulz-von der Gathen. Characteristics of a propagating, self-pulsing, constricted ‘ γ -mode-like’ discharge. *Journal of Physics D: Applied Physics*, 48(5):055206, 2015.
- [60] A. Kruithof and F. Penning. Determination of the townsend. Ionization coefficient α for mixtures of neon and argon. *Physica*, 4(6):430, 1937.
- [61] L. M. Chanin and G. Rork. Primary ionization coefficient measurements in penning mixtures. *Physical Review*, 135(1A):A71, 1964.

- [62] I. Radu, R. Bartnikas, and M. R. Wertheimer. Frequency and voltage dependence of glow and pseudoglow discharges in helium under atmospheric pressure. *IEEE Transactions on plasma science*, 31(6):1363, 2003.
- [63] T. Martens, A. Bogaerts, W. Brok, and J. Dijk. The dominant role of impurities in the composition of high pressure noble gas plasmas. *Applied Physics Letters*, 92(4), 2008.
- [64] K. Niemi, J. Waskoenig, N. Sadeghi, T. Gans, and D. O’Connell. The role of helium metastable states in radio-frequency driven helium–oxygen atmospheric pressure plasma jets: measurement and numerical simulation. *Plasma Sources Science and Technology*, 20(5):055005, 2011.
- [65] F. Iza, J. K. Lee, and M. G. Kong. Electron kinetics in radio-frequency atmospheric-pressure microplasmas. *Physical Review Letters*, 99(7):075004, 2007.
- [66] J. Golda, F. Kogelheide, P. Awakowicz, and V. Schulz-von der Gathen. Dissipated electrical power and electron density in an RF atmospheric pressure helium plasma jet. *Plasma sources science and technology*, 28(9):095023, 2019.
- [67] S. Mouchtouris, G. Kokkoris, and A. G. Boudouvis. Predicting power–voltage characteristics and mode transitions in the COST reference microplasma jet. *Journal of Physics D: Applied Physics*, 55(35):355203, 2022.
- [68] N. Morgan. Atmospheric pressure dielectric barrier discharge chemical and biological applications. *International Journal of Physical Sciences*, 4(13):885, 2009.
- [69] J. Shi, D. Liu, and M. G. Kong. Mitigating plasma constriction using dielectric barriers in radio-frequency atmospheric pressure glow discharges. *Applied physics letters*, 90(3), 2007.
- [70] J. Shi and M. G. Kong. Radio-frequency dielectric-barrier glow discharges in atmospheric argon. *Applied physics letters*, 90(11), 2007.

- [71] R. Brandenburg. Dielectric barrier discharges: progress on plasma sources and on the understanding of regimes and single filaments. *Plasma Sources Science and Technology*, 26(5):053001, 2017.
- [72] A. Fridman, A. Chirokov, and A. Gutsol. Non-thermal atmospheric pressure discharges. *Journal of Physics D: Applied Physics*, 38(2):R1, 2005.
- [73] F. Massines, A. Rabehi, P. Decomps, R. B. Gadri, P. Ségur, and C. Mayoux. Experimental and theoretical study of a glow discharge at atmospheric pressure controlled by dielectric barrier. *Journal of Applied Physics*, 83(6):2950, 1998.
- [74] F. Massines and G. Gouda. A comparison of polypropylene-surface treatment by filamentary, homogeneous and glow discharges in helium at atmospheric pressure. *Journal of Physics D: Applied Physics*, 31(24):3411, 1998.
- [75] J. T. Gudmundsson. On the effect of the electron energy distribution on the plasma parameters of an argon discharge: a global (volume-averaged) model study. *Plasma Sources Science and Technology*, 10(1):76, 2001.
- [76] V. A. Godyak, R. Piejak, and B. Alexandrovich. Electron energy distribution function measurements and plasma parameters in inductively coupled argon plasma. *Plasma Sources Science and Technology*, 11(4):525, 2002.
- [77] C.-S. Yip, C. Jin, W. Zhang, D. Jiang, and G.-S. Xu. Power law fitting of the ion saturation current and the three-temperature Maxwellian EEDF in a multi-dipole confined hot cathode discharge: an experimental revisit. *Plasma Sources Science and Technology*, 31(4):045002, 2022.
- [78] J. Golda, J. Held, and V. Schulz-von der Gathen. Comparison of electron heating and energy loss mechanisms in an RF plasma jet operated in argon and helium. *Plasma Sources Science and Technology*, 29(2):025014, 2020.
- [79] K. Niemi, D. O’Connell, N. de Oliveira, D. Joyeux, L. Nahon, J.-P. Booth, and T. Gans. Absolute atomic oxygen and nitrogen densities in radio-frequency driven

- atmospheric pressure cold plasmas: synchrotron vacuum ultra-violet high-resolution Fourier-transform absorption measurements. *Applied Physics Letters*, 103(3):034102, 2013.
- [80] M. M. Turner. Uncertainty and error in complex plasma chemistry models. *Plasma Sources Science and Technology*, 24(3):035027, 2015.
- [81] A. Brisset, B. Harris, A. Dickenson, K. Niemi, J. Walsh, and E. Wagenaars. Effects of humidity on the dynamics and electron recombination of a pin-to-pin discharge in He+H₂O at atmospheric pressure. *Plasma Sources Science and Technology*, 31(4):045008, 2022.
- [82] T. Murakami, K. Niemi, T. Gans, D. O’Connell, and W. G. Graham. Chemical kinetics and reactive species in atmospheric pressure helium–oxygen plasmas with humid-air impurities. *Plasma Sources Science and Technology*, 22(1):015003, 2012.
- [83] W.-C. Zhu, Q. Li, X.-M. Zhu, and Y.-K. Pu. Characteristics of atmospheric pressure plasma jets emerging into ambient air and helium. *Journal of Physics D: Applied Physics*, 42(20):202002, 2009.
- [84] C. Farah, L. Y. Michel, and J.-L. Balligand. Nitric oxide signalling in cardiovascular health and disease. *Nature Reviews Cardiology*, 15(5):292, 2018.
- [85] R. P. Patel, J. McAndrew, H. Sellak, C. R. White, H. Jo, B. A. Freeman, and V. M. Darley-Usmar. Biological aspects of reactive nitrogen species. *Biochimica et Biophysica Acta (BBA)-Bioenergetics*, 1411(2-3):385, 1999.
- [86] M. Schieber and N. S. Chandel. ROS function in redox signaling and oxidative stress. *Current biology*, 24(10):R453, 2014.
- [87] R. Radi, G. Peluffo, M. N. Alvarez, M. Naviliat, and A. Cayota. Unraveling peroxynitrite formation in biological systems. *Free Radical Biology and Medicine*, 30(5):463, 2001.

- [88] H. Ischiropoulos, L. Zhu, and J. S. Beckman. Peroxynitrite formation from macrophage-derived nitric oxide. *Archives of biochemistry and biophysics*, 298(2):446, 1992.
- [89] C. Lennicke, J. Rahn, R. Lichtenfels, L. A. Wessjohann, and B. Seliger. Hydrogen peroxide–production, fate and role in redox signaling of tumor cells. *Cell communication and signaling*, 13(1):1, 2015.
- [90] J. Kanta. The role of hydrogen peroxide and other reactive oxygen species in wound healing. *Acta Medica (Hradec Kralove)*, 54(3):97, 2011.
- [91] B. Haertel, T. Von Woedtke, K.-D. Weltmann, and U. Lindequist. Non-thermal atmospheric-pressure plasma possible application in wound healing. *Biomolecules & therapeutics*, 22(6):477, 2014.
- [92] J.-W. Lackmann, S. Schneider, E. Edengeiser, F. Jarzina, S. Brinckmann, E. Steinborn, M. Havenith, J. Benedikt, and J. E. Bandow. Photons and particles emitted from cold atmospheric-pressure plasma inactivate bacteria and biomolecules independently and synergistically. *Journal of The Royal Society Interface*, 10(89):20130591, 2013.
- [93] M. Laroussi. Sterilization of contaminated matter with an atmospheric pressure plasma. *IEEE Transactions on Plasma Science*, 24(3):1188, 1996.
- [94] M. Moisan, J. Barbeau, M.-C. Crevier, J. Pelletier, N. Philip, and B. Saoudi. Plasma sterilization. Methods and mechanisms. *Pure and applied chemistry*, 74(3):349, 2002.
- [95] M. Modic, N. P. McLeod, J. M. Sutton, and J. L. Walsh. Cold atmospheric pressure plasma elimination of clinically important single-and mixed-species biofilms. *International journal of antimicrobial agents*, 49(3):375, 2017.
- [96] P. Dadgostar. Antimicrobial resistance: implications and costs. *Infection and drug resistance*, pages 3903–3910, 2019.
- [97] F. Werdin, M. Tennenhaus, H.-E. Schaller, and H.-O. Rennekampff. Evidence-based management strategies for treatment of chronic wounds. *Eplasty*, 9, 2009.

- [98] T. von Woedtke, A. Schmidt, S. Bekeschus, K. Wende, and K.-D. Weltmann. Plasma medicine: A field of applied redox biology. *In vivo*, 33(4):1011, 2019.
- [99] G. Isbary, et al. A first prospective randomized controlled trial to decrease bacterial load using cold atmospheric argon plasma on chronic wounds in patients. *British Journal of Dermatology*, 163(1):78, 2010.
- [100] F. Brehmer, H. A. Haenssle, G. Daeschlein, R. Ahmed, S. Pfeiffer, A. Goerlitz, D. Simon, M. P. Schön, D. Wandke, and S. Emmert. Alleviation of chronic venous leg ulcers with a hand-held dielectric barrier discharge plasma generator (PlasmaDerm® VU-2010): results of a monocentric, two-armed, open, prospective, randomized and controlled trial (NCT 01415622). *Journal of the European Academy of Dermatology and Venereology*, 29(1):148, 2015.
- [101] K. Ishikawa, K. Takeda, S. Yoshimura, T. Kondo, H. Tanaka, S. Toyokuni, K. Nakamura, H. Kajiyama, M. Mizuno, and M. Hori. Generation and measurement of low-temperature plasma for cancer therapy: A historical review. *Free Radical Research*, 57(3):239, 2023.
- [102] G. Fridman, A. Shereshevsky, M. M. Jost, A. D. Brooks, A. Fridman, A. Gutsol, V. Vasilets, and G. Friedman. Floating electrode dielectric barrier discharge plasma in air promoting apoptotic behavior in melanoma skin cancer cell lines. *Plasma Chemistry and Plasma Processing*, 27:163, 2007.
- [103] N. Barezzi and M. Laroussi. Effects of low temperature plasmas on cancer cells. *Plasma Processes and Polymers*, 10(12):1039, 2013.
- [104] M. Laroussi, et al. Low-temperature plasma for biology, hygiene, and medicine: Perspective and roadmap. *IEEE Transactions on Radiation and Plasma Medical Sciences*, 6(2):127, 2021.
- [105] J. Tong, R. He, X. Zhang, R. Zhan, W. Chen, and S. Yang. Effects of atmospheric pressure air plasma pretreatment on the seed germination and early growth of *Andrographis paniculata*. *Plasma Science and Technology*, 16(3):260, 2014.

- [106] M. Giannoglou, P. Stergiou, P. Dimitrakellis, E. Gogolides, N. G. Stoforos, and G. Katsaros. Effect of Cold Atmospheric Plasma processing on quality and shelf-life of ready-to-eat rocket leafy salad. *Innovative Food Science & Emerging Technologies*, 66:102502, 2020.
- [107] J. L. Walsh and M. G. Kong. Contrasting characteristics of linear-field and cross-field atmospheric plasma jets. *Applied Physics Letters*, 93(11), 2008.
- [108] L. Alves, A. Bogaerts, V. Guerra, and M. Turner. Foundations of modelling of nonequilibrium low-temperature plasmas. *Plasma Sources Science and Technology*, 27(2):023002, 2018.
- [109] H. Lee, G. Park, Y. Seo, Y. Im, S. Shim, and H. Lee. Modelling of atmospheric pressure plasmas for biomedical applications. *Journal of Physics D: Applied Physics*, 44(5):053001, 2011.
- [110] M. J. Kushner. Hybrid modelling of low temperature plasmas for fundamental investigations and equipment design. *Journal of Physics D: Applied Physics*, 42(19):194013, 2009.
- [111] A. M. Hirst, F. M. Frame, M. Arya, N. J. Maitland, and D. O’Connell. Low temperature plasmas as emerging cancer therapeutics: the state of play and thoughts for the future. *Tumor Biology*, 37:7021, 2016.
- [112] J. P. Verboncoeur. Particle simulation of plasmas: review and advances. *Plasma Physics and Controlled Fusion*, 47(5A):A231, 2005.
- [113] H. Kim, F. Iza, S. Yang, M. Radmilović-Radjenović, and J. Lee. Particle and fluid simulations of low-temperature plasma discharges: benchmarks and kinetic effects. *Journal of Physics D: Applied Physics*, 38(19):R283, 2005.
- [114] A. Hurlbatt, A. R. Gibson, S. Schröter, J. Bredin, A. P. S. Foote, P. Grondein, D. O’Connell, and T. Gans. Concepts, capabilities, and limitations of global models: A review. *Plasma Processes and Polymers*, 14(1-2):1600138, 2017.

- [115] O. Buneman. Dissipation of currents in ionized media. *Physical Review*, 115(3):503, 1959.
- [116] J. Dawson. One-dimensional plasma model. *The Physics of Fluids*, 5(4):445, 1962.
- [117] C. Birdsall and A. Langdon. *Plasma physics via computer simulation*. McGraw-Hill, 1985.
- [118] C. K. Birdsall. Particle-in-cell charged-particle simulations, plus Monte Carlo collisions with neutral atoms, PIC-MCC. *IEEE Transactions on plasma science*, 19(2):65, 1991.
- [119] C. Sang, J. Sun, C. Ren, and D. Wang. Characteristics of nanosecond pulse needle-to-plane discharges at high pressure: A particle-in-cell Monte Carlo collision simulation. *Journal of Applied Physics*, 105(4), 2009.
- [120] S. Lee, F. Iza, and J. K. Lee. Particle-in-cell Monte Carlo and fluid simulations of argon-oxygen plasma: Comparisons with experiments and validations. *Physics of plasmas*, 13(5), 2006.
- [121] D. B. Graves and K. F. Jensen. A continuum model of DC and RF discharges. *IEEE Transactions on plasma science*, 14(2):78, 1986.
- [122] A. D. Richards, B. E. Thompson, and H. H. Sawin. Continuum modeling of argon radio frequency glow discharges. *Applied physics letters*, 50(9):492, 1987.
- [123] Y. Hong, M. Yoon, F. Iza, G. Kim, and J. Lee. Comparison of fluid and particle-in-cell simulations on atmospheric pressure helium microdischarges. *Journal of Physics D: Applied Physics*, 41(24):245208, 2008.
- [124] G. Hagelaar and L. C. Pitchford. Solving the Boltzmann equation to obtain electron transport coefficients and rate coefficients for fluid models. *Plasma sources science and technology*, 14(4):722, 2005.
- [125] I. Kossyi, A. Y. Kostinsky, A. Matveyev, and V. Silakov. Kinetic scheme of the non-equilibrium discharge in nitrogen-oxygen mixtures. *Plasma Sources Science and Technology*, 1(3):207, 1992.

- [126] D.-X. Liu, P. Bruggeman, F. Iza, M.-Z. Rong, and M. G. Kong. Global model of low-temperature atmospheric-pressure He+ H₂O plasmas. *Plasma Sources Science and Technology*, 19(2):025018, 2010.
- [127] W. Van Gaens and A. Bogaerts. Kinetic modelling for an atmospheric pressure argon plasma jet in humid air. *Journal of Physics D: Applied Physics*, 46(27):275201, 2013.
- [128] D. J. Economou. Hybrid simulation of low temperature plasmas: A brief tutorial. *Plasma Processes and Polymers*, 14(1-2):1600152, 2017.
- [129] Y. Liu, I. Korolov, J. Trieschmann, D. Steuer, V. Schulz-von der Gathen, M. Böke, L. Bischoff, G. Hübner, J. Schulze, and T. Mussenbrock. Micro atmospheric pressure plasma jets excited in He/O₂ by voltage waveform tailoring: a study based on a numerical hybrid model and experiments. *Plasma Sources Science and Technology*, 30(6):064001, 2021.
- [130] F. Iza, J. L. Walsh, and M. G. Kong. From submicrosecond-to nanosecond-pulsed atmospheric-pressure plasmas. *IEEE Transactions on Plasma Science*, 37(7):1289, 2009.
- [131] I. Kovács and L. Nemes. *Rotational structure in the spectra of diatomic molecules*. Akadémiai Kiadó, 1969.
- [132] P. J. Bruggeman, N. Sadeghi, D. Schram, and V. Linss. Gas temperature determination from rotational lines in non-equilibrium plasmas: a review. *Plasma Sources Science and Technology*, 23(2):023001, 2014.
- [133] J. Schulze, E. Schüngel, Z. Donkó, D. Luggenhölscher, and U. Czarnetzki. Phase resolved optical emission spectroscopy: a non-intrusive diagnostic to study electron dynamics in capacitive radio frequency discharges. *Journal of Physics D: Applied Physics*, 43(12):124016, 2010.
- [134] R. Engeln, B. Klarenaar, and O. Guaitella. Foundations of optical diagnostics in low-temperature plasmas. *Plasma Sources Science and Technology*, 29(6):063001, 2020.

- [135] A. Wijaikhum, D. Schröder, S. Schröter, A. R. Gibson, K. Niemi, J. Friderich, A. Greb, V. Schulz-von der Gathen, D. O'Connell, and T. Gans. Absolute ozone densities in a radio-frequency driven atmospheric pressure plasma using two-beam UV-LED absorption spectroscopy and numerical simulations. *Plasma Sources Science and Technology*, 26(11):115004, 2017.
- [136] S. Schröter, et al. Chemical kinetics in an atmospheric pressure helium plasma containing humidity. *Physical Chemistry Chemical Physics*, 20(37):24263, 2018.
- [137] A. Brisset, A. R. Gibson, S. Schröter, K. Niemi, J.-P. Booth, T. Gans, D. O'Connell, and E. Wagenaars. Chemical kinetics and density measurements of OH in an atmospheric pressure He+ O₂+ H₂O radiofrequency plasma. *Journal of Physics D: Applied Physics*, 54(28):285201, 2021.
- [138] T. Verreycken, R. Van der Horst, A. Baede, E. Van Veldhuizen, and P. Bruggeman. Time and spatially resolved LIF of OH in a plasma filament in atmospheric pressure He-H₂O. *Journal of Physics D: Applied Physics*, 45(4):045205, 2012.
- [139] E. Wagenaars, T. Gans, D. O'Connell, and K. Niemi. Two-photon absorption laser-induced fluorescence measurements of atomic nitrogen in a radio-frequency atmospheric-pressure plasma jet. *Plasma Sources Science and Technology*, 21(4):042002, 2012.
- [140] R. Ono. Optical diagnostics of reactive species in atmospheric-pressure nonthermal plasma. *Journal of Physics D: Applied Physics*, 49(8):083001, 2016.
- [141] A. Y. Nikiforov, C. Leys, M. Gonzalez, and J. Walsh. Electron density measurement in atmospheric pressure plasma jets: Stark broadening of hydrogenated and non-hydrogenated lines. *Plasma Sources Science and Technology*, 24(3):034001, 2015.
- [142] S. Reuter, J. S. Sousa, G. D. Stancu, and J. H. van Helden. Review on VUV to MIR absorption spectroscopy of atmospheric pressure plasma jets. *Plasma Sources Science and Technology*, 24(5):054001, 2015.

- [143] X.-M. Zhu, J. L. Walsh, W.-C. Chen, and Y.-K. Pu. Measurement of the temporal evolution of electron density in a nanosecond pulsed argon microplasma: using both Stark broadening and an OES line-ratio method. *Journal of Physics D: Applied Physics*, 45(29):295201, 2012.
- [144] I. E. Gordon, et al. The HITRAN2020 molecular spectroscopic database. *Journal of quantitative spectroscopy and radiative transfer*, 277:107949, 2022.
- [145] H.-J. Kunze. *Introduction to plasma spectroscopy*, volume 56. Springer Science & Business Media, 2009.
- [146] MP1101—Biomedical Applications of Atmospheric Pressure Plasma Technology, European Cooperation in Science and Technology (COST). Available online: <https://www.cost.eu/actions/MP1101/>. Accessed: 2023-06-26.
- [147] Y. Gorbanev, J. Golda, V. Schulz-von der Gathen, and A. Bogaerts. Applications of the COST plasma jet: More than a reference standard. *Plasma*, 2(3):316, 2019.
- [148] A. West, M. van der Schans, C. Xu, M. Cooke, and E. Wagenaars. Fast, downstream removal of photoresist using reactive oxygen species from the effluent of an atmospheric pressure plasma jet. *Plasma Sources Science and Technology*, 25(2):02LT01, 2016.
- [149] D. Shaw, A. West, J. Bredin, and E. Wagenaars. Mechanisms behind surface modification of polypropylene film using an atmospheric-pressure plasma jet. *Plasma Sources Science and Technology*, 25(6):065018, 2016.
- [150] G. Willems, A. Hecimovic, K. Sgonina, E. Carbone, and J. Benedikt. Mass spectrometry of neutrals and positive ions in He/CO₂ non-equilibrium atmospheric plasma jet. *Plasma Physics and Controlled Fusion*, 62(3):034005, 2020.
- [151] S. Vermeulen, et al. Cold atmospheric plasma treatment of melanoma and glioblastoma cancer cells. *Plasma Processes and Polymers*, 13(12):1195, 2016.

- [152] V. Jirásek, Z. Koval'ová, B. Tarabová, and P. Lukeš. Leucine modifications by He/O₂ plasma treatment in phosphate-buffered saline: bactericidal effects and chemical characterization. *Journal of Physics D: Applied Physics*, 54(50):505206, 2021.
- [153] H. L. Wapshott-Stehli, B. G. Myers, M. J. Herrera Quesada, A. Grunden, and K. Stapelmann. Plasma-driven biocatalysis: In situ hydrogen peroxide production with an atmospheric pressure plasma jet increases the performance of OleTJE when compared to adding the same molar amount of hydrogen peroxide in bolus. *Plasma Processes and Polymers*, 19(5):2100160, 2022.
- [154] F. Riedel, J. Golda, J. Held, H. Davies, M. van der Woude, J. Bredin, K. Niemi, T. Gans, V. Schulz-von der Gathen, and D. O'Connell. Reproducibility of 'COST reference microplasma jets'. *Plasma Sources Science and Technology*, 29(9):095018, 2020.
- [155] K. Niemi, S. Reuter, L. Graham, J. Waskoenig, N. Knake, V. Schulz-Von Der Gathen, and T. Gans. Diagnostic based modelling of radio-frequency driven atmospheric pressure plasmas. *Journal of Physics D: Applied Physics*, 43(12):124006, 2010.
- [156] J. Waskoenig, K. Niemi, N. Knake, L. Graham, S. Reuter, V. Schulz-Von Der Gathen, and T. Gans. Atomic oxygen formation in a radio-frequency driven micro-atmospheric pressure plasma jet. *Plasma Sources Science and Technology*, 19(4):045018, 2010.
- [157] Y. Gorbanev, C. Verlackt, S. Tinck, E. Tuenter, K. Foubert, P. Cos, and A. Bogaerts. Combining experimental and modelling approaches to study the sources of reactive species induced in water by the COST RF plasma jet. *Physical Chemistry Chemical Physics*, 20(4):2797, 2018.
- [158] J. Dedrick, S. Schröter, K. Niemi, A. Wijaikhum, E. Wagenaars, N. de Oliveira, L. Nahon, J.-P. Booth, D. O'Connell, and T. Gans. Controlled production of atomic oxygen and nitrogen in a pulsed radio-frequency atmospheric-pressure plasma. *Journal of Physics D: Applied Physics*, 50(45):455204, 2017.

- [159] L. Nahon, N. de Oliveira, G. A. Garcia, J.-F. Gil, B. Pilette, O. Marcouillé, B. Lagarde, and F. Polack. DESIRS: a state-of-the-art VUV beamline featuring high resolution and variable polarization for spectroscopy and dichroism at SOLEIL. *Journal of synchrotron radiation*, 19(4):508, 2012.
- [160] S. Bekeschus, A. Schmidt, K.-D. Weltmann, and T. von Woedtke. The plasma jet kINPen—A powerful tool for wound healing. *Clinical Plasma Medicine*, 4(1):19, 2016.
- [161] R. Matthes, I. Koban, C. Bender, K. Masur, E. Kindel, K.-D. Weltmann, T. Kocher, A. Kramer, and N.-O. Hübner. Antimicrobial efficacy of an atmospheric pressure plasma jet against biofilms of *Pseudomonas aeruginosa* and *Staphylococcus epidermidis*. *Plasma Processes and Polymers*, 10(2):161, 2013.
- [162] G. Daeschlein, S. Scholz, T. von Woedtke, M. Niggemeier, E. Kindel, R. Brandenburg, K.-D. Weltmann, and M. Jünger. In vitro killing of clinical fungal strains by low-temperature atmospheric-pressure plasma jet. *IEEE Transactions on Plasma Science*, 39(2):815, 2010.
- [163] G. Daeschlein, S. Scholz, A. Arnold, T. von Woedtke, E. Kindel, M. Niggemeier, K.-D. Weltmann, and M. Jünger. In vitro activity of atmospheric pressure plasma jet (APPJ) plasma against clinical isolates of *demodex folliculorum*. *IEEE transactions on plasma science*, 38(10):2969, 2010.
- [164] R. Strohal, S. Dietrich, M. Mittlböck, and G. Hämmerle. Chronic wounds treated with cold atmospheric plasmajet versus best practice wound dressings: a multicenter, randomized, non-inferiority trial. *Scientific Reports*, 12(1):3645, 2022.
- [165] M. Schuster, et al. Visible tumor surface response to physical plasma and apoptotic cell kill in head and neck cancer. *Journal of Cranio-Maxillofacial Surgery*, 44(9):1445, 2016.
- [166] M. Baier, M. Görden, J. Ehlbeck, D. Knorr, W. B. Herppich, and O. Schlüter. Non-thermal atmospheric pressure plasma: screening for gentle process conditions and an-

- tibacterial efficiency on perishable fresh produce. *Innovative Food Science & Emerging Technologies*, 22:147, 2014.
- [167] O. Galmiz, M. Stupavska, H. Wulff, H. Kersten, A. Brablec, and M. Cernak. Deposition of Zn-containing films using atmospheric pressure plasma jet. *Open Chemistry*, 13(1):000010151520150020, 2014.
- [168] M. Dünnbier, A. Schmidt-Bleker, J. Winter, M. Wolfram, R. Hippler, K. Weltmann, and S. Reuter. Ambient air particle transport into the effluent of a cold atmospheric-pressure argon plasma jet investigated by molecular beam mass spectrometry. *Journal of Physics D: Applied Physics*, 46(43):435203, 2013.
- [169] S. Iseni, A. Schmidt-Bleker, J. Winter, K.-D. Weltmann, and S. Reuter. Atmospheric pressure streamer follows the turbulent argon air boundary in a MHz argon plasma jet investigated by OH-tracer PLIF spectroscopy. *Journal of Physics D: Applied Physics*, 47(15):152001, 2014.
- [170] A. Schmidt-Bleker, J. Winter, S. Iseni, M. Dünnbier, K. Weltmann, and S. Reuter. Reactive species output of a plasma jet with a shielding gas device—combination of FTIR absorption spectroscopy and gas phase modelling. *Journal of Physics D: Applied Physics*, 47(14):145201, 2014.
- [171] A. Brisset, M. Bieniek, L. Invernizzi, M. Hasan, J. Walsh, K. Niemi, and E. Wagenaars. The formation of O and H radicals in a pulsed discharge in atmospheric pressure helium with water vapour admixtures. *Plasma Sources Science and Technology*, 32(6):065004, 2023.
- [172] B. Harris and E. Wagenaars. The influence of pulse repetition frequency on reactive oxygen species production in pulsed He+H₂O plasmas at atmospheric pressure. *Journal of Applied Physics*, 134(10), 2023.
- [173] S. Tao, L. Kaihua, Z. Cheng, Y. Ping, Z. Shichang, and P. Ruzheng. Experimental study on repetitive unipolar nanosecond-pulse dielectric barrier discharge in air at atmospheric pressure. *Journal of Physics D: Applied Physics*, 41(21):215203, 2008.

- [174] J. Walsh, P. Olszewski, and J. Bradley. The manipulation of atmospheric pressure dielectric barrier plasma jets. *Plasma Sources Science and Technology*, 21(3):034007, 2012.
- [175] Y. Liu, H. Yan, H. Guo, Z. Fan, Y. Wang, Y. Wu, and C. Ren. Effect of parallel magnetic field on repetitively unipolar nanosecond pulsed dielectric barrier discharge under different pulse repetition frequencies. *Physics of Plasmas*, 25(3), 2018.
- [176] G. Pan, Z. Tan, J. Pan, X. Wang, and C. Shan. A comparative study on the frequency effects of the electrical characteristics of the pulsed dielectric barrier discharge in He/O₂ and in Ar/O₂ at atmospheric pressure. *Physics of Plasmas*, 23(4), 2016.
- [177] H. K. Song, H. Lee, J.-W. Choi, and B.-k. Na. Effect of electrical pulse forms on the CO₂ reforming of methane using atmospheric dielectric barrier discharge. *Plasma chemistry and plasma processing*, 24:57, 2004.
- [178] H. Min Joh, S. Ja Kim, T. Chung, and S. Leem. Reactive oxygen species-related plasma effects on the apoptosis of human bladder cancer cells in atmospheric pressure pulsed plasma jets. *Applied Physics Letters*, 101(5), 2012.
- [179] S. A. Norberg, G. M. Parsey, A. M. Lietz, E. Johnsen, and M. J. Kushner. Atmospheric pressure plasma jets onto a reactive water layer over tissue: pulse repetition rate as a control mechanism. *Journal of Physics D: Applied Physics*, 52(1):015201, 2018.
- [180] B. Huang, C. Zhang, H. Sun, D. A. Sorokin, V. F. Tarasenko, and T. Shao. Enhancement of hydrogen radical density in atmospheric pressure plasma jet by a burst of nanosecond pulses at 1 MHz. *Plasma Sources Science and Technology*, 31(2):025019, 2022.
- [181] S. Shen, J. Yan, Y. Wang, Y. Wang, W. Ding, and G. Sun. Stepwise development of atmospheric pressure plasma jet driven by bursts of high-voltage nanosecond pulses at multi-tens MHz. *Plasma Sources Science and Technology*, 31(10):105003, 2022.

- [182] Y. Li, H. Li, Z. Liu, Y. Fu, H. Luo, X. Zou, and X. Wang. Breakdown, discharge modes, and gaseous recovery of atmospheric air with repetitive 10 ns pulses. *Physics of Plasmas*, 28(7), 2021.
- [183] B.-D. Huang, K. Takashima, X.-M. Zhu, and Y.-K. Pu. The influence of the repetition rate on the nanosecond pulsed pin-to-pin microdischarges. *Journal of Physics D: Applied Physics*, 47(42):422003, 2014.
- [184] X. Mao, H. Zhong, Z. Wang, T. Ombrello, and Y. Ju. Effects of inter-pulse coupling on nanosecond pulsed high frequency discharge ignition in a flowing mixture. *Proceedings of the Combustion Institute*, 39(4):5457, 2023.
- [185] J. K. Lefkowitz, S. D. Hammack, C. D. Carter, and T. M. Ombrello. Elevated OH production from NPHFD and its effect on ignition. *Proceedings of the Combustion Institute*, 38(4):6671, 2021.
- [186] A. M. Lietz and M. J. Kushner. Air plasma treatment of liquid covered tissue: long timescale chemistry. *Journal of Physics D: Applied Physics*, 49(42):425204, 2016.
- [187] D. S. Stafford and M. J. Kushner. O₂ (Δ 1) production in He/ O₂ mixtures in flowing low pressure plasmas. *Journal of Applied Physics*, 96(5):2451, 2004.
- [188] S. D. Rockwood. Elastic and inelastic cross sections for electron-Hg scattering from Hg transport data. *Physical Review A*, 8(5):2348, 1973.
- [189] M. M. Turner. Uncertainty and sensitivity analysis in complex plasma chemistry models. *Plasma Sources Science and Technology*, 25(1):015003, 2016.
- [190] C. Vasko, D.-X. Liu, E. Van Veldhuizen, F. Iza, and P. J. Bruggeman. Hydrogen peroxide production in an atmospheric pressure RF glow discharge: comparison of models and experiments. *Plasma Chemistry and Plasma Processing*, 34:1081, 2014.
- [191] Y. Du, G. Nayak, G. Oinuma, Z. Peng, and P. J. Bruggeman. Effect of water vapor on plasma morphology, OH and H₂O₂ production in He and Ar atmospheric pressure

- dielectric barrier discharges. *Journal of Physics D: Applied Physics*, 50(14):145201, 2017.
- [192] Y. Luo, A. M. Lietz, S. Yatom, M. J. Kushner, and P. J. Bruggeman. Plasma kinetics in a nanosecond pulsed filamentary discharge sustained in Ar-H₂O and H₂O. *Journal of Physics D: Applied Physics*, 52(4):044003, 2018.
- [193] B. R. Locke and K.-Y. Shih. Review of the methods to form hydrogen peroxide in electrical discharge plasma with liquid water. *Plasma Sources Science and Technology*, 20(3):034006, 2011.
- [194] G. Nayak, N. Sadeghi, and P. J. Bruggeman. He (23S1) and He₂ (a₃Σ^u+) metastables densities measured in an RF-driven helium plasma using broadband absorption spectroscopy. *Plasma Sources Science and Technology*, 28(12):125006, 2019.
- [195] P. Pędziwiatr, F. Mikołajczyk, D. Zawadzki, K. Mikołajczyk, and A. Bedka. Decomposition of hydrogen peroxide – kinetics and review of chosen catalysts. *Acta Innovations*, 26:45, 2018.
- [196] D. Lary. Catalytic destruction of stratospheric ozone. *Journal of Geophysical Research: Atmospheres*, 102(D17):21515, 1997.
- [197] I. Larin. On Ozone Depletion in the Mesosphere. *Izvestiya, Atmospheric and Oceanic Physics*, 58(2):150, 2022.
- [198] S. W. Benson and A. E. Axworthy Jr. Mechanism of the gas phase, thermal decomposition of ozone. *The Journal of Chemical Physics*, 26(6):1718, 1957.
- [199] B. L. Sands and B. N. Ganguly. Ozone generation in a kHz-pulsed He-O₂ capillary dielectric barrier discharge operated in ambient air. *Journal of Applied Physics*, 114(24), 2013.
- [200] B. Harris, L. Krös, A. Nave, E. Wagenaars, and J. van Helden. The spatial density distribution of H₂O₂ in the effluent of the COST-Jet and the kINPen-sci operated with

- a humidified helium feed gas. *Plasma Sources Science and Technology*, 32(11):115010, 2023.
- [201] J. Winter, et al. Tracking plasma generated H₂O₂ from gas into liquid phase and revealing its dominant impact on human skin cells. *Journal of Physics D: Applied Physics*, 47(28):285401, 2014.
- [202] S. Reuter, J. Winter, S. Iséni, A. Schmidt-Bleker, M. Dünnbier, K. Masur, K. Wende, and K.-D. Weltmann. The influence of feed gas humidity versus ambient humidity on atmospheric pressure plasma jet-effluent chemistry and skin cell viability. *IEEE Transactions on Plasma Science*, 43(9):3185, 2014.
- [203] A. O’Keefe and D. A. Deacon. Cavity ring-down optical spectrometer for absorption measurements using pulsed laser sources. *Review of scientific instruments*, 59(12):2544, 1988.
- [204] N. Lang, U. Macherius, M. Wiese, H. Zimmermann, J. Röpcke, and J. H. van Helden. Sensitive CH₄ detection applying quantum cascade laser based optical feedback cavity-enhanced absorption spectroscopy. *Optics Express*, 24(6):A536, 2016.
- [205] C. Wang and N. Srivastava. OH number densities and plasma jet behavior in atmospheric microwave plasma jets operating with different plasma gases (Ar, Ar/N₂, and Ar/O₂). *The European Physical Journal D*, 60:465, 2010.
- [206] N. Srivastava and C. Wang. Determination of OH radicals in an atmospheric pressure helium microwave plasma jet. *IEEE Transactions on Plasma Science*, 39(3):918, 2011.
- [207] R. Zaplotnik, M. Bišćan, N. Krstulović, D. Popović, and S. Milošević. Cavity ring-down spectroscopy for atmospheric pressure plasma jet analysis. *Plasma Sources Science Technology*, 24(5):054004, 2015.
- [208] J. Benedikt, D. Schröder, S. Schneider, G. Willems, A. Pajdarová, J. Vlček, and V. Schulz-Von Der Gathen. Absolute OH and O radical densities in effluent of a

- He/H₂O micro-scaled atmospheric pressure plasma jet. *Plasma Sources Science and Technology*, 25(4):045013, 2016.
- [209] M. Gianella, S. Reuter, A. L. Aguila, G. A. D. Ritchie, and J. H. van Helden. Detection of HO₂ in an atmospheric pressure plasma jet using optical feedback cavity-enhanced absorption spectroscopy. *New Journal of Physics*, 18(11):113027, 2016.
- [210] M. Gianella, S. Reuter, S. A. Press, A. Schmidt-Bleker, J. H. van Helden, and G. A. D. Ritchie. HO₂ reaction kinetics in an atmospheric pressure plasma jet determined by cavity ring-down spectroscopy. *Plasma Sources Science and Technology*, 27(9):095013, 2018.
- [211] S. J. Klose, K. M. Manfred, H. C. Norman, G. A. D. Ritchie, and J. H. van Helden. The spatial distribution of HO₂ in an atmospheric pressure plasma jet investigated by cavity ring-down spectroscopy. *Plasma Sources Science and Technology*, 29(8):085011, 2020.
- [212] S.-J. Klose, L. Kroes, and J. H. van Helden. The localised density of H₂O₂ in the effluent of a cold atmospheric pressure plasma jet determined by continuous-wave cavity ring-down spectroscopy. *Frontiers in Physics*, 11:1221181, 2023.
- [213] T. Verreycken, R. Mensink, R. Van Der Horst, N. Sadeghi, and P. J. Bruggeman. Absolute OH density measurements in the effluent of a cold atmospheric-pressure Ar–H₂O RF plasma jet in air. *Plasma Sources Science and Technology*, 22(5):055014, 2013.
- [214] S. Yatom, Y. Luo, Q. Xiong, and P. J. Bruggeman. Nanosecond pulsed humid Ar plasma jet in air: shielding, discharge characteristics and atomic hydrogen production. *Journal of Physics D: Applied Physics*, 50(41):415204, 2017.
- [215] S.-J. Klose, J. Ellis, F. Riedel, S. Schröter, K. Niemi, I. L. Semenov, K.-D. Weltmann, T. Gans, D. O’Connell, and J. H. van Helden. The spatial distribution of hydrogen and oxygen atoms in a cold atmospheric pressure plasma jet. *Plasma Sources Science and Technology*, 29(12):125018, 2020.

- [216] S. Schröter, J. Bredin, A. R. Gibson, A. West, J. P. Dedrick, E. Wagenaars, K. Niemi, T. Gans, and D. O'Connell. The formation of atomic oxygen and hydrogen in atmospheric pressure plasmas containing humidity: picosecond two-photon absorption laser induced fluorescence and numerical simulations. *Plasma Sources Science and Technology*, 29(10):105001, 2020.
- [217] B. Myers, E. Barnat, and K. Stapelmann. Atomic oxygen density determination in the effluent of the COST reference source using in situ effective lifetime measurements in the presence of a liquid interface. *Journal of Physics D: Applied Physics*, 54(45):455202, 2021.
- [218] K. Stapelmann, B. Myers, M. H. Quesada, E. Lenker, and P. J. Ranieri. Following O and OH in He/O₂ and He/H₂O gas mixtures—from the gas phase through the liquid phase to modifications on a biological sample. *Journal of Physics D: Applied Physics*, 54(43):434003, 2021.
- [219] D. van den Bekerom, M. M. Tahiyat, E. Huang, J. H. Frank, and T. I. Farouk. 2D-imaging of absolute OH and H₂O₂ profiles in a He–H₂O nanosecond pulsed dielectric barrier discharge by photo-fragmentation laser-induced fluorescence. *Plasma Sources Science and Technology*, 32(1):015006, 2023.
- [220] G. Willems, J. Benedikt, and A. Von Keudell. Absolutely calibrated mass spectrometry measurement of reactive and stable plasma chemistry products in the effluent of a He/H₂O atmospheric plasma. *Journal of Physics D: Applied Physics*, 50(33):335204, 2017.
- [221] A. Perrin, A. Valentin, J. Flaud, C. Camypeyret, L. Schriver, A. Schriver, and P. Arcas. The 7.9- μ m Band of Hydrogen Peroxide: Line Positions and Intensities. *Journal of Molecular Spectroscopy*, 171(2):358, 1995.
- [222] A. Perrin, J.-M. Flaud, C. Camy-Peyret, R. Schermaul, M. Winnewisser, J.-Y. Mandin, V. Dana, M. Badaoui, and J. Koput. Line Intensities in the Far-Infrared Spectrum of H₂O₂. *Journal of Molecular Spectroscopy*, 176(2):287, 1996.

- [223] S. Klee, M. Winnewisser, A. Perrin, and J.-M. Flaud. Absolute Line Intensities for the ν_6 Band of H₂O₂. *Journal of Molecular Spectroscopy*, 195(1):154, 1999.
- [224] G. Berden and R. Engeln. *Cavity ring-down spectroscopy: techniques and applications*. John Wiley & Sons, 2009.
- [225] S. Kelly, J. Golda, M. M. Turner, and V. Schulz-von der Gathen. Gas and heat dynamics of a micro-scaled atmospheric pressure plasma reference jet. *Journal of Physics D: Applied Physics*, 48(44):444002, 2015.
- [226] A. Schmidt-Bleker, S. Reuter, and K. D. Weltmann. Quantitative schlieren diagnostics for the determination of ambient species density, gas temperature and calorimetric power of cold atmospheric plasma jets. *Journal of Physics D: Applied Physics*, 48(17):175202, 2015.
- [227] P. Virtanen, et al. SciPy 1.0: fundamental algorithms for scientific computing in Python. *Nature methods*, 17(3):261, 2020.
- [228] R. V. Kochanov, I. Gordon, L. Rothman, P. Wcisło, C. Hill, and J. Wilzewski. HITRAN Application Programming Interface (HAPI): A comprehensive approach to working with spectroscopic data. *Journal of Quantitative Spectroscopy and Radiative Transfer*, 177:15, 2016.
- [229] A. Yayci, T. Dirks, F. Kogelheide, M. Alcalde, F. Hollmann, P. Awakowicz, and J. E. Bandow. Microscale Atmospheric Pressure Plasma Jet as a Source for Plasma-Driven Biocatalysis. *ChemCatChem*, 12(23):5893, 2020.
- [230] A. B. Murphy. Transport coefficients of helium and argon-helium plasmas. *IEEE Transactions on plasma science*, 25(5):809, 1997.
- [231] J. Jonkers, M. Van De Sande, A. Sola, A. Gamero, and J. Van Der Mullen. On the differences between ionizing helium and argon plasmas at atmospheric pressure. *Plasma Sources Science and Technology*, 12(1):30, 2002.

- [232] M. Moravej, X. Yang, G. Nowling, J. Chang, R. Hicks, and S. Babayan. Physics of high-pressure helium and argon radio-frequency plasmas. *Journal of applied physics*, 96(12):7011, 2004.
- [233] S. Hofmann, A. Van Gessel, T. Verreycken, and P. Bruggeman. Power dissipation, gas temperatures and electron densities of cold atmospheric pressure helium and argon RF plasma jets. *Plasma Sources Science and Technology*, 20(6):065010, 2011.
- [234] J. Shi and M. G. Kong. Expansion of the plasma stability range in radio-frequency atmospheric-pressure glow discharges. *Applied Physics Letters*, 87(20), 2005.
- [235] G. Hübner, L. Bischoff, I. Korolov, Z. Donkó, M. Leimkühler, Y. Liu, M. Böke, V. Schulz-von der Gathen, T. Mussenbrock, and J. Schulze. The effects of the driving frequencies on micro atmospheric pressure He/N₂ plasma jets driven by tailored voltage waveforms. *Journal of Physics D: Applied Physics*, 55(9):095204, 2021.
- [236] S. Park, W. Choe, S. Y. Moon, and J. J. Shi. Electron information in single-and dual-frequency capacitive discharges at atmospheric pressure. *Scientific Reports*, 8(1):7516, 2018.
- [237] H. H. Goto, H.-D. Löwe, and T. Ohmi. Dual excitation reactive ion etcher for low energy plasma processing. *Journal of Vacuum Science & Technology A: Vacuum, Surfaces, and Films*, 10(5):3048, 1992.
- [238] T. Kitajima, Y. Takeo, Z. L. Petrović, and T. Makabe. Functional separation of biasing and sustaining voltages in two-frequency capacitively coupled plasma. *Applied Physics Letters*, 77(4):489, 2000.
- [239] P. Boyle, A. Ellingboe, and M. Turner. Independent control of ion current and ion impact energy onto electrodes in dual frequency plasma devices. *Journal of Physics D: Applied Physics*, 37(5):697, 2004.

- [240] C. O'Neill, J. Waskoenig, and T. Gans. Tailoring electron energy distribution functions through energy confinement in dual radio-frequency driven atmospheric pressure plasmas. *Applied Physics Letters*, 101(15), 2012.
- [241] B. G. Heil, U. Czarnetzki, R. P. Brinkmann, and T. Mussenbrock. On the possibility of making a geometrically symmetric RF-CCP discharge electrically asymmetric. *Journal of Physics D: Applied Physics*, 41(16):165202, 2008.
- [242] Z. Donkó, J. Schulze, B. Heil, and U. Czarnetzki. PIC simulations of the separate control of ion flux and energy in CCRF discharges via the electrical asymmetry effect. *Journal of Physics D: Applied Physics*, 42(2):025205, 2008.
- [243] J. Schulze, E. Schüngel, Z. Donkó, and U. Czarnetzki. The electrical asymmetry effect in multi-frequency capacitively coupled radio frequency discharges. *Plasma Sources Science and Technology*, 20(1):015017, 2011.
- [244] A. Derzsi, B. Bruneau, A. R. Gibson, E. Johnson, D. O'Connell, T. Gans, J.-P. Booth, and Z. Donkó. Power coupling mode transitions induced by tailored voltage waveforms in capacitive oxygen discharges. *Plasma Sources Science and Technology*, 26(3):034002, 2017.
- [245] A. R. Gibson, et al. Disrupting the spatio-temporal symmetry of the electron dynamics in atmospheric pressure plasmas by voltage waveform tailoring. *Plasma Sources Science and Technology*, 28(1):01LT01, 2019.
- [246] I. Korolov, Z. Donko, G. Hübner, L. Bischoff, P. Hartmann, T. Gans, Y. Liu, T. Mussenbrock, and J. Schulze. Control of electron dynamics, radical and metastable species generation in atmospheric pressure RF plasma jets by voltage waveform tailoring. *Plasma Sources Science and Technology*, 28(9):094001, 2019.
- [247] I. Korolov, et al. Helium metastable species generation in atmospheric pressure RF plasma jets driven by tailored voltage waveforms in mixtures of He and N₂. *Journal of Physics D: Applied Physics*, 53(18):185201, 2020.

- [248] I. Korolov, Z. Donkó, G. Hübner, Y. Liu, T. Mussenbrock, and J. Schulze. Energy efficiency of voltage waveform tailoring for the generation of excited species in RF plasma jets operated in He/N₂ mixtures. *Plasma Sources Science and Technology*, 30(9):095013, 2021.
- [249] I. Korolov, D. Steuer, L. Bischoff, G. Hübner, Y. Liu, V. Schulz-Von der Gathen, M. Böke, T. Mussenbrock, and J. Schulze. Atomic oxygen generation in atmospheric pressure RF plasma jets driven by tailored voltage waveforms in mixtures of He and O₂. *Journal of Physics D: Applied Physics*, 54(12):125203, 2021.
- [250] A. Derzsi, T. Lafleur, J.-P. Booth, I. Korolov, and Z. Donkó. Experimental and simulation study of a capacitively coupled oxygen discharge driven by tailored voltage waveforms. *Plasma Sources Science and Technology*, 25(1):015004, 2015.
- [251] B. Bruneau, T. Novikova, T. Lafleur, J.-P. Booth, and E. Johnson. Ion flux asymmetry in radiofrequency capacitively-coupled plasmas excited by sawtooth-like waveforms. *Plasma Sources Science and Technology*, 23(6):065010, 2014.
- [252] T. Lafleur, P.-A. Delattre, J. Booth, E. Johnson, and S. Diné. Radio frequency current-voltage probe for impedance and power measurements in multi-frequency unmatched loads. *Review of Scientific Instruments*, 84(1), 2013.
- [253] C. M. Horwitz. Radio frequency sputtering—the significance of power input. *Journal of Vacuum Science & Technology A: Vacuum, Surfaces, and Films*, 1(4):1795, 1983.
- [254] S. J. Doyle, A. R. Gibson, R. W. Boswell, C. Charles, and J. P. Dedrick. Decoupling ion energy and flux in intermediate pressure capacitively coupled plasmas via tailored voltage waveforms. *Plasma Sources Science and Technology*, 29(12):124002, 2020.
- [255] J. Franek, S. Brandt, B. Berger, M. Liese, M. Barthel, E. Schüngel, and J. Schulze. Power supply and impedance matching to drive technological radio-frequency plasmas with customized voltage waveforms. *Review of Scientific Instruments*, 86(5), 2015.

- [256] F. Schmidt, J. Schulze, E. Johnson, J.-P. Booth, D. Keil, D. M. French, J. Trieschmann, and T. Mussenbrock. Multi frequency matching for voltage waveform tailoring. *Plasma Sources Science and Technology*, 27(9):095012, 2018.
- [257] J. Wang, S. Dine, J.-P. Booth, and E. V. Johnson. Experimental demonstration of multifrequency impedance matching for tailored voltage waveform plasmas. *Journal of Vacuum Science & Technology A*, 37(2), 2019.
- [258] P. W. Atkins and J. De Paula. *Atkins' physical chemistry*. Oxford university press, 2014.
- [259] D. McCaa and J. Shaw. The infrared spectrum of ozone. *Journal of Molecular Spectroscopy*, 25(3):374, 1968.
- [260] A. Barbe, S. Mikhailenko, E. Starikova, and V. Tyuterev. High resolution infrared spectroscopy in support of ozone atmospheric monitoring and validation of the potential energy function. *Molecules*, 27(3):911, 2022.
- [261] Q. Wang, F. Doll, V. M. Donnelly, D. J. Economou, N. Sadeghi, and G. F. Franz. Experimental and theoretical study of the effect of gas flow on gas temperature in an atmospheric pressure microplasma. *Journal of Physics D: Applied Physics*, 40(14):4202, 2007.
- [262] Q. Wang, I. Koleva, V. M. Donnelly, and D. J. Economou. Spatially resolved diagnostics of an atmospheric pressure direct current helium microplasma. *Journal of Physics D: Applied Physics*, 38(11):1690, 2005.
- [263] V. N. Ochkin. *Spectroscopy of low temperature plasma*. John Wiley & Sons, 2009.
- [264] H. Nassar, S. Pellerin, K. Musiol, O. Martinie, N. Pellerin, and J. Cormier. N₂⁺/N₂ ratio and temperature measurements based on the first negative N₂⁺ and second positive N₂ overlapped molecular emission spectra. *Journal of Physics D: Applied Physics*, 37(14):1904, 2004.

- [265] C. E. Nwankire, V. J. Law, A. Nindrayog, B. Twomey, K. Niemi, V. Milosavljević, W. Graham, and D. Dowling. Electrical, thermal and optical diagnostics of an atmospheric plasma jet system. *Plasma chemistry and plasma processing*, 30:537, 2010.
- [266] B. Twomey, A. Nindrayog, K. Niemi, W. Graham, and D. Dowling. Correlation between the electrical and optical properties of an atmospheric pressure plasma during siloxane coating deposition. *Plasma chemistry and plasma processing*, 31:139, 2011.
- [267] D. N. Meehan, K. Niemi, and E. Wagenaars. Gas temperature measurements in a pulsed, low-pressure inductively coupled plasma in oxygen. *Japanese Journal of Applied Physics*, 59:SHHB03, 2020.
- [268] G. Herzberg. *Molecular spectra and molecular structure*. D. van Nostrand, 1945.
- [269] F. Roux, F. Michaud, and M. Vervloet. High-resolution Fourier spectrometry of $^{14}\text{N}_2$ violet emission spectrum: extensive analysis of the $\text{C}^3\Pi_u \rightarrow \text{B}^3\Pi_g$ system. *Journal of molecular spectroscopy*, 158(2):270, 1993.
- [270] I. Kovács. Formulae for rotational intensity distribution of triplet transitions in diatomic molecules. *Astrophysical Journal*, 145:634, 1966.
- [271] A. Schadee. Theory of first rotational lines in transitions of diatomic molecules. *Astronomy and Astrophysics*, 41:203, 1975.
- [272] D. Ellerweg, J. Benedikt, A. von Keudell, N. Knake, and V. Schulz-von der Gathen. Characterization of the effluent of a He/O₂ microscale atmospheric pressure plasma jet by quantitative molecular beam mass spectrometry. *New Journal of physics*, 12(1):013021, 2010.
- [273] C. von Rosenberg Jr and D. W. Trainor. Observations of vibrationally excited O₃ formed by recombination. *The Journal of Chemical Physics*, 59(4):2142, 1973.
- [274] D. Lopaev, E. Malykhin, and S. Zyryanov. Surface recombination of oxygen atoms in O₂ plasma at increased pressure: II. Vibrational temperature and surface production of ozone. *Journal of Physics D: Applied Physics*, 44(1):015202, 2010.

- [275] J.-P. Booth, O. Guaitella, S. Zhang, D. Lopaev, S. Zyryanov, T. Rakhimova, D. Voloshin, A. Chukalovsky, A. Volynets, and Y. Mankelevich. Oxygen atom and ozone kinetics in the afterglow of a pulse-modulated DC discharge in pure O₂: an experimental and modelling study of surface mechanisms and ozone vibrational kinetics. *Plasma Sources Science and Technology*, 32(9):095016, 2023.
- [276] T. Murakami, K. Niemi, T. Gans, D. O’Connell, and W. G. Graham. Afterglow chemistry of atmospheric-pressure helium–oxygen plasmas with humid air impurity. *Plasma Sources Science and Technology*, 23(2):025005, 2014.
- [277] D. Ellerweg, A. Von Keudell, and J. Benedikt. Unexpected O and O₃ production in the effluent of He/O₂ microplasma jets emanating into ambient air. *Plasma Sources Science and Technology*, 21(3):034019, 2012.
- [278] J. D. McClurkin, D. E. Maier, and K. E. Ileleji. Half-life time of ozone as a function of air movement and conditions in a sealed container. *Journal of Stored Products Research*, 55:41, 2013.
- [279] M. Vass, S. Wilczek, J. Schulze, and Z. Donkó. Electron power absorption in micro atmospheric pressure plasma jets driven by tailored voltage waveforms in He/N₂. *Plasma Sources Science and Technology*, 30(10):105010, 2021.
- [280] Z. Zhang, Q. Nie, X. Zhang, Z. Wang, F. Kong, B. Jiang, and J. Lim. Ionization asymmetry effects on the properties modulation of atmospheric pressure dielectric barrier discharge sustained by tailored voltage waveforms. *Physics of Plasmas*, 25(4), 2018.
- [281] Biagi. v8.9 database. Available at: www.lxcat.net (Accessed 29 July 2020) retrieved July 2012.
- [282] S. Biagi. Fortran program, MAGBOLTZ, versions 8.9 and after. URL www.lxcat.net/Biagi, 2004.
- [283] Y. Itikawa and N. Mason. Cross sections for electron collisions with water molecules. *J. Phys. Chem. Ref. Data*, 34:1, 2005.

- [284] M. Yousfi and M. D. Benabdessadok. Boltzmann equation analysis of electron-molecule collision cross sections in water vapor and ammonia. *J. Appl. Phys.*, 80:6619, 1996.
- [285] S. A. Lawton and A. V. Phelps. Excitation of the $b1\Sigma+g$ state of O₂ by low energy electrons. *J. Chem. Phys.*, 69:1055, 1978.
- [286] L. Vriens. Calculation of absolute ionisation cross sections of He, He*, He+, Ne, Ne*, Ne+, Ar, Ar*, Hg and Hg*. *Phys. Lett.*, 8:260, 1964.
- [287] M. R. Flannery, K. J. McCann, and N. W. Winter. Cross sections for electron impact ionisation of metastable rare-gas excimers (He₂*, Kr₂*, Xe₂*). *J. Phys. B: At. Mol. Opt. Phys.*, 14:3789, 1981.
- [288] R. Riahi, P. Teulet, Z. B. Lakhdar, and A. Gleizes. Cross-section and rate coefficient calculation for electron impact excitation, ionisation and dissociation of H₂ and OH molecules. *Eur. Phys. J. D*, 40:223, 2006.
- [289] R. R. Laher and F. R. Gilmore. Updated excitation and ionization cross sections for electron impact on atomic oxygen. *J. Phys. Chem. Ref. Data*, 19:277, 1990.
- [290] M. Gryziński. Classical theory of atomic collisions. I. Theory of inelastic collisions. *Phys. Rev.*, 138:A336, 1965.
- [291] R. I. Hall and S. Trajmar. Scattering of 4.5 eV electrons by ground ($X^3\Sigma_g^-$ state and metastable ($a^1\Delta_g$ oxygen molecules. *J. Phys. B: At. Mol. Opt. Phys.*, 8:L293, 1975.
- [292] K. N. Joshipura, B. K. Antony, and M. Vinodkumar. Electron scattering and ionization of ozone, O₂ and O₄ molecules. *J. Phys. B: At. Mol. Opt. Phys.*, 35:4211, 2002.
- [293] J. McConkey, C. Malone, P. Johnson, C. Winstead, V. McKoy, and I. Kanik. Electron impact dissociation of oxygen-containing molecules—A critical review. *Phys. Rep.*, 466:1, 2008.
- [294] R. Deloche, P. Monchicourt, M. Cheret, and F. Lambert. High-pressure helium afterglow at room temperature. *Phys. Rev. A*, 13:1140, 1976.

- [295] W. Kedzierski, J. Derbyshire, C. Malone, and J. W. McConkey. Isotope effects in the electron impact break-up of water. *J. Phys. B: At. Mol. Opt. Phys.*, 31:5361, 1998.
- [296] T. Harb, W. Kedzierski, and J. W. McConkey. Production of ground state OH following electron impact on H₂O. *J. Chem. Phys.*, 115:5507, 2001.
- [297] K. Ding, M. A. Lieberman, and A. J. Lichtenberg. Hybrid model of neutral diffusion, sheaths, and the alpha to gamma transition in an atmospheric pressure He/H₂O bounded rf discharge. *J. Phys. D: Appl. Phys.*, 47, 2014.
- [298] S. J. B. Corrigan. Dissociation of molecular hydrogen by electron impact. *J. Chem. Phys.*, 43:4381, 1965.
- [299] M. Hayashi. Monte Carlo simulation of electron avalanche in hydrogen. *J. Phys. Colloq.*, 40:C7, 1979.
- [300] L. W and V. G. A. Electron Energy Deposition in Carbon Monoxide Gas. *Astrophys. J.*, 435:909, 1994.
- [301] I. A. Soloshenko, V. V. Tsiolko, S. S. Pogulay, A. G. Kalyuzhnaya, V. Y. Bazhenov, and A. I. Shchedrin. Effect of water adding on kinetics of barrier discharge in air. *Plasma Sources Sci. Technol.*, 18, 2009.
- [302] M. Gupta and K. L. Baluja. Electron collisions with an ozone molecule using the R-matrix method. *J. Phys. B: At. Mol. Opt. Phys.*, 38:4057, 2005.
- [303] E. Krishnakumar and S. Srivastava. Cross-sections for electron impact ionization of O₂. *Int. J. Mass Spectrometry and Ion Processes*, 113:1, 1992.
- [304] C. E. Melton and G. A. Neece. Rate constants and cross sections for the production of OH- from O- and H- in water. *J. Am. Chem. Soc.*, 93:6757, 1971.
- [305] D. Nandi, E. Krishnakumar, A. Rosa, W.-F. Schmidt, and E. Illenberger. Dissociative electron attachment to H₂O₂: a very effective source for OH and OH- generation. *Chem. Phys. Lett.*, 373:454, 2003.

- [306] P. D. Burrow. Dissociative attachment from the $O_2(a^1\Delta_g)$ state. *J. Chem. Phys.*, 59:4922, 1973.
- [307] S. Matejcek, A. Kiendler, P. Cicman, J. Skalny, P. Stampfli, E. Illenberger, Y. Chu, A. Stamatovic, and T. D. Märk. Electron attachment to molecules and clusters of atmospheric relevance: oxygen and ozone. *Plasma Sources Sci. Technol.*, 6:140, 1997.
- [308] R. K. Janev, W. D. Langer, K. J. Evans, and D. E. J. Post. *Elementary Processes in Hydrogen-Helium Plasmas: Cross Sections and Reaction Rate Coefficients*. Springer, 1987.
- [309] H. B. Pedersen, N. Djurić, M. J. Jensen, D. Kella, C. P. Safvan, H. T. Schmidt, L. Vejby-Christensen, and L. H. Andersen. Electron collisions with diatomic anions. *Phys. Rev. A*, 60:2882, 1999.
- [310] H. Deutsch, P. Scheier, K. Becker, and T. D. Märk. Calculated cross-sections for the electron-impact detachment from negative ions using the Deutsch-Märk (DM) formalism. *Chem. Phys. Lett.*, 382:26, 2003.
- [311] H. Deutsch, K. Becker, M. Probst, W. Zhu, and T. Märk. Calculated absolute cross-sections for the electron-induced detachment of the B_2^- , O_2^- , BO^- , and CN^- anions using the Deutsch-Märk (DM) formalism. *Int. J. Mass Spectrometry*, 277:151, 2008.
- [312] K. Seiersen, J. Bak, H. Bluhme, M. J. Jensen, S. B. Nielsen, and L. H. Andersen. Electron-impact detachment of O_3^- , NO_3^- and SO_2^- ions. *Phys. Chem. Chem. Phys.*, 5:4814, 2003.
- [313] B. M. A. *Principles of Laser Plasmas*. G Bekefi, 1976.
- [314] A. I. Florescu-Mitchell and J. B. A. Mitchell. Dissociative recombination. *Phys. Rep.*, 430:277, 2006.
- [315] D. McElroy, C. Walsh, A. J. Markwick, M. A. Cordiner, K. Smith, and T. J. Millar. The UMIST database for astrochemistry 2012. *Astron. Astrophys.*, 550:A36, 2013.

- [316] S. Rosén, et al. Recombination of simple molecular ions studied in storage ring: dissociative recombination of H_2O^+ . *Faraday Discuss.*, 115:295, 2000.
- [317] M. J. Jensen, R. C. Bilodeau, C. P. Safvan, K. Seiersen, L. H. Andersen, H. B. Pedersen, and O. Heber. Dissociative Recombination of H_3O^+ , HD_2O^+ , and D_3O^+ . *Astrophys. J.*, 543:764, 2000.
- [318] O. Novotny, et al. Fragmentation channels in dissociative electron recombination with hydronium and other astrophysically important species. *J. Phys. Chem. A*, 114:4870, 2010.
- [319] M. H. Bortner and T. Baurer. *Defense Nuclear Agency Reaction Rate Handbook*. Space Div., General Electric Co., 1978. Revision Number 7.
- [320] C.-M. Huang, M. Whitaker, M. A. Biondi, and R. Johnsen. Electron-temperature dependence of recombination of electrons with H_3O^+ . $(\text{H}_2\text{O})_n$ -series ions. *Phys. Rev. A*, 18:64, 1978.
- [321] M. T. Leu, M. A. Biondi, and R. Johnsen. Measurements of the recombination of electrons with H_3O^+ . $(\text{H}_2\text{O})_n$ -Series Ions. *Phys. Rev. A*, 7:292, 1973.
- [322] R. Peverall, et al. Dissociative recombination and excitation of O_2^+ : cross sections, product yields and implications for studies of ionospheric airglows. *J. Chem. Phys.*, 114:6679, 2001.
- [323] V. Zhaunerchyk, W. D. Geppert, F. Österdahl, M. Larsson, R. D. Thomas, E. Bahati, M. E. Bannister, M. R. Fogle, and C. R. Vane. Dissociative recombination dynamics of the ozone cation. *Phys. Rev. A*, 77, 2008.
- [324] J. L. Dulaney, M. A. Biondi, and R. Johnsen. Electron-temperature dependence of the recombination of electrons with O_4^+ ions. *Phys. Rev. A*, 37:2539, 1988.
- [325] Morgan (Kinema Research & Software) database. Available at: www.lxcat.net.

- [326] S. S. Prasad and J. H. W. T. A model for gas phase chemistry in interstellar clouds: I. The basic model, library of chemical reactions, and chemistry among C, N, and O compounds. *Astrophys. J. Suppl. Ser.*, 43:1, 1980.
- [327] G. Mauclaire, R. Derai, and R. Marx. ICR determination of kinetically excited ions produced in water and methane by charge transfer from thermal rare gas ions. *Int. J. Mass Spectrom. Ion Phys.*, 26:289, 1978.
- [328] B. R. Eichelberger, T. P. Snow, and V. M. Bierbaum. Collision rate constants for polarizable ions. *J. Am. Soc. Mass Spectrom.*, 14:501, 2003.
- [329] M. P. Langevin. Une formule fondamentale de theorie cinetique. *Annales De Chimie Et De Physique, Series*, 5:245, 1905.
- [330] T. M. Miller. *Atomic and molecular polarizabilities—CRC Handbook of Chemistry and Physics*, volume vol 77. CRC Press, 2000.
- [331] N. G. Adams and D. Smith. Product-ion distributions for some ion-molecule reactions. *J. Phys. B: At. Mol. Opt. Phys.*, 9:1439, 1976.
- [332] Y. Ikezoe. *Gas Phase Ion-molecule Reaction Rate Constants through 1986*. Ion Reaction Research Group of the Mass Spectroscopy Society of Japan, 1987. [Http://www.mssj.jp/english/publications/books.html](http://www.mssj.jp/english/publications/books.html).
- [333] J. D. C. Jones, K. Birkinshaw, and N. D. Twiddy. Rate coefficients and product ion distributions for the reactions of OH⁺ and H₂O⁺ with N₂, O₂, NO, N₂O, Xe, CO, CO₂, H₂S and H₂ at 300 K. *Chem. Phys. Lett.*, 77:484, 1981.
- [334] W. T. Huntress and R. F. Pinizzotto. Product distributions and rate constants for ion-molecule reactions in water, hydrogen sulfide, ammonia, and methane. *J. Chem. Phys.*, 59:4742, 1973.
- [335] A. B. Rakshit and P. Warneck. Reactions of CO₂⁺, CO₂CO₂⁺ and H₂O⁺ ions with various neutral molecules. *J. Chem. Soc. Faraday Trans.*, 76:1084, 1980.

- [336] A. A. Viggiano, D. L. Albritton, F. C. Fehsenfeld, N. G. Adams, D. Smith, and F. Howorka. Laboratory studies of some ion-atom reactions related to interstellar molecular synthesis. *Astrophys. J.*, 236:492, 1980.
- [337] V. G. Anicich. Evaluated bimolecular ion-molecule gas phase kinetics of positive ions for use in modeling planetary atmospheres, cometary comae, and interstellar clouds. *J. Phys. Chemical Ref. Data*, 22:1469, 1993.
- [338] L. W. Sieck, J. T. Heron, and D. S. Green. Chemical kinetics database and predictive schemes for humid air plasma chemistry. Part I: positive ion-molecule reactions. *Plasma Chem. Plasma Process.*, 20:235, 2000.
- [339] D. Smith, N. G. Adams, and T. M. Miller. A laboratory study of the reactions of N^+ , N_2^+ , N_3^+ , N_4^+ , O^+ , O_2^+ , and NO^+ ions with several molecules at 300 K. *J. Chem. Phys.*, 69:308, 1978.
- [340] M. McFarland, D. L. Albritton, F. C. Fehsenfeld, E. E. Ferguson, and A. L. Schmeltekopf. Flow-drift technique for ion mobility and ion-molecule reaction rate constant measurements. II. Positive ion reactions of N^+ , O^+ , and H_2^+ with O_2 and O^+ with N_2 from thermal to “2 eV. *J. Chem. Phys.*, 59:6620, 1973.
- [341] D. A. Crosby and J. C. Zorn. Dipole polarizability of 23S1 and 21S0 metastable helium measured by the electric deflection time-of-flight method. *Phys. Rev. A*, 16:488, 1977.
- [342] G. de Petris. Atmospherically relevant ion chemistry of ozone and its cation. *Mass Spectrom. Rev.*, 22:251, 2003.
- [343] A. B. Rakshit and P. Warneck. A drift chamber study of the formation of water cluster ions in oxygen. *J. Chem. Phys.*, 73:5074, 1980.
- [344] R. K. Nesbet. Atomic polarizabilities for ground and excited states of C, N, and O. *Phys. Rev. A*, 16:1, 1977.
- [345] R. L. Champion, L. D. Doverspike, and S. K. Lam. Electron detachment from negative ions: the effects of isotopic substitution. *Phys. Rev. A*, 13:617, 1976.

- [346] H. Bruhns, H. Kreckel, K. A. Miller, X. Urbain, and D. W. Savin. Absolute energy-resolved measurements of the $\text{H} + \text{H} \rightarrow \text{H}_2 + e^-$ associative detachment reaction using a merged-beam apparatus. *Phys. Rev. A*, 82, 2010.
- [347] O. Martinez, Z. Yang, N. J. Demarais, T. P. Snow, and V. M. Bierbaum. Gas-phase reactions of hydride anion, H^- . *Astrophys. J.*, 720:173, 2010.
- [348] E. E. Ferguson. Rate constants of thermal energy binary ion-molecule reactions of aeronomic interest. *Atomic Data and Nuclear Data Tables*, 12:159, 1973.
- [349] F. C. Fehsenfeld and E. E. Ferguson. Laboratory studies of negative ion reactions with atmospheric trace constituents. *J. Chem. Phys.*, 61:3181, 1974.
- [350] D.-X. Liu, M.-Z. Rong, X.-H. Wang, F. Iza, M. G. Kong, and P. Bruggeman. Main species and physicochemical processes in cold atmospheric-pressure $\text{He} + \text{O}_2$ plasmas. *Plasma Processes Polym.*, 7:846, 2010.
- [351] F. Penent, J. P. Grouard, R. I. Hall, J. L. Montmagnon, R. L. Champion, L. D. Doverspike, and V. A. Esaulov. Fundamental processes in collisions of O^- with atoms and molecules; mechanisms of one- and two-electron loss. *J. Phys. B: At. Mol. Phys.*, 20:6065, 1987.
- [352] S. G. Belostotsky, D. J. Economou, D. V. Lopaev, and T. V. Rakhimova. Negative ion destruction by $\text{O}^+(^3P)$ atoms and $\text{O}_2(a^1\Delta_g)$ molecules in an oxygen plasma. *Plasma Sources Sci. Technol.*, 14:532, 2005.
- [353] S. G. Ard, J. J. Melko, B. Jiang, Y. Li, N. S. Shuman, H. Guo, and A. A. Viggiano. Temperature dependences for the reactions of O_2^- and O^- with N and O atoms in a selected-ion flow tube instrument. *J. Chem. Phys.*, 139, 2013.
- [354] A. Midey, I. Dotan, and A. A. Viggiano. Temperature Dependences for the Reactions of O^- and O_2^- with $\text{O}_2(a^1\Delta_g)$ from 200 to 700 K. *J. Phys. Chem. A*, 112:3040, 2008.
- [355] C. Lifshitz, R. L. C. Wu, J. C. Haartz, and T. O. Tiernan. Associative detachment reactions of negative ions with O_3 . *J. Chem. Phys.*, 67:2381, 1977.

- [356] S. D. T. Axford and A. N. Hayhurst. Mass spectrometric sampling of negative ions from flames of hydrogen and oxygen: the kinetics of electron attachment and detachment in hot mixtures of H₂O, O₂, OH and HO₂. *Proc. R. Soc. A*, 452:1007, 1996.
- [357] H. Bohringer, W. Glebe, and F. Arnold. Temperature dependence of the mobility and association rate coefficient of He⁺ ions in He from 30-350K. *J. Phys. B: At. Mol. Opt. Phys.*, 16:2619, 1983.
- [358] Y. K. Lau, S. Ikuta, and P. Kebarle. Thermodynamics and kinetics of the gas-phase reactions H₃O+(H₂O)_{n-1} + water = H₃O+(H₂O)_n. *J. Am. Chem. Soc.*, 104:1462, 1982.
- [359] H. Böhringer, F. Arnold, D. Smith, and N. Adams. A study of the temperature dependences of the N₂ + N₂ → N₄ + and O₂ + O₂ → O₄ + association reactions using the selected-ion flow-tube and drift-tube techniques. *Int. J. Mass Spectrometry and Ion Phys.*, 52:25, 1983.
- [360] J. de Urquijo, A. Bekstein, G. Ruiz-Vargas, and F. J. Gordillo-Vázquez. Drift and clustering of daughter negative ions of H₂O in parent gas. *J. Phys. D: Appl. Phys.*, 46, 2012.
- [361] H. S. Johnston. *Gas phase reaction kinetics of neutral oxygen species Technical Report NSRDS-NBS-20, National Bureau of Standards*. National Standard Reference Data System, 1968. <https://apps.dtic.mil/sti/citations/ADD095263>.
- [362] R. F. Heidner and D. Husain. A study of the collisional quenching of O(21D₂) by the noble gases employing time-resolved attenuation of atomic resonance radiation in the vacuum ultraviolet. *Int. J. Chem. Kinet.*, 6:77, 1974.
- [363] K. H. Becker, W. Groth, and U. Schurath. The quenching of metastable O₂ 1Δ_g and O₂ 1Σ_g + molecules. *Chem. Phys. Lett.*, 8:259, 1971.
- [364] D. S. Stafford and M. J. Kushner. O₂ 1Δ) production in He/O₂ mixtures in flowing low pressure plasmas. *J. Appl. Phys.*, 96:2451, 2004.

- [365] C. B. Collins and F. W. Lee. Measurement of the rate coefficients for the bimolecular and termolecular de-excitation reactions of He(2 3S) with selected atomic and molecular species. *J. Chem. Phys.*, 70:1275, 1979.
- [366] R. A. Sanders and E. E. Muschlitz. Chemiionization and secondary ion reactions in H₂O and D₂O. *Int. J. Mass Spectrom. Ion Phys.*, 23:99, 1977.
- [367] J. M. Pouvesle, A. Khacef, J. Stevefelt, H. Jahani, V. T. Gylys, and C. B. Collins. Study of two-body and three-body channels for the reaction of metastable helium atoms with selected atomic and molecular species. *J. Chem. Phys.*, 88:3061, 1988.
- [368] A. V. Phelps and J. P. Molnar. Lifetimes of metastable states of noble gases. *Phys. Rev.*, 89:1202, 1953.
- [369] J. M. Pouvesle, J. Stevefelt, F. W. Lee, H. R. Jahani, V. T. Gylys, and C. B. Collins. Reactivity of metastable helium molecules in atmospheric pressure afterglows. *J. Chem. Phys.*, 83:2836, 1985.
- [370] W. Tsang and R. F. Hampson. Chemical kinetic data base for combustion chemistry. Part I. Methane and related compounds. *J. Phys. Chem. Ref. Data*, 15:1087, 1986.
- [371] R. Atkinson, D. L. Baulch, R. A. Cox, J. N. Crowley, R. F. Hampson, R. G. Hynes, M. E. Jenkin, M. J. Rossi, and J. Troe. Evaluated kinetic and photochemical data for atmospheric chemistry: volume I—gas phase reactions of Ox, HOx, NOx and SOx species. *Atmos. Chem. Phys.*, 4:1461, 2004.
- [372] D. Baulch, et al. Evaluated kinetic data for combustion modeling: supplement II. *Journal of physical and chemical reference data*, 34(3):757, 2005.
- [373] J. B. Burkholder, S. P. Sander, J. P. D. Abbatt, J. R. Barker, R. E. Huie, C. E. Kolb, M. J. Kurylo, V. L. Orkin, D. M. Wilmouth, and P. H. Wine. *Chemical Kinetics and Photochemical Data for Use in Atmospheric Studies: Evaluation Number 18*. Jet Propulsion Laboratory, National Aeronautics and Space Administration, 2015.

- [374] J. A. Manion, et al. NIST chemical kinetics database. In *NIST Standard Reference Database 17, Version 7.0 (Web Version), Release 1.6.8, Data version 2015.12. National Institute of Standards and Technology, Gaithersburg, Maryland, 20899-8320 (<http://kinetics.nist.gov/>)*. 2015.
- [375] V. L. Orkin, S. N. Kozlov, G. A. Poskrebyshev, and M. J. Kurylo. Rate constant for the reaction of OH with H₂ between 200 and 480 K. *J. Phys. Chem. A*, 110:6978, 2006.
- [376] L. F. Keyser. Kinetics of the reaction OH + HO₂ → H₂O + O₂ from 254 to 382 K. *J. Phys. Chem.*, 92:1193, 1988.
- [377] R. S. Lewis and R. T. Watson. Temperature dependence of the reaction O(3P) + OH(2II) → O₂ + H. *J. Phys. Chem.*, 84:3495, 1980.
- [378] M. J. Howard and I. W. M. Smith. Direct rate measurements on the reactions N + OH → NO + H and O + OH → O₂ + H from 250 to 515 K. *J. Chem. Soc. Faraday Trans.*, 77:997, 1981.
- [379] T. G. Slanger and G. Black. O(1S) interactions—the product channels. *J. Chem. Phys.*, 68:989, 1978.
- [380] I. S. Fletcher and D. Husain. The collisional quenching of electronically excited oxygen atoms, O(21D₂), by the gases NH₃, H₂O₂, C₂H₆, C₃H₈, and C(CH₃)₄, using time-resolved attenuation of atomic resonance radiation. *Can. J. Chem.*, 54:1765, 1976.
- [381] V. J. Abreu, J. H. Yee, S. C. Solomon, and A. Dalgarno. The quenching rate of O(1D) by O₃P). *Planet. Space Sci.*, 34:1143, 1986.
- [382] K. Schofield. Rate constants for the gaseous interaction of O(21D₂ and O(21S₀)—a critical evaluation. *J. Photochem.*, 9:55, 1978.
- [383] P. H. Wine, J. M. Nicovich, R. J. Thompson, and A. R. Ravishankara. Kinetics of atomic oxygen(3P_J) reactions with hydrogen peroxide and ozone. *J. Phys. Chem.*, 87:3948, 1983.

- [384] T. G. Slanger and G. Black. The product channels in the quenching of O(1S) by O₂(a 1Δg). *J. Chem. Phys.*, 75:2247, 1981.
- [385] T. G. Slanger and G. Black. Quenching of O(1S) by O₂(a1Dg). *Geophys. Res. Lett.*, 8:535, 1981.
- [386] R. D. Kenner and E. A. Ogryzlo. A direct determination of the rate constant for the quenching of O(1S) by O₂(a 1Δg). *J. Photochem.*, 18:379, 1982.
- [387] J. I. Steinfeld, S. M. Adler-Golden, and J. W. Gallagher. Critical survey of data on the spectroscopy and kinetics of ozone in the mesosphere and thermosphere. *J. Phys. Chem. Ref. Data*, 16:911, 1987.
- [388] G. R. Derwent and B. A. Thrush. Measurements on O₂ 1 Δg and O 2 1 Σ + g in discharge flow systems. *Trans. Faraday Soc.*, 67:2036, 1971.
- [389] R. F. Heidner, C. E. Gardner, T. M. El-Sayed, G. I. Segal, and J. V. V. Kasper. Temperature dependence of O₂ 1Δ)+O₂ 1Δ) and I₂P1/2+O₂ 1Δ) energy pooling. *J. Chem. Phys.*, 74:5618, 1981.
- [390] G. Myers and A. J. Cunningham. Rate measurements of reactions of helium metastable species at atmospheric pressures. I. He (2 3S) in pure afterglows. *J. Chem. Phys.*, 67:247, 1977.
- [391] S. R. Sellevåg, Y. Georgievskii, and J. A. Miller. The temperature and pressure dependence of the reactions H + O₂ (+M) → HO₂ (+M) and H + OH (+M) → H₂O (+M). *J. Phys. Chem. A*, 112:5085, 2008.
- [392] R. Zellner, K. Erler, and D. Field. Kinetics of the recombination reaction OH + H + M → H₂O + M at low temperatures. In *Symp. (Int.) on Combustion*, volume vol 16, pages 939–48. 1977.
- [393] K.-J. Hsu, J. L. Durant, and F. Kaufman. Rate constants for H + O₂ + M at 298 K for M = He, N₂, and H₂O. *J. Phys. Chem.*, 91:1895, 1987.

- [394] T. G. Slanger and R. A. Copeland. Energetic oxygen in the upper atmosphere and the laboratory. *Chem. Rev.*, 103:4731, 2003.
- [395] C. L. Lin and M. T. Leu. Temperature and third-body dependence of the rate constant for the reaction $O + O_2 + M \rightarrow O_3 + M$. *Int. J. Chem. Kinet.*, 14:417, 1982.
- [396] V. N. Azyazov, P. Mikheyev, D. Postell, and M. C. Heaven. $O_2(a^1\Delta)$ quenching in the $O/O_2/O_3$ system. *Chem. Phys. Lett.*, 482:56, 2009.
- [397] O. V. Braginskiy, A. N. Vasilieva, K. S. Klopovskiy, A. S. Kovalev, D. V. Lopaev, O. V. Proshina, T. V. Rakhimova, and A. T. Rakhimov. Singlet oxygen generation in O_2 flow excited by RF discharge: I. Homogeneous discharge mode: alpha-mode. *J. Phys. D: Appl. Phys.*, 38:3609, 2005.
- [398] R. Forster, M. Frost, D. Fulle, H. F. Hamann, H. Hippler, A. Schlegegell, and J. Troe. High pressure range of the addition of HO to HO, NO, NO_2 , and CO. I. Saturated laser induced fluorescence measurements at 298 K. *J. Chem. Phys.*, 103:2949, 1995.
- [399] D. Fulle, H. F. Hamann, H. Hippler, and J. Troe. High-pressure range of the addition of HO to HO. III. Saturated laser-induced fluorescence measurements between 200 and 700 K. *J. Chem. Phys.*, 105:1001, 1996.